



HAL
open science

Biophysical and Electrochemical studies of Carbon Monoxide Dehydrogenase: Towards the design of bio-electrocatalysts for the CO₂-CO interconversion

Umberto Contaldo

► **To cite this version:**

Umberto Contaldo. Biophysical and Electrochemical studies of Carbon Monoxide Dehydrogenase: Towards the design of bio-electrocatalysts for the CO₂-CO interconversion. Inorganic chemistry. Université Grenoble Alpes [2020-..], 2021. English. NNT: 2021GRALV057 . tel-03889374

HAL Id: tel-03889374

<https://theses.hal.science/tel-03889374>

Submitted on 8 Dec 2022

HAL is a multi-disciplinary open access archive for the deposit and dissemination of scientific research documents, whether they are published or not. The documents may come from teaching and research institutions in France or abroad, or from public or private research centers.

L'archive ouverte pluridisciplinaire **HAL**, est destinée au dépôt et à la diffusion de documents scientifiques de niveau recherche, publiés ou non, émanant des établissements d'enseignement et de recherche français ou étrangers, des laboratoires publics ou privés.

THÈSE

Pour obtenir le grade de

DOCTEUR DE L'UNIVERSITE GRENOBLE ALPES

Spécialité : **Chimie inorganique et bio-inorganique**

Arrêté ministériel : 25 mai 2016

Présentée par

Umberto Contaldo

Thèse dirigée par **Christine Cavazza, Directrice de Recherche, CEA Grenoble**, et codirigée par **Alan Le Goff, Directeur de Recherche, CNRS**

préparée au sein du **Laboratoire de Chimie et Biologie des Métaux, UMR 5249, Grenoble**
dans l'**École Doctorale de Chimie et Science du Vivant**

Etudes biophysiques et électrochimiques de la monoxyde de carbone déshydrogénase : Vers la conception de bio-électro-catalyseurs pour l'interconversion entre le CO et le CO₂

Thèse soutenue publiquement le **7 décembre 2021**,
devant le jury composé de :

Dr. Carole BAFFERT

Maître de Conférences, Aix-Marseille Université, Rapportrice

Pr. Luis M. RUBIO

Professeur, Université Polytechnique de Madrid, Rapporteur

Dr. Carole DUBOC

Directrice de Recherche CNRS Grenoble, Présidente

Pr. Stefano CIURLI

Professeur, Université de Bologne, Examineur

Dr. Christine CAVAZZA

Directrice de Recherche, CEA Grenoble, Directrice de thèse

Dr. Alan LE GOFF

Directeur de Recherche, CEA Grenoble, Co-Directeur de thèse



TABLE OF CONTENTS

Preface	5
CHAPTER 1 – Introduction	
1.1 Energy and alternatives to fossil-based fuel.....	9
1.2 CO/CO ₂ metabolism in microorganisms.....	16
1.2.1 Our study model: the hydrogenogens <i>Rhodospirillum rubrum</i>	24
1.3 Ni enzymes.....	28
1.3.1 Ni enzymes involved in Biological WGS in <i>R. rubrum</i>	30
1.3.2 [NiFe]-CODHs.....	32
1.3.2.1 X-ray structures of bifunctional [NiFe]-CODHs.....	33
1.3.3 Monofunctional [NiFe]-CODH.....	37
1.3.3.1 Biosynthesis of the Active Site.....	40
1.3.3.2 Metallochaperones.....	44
1.3.3.2.1 CooC.....	46
1.3.3.2.2 CooT.....	49
1.3.3.2.3 CooJ.....	50
1.3.3.3 Heterologous Production.....	53
1.3.3.4 Reaction mechanism.....	53
1.4 Electrochemistry of enzymes.....	64
1.4.1 Mediated and Direct Electron transfer.....	65
1.4.2 Enzyme immobilization techniques.....	67
1.4.3 Carbon Nanotubes and Enzyme immobilization.....	71
1.4.3.1 Non-specific Adsorption.....	74
1.4.3.2 π - π interactions of polyaromatics.....	75
1.4.3.3 Polymer coating.....	78
1.4.3.4 Covalently CNT functionalization.....	79
1.4.4 Enzymes integration in functional devices.....	82
1.4.4.1 Biofuel Cells.....	83
1.4.4.2 Microbial Electrolysis Cells.....	87
1.4.4.3 Electroenzymatic Synthesis.....	88
1.4.5 Electrochemistry of [NiFe]-CODH.....	89
1.4.6 Catalyst for CO ₂ reduction.....	95
1.4.6.1 Formate Dehydrogenase.....	96
1.4.6.2 Enzyme-assisted Photoreduction of CO ₂	97
1.4.6.3 CO ₂ Electrolyzers.....	99

CHAPTER 2 - Article 1: Efficient electrochemical CO₂/CO Interconversion by an Engineered Carbon Monoxide Dehydrogenase on a Gas-Diffusion Carbon Nanotube Based Bioelectrode.....	103
2.1 Preface.....	105
2.2 Highlighted results.....	106
2.2 ACS catalysis original paper and Supporting information.....	109
CHAPTER 3 - Article 2: A pyrene-triazacyclononane anchor affords high operational stability for CO₂RR by a CNT-supported histidine-tagged CODH.....	139
3.1 Preface.....	141
3.2 Original paper and Supporting information.....	143
3.3 Annex Data.....	156
3.4 Highlighted results.....	159
CHAPTER 4 The role of D-cluster in [NiFe]-CODH from <i>R. rubrum</i>.....	162
4.1 Introduction.....	162
4.2 Results.....	166
4.2.1 RrCODH mutants are produced in <i>E. coli</i> under Aerobic and Anaerobic Conditions.....	166
4.2.2 SEC MALLS-RI.....	166
4.2.3 UV-visible spectroscopy.....	169
4.2.4 In Solution and Electrochemical CO oxidation and CO ₂ reduction activities.....	172
4.2.5 Crystallization of RecRrCODH.....	176
4.3 Discussion & Conclusion.....	181
4.4 Perspectives.....	183
4.5 Material & Methods.....	184
CHAPTER 5 Conclusion & Perspectives.....	189
Acknowledgments.....	193
References.....	197

“Flattening the curve!”

This is a phrase that we are used to hearing lately, too bad that the latter is almost exclusively referring to the Covid-19 pandemic. Humanity is facing several problems including the one just mentioned, but this must not distract out attention from flattening the **climate change** curve.

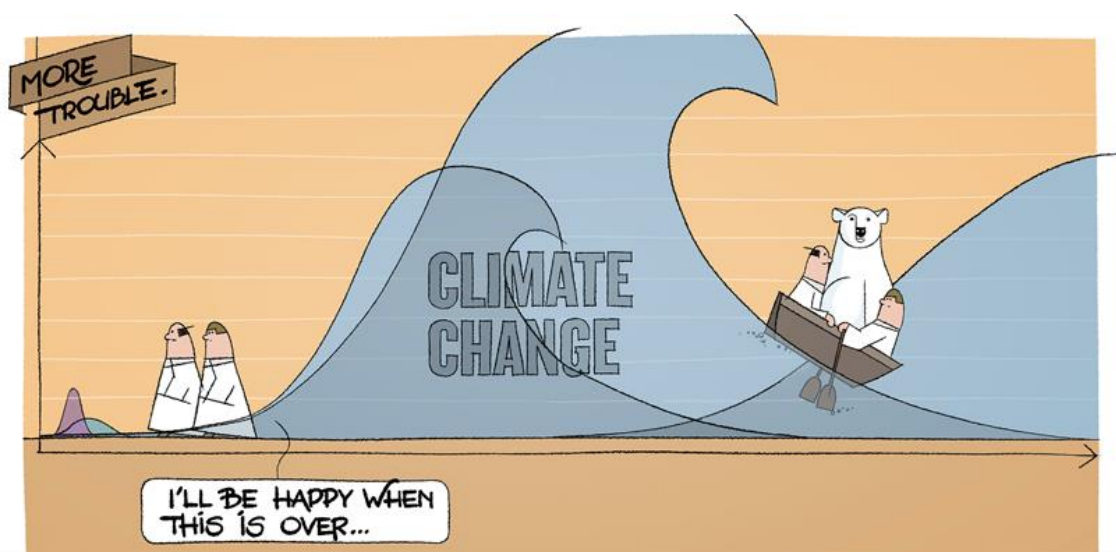


Figure 0 ©Statistically Insignificant by Raf S.

Climate change can be translated into two related themes: the **warming of the earth** due to human activity linked to excessive emissions of **greenhouse gases** and the resulting change in weather patterns (as ironically highlighted in Figure 0).

If we type one of the terms in bold above on any browser, we will find infinite content, but in all of them we will also find: **carbon dioxide** or **CO₂**. This is because CO₂ is the main actor of climate change, accounting for 80 % of the total composition of greenhouse gases, other gases being methane (10 %), nitrous oxide (7 %) and fluorinated gases (3 %).

Hence, greenhouse gases emissions can easily be expressed in CO₂ emissions. Consequently, the flattening of the climate change curve can be thought of as avoiding excessive CO₂ emissions or in other words **achieving net CO₂ emissions of zero**.

After this brief introduction, CO₂ sounds like a very bad enemy to humanity. However, we are made of carbon and our life on earth will always involve the production and emission of CO₂ into the atmosphere.

CO₂ in biology doesn't sound so bad, since its metabolism plays a fundamental role as "building block" for the synthesis of organic molecules in living organisms. As I said above, every human activity as a cost of CO₂, even the development and use of technologies with the aim of reducing CO₂ emissions. Therefore, it is crucial to find cheaper alternatives, in terms of CO₂ emissions.

As often observed in recent years, the use and development of technologies based on biological processes results in a better ecological impact on climate change. This is related to the fact that in biology there are no terms such as waste, garbage and trash, the latter terms being coined by the humans. What for us can be a waste, like the CO₂ from our metabolism, represents a substrate for other organisms leading to the production of other products. As reported in the title of this thesis, our approach is based on the study and use of biological alternatives for CO₂/CO inter-conversion. Furthermore the attention will be focused on a biocatalyst in particular: the Carbon Monoxide Dehydrogenase (CODH).

CODH catalyzes the reversible reduction of CO₂ to CO and represents an attractive biocatalyst in terms of activity, selectivity, ability to operate in mild conditions with low overpotentials. In addition, it does not require high production costs and uses earth abundant-metals. For these reasons, several studies have been conducted on [NiFe]-CODHs for applications in electro-catalytic CO₂ reduction reaction (**CO₂RR**). [NiFe]-CODHs consist of a complex multi-metallic NiFe₄S₄ active site, unique in biology, and additional FeS clusters are present to transfer electrons from the buried active site to the protein surface.

During my PhD, I have worked on the [NiFe]-CODH from *Rhodospirillum rubrum* (*RrCODH*). Historically this CODH has been isolated and characterized from the native bacterium in the early 80's but its studies have been limited due to the difficulties encountered during its production and purification. In this manuscript, I describe a new method for the heterologous production of a recombinant *RrCODH* in *E. coli*, which allows its production and purification in a single step with high yields and high specific activities towards the two carbonaceous substrates.

This manuscript is structured as follows: the first part consists in a bibliographic introduction, with the aim of providing a general overview of CO₂ and its role in biology, and then focusing on [NiFe]-CODHs and its possible integration in biotechnological devices. A second section describes our findings on *Rr*CODH and concern the characterization of the recombinant enzyme and its immobilization on functionalized carbon nanotubes, subsequently integrated in a functional device (Chapters 2 and 3). Chapter 4 is dedicated to a preliminary study of electron transfer from the buried active site of *Rr*CODH to an external partner, with the aim of understanding its mechanisms for its integration and possible future use in CO₂RR devices. The last section will summarize the findings highlighted in the other chapters and provide future perspectives for the project (Chapter 5).

Chapter 1

Introduction

In the last two centuries, the industrial revolution has led to the development and diffusion of new technologies to improve human life. Many of the discoveries have been and are still focused on energy demand, required for almost all economic sectors. Nowadays most of the energy is produced from fossil sources (Figure 1) (IEA, 2021). This development model has improved the quality of human life but at the same time has brought to light severe problems such as the increase of carbon dioxide (CO₂) emissions. This has led to a reduction in air quality and mainly contributed to climate change with serious consequences on our eco system. Reducing CO₂ emissions is currently a main objective of scientific and technological research. CO₂ is the main carbon component of greenhouse gases and its atmospheric concentration increases at an average speed of 2.5 ppm per year (calculation based on the last ten years, 2010-2020) reaching 420 ppm in May 2021 (Ed & Pieter, 2021).

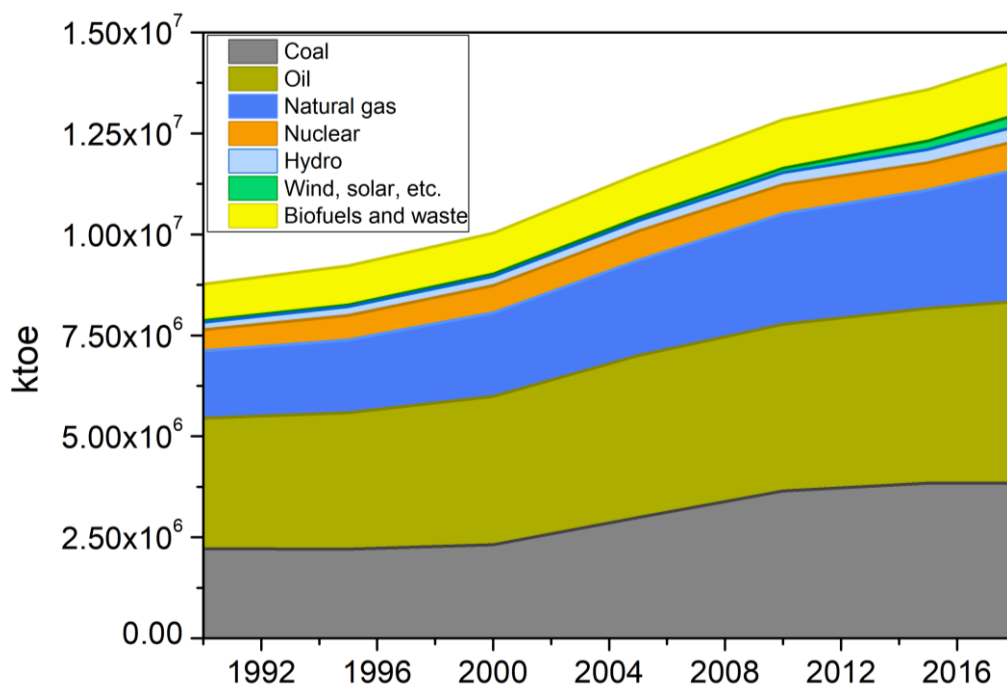


Figure 1 Total Primary Energy Supply (TPES) by source, referred to World 1990-2018. The tons of oil equivalent or toe is a unit of energy defined as the amount of energy released by burning one ton of crude oil. It is approximately 42 GJ or 11.63 MWh. (Adapted from International Energy Agency, 2021)

Therefore, it is important to adopt a sustainable development model and move from the current political model. As the International Energy Agency (IEA) says, "The sustainable development scenario sets out the main changes that would be needed to achieve the key energy goals of the United Nations agenda for sustainable development". The sustainable development scenario of the IEA shows the possibility of reaching global "net zero" CO₂ emissions in 2070, providing the reduction of air pollution and climate change (IEA, 2020). As shown in Figure 2, the use of fossil resources must be reduced in favor of renewable resources. However nowadays, a radical change turns out to be utopian, so it is necessary to focus our attention on what can be implemented in our current economic model.

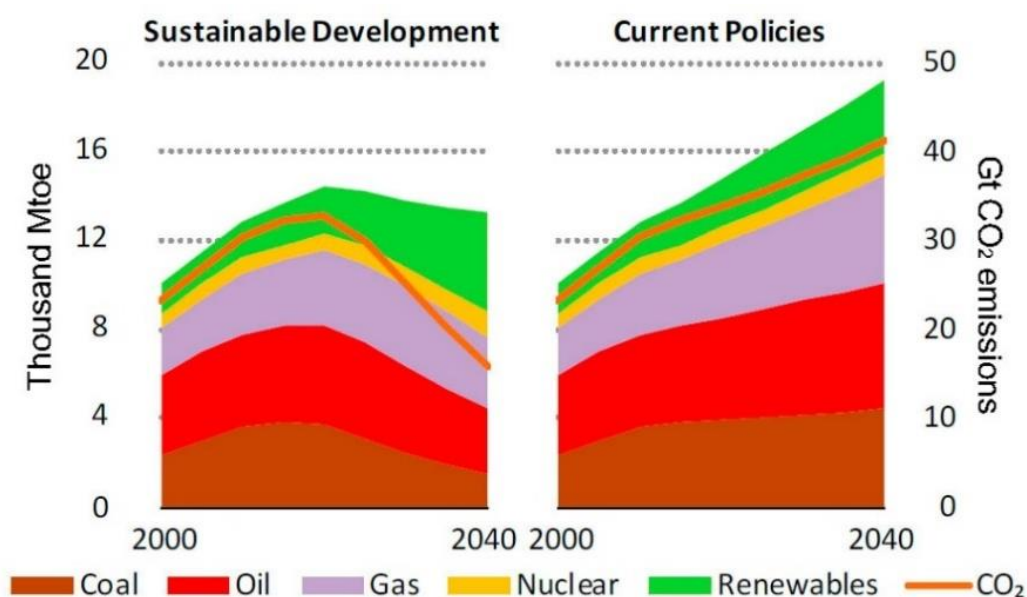


Figure 2 Comparison between energy development models and related CO₂ emissions. Existing policies (Current Policies) and announced targets (Sustainable Development) slow the growth of global CO₂ emissions until 2040 but are not strong enough to force a peak in an expanding energy system. (IEA, 2020)

This economic model introduces the concept of "closing the carbon cycle". At this point two questions spontaneously arise: what is the carbon cycle? What does it mean to close it? Carbon is the backbone of life on Earth. We are made of carbon, we eat carbon and our civilizations, our economies, our houses, our means of transport are built on carbon. The carbon cycle is the natural way to circulate this element through different reservoirs with processes such as photosynthesis, respiration, weathering and fossilization (Figure 3). Today, changes in the carbon cycle are happening due to human activity. The latter is mainly related to the exploitation and combustion of fossil fuels. Then, carbon is released by combustion (or oxidation) into the atmosphere as CO₂, and while the oceans

and biomass grab about half of what we emit, the other stays in the atmosphere adding to the greenhouse effect (Riebeek, 2011)(Styring et al., 2015)(Birdsey et al., 2018). As can be seen in Figure 3, the human effect increases net CO₂ emissions year after year.

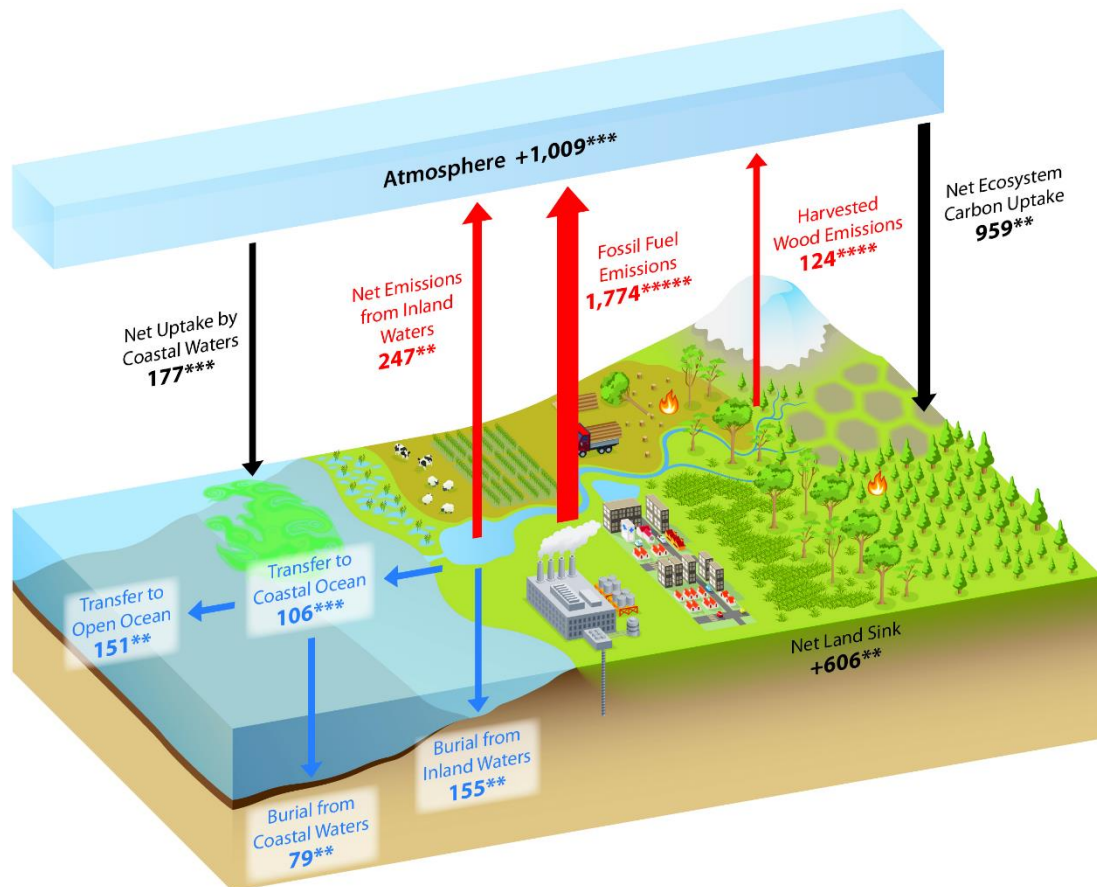


Figure 3 Net fluxes and transfers of carbon among the atmosphere, land, and water are depicted in this simplified representation of the carbon cycle. The diagram includes only fluxes of CO₂ but no other carbon-containing greenhouse gases. These carbon flows include 1) emissions (red arrows); 2) uptake (black arrows); 3) lateral transfers (blue arrows); and 4) burial (blue arrows), which involves transfers of carbon from water to sediments and soils. Values are expressed in teragrams of carbon (TgC) per year. The increase in atmospheric carbon, denoted by a positive value, represents the net annual change resulting from the addition of carbon emissions minus net uptake of atmospheric carbon by ecosystems and coastal waters. The estimated increase in atmospheric carbon of +1,009 TgC per year. Asterisks indicate that there is 95% confidence that the actual value is within 10% (*****), 25% (****), 50% (**), 100% (**), or >100% (*) of the reported value. (Adapted from Birdsey et al., 2018)

Hence, there are many actions that can be put in place to close the carbon cycle as well as achieve the reduction of CO₂ emissions. Among them, the three main strategies are: **decarbonization, carbon sequestration and carbon recycling.**

Decarbonization is directly based on reduction or, at best, abolition the use of fossil fuels to switch to a renewable source. But this aim is difficult to achieve: firstly because renewable sources show limits in terms of scalability, versatility and storage time (Nitopi et al., 2019). Secondly, some sectors always require liquid fuels, such as transport.

Ultimately, some sectors, not related to energy, always involve CO₂ emissions, such as intensive farming (Nitopi et al., 2019).

The carbon sequestration, known as Carbon Capture and Storage (**CCS**) limits CO₂ emissions into the atmosphere. The CCS involves the capturing of industrially produced CO₂, compressing it for transportation and then injecting it underground (deep rock cavities, under sea and land) where it is permanently stored. In 2020, 26 large-scale CCS facilities are operating around the world which can capture and permanently store 40 Mtons of CO₂ every year, representing less than 0.1 % of global carbon emissions (CCS Global Institute, 2020). The latter percentage is set to increase in the next years, with the development of 37 CCS facilities and the possibility of applying CCS facilities to every industrial plant (CCS Global Institute, 2020). The advantage of carbon sequestration is that, regardless of the source, fossil fuels or biomass for example, total net emissions are zero or negative in case of biomass. Unfortunately, the CCS facilities induce a price increase. For example, for a power plant the resulting energy displays an increase of more than 25% in the generated energy (Nitopi et al., 2019). Other problems are related to transportation and limited underground reservoirs.

The third strategy is based on the possibility to recycle or convert the CO₂ into more reduced forms known as Carbon Capture and Utilization (**CCU**). The CCU is the most promising strategy, because it allows to reduce atmospheric CO₂ and also to reduce the use of fossil fuels at the same time. The CO₂ is a highly stable molecule and its conversion to other carbon-based molecules is difficult. However, several methods have been developed, such as chemical reduction, photochemical reduction, biological transformation and electrochemical reduction (Duan et al., 2017). Among these strategies, the electrochemical CO₂ reduction reaction (**CO₂RR**) allows to operate in mild conditions at ambient temperature and pressure. Furthermore, the accurate control of the applied potential, of the electrolyte and of the current allows the regulation of the reaction rates and products. In contrast, homogeneous reactions are based on indirect electrolysis, where the catalyst first accepts electrons from the electrodes and then donates electrons to the CO₂. CO₂RR shows several issues: the activation of the CO double bond is difficult due to its short bond length, the electron affinity of CO₂ is low, and there is a large energy gap between the highest occupied and lowest unoccupied molecular orbitals (Liang et al., 2021). Furthermore, some side reactions can reduce the

efficiency of the reaction, such as the hydrogen evolution reaction (HER) (Liang et al., 2021). When the goal is to apply CO₂RR to energy conversion, the improvement of electrocatalysts is essential to overcome the mentioned drawbacks. Furthermore, an ideal CO₂RR electrocatalyst should display a high selectivity combined to a strong CO binding energy and weak H binding energy (Duan et al., 2017). CO₂RR technologies are studied and developed for two types of energy conversion: metal-CO₂ based batteries and **CO₂ electroreduction to fuels**.

CO₂ can be electroreduced to a variety of carbonaceous products, such as carbon monoxide (CO), methane, formic acid, ethylene, ethanol, methanol and others (Figure 4).

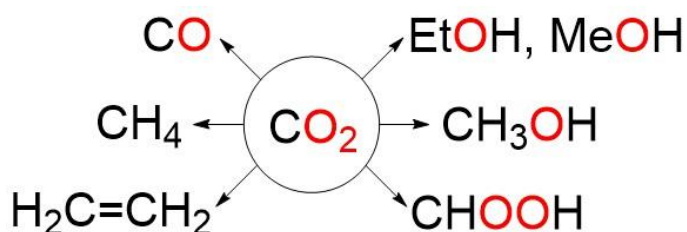


Figure 4 Main valuable commodity chemicals from the CO₂RR

When the goal is a large-scale production, selectivity and high yield are important factors. Among all the products mentioned above, CO is the most promising for several reasons. As a gas, CO directly allows its selective production and also does not require separation processes from the electrolyte solution. CO is an important “building block” in several industrial sectors, with a wide range of applications. The main uses of CO include the synthesis of acetic acid by catalytic carbonylation of methanol and formic acid by hydrolysis of methyl formate (Küngas, 2020). Other applications include the production of various chemicals such as: acrylic acid, propanoic acid, acetic anhydride and dimethylformamide (Küngas, 2020). In metallurgy, CO is used to reduce oxides to metals in blast furnaces and to produce highly pure Ni, Fe, Co, Cr, W and Mo via the metal carbonyl pathway (Küngas, 2020). CO is also used as the main constituent of synthesis gas (syngas) along with H₂. Syngas is used at very large scale for the production of liquid fuels and commodity products, such as: ammonia, methanol, mixed alcohols and others (Chan et al., 2021)(Drahansky et al., 2016)(Alfano & Cavazza, 2018). Most CO₂RRs are endergonic processes and require energy input. To give an idea of the energy

required, Table 1 shows the standard potentials of thermodynamic reduction in aqueous solution at pH 7.0 (Schlager et al., 2017).

Table 1 Theoretical formal reduction potentials (E^0) of CO_2 reduction to several products. The potentials are referred for aqueous solutions at pH 7.0 (Adapted from Schlager et al., 2017)

Reaction				E^0 [V vs. NHE]
CO_2		$+ 1 e^-$	\rightarrow	CO_2^- -1.90
2CO_2		$+ 2 e^-$	\rightarrow	$\text{CO} + \text{CO}_2^{2-}$ -1.33
CO_2	$+ 2 \text{H}^+$	$+ 2 e^-$	\rightarrow	$\text{CO} + \text{H}_2\text{O}$ -0.53
CO_2	$+ 2 \text{H}^+$	$+ 2 e^-$	\rightarrow	HCOOH -0.61
CO_2	$+ 4 \text{H}^+$	$+ 4 e^-$	\rightarrow	$\text{H}_2\text{CO} + \text{H}_2\text{O}$ -0.48
CO_2	$+ 6 \text{H}^+$	$+ 6 e^-$	\rightarrow	$\text{CH}_3\text{OH} + \text{H}_2\text{O}$ -0.38
CO_2	$+ 8 \text{H}^+$	$+ 8 e^-$	\rightarrow	$\text{CH}_4 + 2\text{H}_2\text{O}$ -0.24

To perform any CO_2 reduction process shown in Table 1 it is essential to take into account the energy barrier, which in the practical approach also means considering the overpotential of the reaction. To reduce these energy barriers, specific thermodynamic conditions are required, such as high pressures and/or high temperatures (above 300 °C) (Schlager et al., 2017)(Ünlü et al., 2021) which result in unprofitable amounts of energy. In addition, conventional CO_2RR methods also show poor selectivity and low yield (Ünlü et al., 2021). Furthermore, the catalyst should be able to carry out the reaction with the lowest overpotential in other words as close as possible to the standard reaction potential. All of these strategies always require a source of electrons. The latter can have a CO_2 cost if it comes from non-renewable energy. An ideal sustainable strategy for CO_2RR should use a renewable source of energy provided by solar irradiation, wind, hydroelectric or geothermal energy. For these reasons, bioinspired materials such as models for artificial photosynthesis and other biological approaches have raised research interests in recent decades. Several bioinspired approaches for CO_2RR have recently been developed, based on the direct use of biocatalysts such as enzymes or microorganisms (Y. Chen et al., 2020)(Ünlü et al., 2021)(Anwar et al., 2020). For example, microalgae (such as *Nannochloropsis* genus) can be used for the production of biofuels, in this case the microorganism can be genetically modified or evolved to increase the production of the desired products

(Maréchal, 2021). For now, these processes are generally on a laboratory scale, but some have been exploited at the industrial scale (e.g., LanzaTech).

Compared to other catalytic systems, biocatalysts show a very high selectivity and catalytic efficiency (Schlager et al., 2017)(Anwar et al., 2020). Being a natural process, the reactions are carried out in mild conditions such as ambient temperature (20-30 °C), atmospheric pressure and aqueous solvents (Ünlü et al., 2021). Moreover, the catalyzed reactions are reversible. For these reasons the use of enzymes for CO₂RR is interesting, in particular the use of dehydrogenases (Figure 5). Moreover, multiple enzymes can be coupled to perform multistep reactions (Figure 5B).

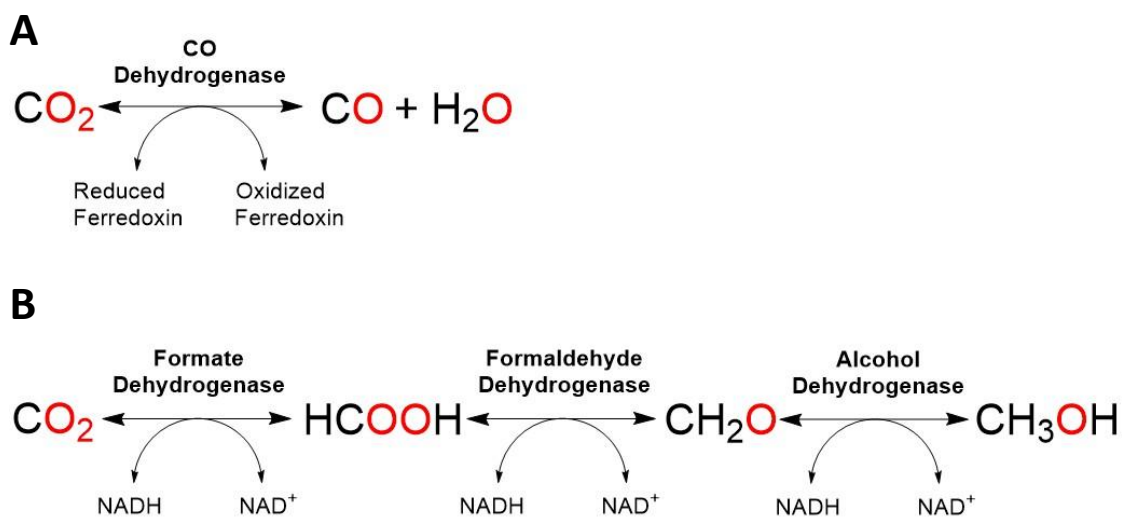


Figure 5 Reaction steps for enzyme catalyzed CO₂RR. **(A)** CO₂ reduction to CO catalyzed by Carbon Monoxide Dehydrogenase and **(B)** CO₂ reduction to CH₃OH catalyzed by a three-step cascade of dehydrogenases.

For all the purposes listed above, it is critical to deeply characterize these biocatalysts, such as their role in native microorganisms, electron donor partners and catalytic properties (e.g., optimal pH and temperature). The following paragraphs will focus on CO₂/CO metabolism in microorganisms suitable as a model for developing bioinspired CO₂RR processes.

The microorganisms capable of metabolizing CO/CO₂, therefore interesting for the bioinspiration or mimicry of CO₂RR, all belong to the class of **autotrophic** organisms. All living forms of our planet can be distinguished in two categories based upon how they obtain their carbon sources: heterotrophs or autotrophs. Autotrophs are also known as **primary producers** because they are able to produce their own food from raw materials, such as CO₂ and H₂O, and energy. The organisms that belong to this category are plants, algae and some classes of bacteria and archaea. On the other hand, heterotrophs are known as consumers because they consume primary producers or other consumers, for example animals, fungi and many bacteria. This brief description and classification of living organisms should lead us to reflect on how the permanence of humans on the earth is strictly dependent on autotrophic microorganisms.

As shown in Figure 3, a key step in the global carbon cycle is the fixation of CO₂ into organic carbon-based molecules. The microbial CO₂ fixation proceeds through different pathways and different sources of energy. The latter allow to distinguish two types of autotrophs: **photoautotrophs** that like plants are able to harvest solar energy and **chemoautotrophs** where the energy source are reduced compounds such as hydrogen, sulfite, nitrite and other (Nybo et al., 2015). To date, six natural carbon fixation pathways have been discovered (Figure 6)(F. Gong et al., 2016): the Calvin-Benson-Bassham cycle (**CBB** cycle), the reductive tricarboxylic acid cycle (**rTCA** cycle), the Wood-Ljungdahl pathway (**WL** pathway), the 3-hydroxypropionate bicycle (**3HP** bicycle), the dicarboxylate/4-hydroxybutyrate cycle (**di-4HB** cycle) and the 3-hydroxypropionate-4-hydroxybutyrate cycle (**3HP-4HB** cycle).

The CBB cycle discovered in the 1940s is the best known and characterized carbon fixation pathway (Calvin & Benson, 1948). About 90 % of the natural CO₂ fixation, carried out by microorganisms, algae and plants, uses this pathway (F. Gong et al., 2019). In short, the CBB cycle allows for the conversion of three CO₂ into one molecule of glyceraldehyde-3-phosphate using nine molecules of ATP and six molecules of NADPH.

Compared to the other five pathways this is the most expensive in term of energy (Figure 6).

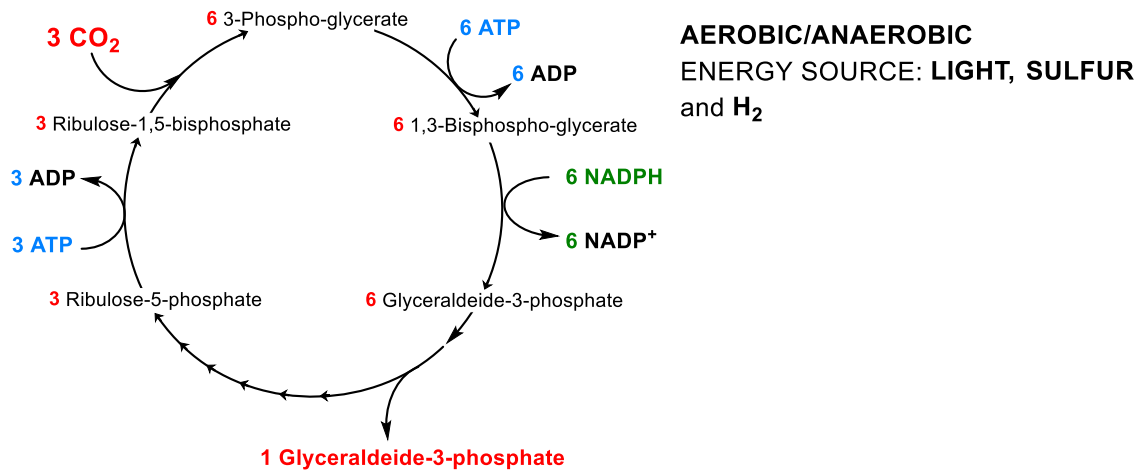


Figure 6 Schematic Calvin-Benson-Bassham cycle. Input and output molecules are highlighted in red. (Adapted from F. Gong et al., 2016)

The rTCA cycle consumes two molecules of CO₂ to synthesize one molecule of Acetyl coenzyme A (Acetyl-CoA), using two molecules of ATP and four molecules of NAD(P)H (Figure 7). This pathway has been found in some anaerobic bacteria and photosynthetic green sulfur bacteria (F. Gong et al., 2016).

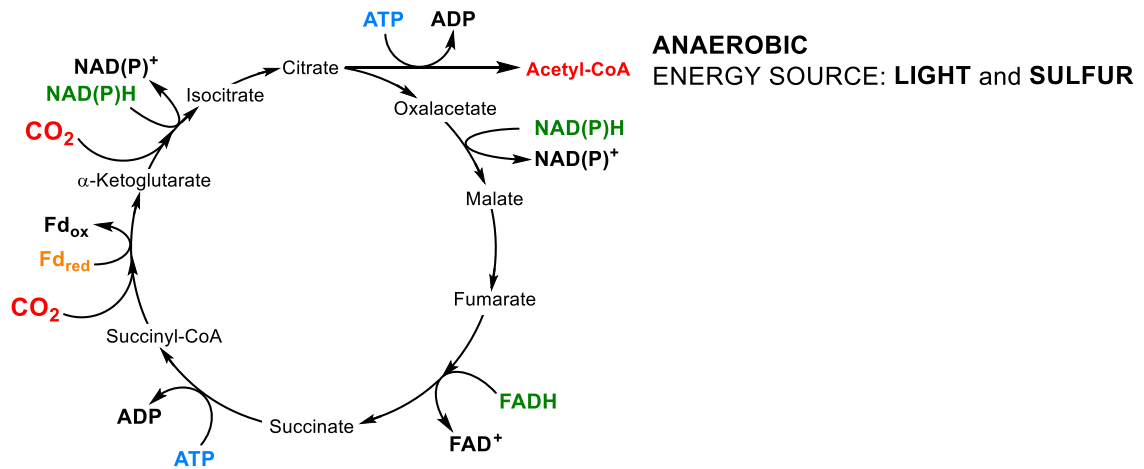


Figure 7 Schematic reductive Tricarboxylic Acid cycle. Input and output molecules are highlighted in red. (Adapted from F. Gong et al., 2016)

The WL pathway is the only non-cyclic pathway, mainly present in anaerobic acetate-producing microorganisms (F. Gong et al., 2019). The energy source is the hydrogen and it converts two molecules of CO₂, or one molecule of CO₂ and one molecule of CO into one molecule of Acetyl-CoA, using one molecule of ATP and four of NAD(P)H (Figure 8).

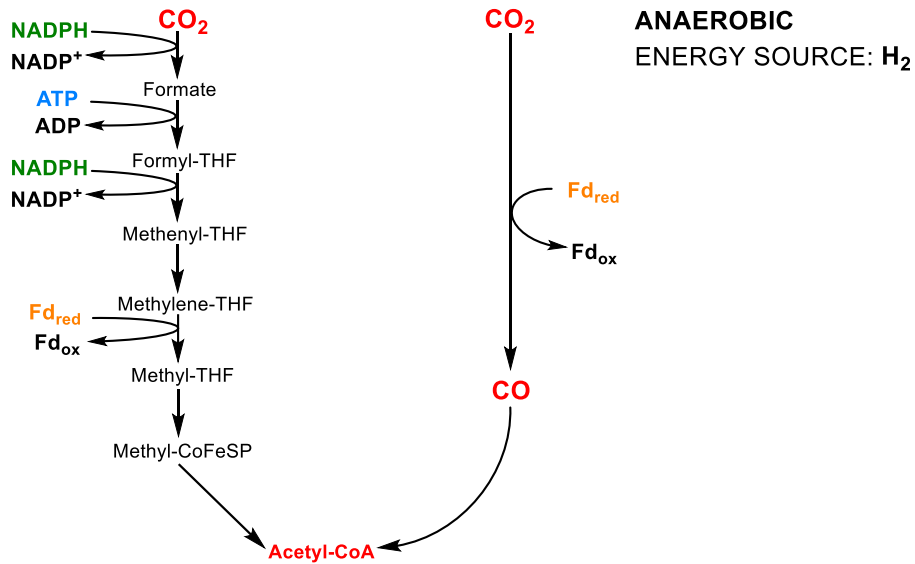


Figure 8 Schematic Wood-Ljungdahl pathway. Input and output molecules are highlighted in red. (Adapted from F. Gong et al., 2016)

The 3HP bicycle found in non-sulfur green photosynthetic bacteria (F. Gong et al., 2016), uses three bicarbonate ions to synthesize one molecule of pyruvate and requires five molecules of ATP and five of NAD(P)H (Figure 9).

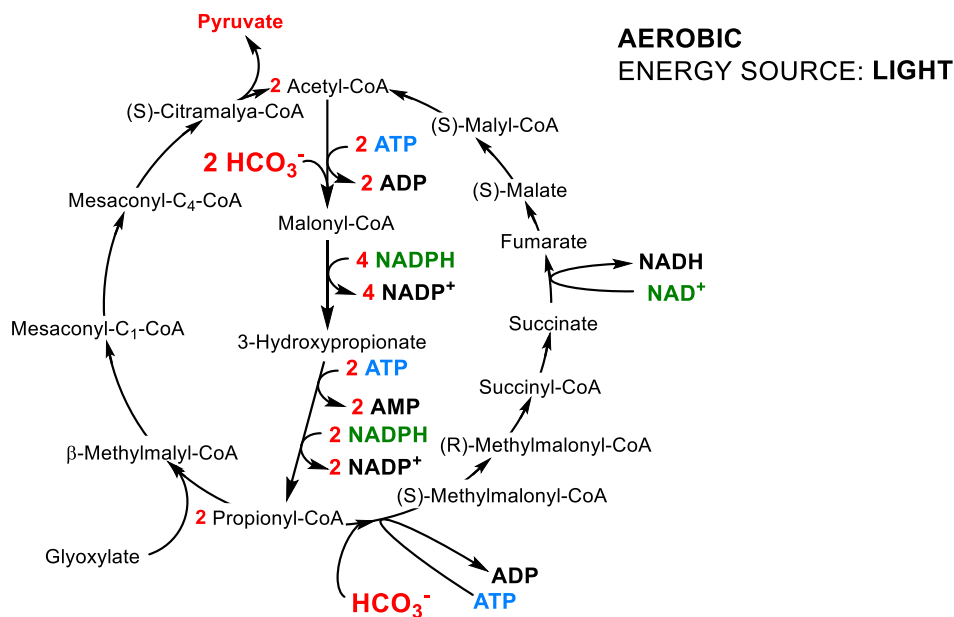


Figure 9 Schematic 3-hydroxypropionate bicycle. Input and output molecules are highlighted in red. (Adapted from F. Gong et al., 2016)

The **3HP-4HB** discovered in 2007 in some archaea use both hydrogen and sulfur as energy sources (Berg et al., 2007). Each cycle involves two bicarbonate ions to synthesize one molecule of Acetyl-CoA, consuming four molecules of ATP and four molecules of NAD(P)H (Figure 10).

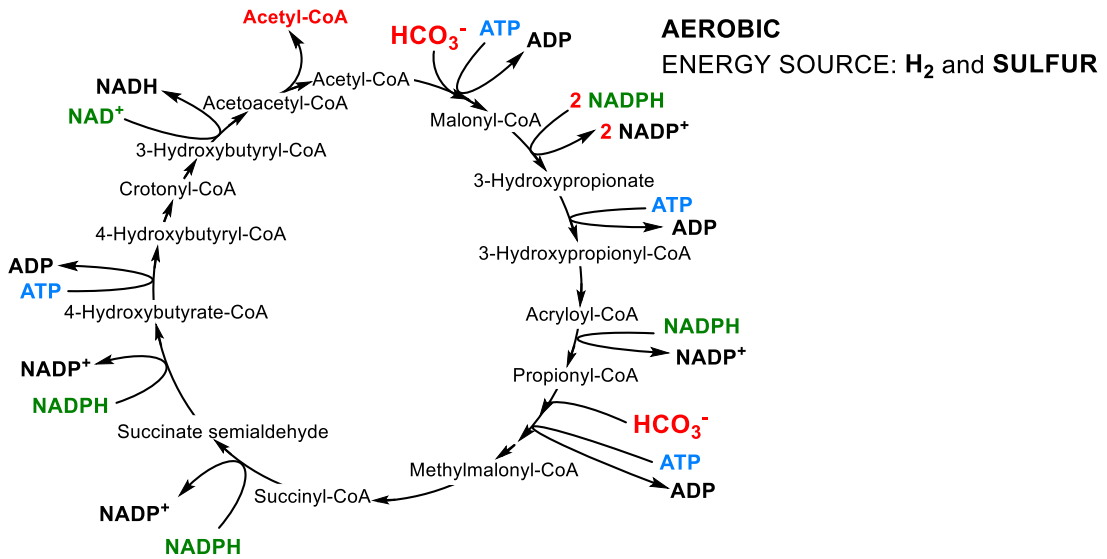


Figure 10 Schematic 3-hydroxypropionate-4-hydroxybutyrate cycle. Input and output molecules are highlighted in red. (Adapted from F. Gong et al., 2016)

The **di-4HB** reported in 2008 is the latest discovered CO₂ fixation pathway (Huber et al., 2008). Present in anaerobic microbes, driven by hydrogen and sulfur, it uses a molecule of CO₂ and a bicarbonate ion to synthesize one molecule of Acetyl-CoA by consuming three molecules of ATP and three molecules of NAD(P)H (Figure 11).

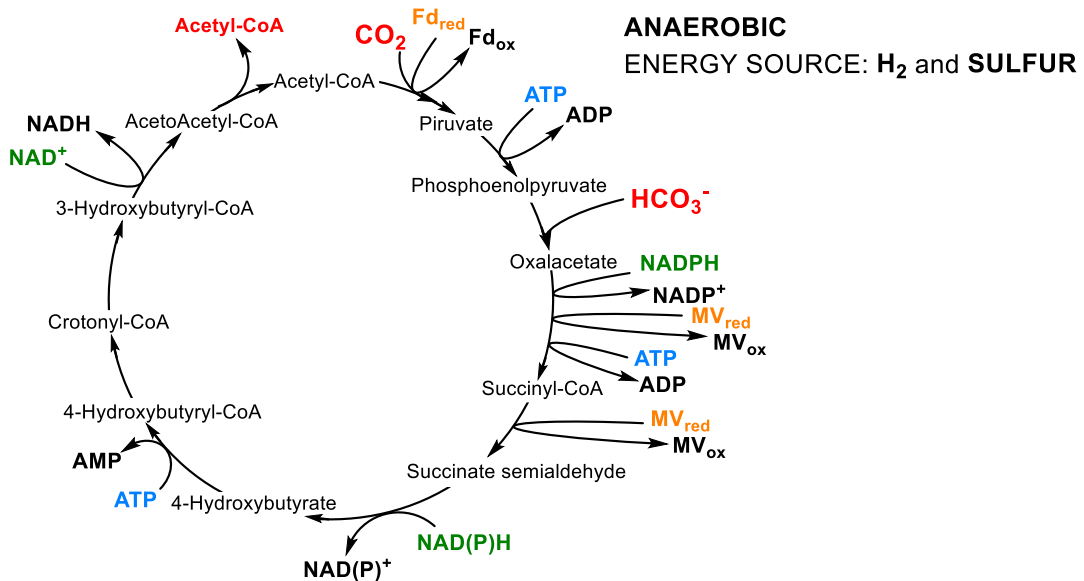


Figure 11 Schematic dicarboxylate/4-hydroxybutyrate cycle. Input and output molecules are highlighted in red. (Adapted from F. Gong et al., 2016)

Table 2 Summary and comparison of the six natural carbon fixation pathways

Pathway	Reaction	Energy inputs	Energy source(s)	Reference
CBB cycle	3CO ₂ → Glyceraldeide-3-Phospate	9 ATP, 6 NAD(P)H	Light, sulfur and H ₂	(Calvin & Benson, 1948)(Sharkey, 2019)(Asplund-Samuelsson & Elton P, 2021)
rTCA cycle	2CO ₂ → Acetyl-CoA	2 ATP, 4 NAD(P)H	Light and sulfur	(M. C. Evans et al., 1966)
WL pathway	2CO ₂ → Acetyl-CoA	1 ATP, 4 NAD(P)H	H ₂	(Schulman et al., 1972)
3HP bicycle	3HCO ₃ ⁻ → Pyruvate	5 ATP, 5 NAD(P)H	Light	(M. C. Evans et al., 1966)
3HP-4HB cycle	CO ₂ + HCO ₃ ⁻ → Acetyl-CoA	3 ATP, 4 NAD(P)H	H ₂ and sulfur	(Berg et al., 2007)
di-4HB cycle	2HCO ₃ ⁻ → Acetyl-CoA	4 ATP, 4 NAD(P)H	H ₂ and sulfur	(Huber et al., 2008)

After this brief description of the microbial CO₂ metabolisms the attention will now be focused on a specific class of autotrophs microorganisms that can metabolize CO. The term **carboxydrotrophs** has been coined to indicate these microbial organisms (Meyer & Schlegel, 1983). These microorganisms are able to interconvert CO and CO₂ according to the so-called Water-Gas Shift Reaction (WGSR):



Carboxydrotrophs, such as archaea, aerobic and anaerobic bacteria, are able to use CO as sole source of energy. In addition, some of them may also use CO as sole carbon source (Robb & Techtmann, 2018).

This process is made such by the ubiquitous presence of the enzyme **carbon monoxide dehydrogenase** (CODH, CO oxidoreductase). CODH is widely conserved and distributed among aerobic and anaerobic microorganisms that are physiologically and phylogenetically different and presumably represents a very ancient metabolic activity. CODH has the function of oxidizing CO, synthesizing acetyl-CoA (as in the WL pathway) or cleave it down into a variety of energy-producing pathways. The details on the different type of CODHs will be described in the following section, for now its role in CO metabolism in microorganisms will be presented.

It is noteworthy that in recent years, more and more **aerobic** CO oxidizing bacteria have been discovered and isolated, including Actinobacteria, Firmicutes and α-Proteobacteria (Table 3). These bacteria are unusual carboxydrotrophs, as they prefer organic substrates

as carbon and energy sources. However, they are still able to grow in the presence of high concentrations of CO (> 10%) (King & Weber, 2007). In these bacteria the reducing equivalents resulting from the oxidation of CO are channeled through a respiratory chain insensitive to CO composed of ubiquinone and cytochromes, which ultimately lead to the reduction of oxygen (Tiquia-arashiro, 2014), or nitrates (Oelgeschläger & Rother, 2008). In some aerobic carboxydrotrophs, the energy conserved by CO metabolism can be used to fix CO₂ to biomass through the CBB cycle (Tiquia-arashiro, 2014).

Table 3 Chemolithotrophic growth on CO or H₂/CO₂ of aerobic carboxydrotrophs. + CO and + H₂/CO₂ growth refer to the ability of the indicated cultures to grow in mineral media with CO or H₂/CO₂ as the sole carbon and energy source. + CBB refers to the potential for CO₂ incorporation by the CBB cycle; s for slow; w for weak. (adapted from King & Weber, 2007).

	Source	CO growth	H ₂ or CO ₂ growth	CBB cycle
α-Proteobacteria				
<i>Oligotropha carboxidovorans</i>	Wastewater	+	+	+
<i>Pseudomonas thermocarboxydovorans</i>	Compost	+	-	+
<i>Pseudomonas carboxydohydrogena</i>	Sewage	+	+	+
<i>Bradyrhizobium japonicum</i> USDA 110	Rhizosphere	s	+	+
Firmicutes				
<i>Bacillus schlegelii</i>	Freshwater sediment	+	+	+
Actinobacteria				
<i>Streptomyces thermoautotrophicus</i>	Coal heap	+	+	?
<i>Mycobacterium smegmatis</i>	Environment, human	+	+	+
<i>Mycobacterium goodnae</i>	Human, water	+	+	?
<i>Mycobacterium tuberculosis</i> H37Ra	Lung isolate	w	-	-
<i>Mycobacterium</i> sp.JC1	Soil	+	-	+

These aerobic carboxydrotrophs possess an **aerobic CODH**, phylogenetically different from anaerobic CODHs. The main difference is the metal content of the active site: anaerobic CODHs use metals available in anoxic atmosphere, such as nickel and iron, and are highly sensitive to oxygen inactivation. Differently, the aerobic CODHs use metals such as **copper** and **molybdenum** (Figure 12) which have become more bioavailable in oxic atmosphere. Other differences between the aerobic and anaerobic CODHs are the biologic roles as well as their oligomeric composition of the subunits.

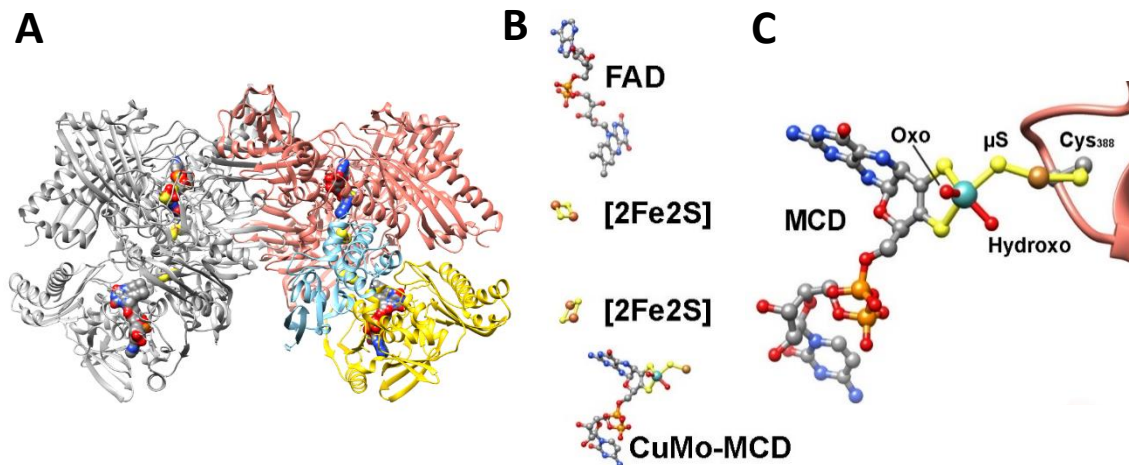


Figure 12 (A) Ribbon diagram of *Oligotropha carboxydovorans* [CuMo]-CODH (PDB code: 1N63) the overall structure is a dimer of heterotrimers. Right monomer is colored according to subunit with salmon for the CoxL subunit, gold for the CoxM subunit and cyan for the CoxS subunit. Cofactors in van der Waals representation. (B) Cofactors representation for the electron transfer. Distances are: 8.7 Å between FAD and the nearest [Fe₂S₂]-cluster, 12.4 Å between the two [Fe₂S₂]-clusters and 14.6 Å between the CuMo-MCD (molybdopterin cytosine dinucleotide) and its nearest [Fe₂S₂]-cluster (C) Active site is built from the bimetallic [CuSMo(=O)OH] cluster in which the two metals are bridged by a μ-sulfido ligand (μS). Cu is further coordinated by a thiolate of cysteine 388. While Mo is further coordinated with the dithiolate pyran ring of MCD, an hydroxo-group and an oxo-group. Molybdenum is green water, copper is brown, phosphor is orange, sulphur is yellow, nitrogen is blue, oxygen is red, and carbon is grey.

Furthermore, the aerobic CODHs only catalyze the CO oxidation to CO₂, with a specific activity of 23.2 U·mg⁻¹ (Holger Dobbek et al., 2002), while the anaerobic ones catalyze the reversible oxidation of CO to CO₂. The [NiFe]- or **anaerobic-CODHs** can be classified according to their biological role in **monofunctional** or **bifunctional**, the latter forming a complex with acetyl-CoA synthase (CODH/ACS). Based on the **respiratory** processes associated with CO oxidation, these anaerobic carboxydotrophs are classified in four groups: **acetogens**, **methanogens**, **sulfate-reducers** and **hydrogenogens** (Figure 13).

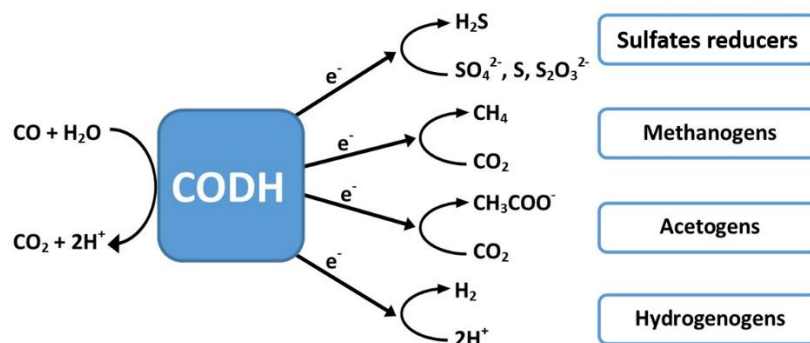


Figure 13 Scheme of anaerobic respirations, which can be coupled to CO oxidation. CODH for carbon monoxide dehydrogenase; arrow with e⁻ for electron transport chain, some components of which are unknown.

Properties of some anaerobic carboxydrotrophs are given in Table 4 (Sokolova et al., 2009)(Diender et al., 2015)(Robb & Techtmann, 2018). These respiratory processes include: hydrogenogenesis, desulfurization, acetogenesis and methanogenesis (Tiquia-arashiro, 2014).

Table 4 Properties of several carboxydrotrophs anaerobic (Diender et al., 2015) (Robb & Techtmann, 2018)

Organism	Domain	CO-tolerance (kPa) ^a	Products formed ^b
Sulfate reducers			
<i>Desulfovibrio vulgaris</i>	Bacteria	< 4.5	CO ₂ , H ₂ , H ₂ S
<i>Desulfotomaculum kutznetsovii</i>	Bacteria	< 70	CO ₂ , H ₂ , CH ₃ COO ⁻ , H ₂ S
<i>Desulfotomaculum thermobenzoicum</i>	Bacteria	< 70	CO ₂ , H ₂ , CH ₃ COO ⁻ , H ₂ S
<i>Desulfotomaculum carboxydovorans</i>	Bacteria	101	CO ₂ , H ₂ , H ₂ S
<i>Sulfurspirillum carboxydovorans</i>	Bacteria	101	CO ₂ , H ₂ , H ₂ S
<i>Archaeoglobus fulgidus</i>	Archaea	101	CO ₂ , H ₂ , CH ₃ COO ⁻ , HCOO ⁻ , H ₂ S
<i>Thermoproteus tenax</i>	Archaea	n.d.	CO ₂ , H ₂ S
Hydrogenogens			
<i>Rhodospirillum rubrum</i>	Bacteria	101	CO ₂ , H ₂
<i>Rubrivivax gelatinosus</i>	Bacteria	101	CO ₂ , H ₂
<i>Carboxydotherrmus hydrogenoformans</i>	Bacteria	101	CO ₂ , H ₂
<i>Thermococcus</i> strain AM4	Archaea	101	CO ₂ , H ₂
Acetogens			
<i>Moorella thermoacetica</i>	Bacteria	72	CO ₂ , CH ₃ COO ⁻
<i>Acetobacterium woodii</i>	Bacteria	30	CO ₂ , CH ₃ COO ⁻
Methanogens			
<i>Methanosarcina acetivorans</i>	Archaea	300	CH ₄ , CH ₃ COO ⁻ , HCOO ⁻ , CH ₄ S, C ₂ H ₆ S
<i>Methanosarcina barkeri</i>	Archaea	101	H ₂ , CH ₄ , CO ₂
<i>Methanothermobacter thermautotrophicus</i>	Archaea	45	H ₂ , CH ₄ , CO ₂

^a Maximal CO concentration tested; not necessarily the maximally tolerated CO concentration

^b Either experimentally demonstrated or deduced from the respective genome sequence

CO is considered an excellent source of energy since the redox potential (E°) of the CO₂/CO couple is very low (-524 to -558 mV) (Tiquia-arashiro, 2014).

Acetogens and **methanogens** possess mainly bifunctional CODH/ACS involved in the WL pathway (Robb & Techtmann, 2018). **Sulfate reducers** couple the oxidation of CO to CO₂ with the reduction of sulfate. The latter is used as a terminal electron acceptor of the respiratory chain, thus producing sulfide (Marietou et al., 2018). **Hydrogenogens** includes bacteria such as *Rhodospirillum rubrum* and *Carboxydotherrmus hydrogenoformans*, which are able to grow by converting CO to CO₂ and subsequently

reduce protons to H_2 derived from H_2O . This process is known as the **biological WGSR** (Fox, Kerby, et al., 1996)(Fox, Yiping, et al., 1996)(Soboh et al., 2002), is performed by a membrane associated multiprotein complex (Figure 14). Involving the monofunctional CODH for the oxidation of CO to CO_2 from which the electrons are transferred through a ferredoxin (called CooF) to an Energy-Conserving Hydrogenase (ECH), which ultimately reduce protons to H_2 . This process is coupled to the translocation of protons across the cytoplasmic membrane leading to the formation of ATP by an ATP-synthase (Figure 14).

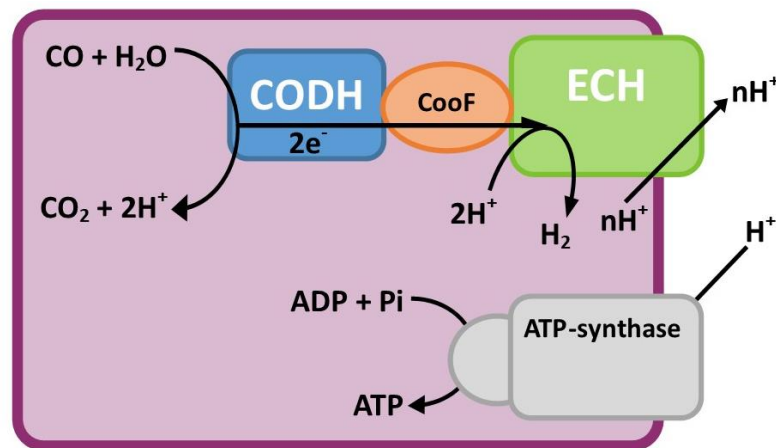


Figure 14 Scheme of Hydrogenogens CO metabolism. Biologic WGSR multiprotein complex CODH:CooF:Energy-Conserving Hydrogenase (ECH) for H_2 evolution from CO oxidation and protons translocation across the cytoplasmic membrane. Protons gradient usage by ATP-synthase to phosphorylate ADP to ATP.

1.2.1

Our study model: the Hydrogenogens *Rhodospirillum rubrum*

Rhodospirillum rubrum is a Gram negative, facultative photosynthetic purple non-sulfur proteobacterium with a versatile metabolism. It is able to grow as a chemoautotroph, a photoheterotroph or a chemoheterotroph, aerobically or anaerobically. Being a spirilla



Figure 15 *Rhodospirillum rubrum*, TEM. Length: 4 microns (© Bergey's Manual Trust 1995)

possess a spiral shape and it is polar flagellated (Christine Munk et al., 2011). Its length is 3-10 μm , with a width of 0.8-1.0 μm . *R. rubrum* prefers to grow in habitats with a pH of 6.8-7.2 (Bergey & Holt, 1994). Its optimal growth temperature is 22-35 degrees Celsius (Weaver, 1971). Under **aerobic** conditions the cells are colorless, and photosynthesis is

repressed. With a **lower oxygen concentration**, it is able to grow through an alcoholic fermentation. Under **anaerobic** conditions it can grow photosynthetically using bacteriochlorophyll which allows the absorption of light at wavelengths longer than those absorbed by plants (near infrared) (Christine Munk et al., 2011). Under these conditions the colonies are purple because the cells express the carotenoid pigment necessary to gather the energy of light for photosynthesis. Furthermore, *R. rubrum* does not produce oxygen, but elemental sulfur as a by-product of photosynthesis (Christine Munk et al., 2011). *R. rubrum* is a well-established model organism for studies on **nitrogen fixation** and the organism possesses two related but distinct nitrogenase systems that utilize a MoFe- and Fe-nitrogenases (Lehman & Roberts, 1991). *R. rubrum* has a great interest in scientific research and biotechnological applications, including its capacity of producing **biodegradable plastic**. In fact, when the bacterium grows on CO the CO₂ produced via the biological WGSR can be accumulated into cell material and poly(3-hydroxybutyrate) (PHB) (Figure 16). PHB is a polyhydroxyalkanoate (PHA), the latter are polyesters synthesized by many bacteria as energy and carbon storage molecules (Revelles et al., 2016).

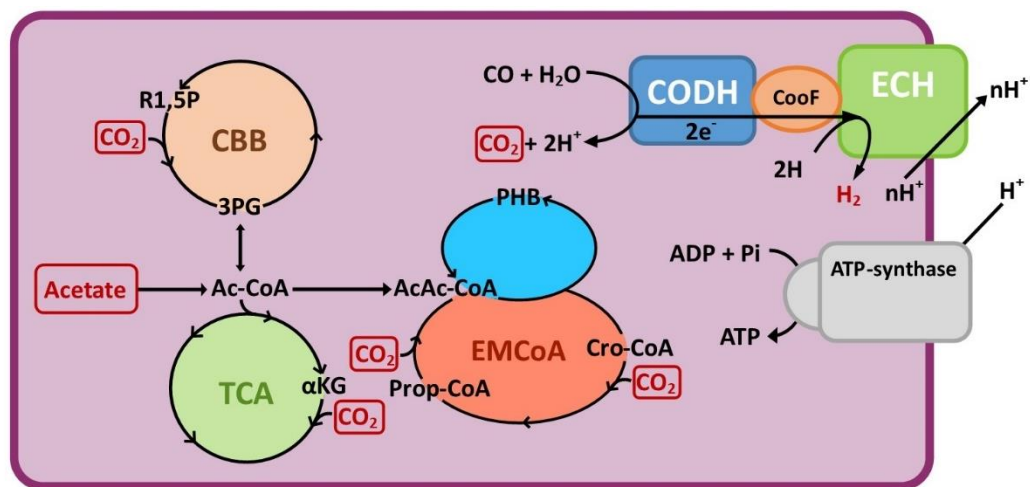


Figure 16 Simplified metabolic map of *R. rubrum* with CO and acetate as carbon source. The biologic WGSR multiprotein complex catalyze the H₂ evolution from CO and led protons translocation across the cytoplasmatic membrane. Protons gradient usage by ATP-synthase to phosphorylate ADP to ATP. CO₂ can then be fixed through the CBB cycle, the TCA, or the EM-CoA. R1,5P: ribulose-1,5-bisphosphate, 3PG: 3-phosphoglycerate, Ac-CoA: acetyl coenzyme A, αKG: α-ketoglutarate, AcAc-CoA: acetoacetyl-CoA, Cro-CoA: crotonyl-CoA, PHB: poly([R]-3-hydroxybutyrate) (Modified from Revelles et al., 2016).

These polymers are biodegradable plastic materials that offer an alternative to petroleum-derived plastic, in addition the monomers can be combined within this family giving life to materials that make these bioplastics suitable for different commercial applications, such as biomedical implants or packaging articles (Revelles et al., 2016).

For example, *R. rubrum* was cultivated in a bioreactor fed with CO and acetate, with a maximum yield of the PHB content for biomass of 30% w/w (Karmann et al., 2019).

R. rubrum has also provided information on **radiation resistance**. The European Space Agency is currently working on "MELISSA life support system", a project for the development of numerous interconnected bioreactors inhabited by microorganisms and higher plants, with the aim of producing oxygen, water and food by recycling organic waste (Mastroleo et al., 2010). This technology will be integrated in space, where it will be exposed to higher doses and different ionizing radiation spectra. Hence, it is necessary to screen the radiotolerance of the organisms that will be used. *R. rubrum* was subjected to sub-lethal doses of ionizing radiation, Cobalt-60 gamma rays, and specific marker genes for resistance to ionizing radiation were discovered and characterized (Mastroleo et al., 2010). This may lead to advances in radiation resistance applied in research. Finally, *R. rubrum* is a hydrogenogenic bacterium and can be used in the field of renewable energies, in particular to **upgrade synthesis gas (syngas)**. Syngas is a mixture of gasses which, to date, derive mainly from the gasification of fossil fuels. Raw syngas are mainly composed of CO and H₂, with a ratio of less than 0.6 (Alfano & Cavazza, 2018). Syngas represents a substrate for obtaining many chemicals, such as H₂, ammonia, ethanol, methanol and other alcohols or liquid fuels *via* the Fischer-Tropsch processes (Drahansky et al., 2016)(Spath & Dayton, 2003). To this end it is necessary to increase the H₂/CO ratio (e.g., Fischer-Tropsch 4/1) and this is possible through the WGSR which is carried out industrially through inorganic metal catalysts and at high temperatures (350-500 °C) (Nanda et al., 2017)(Shafer et al., 2019). Najafpour, Younesi and collaborators explored different conditions for better fermentation of *R. rubrum* and production of H₂ from syngas. The best hydrogen production and production speed was $16 \pm 1.1 \text{ mmol g}^{-1} \text{ cell h}^{-1}$ and $87 \pm 2.4\%$ at a fixed stirring speed of 500 rpm and a syngas flow rate of 14 ml/min, respectively (Younesi et al., 2008).

These systems can be attractive alternatives for the upgrading of syngas as well as for the production of H₂. However, they are still at laboratory scale, because there are disadvantages such as the main represented by the gas/liquid mass transport. In addition, the high gas pressure can also limit or inhibit the microbial growth. For these reasons, it is essential to characterize and fully understand the chemistry behind these biological catalysts.

The metabolisms and microorganisms presented above have one factor in common: they all possess enzymes with cofactors containing transition metals, mainly iron and nickel. This common feature is directly related to the origin of life on earth. At the beginning of life, the earth was different from what it is now, the atmosphere was rich in gases such as H_2 , CO, CO_2 , N_2 and CH_4 (Wächtershäuser, 2006). These molecules were escaped from the interior of the Earth by magmatic or volcanic exhalations. Furthermore, the presence of these events has made the oceans hot and well supplied with transition metals such as Fe(II) and Ni(II) (Alfano & Cavazza, 2020). Under these environmental conditions, nickel could be considered as the fuel for the engine of life, the engine being the catalysts and the fuel the nickel as cofactor. These nickel-containing catalysts have allowed the development of the metabolism of microorganisms such as methanogenic archaea (Alfano & Cavazza, 2020). These organisms can be considered as pioneers that triggered the complex evolution of life, because they have been able to promote the growth of the organic superstructure through carbon fixation, guided by inorganic substructures (catalysts with metal centers) (Wächtershäuser, 2006). The second most important evolutionary event was the change in the pioneering environment with a decrease in the volcano activity or magmatic fumes and consequent cooling of the upper mantle of the oceans. These geothermal events also reduced the nickel rich environment leading to a "nickel famine" drastically reducing the growth of methanogens (Alfano & Cavazza, 2020). This environmental change of the earth is called the "great oxidation event" which has allowed the proliferation of other microorganisms, such as oceanic cyanobacteria. The latter developed photosynthetic metabolisms in which the final product was dioxygen, leading to a drastic change in the atmospheric composition. The appearance of oxygen in the atmosphere and the oxidative environment has induced the segregation of these ancestral microorganisms in anoxic niches where scientists have isolated them in recent centuries. To date, nine nickel-dependent enzymes have been identified in archaea, bacteria, plants, fungi and

some rare invertebrates, which are: [NiFe]-CODH, acetyl-CoA decarbonylase/synthase (ACDS/ACS), [NiFe]-hydrogenase, methyl-CoM reductase, urease, Ni-superoxide dismutase, lactate racemase, glyoxylase I, and acireductone dioxygenase. Concerning mammalian species, no nickel enzyme has been described (Zambelli et al., 2016). As mentioned earlier, nickel enzymes perform key functions in fundamental processes such as energy metabolism and virulence. These enzymes are either **redox** or **non-redox**. Non-redox enzymes, such as urease (amidohydrolase), that catalyzes the hydrolysis of urea, use Ni(II) as a Lewis acid (Mazzei et al., 2019). The advantage of the Ni-containing catalytic center is the flexible coordination geometry which allows the ability to catalyze a wide range of reactions. The protein environment is then fundamental and is directly linked to the catalytic properties. The latter are closely related to the nature of **donor ligands** involved in Ni coordination and **solvent exposure**. Frequently, the active site is in a buried pocket, where the surrounding protein environment protects it from oxidative damage. This feature requires dedicated channels for substrates/products diffusion, proton channels and electron relays that electro-connect the active site to the physiological partner(s), such as FeS clusters. Furthermore, the coordinating ligands drive the redox properties of the metals giving access to the different redox states involved during the catalysis, allowing the enzyme to catalyze the reactions as close as possible to the standard potential of the reaction. To satisfy these parameters, **S-donor rich** environments are favored in the **redox** enzymes, while for the **non-redox** enzymes the **O/N-donor rich** ligands are favored (Figure 17) (Alfano & Cavazza, 2020).

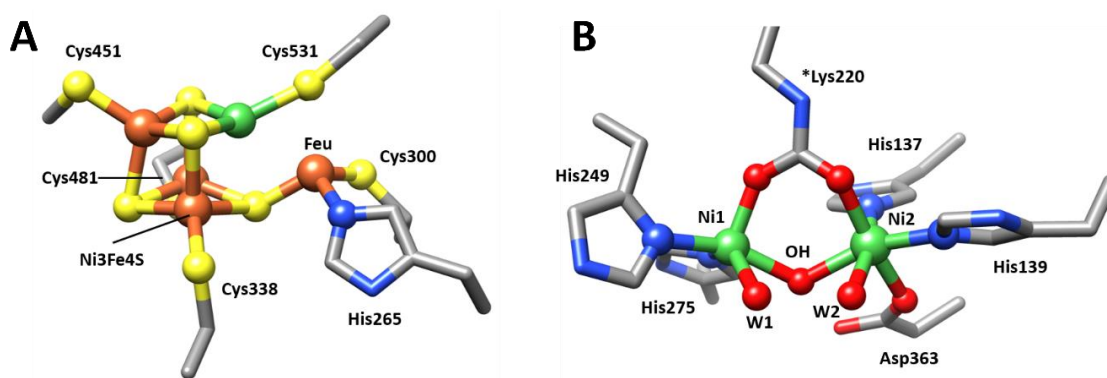


Figure 17 Active site of (A) *Rhodospirillum rubrum* CODH (1JQK) as an example for S-donor rich ligands and (B) *Sporosarcina pasteurii* Urease (4CEU) as an example for O/N-donor rich ligands, a distal water molecule (W3) was omitted because only the O-donors are shown.

As discussed above, redox Ni enzymes are mainly present in ancestral metabolisms of pioneer microorganisms. Another observation confirming this theory is that the NiFe active sites of Hydrogenase, CODH and ACS are coordinated to the protein via several cysteine residues that show structural affinities with natural metal sulfide catalysts (Figure 18) (Nitschke et al., 2013). In fact, these enzymes are defined as pre-Last Universal Common Ancestor (pre-LUCA) catalysts (Nitschke et al., 2013).

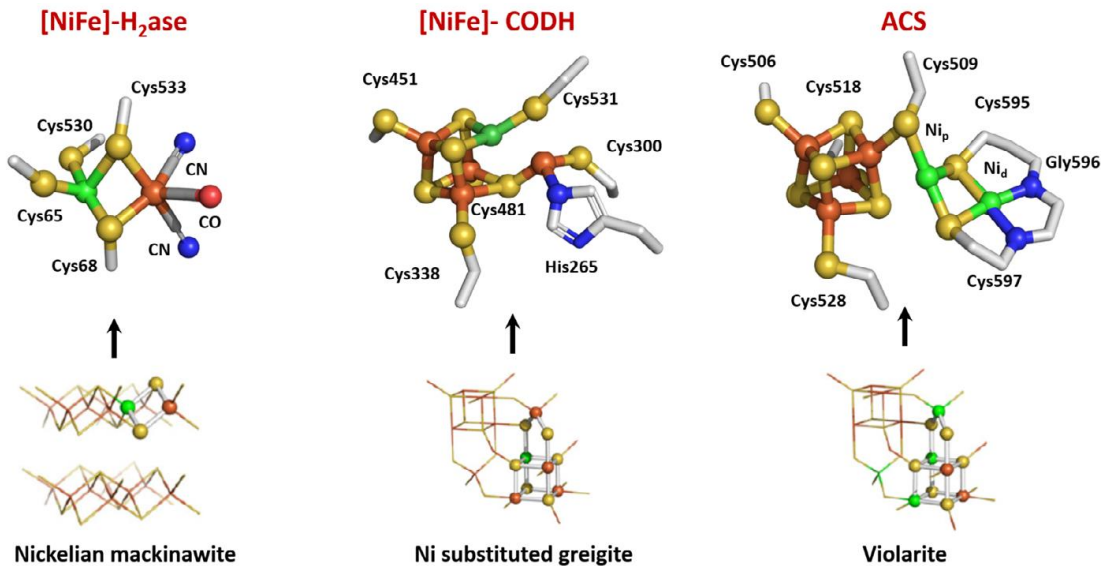


Figure 18 Diagram demonstrating the affinities between the natural sulfide nickelian mackinawite, greigite and violarite with the active centres of early metalloenzymes [NiFe]-H₂ase, [NiFe]-CODH and acetyl coenzyme-A synthase, respectively. (Alfano & Cavazza, 2020).

1.3.1

Ni-Enzymes involved in Biological WGSR in *R. rubrum*

In this section the focus will be on the two key enzymes involved in biological WGSR in *Rhodospirillum rubrum*: CODH and Energy-Conserving Hydrogenase (ECH). The latter belongs to the [NiFe]-Hydrogenase family which represents one of the most ancestral biological systems for the energy metabolism of organisms. They depict an ancient link between hydrogen metabolism and energy conservation, by coupling the exergonic electron transfer to the establishment of a transmembrane proton gradient ($\Delta\mu H^+$) and are progenitors of complex I (NADH dehydrogenase) found in the respiratory chain (Schoelmerich & Müller, 2019). In *R. rubrum*, the WGSR complex is encoded by two operons: *cooMKLXUH* and *cooFSCTJ* (Figure 19A). The *cooMKLXUH* operon encodes a

CO-induced ECH. The *cooFSCTJ* operon encodes the ferredoxin (CooF), CODH (CooS) and related proteins (CooC, CooT and CooJ) for the insertion of nickel into the CODH (Kerby et al., 1997). Present downstream of these two operons the *cooA* gene which encodes for the transcriptional regulator CooA. Its activation depends on CO and it induces the expression of the *cooMKLXUH* and *cooFSCTJ* operons (Fox, Yiping, et al., 1996). CooA possesses a DNA binding domain and two heme domains.

The latter are responsible for the sensing and binding of CO, which induces an allosteric conformational change on CooA which allows interaction with the promoters of the CODH and ECH genes clusters (Roberts et al., 2005). In the true hydrogenogenic thermophilic *C. hydrogenoformans*, which grows in the presence of 100% CO as the only source of carbon and energy and produces equimolar quantities of H₂ (Svetlichny et al., 1991), this multiprotein complex is encoded by the *cooA2CMKLXUH* cluster and by the *cooFS1* genes, interspaced by a 116-bp noncoding region (Figure 19B).

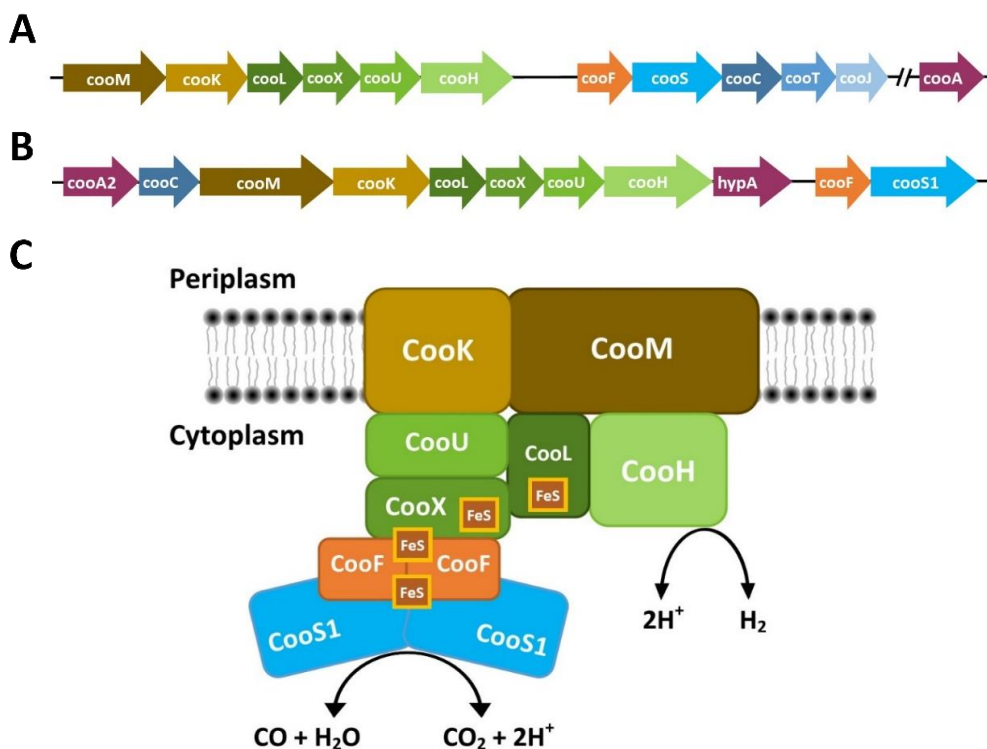


Figure 19 Schematic models of (A) *R. rubrum* ECH (*cooMKLXUH*) and Ferredoxin/CODH (*cooFSCTJ*) operons regulated via the downstream transcriptional activator CooA (*cooA*). (B) *C. hydrogenoformans* Z-2901 ECH (*cooMKLXUHA2*) and Ferredoxin/CODH (*cooFS1*) operons. (C) Schematic model of the CO-oxidizing:H₂-forming enzyme complex from *C. hydrogenoformans*. Capital letters indicate the subunits of the enzyme complex. CO oxidation only at one active site of CO dehydrogenase is shown. FeS box indicate the presence of iron-sulphur clusters into the different subunits. The iron-sulphur clusters of the *CooS1* and *CooH* are not shown. (Adapted from Hedderich & Forzi, 2006).

The whole complex was purified (Soboh et al., 2002) and it is formed by a homodimeric Ni-containing CODH (CooS1), two ferredoxin (CooF) equipped with four iron sulfur

clusters and a membrane bound [NiFe]-H₂ase (CooMKLXUH) composed by four hydrophilic subunits and two membrane integral subunits (Figure 19C). This six subunits cluster that build the membrane-bound hydrogenase share similarity with subunits that form the catalytic core of energy-conserving NADH:quinone oxidoreductases (complex I) from *E. coli* (Hedderich & Forzi, 2006). The isolated complex showed maximal CO-oxidizing:H₂-evolving activity of 450 U·mg⁻¹ protein with 5% CO, higher concentration of CO inhibiting the hydrogenase (Soboh et al., 2002). Further, the complex also catalyzed the CO- and H₂-oxidation which independently specific activity of 5 900 and 180 U·mg⁻¹, respectively (Soboh et al., 2002).

The CODH:CooF:ECH complex coupled to the ATP-synthase may be the simplest form of respiration which combines CO/CO₂ fixation with ATP synthesis in an ancestral pathway. After this brief description of the ECHs, the second enzymatic partner of the biological WGSR, CODH will now be described in details.

1.3.2 [NiFe]-CODHs

[NiFe]-CODHs can be divided into four classes (Figure 20) (Lindahl, 2002): Enzymes found in classes I and II are called acetyl-CoA decarbonylase/synthase (**ACDS**). They are considered as ancestral CODH, found in archaea (mainly methanogens) and consist of five different subunits ($\alpha\beta\gamma\delta\epsilon$) that form oligomeric complexes where the alpha subunit displays the CODH activity.

Class III CODHs are generally found in acetogens where CODH forms a bifunctional complex with acetyl-CoA synthase (**CODH/ACS**). The gene encoding ACS is generally contiguous to the one encoding [NiFe]-CODH, and ACS that is tightly associated with [NiFe]-CODH. Finally, class IV CODHs are **monofunctional** enzymes and their major physiological function is the oxidation of CO as for example, in the WGSR where CO is an energy substrate.

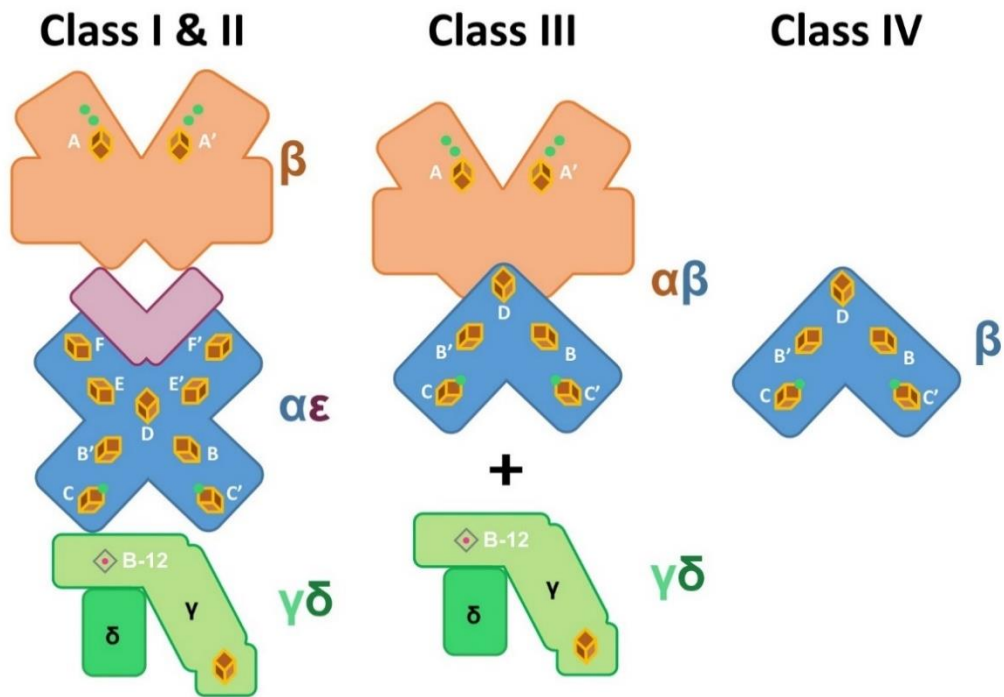


Figure 20 Subunit composition of [NiFe]-CODHs. Monofunctional and bifunctional CODHs may be distinguished according to their subunit composition and physiological function. Multiprotein complexes are indicated by overlapping the forms of the corresponding subunits. Homology within classes is indicated by the same coloration.

1.3.2.1

X-ray structures of bifunctional [NiFe]-CODHs

The ACDS complex catalyzes the transformation of three substrates: CO generated by the reduction of CO₂ (CODH activity), a methyl group donated by a methylated B₁₂ protein (corrinoid iron-sulfur protein or CFeSP, corresponding to the Y subunit) and coenzyme A (CoA) (Can et al., 2014). CoA reacts with CO and the methyl group to form acetyl-CoA, a source of energy and cellular carbon.



The reaction is involved both in the fixation of CO/CO₂ and in acetoclastic methanogenesis in the reverse direction. In this case, this reaction is used for the cleavage of acetyl-CoA to form CoA, methylated CFeSP and CO.

The reactions of synthesis and cleavage of the acetyl C-C and C-S bonds of acetyl-CoA are carried out at the active site called A-cluster (Figure 24A), located in the α subunit for ACS and β subunit for ACDS. The A-cluster is composed of a binuclear Ni-Ni site bridged with a cysteine thiolate to a $[\text{Fe}_4\text{S}_4]$ cluster (Gu et al., 2003). The CODH activity in the ACDS complex is carried out by the α subunit, while β subunit for ACS. The crystal structure of the CODH component of the ACDS from *Methanosarcina barkeri* is available (W. Gong et al., 2008). The structure revealed an oligomerization between two CODH (α) subunits and two ϵ subunits ($\alpha_2\epsilon_2$) (Figure 21AB). The $\alpha_2\epsilon_2$ oligomer shows a total of nine iron sulfur clusters (Figure 21C), in which each α subunit harbors a $[\text{Fe}_4\text{S}_4]$ cluster (B- and B'-clusters) and a Ni-Fe-S cluster (C- and C'-clusters). Another $[\text{Fe}_4\text{S}_4]$ cluster (D-cluster) connects the two α subunits. This organization of five iron sulfur clusters has also been observed in the other $[\text{NiFe}]$ -CODHs classes (see below). Differently from the other $[\text{NiFe}]$ -CODHs classes, the $\alpha_2\epsilon_2$ oligomer harbors two additional $[\text{Fe}_4\text{S}_4]$ clusters (namely, E-, E'-, F- and F'-clusters).

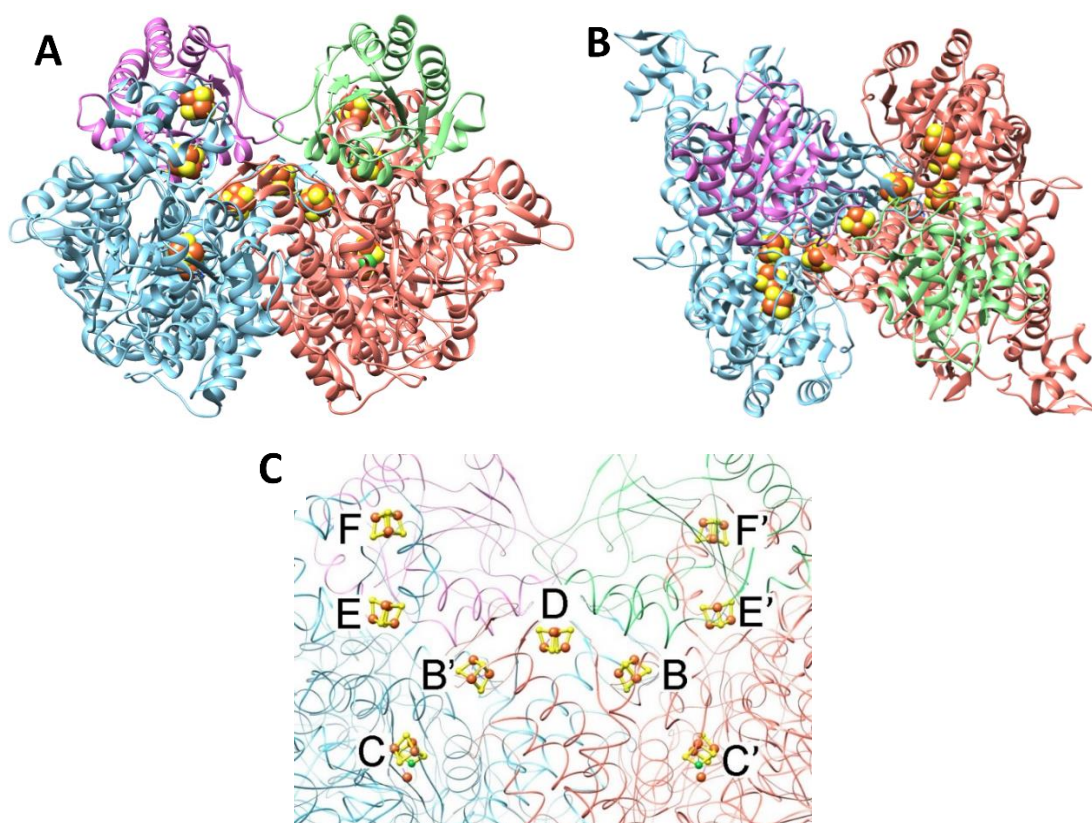


Figure 21 (A) Ribbon diagram of *Methanosarcina barkeri* $\alpha_2\epsilon_2$ $[\text{NiFe}]$ -CODH component of the ACDS (PDB code: 3CF4). Side view of the $\alpha_2\epsilon_2$, the α -subunits coloured in cyan and salmon and the ϵ -subunits in purple and green. (B) Top view of the $\alpha_2\epsilon_2$ component (C) Side view of metal clusters in the $\alpha_2\epsilon_2$ complex.

The role of the ϵ subunits is unknown, it has been hypothesized that they can bind nucleotide cofactors and/or that they are involved in protein-protein interactions and electrons transfer with the other ACDS subunits (Drennan et al., 2001).

The **CODH/ACS** complex was purified from *Moorella thermoacetica* cultures and crystallized. Its crystal structural revealed an $\alpha_2\beta_2$ oligomerization state (Figure 22), in which the central nucleus consists of two CODH subunits (β) and one ACS subunit (α) on each side of CODH.

ACS is made up of three main domains, the first one interacting with CODH via a ferredoxin interaction domain. The second domain is involved in the binding of CoA and the third domain contains the A-cluster. The latter domain undergoes structural rearrangements during the reaction, as shown by X-ray crystallography. Indeed, two different conformations (open and closed states) are observed in the X-ray structure (Figure 22) (Darnault et al., 2003).

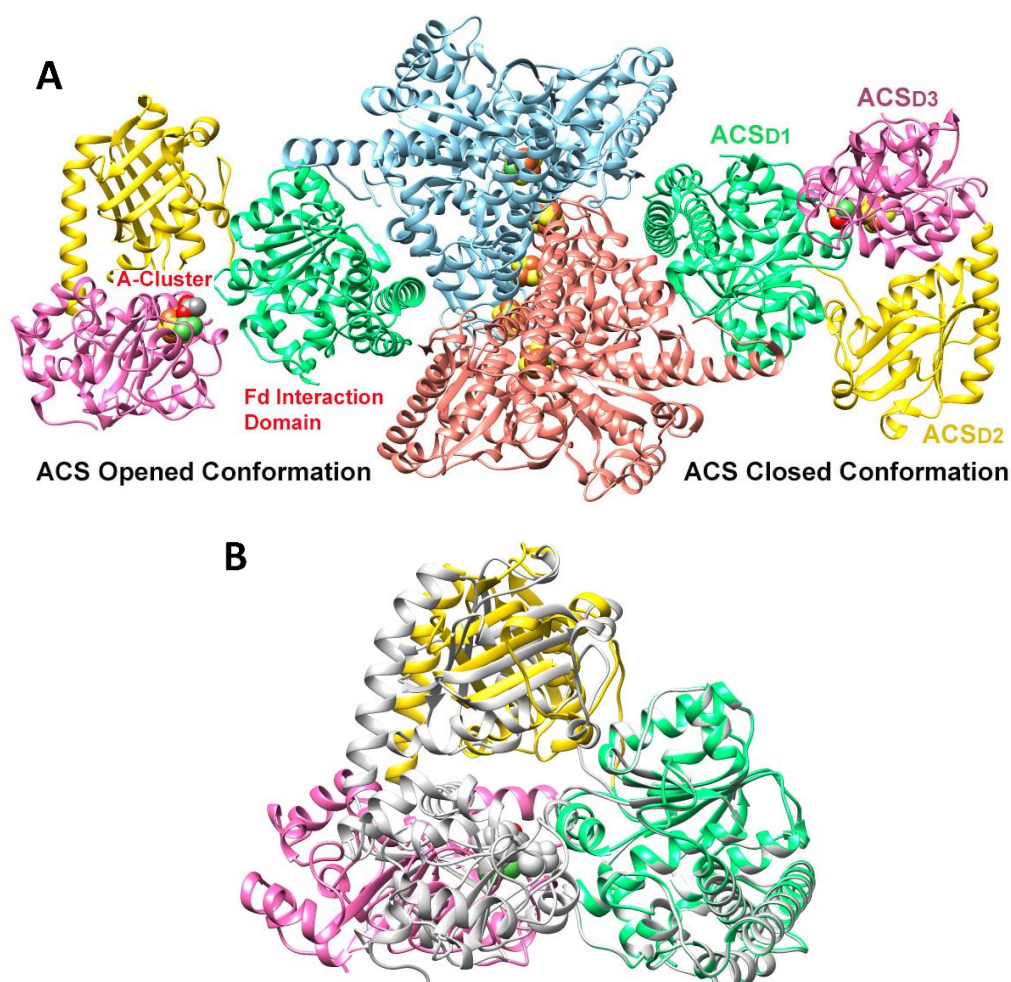


Figure 22 Ribbon diagram of *Moorella thermoacetica* $\alpha_2\beta_2$ CODH/ACS (PDB code: 1OAO). **(A)** Overall structure of CODH/ACS, the two CODH subunits are salmon and cyan, the left ACS subunit is in the opened conformation, the right ACS subunit is in the closed conformation. The three domains of the ACS are green (first), gold (second) and purple (third). **(B)** Superimposition of the ACS subunit in opened and closed conformation, the latter is light gray.

In addition, the CODH/ACS complex was crystallized in the presence of high-pressure xenon gas (Figure 23)(Darnault et al., 2003). The crystal structure revealed the presence of 140 Å long gas tunnels that connect the CODH active site (C-cluster) to the ACS active site (A-cluster). The distance from these two active sites is 67 Å. The CO produced in the CODH subunit remains sequestered inside the enzyme and transferred to the ACS active site through these tunnels. They consist of a series of hydrophobic pockets in which the CO released by C-cluster induces the transfer of another CO into the next pocket to finally reach the A-cluster. This mechanism has been proposed based on the position of Xe atoms in the enzyme, with the Xe closest to A-cluster (Ni) at a distance of only 3.5 Å.

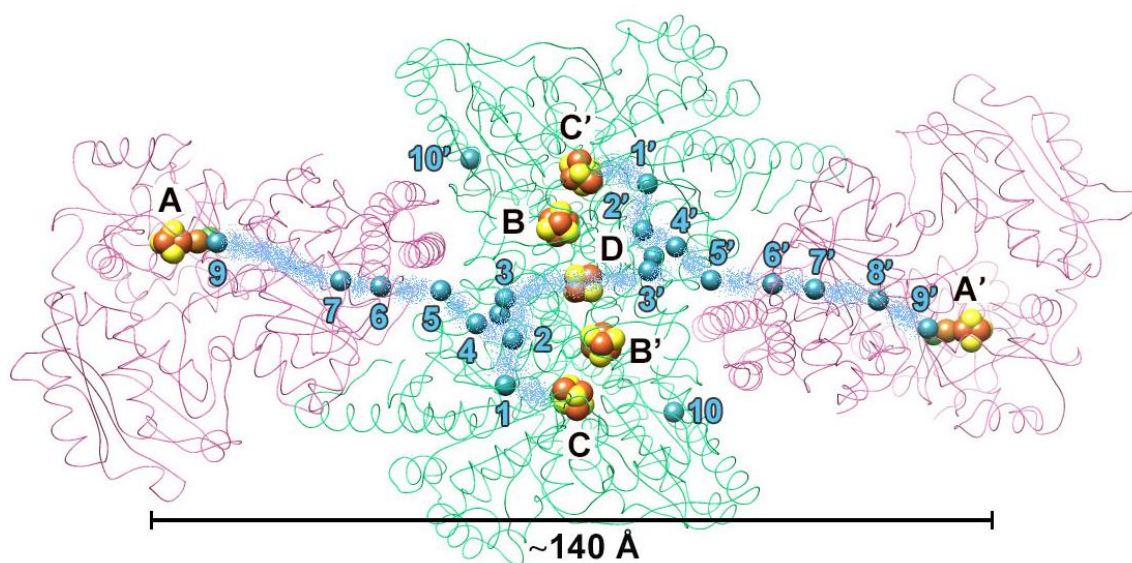


Figure 23 Liquorice ribbon diagram of *Moorella thermoacetica* $\alpha_2\beta_2$ CODH/ACS (PDB code: 2Z8Y). Location of xenon (numbered blue spheres) sites within the structure of the CODH/ACS complex. CODH β -subunits are shown in green and ACS α -subunits are in purple. The predicted hydrophobic CO tunnel pathway is highlighted with dots brush blue. (Adapted from Darnault et al., 2003)

In the closed conformation of ACS subunit, the CO channel is open to allow the CO to reach A-cluster. However, in this configuration, the latter has no access to the physiological partner CFeSP. In the opened conformation, the A-cluster is rotated to allow the interface with CFeSP and the channel is blocked to prevent the release of CO. During the formation of the acetyl-metal center intermediate, another closed conformation is necessary. Hence, A-cluster must be rotated to a more opened conformation to allow for CoA binding, thiolytic cleavage of the acetyl group and the formation and release of acetyl-CoA (Can et al., 2014).

NiFeS clusters are present in both active sites of ACS (in subunit β of ACS and subunit α of CODH/ACS) and CODH (in subunit α of ACS and β subunit of CODH/ACS) (Figure

24A). In A-cluster there are two Ni atoms, namely the proximal Ni_p closest to the [4Fe4S] cluster and the distal Ni_d which is bridged to Ni_p through two cysteine thiolates and further coordinated by the two cysteine backbone amides. Ni_d is in square planar geometry and in the redox state 2+, while the Ni_p is coordinated by three S atoms and a labile position for substrate/product binding (a water molecule in the resting state), which completes a distorted square planar coordination (Doukov et al., 2002).

The presence of the acetyl group in this position has been demonstrated with an enzyme in which Ni_p is replaced by Cu (Figure 24B) (Doukov et al., 2002). The enzyme containing Cu shows a lower activity than the native one, which demonstrates the importance of Ni in A-cluster.

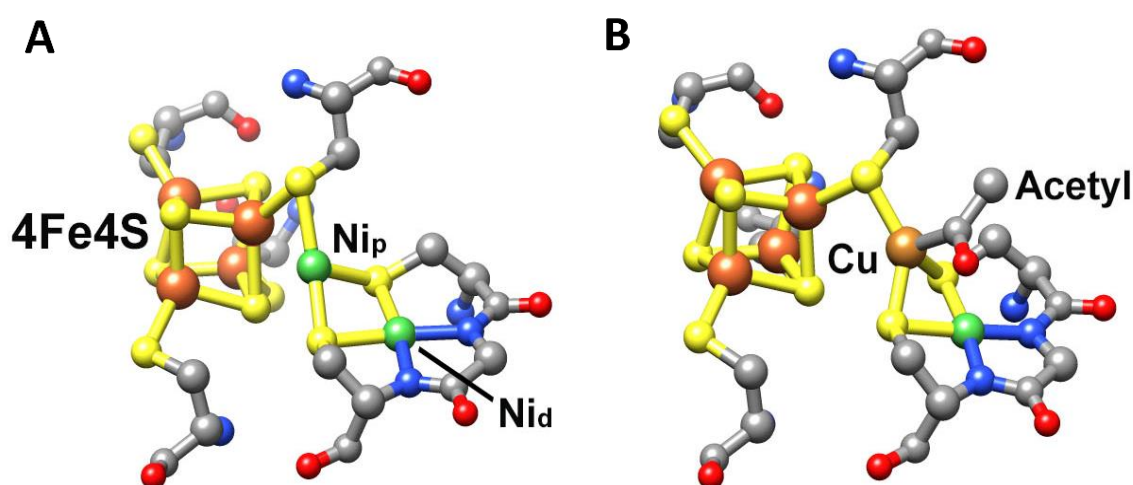


Figure 24 Structures of the A-cluster of *Moorella thermoacetica* (A) from PDB code: 1OAO (B) from PDB code: 1MJG.

The importance of Ni and the role of the C-cluster in CODH will be dealt exhaustively in the following section relating to class IV or monofunctional CODH.

1.3.3 Monofunctional [NiFe]-CODHs

The class IV of [NiFe]-CODHs corresponds to monofunctional CODH. The most studied and characterized enzymes come from the mesophile *R. rubrum* and the thermophile *C. hydrogenoformans*.

R. rubrum possesses only one [Ni-Fe]-CODH (*RrCODH*) which is involved in the WGSR, while in *C. hydrogenoformans*, five genes were identified encoding 5 potential CODHs:

- *ChCODH-I*, like *RrCODH*, is the one involved in WGSR (Svetlitchnyi et al., 2001).
- *ChCODH-II* is associated with the membrane and its role would be related to the generation of NADPH (Svetlitchnyi et al., 2001).
- *ChCODH-III* belongs to the class III of [NiFe]-CODHs, and is part of a bifunctional ACS/CODH complex (Wu et al., 2005).
- *ChCODH-IV* is found in a gene cluster close to an enzyme that reduces peroxide and shows a better oxygen tolerance than other CODHs. Hence, it was proposed to be involved in the response to oxidative stress via an O₂/CO detoxification mechanism (Domnik et al., 2017).
- *ChCODH-V* has an unknown function. However, its X-ray structure shows differences in the organization of the iron-sulfur clusters compared to other monofunctional [NiFe]-CODHs (Domnik, 2018). In fact, it shares similarities with Hybrid Cluster Proteins (HCPs) which contains a [Fe₄S₂O₂] cluster. HCPs protect bacteria from nitrosative stress (J. Wang et al., 2016). Furthermore, this enzyme cannot oxidize CO, therefore it may not be considered anymore as a CODH but rather as an HCP. However, an evolutionary link between the two families of enzymes is strongly suggested (Alfano, 2019).

To date, several structures of monofunctional [NiFe]-CODHs have been solved: *ChCODH II* and *IV*, *RrCODH*, CODH from *Desulfovibrio vulgaris* (*DvCODH*) and CODH I and II from *Thermococcus* sp. AM4 (*TcCODH*), which display a similar overall structure (Drennan et al., 2001)(H. Dobbek et al., 2001)(Wittenborn et al., 2019a)(Domnik et al., 2017)(Benvenuti et al., 2020).

ChCODH II and *RrCODH* possess sequence similarities of 46 % and 63 % with the CODH subunit of the *MtCODH/ACS* complex, respectively (Can et al., 2014). In addition, *MtCODH/ACS* and *RrCODH* structures are nearly identical with a RMSD of ~0.95 Å (Can et al., 2014). Like the CODH subunits of ACS and CODH/ACS complexes, the monofunctional enzymes are homodimers (β_2) which contains five metal clusters: two [NiFeS] active sites called C-clusters, two [4Fe4S] clusters called B-clusters and one intermolecular [4Fe4S] cluster called D-cluster (Figure 25A). The overall organization of the clusters is C-B'-D-B-C' (Fig. 25A), where the D-cluster bridges the two monomers.

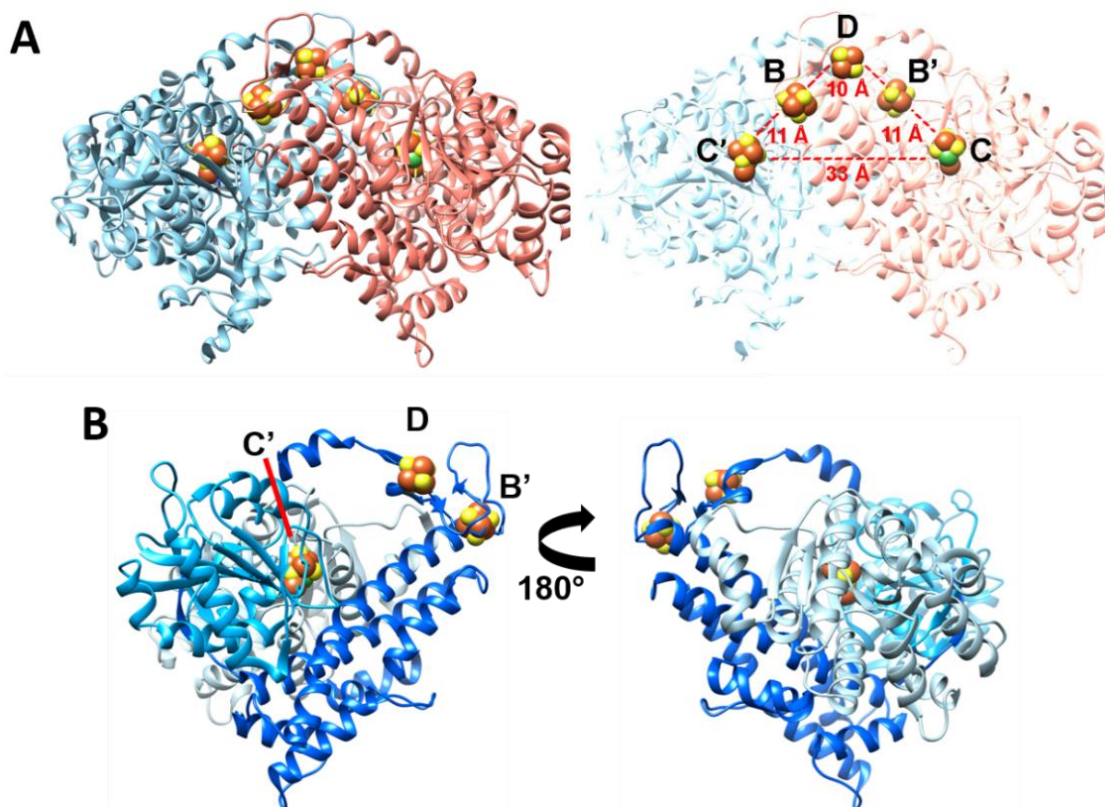


Figure 25 Ribbon diagrams of *Rhodospirillum rubrum* monofunctional CODH (PDB code: 1JQK). Homodimer (β_2) contains two unique $[\text{Ni}_3\text{Fe}_4\text{S}]$ clusters (C and C') and three $[\text{4Fe}_4\text{S}]$ clusters (B, B' and D). Relative clusters distance indicates in Angstrom. **(B)** monomer (β) domains composition: helical N-terminal in electric blue, central α/β Rossmann-like is blue and C-terminal α/β Rossmann-like is light blue.

Each monomer is composed of three domains: a helical N-terminal domain, a central α/β domain (Rossmann-like) and a C-terminal α/β domain (Rossmann-like) (Figure 25B). The two N-terminal domains contribute to the coordination of D- and B-clusters, via cysteine thiolates (Figure 26A), while the two Rossmann-like domains contribute to the coordination of C-cluster. (Drennan et al., 2001). The C-cluster is a distorted $[\text{Ni}_3\text{Fe}_4\text{S}]$ cubane coordinated to a mononuclear iron (Fe_u), unique in biology (Figure 26B). This cluster is coordinated by four cysteine thiolates (Cys338, Cys451, Cys481 and Cys531 in *R. rubrum*) and Fe_u is coordinated by the thiolate group of Cys300 (in *R. rubrum*) and the imidazole group of His265 (in *R. rubrum*). As mentioned above, the interconversion of CO/CO_2 takes place at the C-cluster, according to:



CO oxidation yields CO_2 , protons and electrons, transferred from the buried active site to the protein surface, in order to reach the protein partners. B-clusters are the most

likely candidates for electron transfer, due to their proximity to the active site (11 Å). The role of the D-cluster is not entirely known and it will be discussed in Chapter 4.

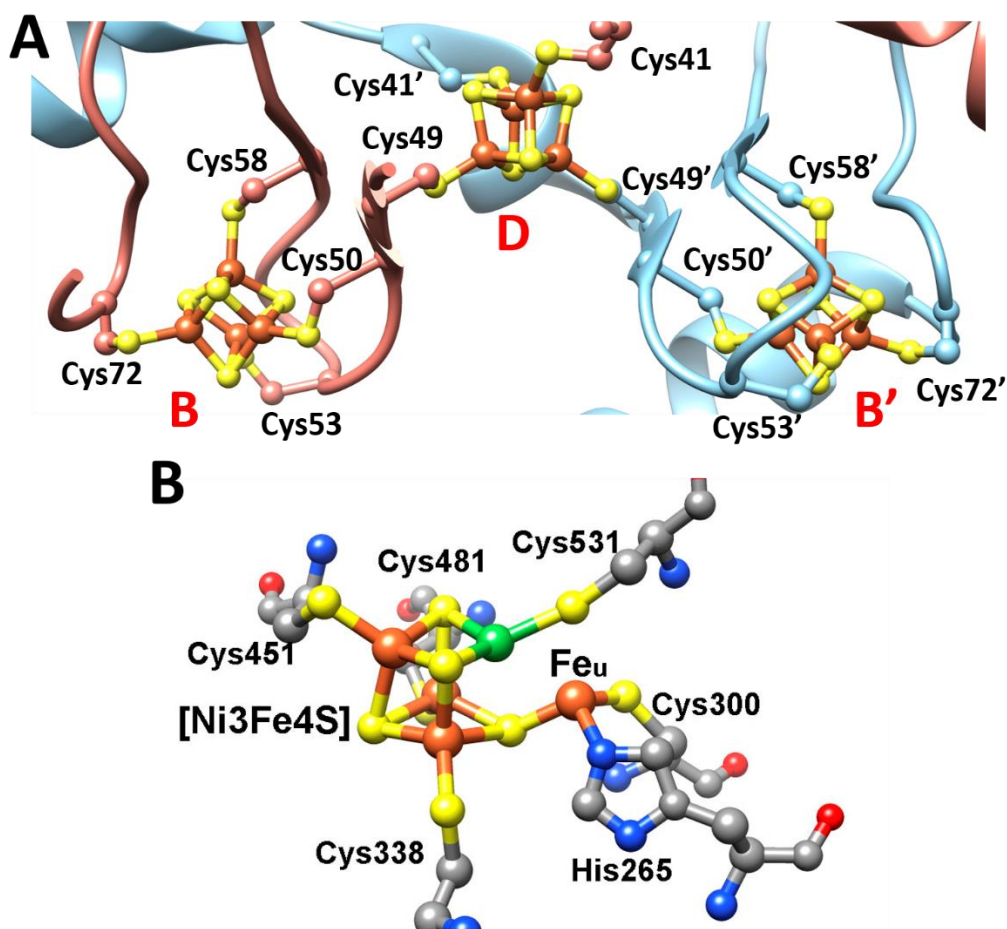


Figure 26 (A) D-, B- and B'-cluster coordination by cysteine thiolates from the two helical N-terminal domains. (B) Structure of *R. rubrum* C-cluster. [Ni₃Fe₄S] cubane is coordinated by four cysteine thiolates: 338, 451, 481, 531 and the Fe_u is coordinated by a cysteine 300 thiolate and histidine 265.

1.3.3.1 Biosynthesis of the Active Site

The synthesis and insertion of C-cluster into the enzyme involves two sequential steps: I) the biogenesis and insertion of Fe and S atoms to form a Fe₄S₄ pre-C-cluster and II) the insertion of the Ni atom to form the active C-cluster. Concerning the first step, in bacteria the **Isc/Suf machinery** is involved in the biogenesis of FeS clusters (F. Gao, 2020). The first step of maturation of C-cluster was shown in *R. rubrum*, by growing the cells in the absence of Ni in the media in order to produce a Ni-deficient CODH in which the active site consists only of the [4Fe4S] cluster (Spangler et al., 1996)(Bonam et al.,

1988)(Ensign et al., 1989). This Ni-deficient CODH is inactive, but can be partially activated *in vitro* by adding nickel salt under reducing conditions (Spangler et al., 1996). Furthermore, it also showed that the Fe_u atom is not present in the Ni-deficient enzyme and that the spectroscopic properties correspond to a classical [4Fe4S] cluster (Spangler et al., 1998). As shown above, C-cluster is coordinated to the protein via five cysteines and one histidine residues (Figure 26), in particular **Cys₃₃₈**, **Cys₄₅₁** and **Cys₄₈₁** coordinate the **three iron** of the [Ni₃Fe₄S] cluster, **Cys₅₃₁** coordinates the **Ni atom** and the **Fe_u** is coordinated by the **His₂₆₅** and **Cys₃₀₀** residues. In addition, Fe_u is linked to the cluster *via* a bridging sulfide. Site-directed mutagenesis was used to discover and understand the precise role of each residue in the electronic properties as well as in the biosynthesis of the C-cluster. Unexpectedly, when the coordinating Cys were mutated (**Cys₃₃₈Ala**, **Cys₄₅₁Ala**, **Cys₄₅₁Ser** and **Cys₅₃₁Ala**), the Ni content was comparable to that of the wild-type enzyme, although the CO oxidation activities were reduced (Table 5) (Jeon et al., 2005). In contrast, The **His₂₆₅Val** mutant exhibits reduced nickel content and drastically abolished activity (Table 5) (Spangler et al., 1998).

Table 5 Metal content and specific CO oxidation activity of wild type CODH and variant of the C-cluster coordinating residues.

CODH variant	Metal content (mol · mol CODH ⁻¹)		Specific Activity (μmol CO oxidized · min · mg CODH ⁻¹)	Reference
	Ni	Fe		
WT	0.97 ± 0.09	8.3 ± 0.9	4,000	(Spangler et al., 1998)
H ₂₆₅ V	0.24 ± 0.02	7.9 ± 0.6	0.67	
H ₂₆₅ V+Ni	2.4 ± 0.1	8.1 ± 0.4	2.4	
WT	0.85 ± 0.05	8.97 ± 0.1	6,230 ± 74.9	(Jeon et al., 2005)
C ₃₃₈ A	0.87 ± 0.06	7.29 ± 0.3	< 0.1	
C ₄₅₁ A	0.92 ± 0.08	6.58 ± 0.7	< 0.1	
C ₄₅₁ S	0.84 ± 0.09	7.59 ± 0.7	86.3 ± 7.5	
C ₅₃₁ A	0.92 ± 0.08	8.9 ± 0.1	6.9 ± 1.8	

These results established that the histidine and cysteine ligands of the C-cluster are critical for CO oxidation activity, although they are not fundamental for Ni insertion into the C-cluster. Concerning the iron content, the CODH variants show a slightly lower content but still in agreement with full metallated FeS clusters. The only ligand that affects the Ni content is His₂₆₅. Interestingly, *in vitro* Ni(II) reconstituted H₂₆₅V shows a Ni content approximately twice as high as the native enzyme one (Table 5), suggesting that **multiple Ni binding sites** could be present.

These results has led to the proposal of a mechanism for the nickel insertion step (Figure 27)(Jeon et al., 2005). Prior to the conversion of the [4Fe4S] cluster to a [3Fe4S] subcluster, the latter can bind Ni to form Ni•[Fe]-complex intermediate. This mechanism involves a bond breaking in the cluster to allow the insertion of the Ni atom. The Fe_u may facilitate the deprotonation of the thiol group of Cys₅₃₁ which allows the mature C-cluster assembly.

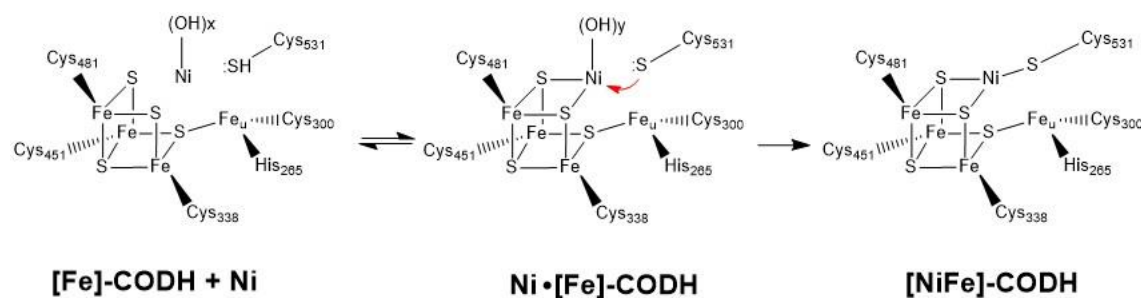


Figure 27 Proposed model for the mechanism of Ni insertion into Ni-free CODH in *R. rubrum* (Adapted from Jeon et al., 2005)

An alternative mechanism has recently been proposed for the Ni insertion, based on crystallographic and spectroscopic studies (Wittenborn et al., 2018). Drennan et al., solved the structure of *Dv*CODH where the C-cluster is fully oxidized. The structure revealed different organizations of the metallocluster (Figure 28). The proposed model is in agreement with the “bond breaking” theory and the displacement of an iron atom and one sulfur atom. This is supported by the structure of C-cluster in an oxidized state, in which Ni, Fe_u and a sulfur are shifted, accompanied by conformational changes of different side chain residues, while the position of the remaining [3Fe3S] sub-cluster is unchanged. Ni occupies the Fe_u site present in the reduced C-cluster form and is coordinated by two cysteines (Cys₃₀₂ and Cys₅₁₉ in *Dv*) and one histidine (His₂₆₆ in *Dv*). Cys₅₁₉ that normally binds Ni in the reduced state adopts an alternative rotamer conformation. An additional Ni ligand is Lys₅₅₆, which normally does not coordinate the reduced C-cluster. Fe_u and the sulfur ion also undergo changes in their coordination while remaining associated with the [3Fe-3S] partial cubane. Two additional Fe_u ligands are Cys₃₀₂ and a conserved cysteine residue (Cys₃₀₁) which is normally not involved in the coordination of C-cluster in the reduced state. The plasticity of these two conformations of C-cluster was demonstrated by the recovering of a canonical organization of C-cluster when oxidized CODH crystals were chemically reduced by sodium dithionite (Wittenborn et al., 2019b).

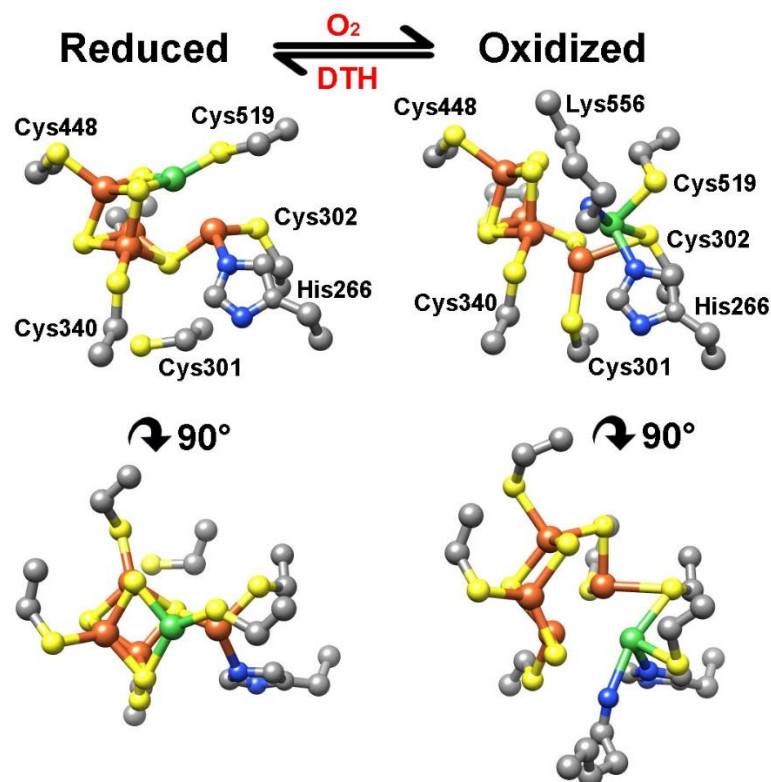


Figure 28 Proposed model for the conversion between oxidized and reduced state of C-cluster in DvCODH (PDB codes: 6B6V and 6B6Y). For example, the conversion from reduced to oxidized state is made possible by oxygen exposure, while the opposite is made possible by sodium dithionite (DTH) reduction. In the reduced state the atoms adopt the canonical conformation of C-cluster CODHs, while in the oxidized state the Ni, Fe_u and one of the sulfur are in a shifted position and the Cys₃₀₁ Lys₅₅₆ appears as new coordinating residues.

In the same manner, the exposure of reduced CODH crystals to O₂ led to a structure with the non-canonical oxidized C-cluster. The structure of the C₃₀₁S mutant, which is catalytically inactive, and does not contain any Ni shows an intact [3Fe-4S] C-cluster core with a Fe_u ion that adopts two conformations: 70% of Fe_u is in its canonical position coordinated by His₂₆₆ and Cys₃₀₂, and 30% is in the canonical position of the Ni of full mature C-cluster (Figure 29).

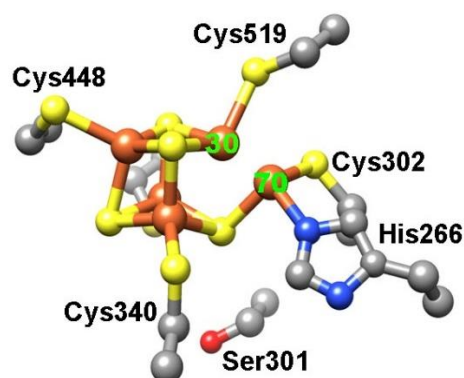


Figure 29 The DvCODH(C₃₀₁S) C-cluster is a mixture of species. The C-cluster has been refined with an alternative conformation of Fe_u. At 70% occupancy, Fe_u is ligated by His₂₆₆ and Cys₃₀₂ in its canonical binding site. At 30% occupancy, Fe_u is incorporated into the Fe-S cubane portion of the cluster.

Taken together, these results suggest that Cys₃₀₁ plays a role in the biogenesis of C-cluster, as well as in the Ni incorporation mechanism. All together these results led to the proposition of an alternative Ni insertion mechanism (Figure 30) (Wittenborn et al., 2019b).

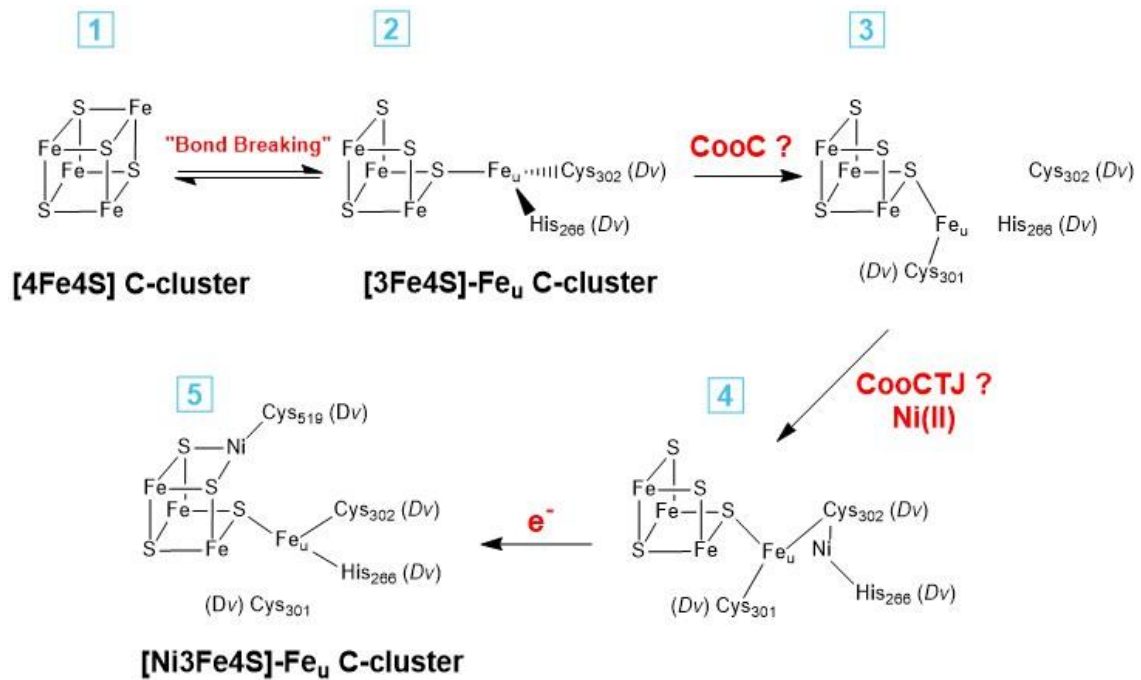


Figure 30 Alternative proposed mechanism for Ni insertion into C-cluster. **1** The C-cluster is produced as [4Fe4S] scaffold. **2** The latter should be converted in a [3Fe4S]-Fe_u subcluster based on the "bond breaking" theory. **3** CooC may be involved in inducing a conformational change in the C-cluster in which the Fe_u becomes ligated by Cys₃₀₁ (Dv). **4** CooCTJ may be involved in Ni insertion into the canonical Fe_u-binding site (as observed by crystallography). **5** Cluster reduction could then result in formation of the fully mature C-cluster (as observed by crystallography). (Adapted from Wittenborn et al., 2019b)

These two model mechanisms raise several questions: is an open distorted [3Fe4S]-Fe_u subcluster a true intermediate of the maturation process? How can His₂₆₅ (Rr) directly drive C-cluster assembly? Could it be spectroscopically and/or crystallographically possible to observe the proposed intermediate 2 and 3 shown in Figure 30?

1.3.3.2

Metallochaperones

A source of information that could shed light on CODHs maturation can be found in the identification of CODHs gene clusters from different bacteria. Actually, recent studies revealed that CODH operons present different organization of the accessory genes

involved in the maturation of the enzyme (Figure 31). Many of them contain the *cooC* gene and some of them do not contain **any maturation protein**. In addition to the *cooC* gene some operons also contain *cooT* genes alone or in association with *cooJ* genes.

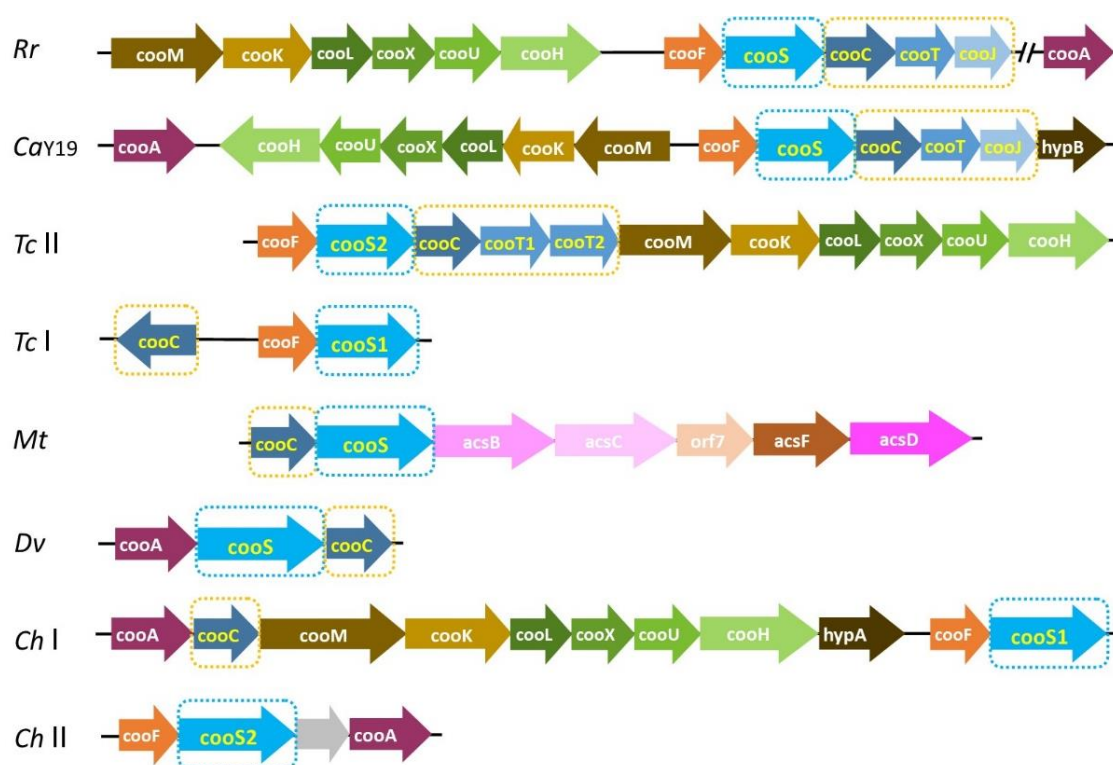


Figure 31 Representative operons encoding for CODH in: *Rhodospirillum rubrum* (Rr), *Citrobacter amalonaticus* Y19 (Cay19), *Thermococcus* sp. AM4 (Tc I and II for CODH I and II, respectively), *Moorella thermoacetica* (Mt), *Desulfovibrio vulgaris* Hildenborough (Dv) and *Carboxydotherrnus hydrogenoformans* (Ch I and II for CODH I and II, respectively). CODHs *cooS* genes and CODH maturation genes are highlighted with a cyan and yellow dot frames, respectively. Electron-conserving hydrogenase genes (*cooM**K**L**X**U**H*) and Acetyl-CoA Synthase genes (*acsBCD*) are also reported. Ferredoxin (*cooF*) is orange, CO-dependent transcriptional activator (*cooA*) is purple.

The physiological functions of *CooC*, *CooT* and *CooJ*, when present in CODH operons, have been demonstrated in *R. rubrum* (Figure 32) (Kerby et al., 1995)(Kerby et al., 1997). First, *R. rubrum* in the absence of light is able to grow using CO as an energy source and is strictly dependent on CODH. The inactivation of the *cooS* gene hinders the growth of *R. rubrum* in the dark under CO (Figure 32). The same results were observed if the three *cooC*, *cooT* and *cooJ* genes are inactivated. However, in this latter case, a nickel supply to the growth medium compensates for the absence of the three genes. When only *cooC* gene is inactivated, *R. rubrum* cells require a nickel concentration 1000 times higher (650 μ M) than wild type cells (0.5 μ M) in order to grow in the dark. When the *cooT* and/or *cooJ* genes are inactivated, the cells require a nickel concentration of at least 50 times higher (better growth with 75 μ M) than wild type cells.

However, in all cases, the CODH activity is not fully restored by Ni addition (at the most 50 % of the active enzyme), showing the importance of the three accessory proteins in CODH maturation and activation. However, the precise role of each of them is not yet clear: they could be either involved in the nickel delivery to C-cluster or in the trafficking and storage of intracellular nickel. In contrast, they were shown to be not involved in nickel uptake from the environment (Watt & Ludden, 1999).

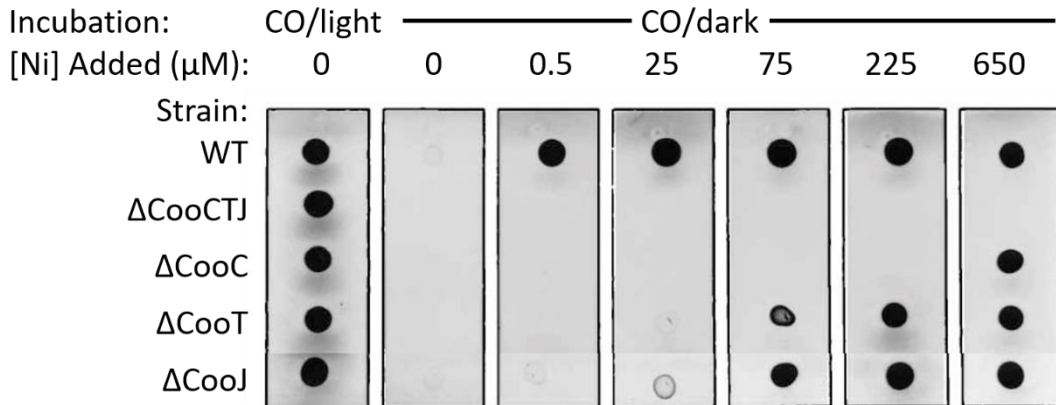


Figure 32 Ni concentration dependence of photosynthetic and CO-dependent growth of *R. rubrum* strains. Cultures were spotted onto plates containing SAN medium supplemented with the indicated concentration of Ni and then incubated in the presence of CO either illuminated or in the dark. Δ followed by the Coo protein indicate the gene that were inactivated. (Adapted from Kerby et al., 1997)

1.3.3.2.1 CooC

CooC is an ATPase described as the major player in CODH maturation, similar to UreG and HypB which are GTPases involved for the maturation of urease and hydrogenase, respectively (Table 6) (Jeon et al., 2001). All CooC homologues have a strictly conserved CXC motif for the metals binding (Ni or Zn) and a conserved GKGGVGKS motif in the phosphate binding loop (P-loop), present in the N-terminal domain. Different crystal structures of *Ch*CooC1 are available, while there is no structure of *Rr*CooC.

According to the *Ch*CooC1 structure obtained in the presence of Zn, CooC is a monomer and dimerize upon addition of Zn and ADP (Figure 33A) to form a presumably active homodimer. The metal is covalently bound to the interface of two monomers by two cysteine residues from each monomer (Cys₁₁₂ and Cys₁₁₄) (Figure 33B). The structures

show that ADP binding induces conformational changes in the metal site and the distances between Zn and the thiolates of Cys₁₁₄ become shorter (from 2.5 to 2.2 Å) (J. H. Jeoung et al., 2010).

Table 6 Comparison between *R. rubrum* CooC, *Methanocaldococcus jannaschii* UreG and *Escherichia coli* HypB.

Protein	P-loop motif	Molecular mass (kDa)	Nucleotide hydrolysis	Reference
<i>RrCooC</i>	GKGGVGKS	27.8	ATP K_M 24.4 μ M GTP K_M 26.0 μ M	(Jeon et al., 2001)
<i>MjUreG</i>	GTPGAGKT	26.2	k_{cat} 0.026 min ⁻¹	(Miraula et al., 2015)
<i>EcHypB</i>	SSPGSGKT	31.6	k_{cat} 0.2 min ⁻¹ K_M 4-7 μ M	(Gasper et al., 2006)

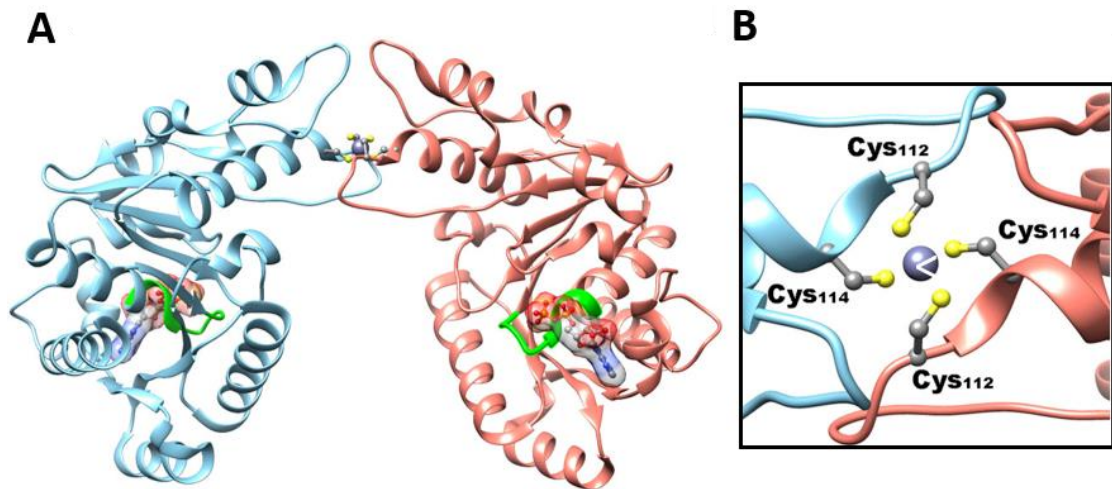


Figure 33 (A) Ribbon diagram of *Carboxydothemus hydrogenoformans* CooC1 (PDB code: 3KJI) in complex with Zn and ADP. The monomers are cyan and salmon. The nucleotide binding domain (P-loop) is green. ADP molecules are depicted with van der Waals surface. (B) The metal binding site at the dimer interface. The Zn atom is grey which is coordinated by two cysteine residues from each monomer (Cys₁₁₂ and Cys₁₁₄).

Thus, the presence of ADP seems to favor the metal binding. A model for the binding and release of nickel was proposed from these studies (Figure 34) (J. H. Jeoung et al., 2010): the Ni(II) binding induces the stabilization of the homodimer, in which the P-loop would be in an open conformation. The ATP binding promotes a conformational change that allows the release of the metal. The way in which this conformational change occurs is not clear and is probably related to the hydrolysis of ATP which can modulate the interaction of CooC with other protein partners (such as CODH). Hence, *ChCooC1* will

perform a dynamic cycle between an open Ni(II) state and a close ATP dependent state that drives the metal release.

For *RrCooC*, the available information comes from its purification from *R. rubrum* cells. Once purified, the protein is a homodimer, containing less than 0.1 atoms of Ni²⁺ or Zn²⁺ and can catalyze the hydrolysis of ATP or GTP (Jeon et al., 2001). The *RrCooC*-K₁₃Q mutant presents a mutation in the P-loop and was inactive for both the ATP hydrolysis *in vitro* and nickel insertion in the Fe-CODH *in vivo* (Jeon et al., 2001). The *in vitro* nickel activation of Fe-CODH in cell extracts (in the presence of CooCTJ), was enhanced by the addition of ATP and Ni salt, while GTP and Ni salt caused a loss of activity, suggesting that ATP is the physiological cofactor in *RrCooC* (Jeon et al., 2001).

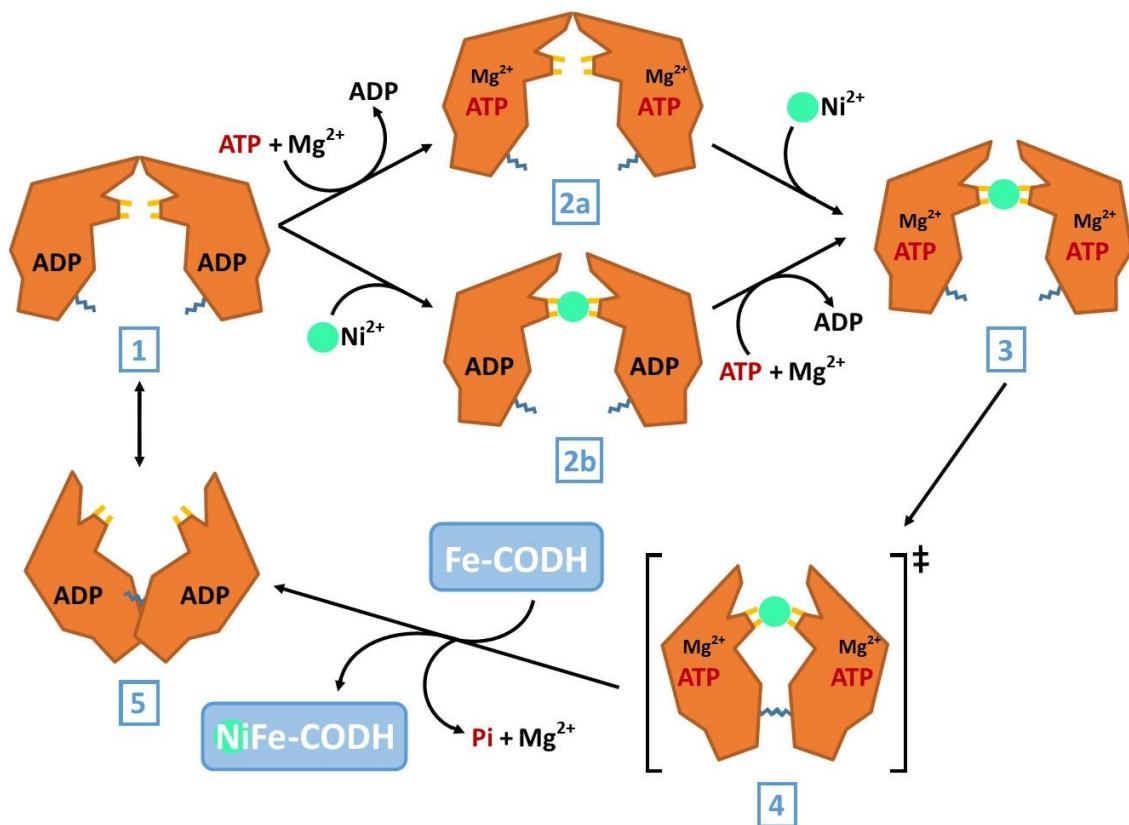


Figure 34 Proposed model for nickel binding and releasing for ChCooC1. The ADP-bound dimeric state (1) was described via X-ray crystallography (PDB code: 3KJG). While the Zn/ADP-bound ChCooC1 (PDB code: 3KJI) is used as a model for Ni/ADP-bound ChCooC1 (2a, 2b and 3), because it is not possible to crystallize ChCooC1 with Ni. The possible ATP triggered conformational change is shown in the state (4) which allow the interaction with CODH and ATP hydrolysis dependent release of Ni (5). The cysteines in the CXC motif are represented in yellow, and the signature lysine is shown in blue. (Adapted from J. H. Jeoung et al., 2010)

CooT proteins are small nickel chaperones with a size of about 7 kDa. Recently, the crystal structures of CooT from *Rhodospirillum rubrum* (*RrCooT*) and of a putative CooT from *Carboxydothemus hydrogenoformans* (*ChCooT*) have been solved. Despite their low sequence identities (about 19 %) *RrCooT* and *ChCooT* possess similar overall structures. Both proteins form homodimers in solution (Figure 35) and each monomer is composed of seven β -sheets. They also both possess a solvent exposed Ni(II) binding site at the dimer interface. Until a few years ago, CooT was only described in *R. rubrum*. Recent phylogenetic analysis revealed the existence of at least 111 CooT homologues in anaerobic bacteria and archaea, with a strictly conserved cysteine in position 2 (Timm et al., 2017). Among the *cooT*-containing genomes, 83 contain also CooC and CODH, strongly suggesting its role in CODH maturation, which is probably more widespread than previously expected (Alfano et al., 2018).

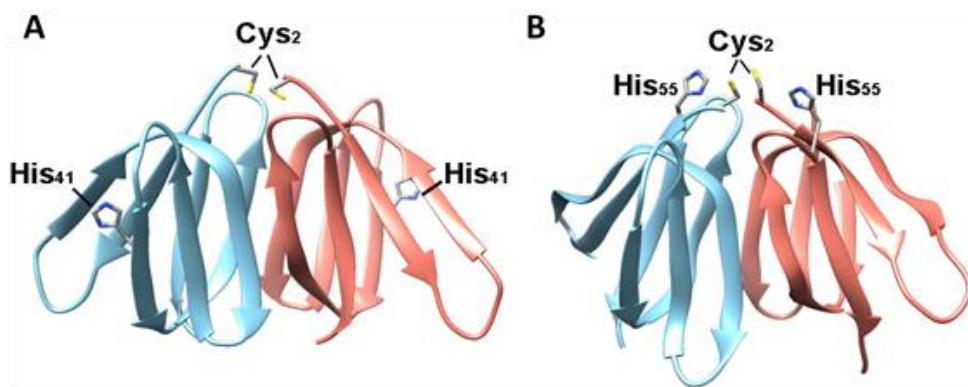


Figure 35 Ribbon diagram of apo-CooT structures from *Rhodospirillum rubrum* (PDB code: 5N76) (A) and *Carboxydothemus hydrogenoformans* (PDB code: 6FAN) (B). The structures show the solvent exposed Ni(II) binding motifs: "Cys₂" for *RrCooT* and "Cys₂-His₅₅" for *ChCooT*.

The alignment of 91 non-redundant CooT sequences revealed the existence of three distinct nickel-binding motifs in the CooT family: the "Cys₂-His_{55/56}" motif, present in *ChCooT*, is preserved in 70.3 % of all sequences, the "Cys₂-Cys₄" motif, (not characterized to date) present in 3.3 % of all sequences and observed only in archaeal CooT, and the remaining sequences displays a "Cys₂" motif, present in *RrCooT* (Alfano et al., 2019). In

the genomes, the *cooT* gene can be present alone (*C. hydrogenoformans*), in duo with CooC and sometimes in several copies as observed in *Thermococcus* sp. AM4 (Figure 31) or in trio with *cooJ* and CooC, as observed in *Thermococcus onnurineus* or *R. rubrum* (Alfano et al., 2018). The coordination of Ni(II) to CooT depends on the nature of the nickel binding motif. Site-directed mutagenesis and biophysical studies showed that both Cys2 and His55 are involved in Ni(II) binding to ChCooT. In RrCooT, Cys2 provides the four Ni ligands (Figure 36A). This bisamidate/bisthiolate Ni(II) coordination via a single cysteine, is unique in biology and raises the question of its role in CODH activation.

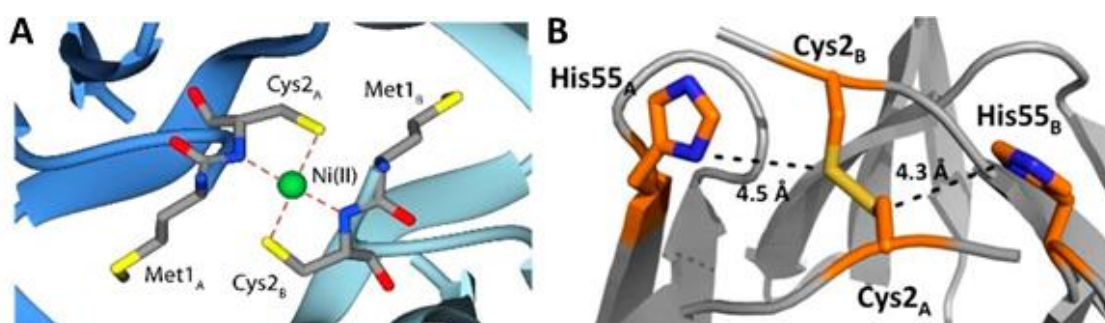


Figure 36 Ni(II) binding motifs: **(A)** RrCooT where the Ni(II) is probably coordinated by two groups thiolate and amidate of both residues of Cys₂ and **(B)** ChCooT where the Ni(II) is probably coordinated by two Cys₂ thiolates and two nitrogen from His₅₅ residues. (Alfano et al., 2018)

1.3.3.2.3

CooJ

CooJ from *R. rubrum* is a 12.5 kDa metallochaperone that contains a His-rich region (HRR) in the C-terminal, formed by 16 His and 2 Cys. CooJ was first purified directly from *R. rubrum* cells (Watt & Ludden, 1998). Interestingly, during the purification CooJ was eluted with CODH and other proteins strongly suggesting the formation of a multiprotein complex between CODH, CooJ and other partners. Recently, CooJ was shown to form a homodimer containing a central coil coiled domain flanked by two independent and highly flexible histidine tails (Figure 38). The His tails possess four metal binding sites with a K_D of 1.6 μM , similar to that was previously observed (Alfano & et al., 2019). Furthermore, the dimer possesses an additional Ni binding site at the interface of the dimer, which binds Ni(II) with an affinity of 0.38 μM and is defined as a high-affinity site (HAS) (Alfano & et al., 2019).

This study also reveals the presence of 46 bacterial homologues, all of which possess two spatially separated nickel binding motifs: a variable C-terminal HRR and a strictly conserved “H-(W/F)-X₂-H-X₃-H” motif, suggesting a double function for CooJ both as a Ni chaperone and as a Ni storage protein. To confirm this dual role of CooJ, it has been shown that a C-terminal truncated version of CooJ with only 6 histidines and no cysteine is still able to activate CODH *in vivo*, suggesting that its tails are dispensable for CODH maturation (Kerby et al., 1997). The role of Ni-binding HRR in proteins is generally proposed to be related to nickel storage and/or detoxification. HRR are also present in other Ni-chaperones with variable location in the protein sequence (C- or N-terminal), such as UreE (N-terminal) and UreG (C-terminal) involved on the maturation of urease or HypB (N-terminal) and SlyD (C-terminal) and HypB (internal position) for the maturation of hydrogenase (Alfano & et al., 2019). The X-ray structure of a truncated *RrCooJ*, without its His tails, is available (Figure 37A). The structure shows that the HAS is exposed to the solvent, which is compatible with a rapid metal transfer to the physiological partner(s) (Alfano & et al., 2019). The Ni(II) ion is coordinated by four histidine residues, two from each monomer. The Ni(II) ion is coordinated by four histidine residues, two from each monomer.

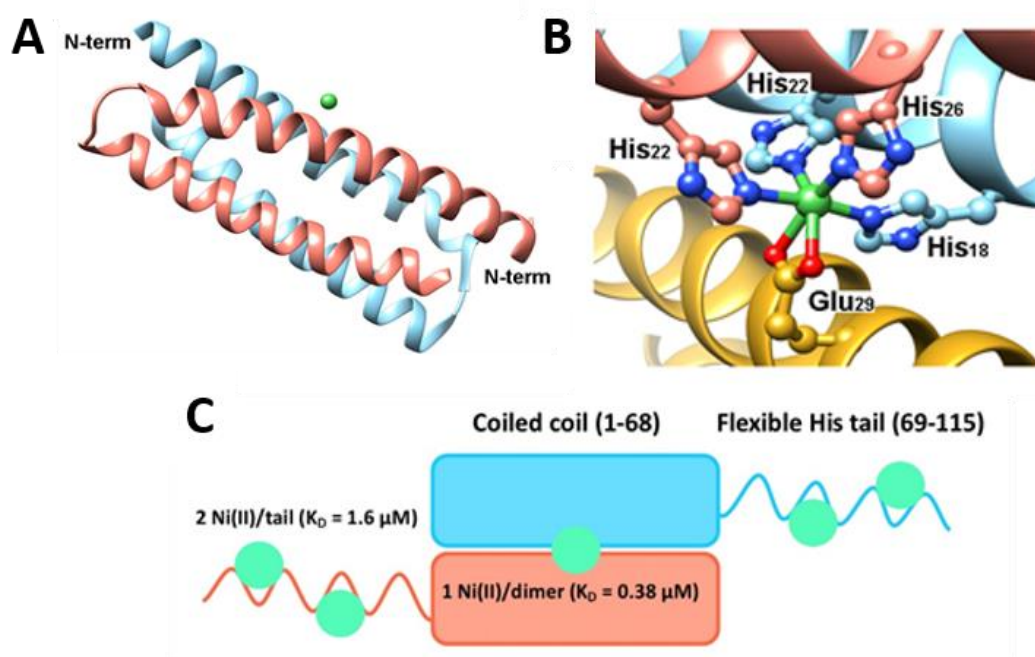


Figure 37 (A) Ribbon diagram of the truncated *Rhodospirillum rubrum* CooJ (PDB code: 6HK5). Each monomer of the homodimer are in cyan and salmon, Ni(II) is depicted as a green sphere. (B) Structure of the Ni(II)-binding site. Ni(II) is coordinated by four histidines, two for each monomer. Additional two Ni ligands from a glutamate from a second homodimer (in gold) of the crystal. In solution these two ligands can be water molecules. (C) Diagram of the *RrCooJ* homodimer composed by the two coiled coil monomer (residues from 1 to 68) and the two independent flexible histidine tails (residues from 69 to 115). Each dimer bound one Ni(II) at the interface of the coiled coil monomer with a K_D in nanomolar range. Additional four Ni(II) are bound two for each histidine tail with a K_D in micromolar range.

In the crystal structure two additional Ni ligands from a glutamate present in a close dimer completes an octahedral coordination geometry (Figure 37B), where in a solvent-exposed Ni(II) binding site, water molecules can easily replace the glutamate residue in solution (Alfano & et al., 2019). To date, the maturation mechanism of CODH remains unclear. Two models have been proposed, implying CooC and CooJ (Figure 38) (Jeon et al., 2001). In the first one, CooJ binds Ni(II) at first and transfer it to apo-CooC which acts as an insertase to deliver the Ni to the CODH active site. In the second model, CooC uses ATP hydrolysis to fold the nickel center and CooJ would be in charge of delivering nickel to the CODH active site. The role of CooT in these models has not been taken into account and it has yet to be clarified (Kerby et al., 1997).

To conclude, the maturation of CODH appears to function differently among microorganism, based on the presence and genomic context of CooC, CooT and CooJ. The ability to produce recombinant CODH from different biological sources in various heterologous systems sheds light on these mechanisms.

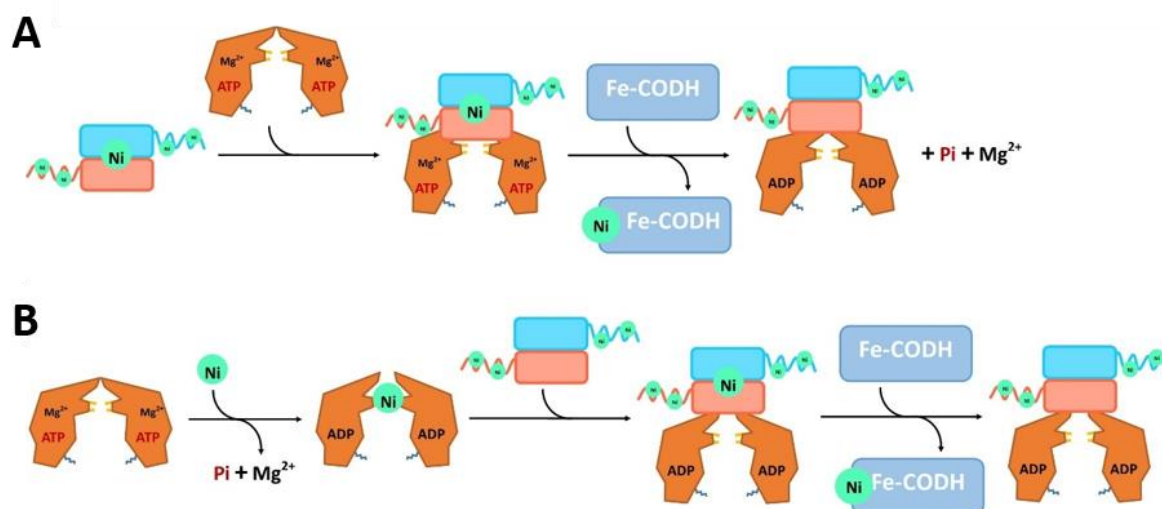


Figure 38 Two proposed model for CooC-CooJ mediated Ni insertion into [Fe]-CODH: **(A)** CooJ binds the free nickel in the cell and transfer it to the apo-CooC. The ATP hydrolysis allow the transfer of the Nickel from CooJ to the [Fe]-CODH to make the [NiFe]-CODH. **(B)** CooC use the ATP hydrolysis to fold its proper nickel centre which allow its transfer to CooJ that finally insert the Ni into the [Fe]-CODH to make the [NiFe]-CODH.

The possibility of heterologously produce CODH in the easy-to-grow bacterium *E. coli* with plasmids containing both the target enzyme and the accessory proteins has opened up a new way in the study of CODH, known to be difficult to purify from natural bacteria (H. Inoue et al., 1990). For example, the growth of *R. rubrum* in order to produce CODH requires anaerobic conditions and management of CO, a toxic gas, which also results in a low yield of pure enzymes, 0.3-3 mg L⁻¹ (starting from 107-135 grams of crude cells) (Bonam & Ludden, 1987)(Bonam et al., 1988). Furthermore, when the industrial applications are the final goal, it is essential to develop a stable and reproducible expression and purification system for the large-scale production of enzymes. However, it is important to consider that in the case of metalloproteins, the establishment of an efficient overexpression system is not an easy challenge, due to the complexity of the maturation processes necessary to build and insert their metallic active centers (Windsor & Steele, 2010). To date, several groups have succeeded in the recombinant production of CODHs in *E. coli* or other host bacteria.

First of all, in 2007 Jeoung and Dobbek expressed and purified *Ch*CODH-II, which has no associated chaperone in the native operon (J.-H. Jeoung & Dobbek, 2007). His-tagged Rec*Ch*CODH-II was produced anaerobically in *E. coli* under reducing conditions with a nickel supply in the culture medium (200 μM NiCl₂). Thanks to the His tag, the enzyme was purified in one step and showed a specific CO oxidation activity of 12 229 U·mg⁻¹, which is close to that of the native enzyme (14 200 U·mg⁻¹). The activity was assayed in the same conditions as the wild type (at 70 °C in buffer at pH 8.0).

In 2014, Inoue et al. expressed and purified *Ch*CODH-I, which unlike *Ch*CODH-II possesses a *CooC* gene (*cooC3*) in the native operon (T. Inoue et al., 2014). The His-tagged Rec*Ch*CODH-I was produced in *E. coli* with a protocol based on that of Jeoung and Dobbek, with the only difference that the bacteria were grown aerobically before IPTG induction. Purified Rec*Ch*CODH-I showed a specific activity of 2 270 U·mg⁻¹ which is equivalent to 12% of the wild type enzyme activity. The co-production of the enzyme

with its accessory protein *CooC3* resulted in an increase of the specific activity to reach 8 060 U·mg⁻¹, corresponding to 43% of the native enzyme activity. Interestingly, both the *RecChCODH-I* and *RecChCODH-I^{CooC3}* enzymes showed a lower nickel content than the wild type enzyme, with values of 14 and 42%, respectively. The percentage of Ni in the recombinant enzymes coincides with the percentage of specific activity compared to the native *ChCODH-I*. The authors suggested that when *CooC* is in the same operon as *CODH*, its co-expression is necessary for Ni insertion into the recombinant *CODH* (T. Inoue et al., 2014). However, these results would suggest that additional partners seem to be required for the production of fully mature enzyme, which may not be in the same operon as *ChCODH-I* and *ChCooC3*.

Table 7 Specific activity (U·mg⁻¹) of CO oxidation and Nickel content of wild type and recombinant *Carboxydotherrmus hydrogenoformans* *CODH-I* and *-II*.

ChCODH-II (No maturase in the operon)	Ni/dimer	U·mg ⁻¹ at 70°C and pH 8.0	Reference
Wild Type	2	14,200	(Svetlitchnyi et al., 2001)
Recombinant	N. D.	12,229	(J.-H. Jeoung & Dobbek, 2007)
ChCODH-I (CooC3 present in the operon)			
Wild Type	1.42	18,900	(Svetlitchnyi et al., 2001)
Rec-CODH	0.2	2,270	(T. Inoue et al., 2014)
Rec-CODH+CooC3	0.6	8,060	

A few years later, the recombinant *DvCODH* was successfully produce, not in *E. coli* but in *Desulfovibrio fructosovorans* (Hadj-Saïd et al., 2015). *D. fructosovorans* cells were grown anaerobically in a nickel supplemented medium. To date, the wild type enzyme has not yet been purified. The *DvCODH* operon harbors the accessory protein *CooC*. Pure *RecDvCODH* displays a very low specific activity (<5 U·mg⁻¹) and its co-expression with *CooC* has a positive effect on the specific activity (160 U·mg⁻¹). Although this value is still far from those obtained with described *CODH*, these results confirm the importance of *CooC* when present in the operon. *RecDvCODH^{CooC}* can be further activated by incubation with NiCl₂ under reductive conditions, leading to a specific activity of 1 660 U·mg⁻¹. Although the specific activity of the native enzyme is not known, it is possible to hypothesize that some accessory proteins would be missing to heterologously produce a fully active *DvCODH*, considering the improvement of the activity by *in vitro* incubation with Ni salts.

Table 8 Specific activity ($U \cdot mg^{-1}$) of CO oxidation and Nickel content of recombinant *Desulfovibrio vulgaris* CODH.

Sample	Ni/dimer	$U \cdot mg^{-1}$ at 37°C and pH 10.0
DvCODH	0-0.5	< 5
DvCODH+CooC	0.8-1.8	160
DvCODH+CooC+Ni activation	N.D.	1 660

Recently the same group has performed the production of the recombinant CODH-I and -II from *Thermococcus sp.* AM4 in *Desulfovibrio fructosovorans* using the same protocol (Benvenuti et al., 2020). Again, for *Tc*CODHs, the specific activities of wild type enzymes are not yet known. The genome of *Thermococcus sp.* AM4 possesses three *cooC* genes: *cooC1* inside the CODH-I operon, *cooC2* inside the CODH-II operon and an additional *cooC3* inside an operon not related to CODH. Rec*Tc*CODH-I and -II were co-expressed with the three different *cooC* genes. As observed with RecDvCODH, the pure Rec*Tc*CODH-I and -II showed a higher specific activity and Ni content when they are co-produced with *CooC*, except in the case of *CooC3* (Table 9). In addition, *Tc*CODH-I reaches a better activity when it has been co-expressed with *CooC2* (twice compared to the co-expression with *CooC1*) whose gene is present in the same operon as CODH-II, suggesting that *CooC* can be interchangeable for CODH activation (Figure 39).

Table 9 Specific activity ($U \cdot mg^{-1}$) of CO oxidation and Nickel content of recombinant *Thermococcus sp.* AM4 CODHs.

Sample	Ni/dimer	$U \cdot mg^{-1}$ at 37°C and pH 8.0
<i>Tc</i> CODH-I	0.32	5.5
<i>Tc</i> CODH-I + <i>CooC1</i>	0.98	27
<i>Tc</i> CODH-I + <i>CooC2</i>	1.50	62
<i>Tc</i> CODH-I + <i>CooC3</i>	0.28	6.4
<i>Tc</i> CODH-II	0.22	10.5
<i>Tc</i> CODH-II + <i>CooC1</i>	1.40	210
<i>Tc</i> CODH-II + <i>CooC2</i>	1.82	262
<i>Tc</i> CODH-II + <i>CooC3</i>	0.30	12.4

Another question arises on the role of *CooC3*, which is not present in any *Tc*CODHs operon (Figure 39) and its co-expression with both *Tc*CODHs does not have any impact on the enzyme activity. Furthermore, the low activities obtained in all combinations of CODH and *CooC* genes strongly suggest that, in addition to *CooC*, other metallochaperones are required for the C-cluster biosynthesis. In fact, in the *Tc*CODH-II

operon, two *cooT* genes are present downstream *CooC2* (Figure 39). Their presence strongly suggests their implication in the maturation pathway of the enzyme.

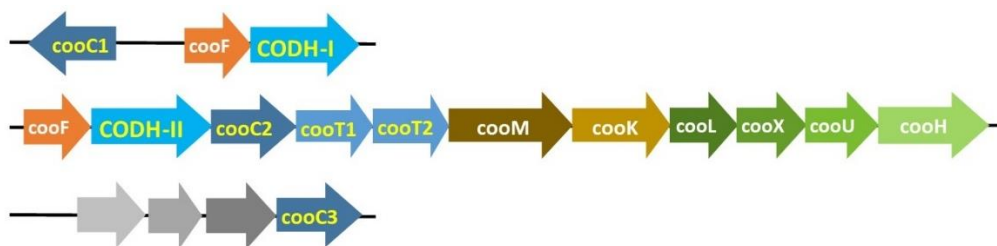


Figure 39 Organization of TcCODHs gene clusters. TcCODH-I gene cluster also contain *cooF* and *cooC1*. TcCODH-II also contain *cooF* (upstream), *cooC2*, *cooT1*, *cooT2* and *ECH* genes (downstream). *CooC3* is present in a gene cluster not related to CODHs gene. (Adapted from Benvenuti et al., 2020)

Another reason of their low CO oxidation activity could be that the role of CODHs would not be related to CO/CO₂ interconversion. It would be rather related to other functions as proposed for *ChCODH-IV* which acts as a CO scavenger in defense against oxidative stress (Domnik et al., 2017). Taken together, these results on the heterologous production of various CODHs allow us to hypothesize that there are different mechanisms for Ni insertion into CODHs and further studies are needed to elucidate these mechanisms.

1.3.3.4 Reaction Mechanism

[NiFe]-CODHs have been studied in depth by various approaches, such as X-ray crystallography, spectroscopy and electrochemistry, allowing the postulation of a common catalytic mechanism. First of all, several CODH were co-crystallized with substrates/products (CO, CO₂ and H₂O), analogues of substrates and products as well as inhibitors (cyanide, cyanate, *n*-butyl isocyanate). The 2.0 Å resolution structure of *MbCODH* (W. Gong et al., 2008) shows that CO is bound to Ni and a water molecule is bound to the Fe_u (Figure 40A). These results are supported by the *MtCODH/ACS* structure at 2.15 Å resolution (Kung et al., 2009) which was solved after crystal soaking with cyanide (CN⁻ a CODH inhibitor). CN is bound to Ni and a water molecule is bound to Fe_u (Figure 40B). In both structures, CO/CN⁻ appears in a bent geometry, confirmed in the *ChCODH* structure co-crystallized with *n*-butyl isocyanate (*n*-BIC) (J. H. Jeoung &

Dobbek, 2012), where *n*-BIC is bound to Ni and water still bound to Fe_u (Figure 40C). This bending is due to the steric hindrance of a conserved isoleucine.

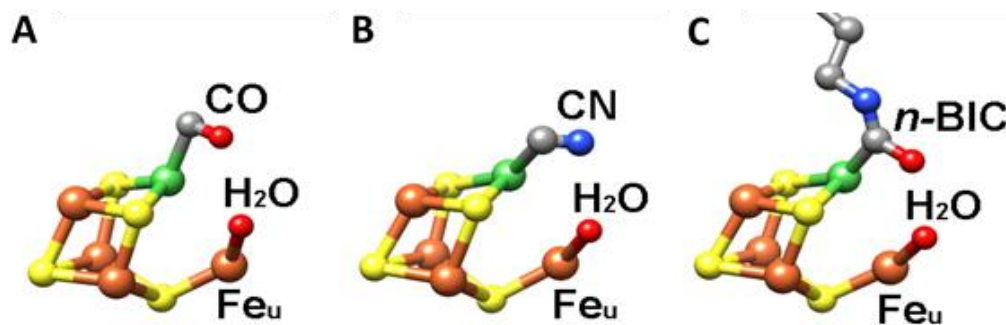


Figure 40 Structures of CODH C-clusters bound to (A) CO and water (PDB: 3CF4), (B) CN and water (PDB: 3I04), (C) *n*-BIC and water (PDB: 2YIV). Only the [Ni₃Fe₄S] cubane coordinated to the mononuclear iron (Fe_u) are shown.

A *Ch*CODH structure obtained at 1.36 Å resolution with Ni bound to the CN⁻ without water molecule at Fe_u shows a CN⁻ with a more linear geometry (Figure 41A). The CN⁻ competes with CO for the binding to Ni, as confirmed by the presence of cyanide in both *Ch*CODH and *Mt*CODH/ACS structures, and can also displace the water molecule in order to create room leading to a more stable linear geometry (Ciaccafava et al., 2016). Furthermore, the *Ch*CODH structures in the presence of either CO₂ or cyanate (NCO⁻) (Figure 41BC), were solved at the real atomic resolutions of 1.03 and 1.06 Å, respectively. In both structures, CO₂/NCO⁻ carbon is bound to Ni and oxygen to Fe_u. In the case of CO₂, the oxygen bound to Fe_u comes from a water molecule.

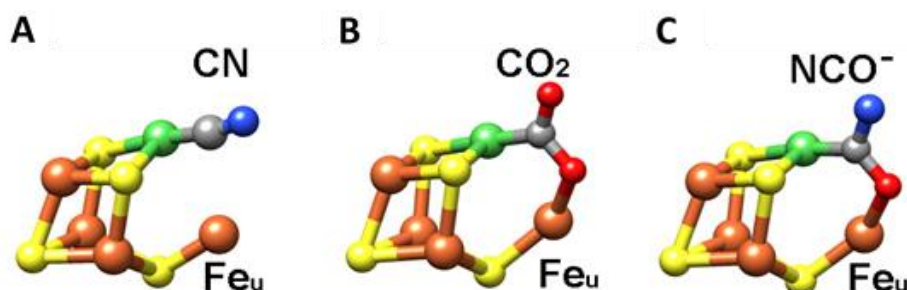


Figure 41 Structures of CODH C-cluster bound to (A) CN (PDB: 3I39), (B) CO₂ (PDB: 4UDX), (C) NCO⁻ (PDB: 4UDY). Only the [Ni₃Fe₄S] cubane coordinated to the mononuclear iron (Fe_u) are shown.

Based on spectroscopic investigations and chemical reasoning, the C-cluster exists in three different oxidation states: a fully oxidized and catalytically inactive C_{ox} state, a one electron reduced C_{red1} state which binds CO and a three electrons reduced C_{red2} state which binds CO₂ (Can et al., 2014). At redox potentials above -200 mV, C-cluster is in the C_{ox} state, which is diamagnetic (*S* = 0) and probably corresponds to a {[Ni²⁺Fe³⁺]:[Fe₃S₄]¹⁻} state (J. Feng & Lindahl, 2004). Below -200 mV, C_{ox} is reduced by one electron and forms the paramagnetic C_{red1} state (*S* = 1/2) which can be assigned as a {[Ni²⁺Fe²⁺]:[Fe₃S₄]¹⁻}

state (J. Feng & Lindahl, 2004). The C_{red1} state is ready to bind and react with CO, accepting two electrons, from the oxidation of CO to CO_2 , and forming the paramagnetic state C_{red2} ($S = 1/2$) (J. H. Jeoung et al., 2019). The latter is the redox state required for CO_2 reduction.

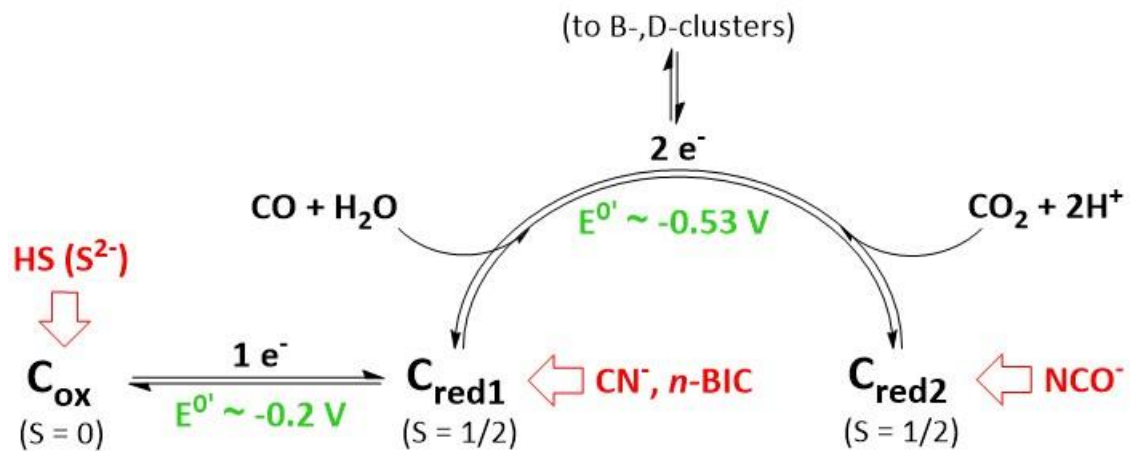


Figure 42 Mechanism of CO/CO_2 redox catalysis by CODHs C-cluster. The electronic states of C-cluster are reported with their relative spin states and mid-point potentials (in green). The inhibitors of C_{red1} and C_{red2} states are also reported (in red). Sulfide binds the C_{ox} state and can inhibit CO oxidation but no CO_2 reduction. CN^- compete with CO for C_{red1} bind but it does not inhibit C_{red2} state for CO_2 reduction. NCO^- inhibits CO_2 reduction by binding C_{red2} state but it does not inhibit C_{red1} state for CO oxidation. (Modified from Feng & Lindahl, 2004).

Thus, C-cluster has several redox midpoints depending on its redox state: $C_{ox}/C_{red1} \sim -200$ mV and $C_{red1}/C_{red2} \sim -530$ mV. B-clusters show a midpoint potential between -300 and -530 mV ($B_{ox}/B_{red} \sim -418$ mV), consistent with its role in electron transfer (J. Feng & Lindahl, 2004), while D-cluster adopts a diamagnetic state ($S = 2$) at potentials higher than -530 mV, which is coherent with the possible role in electron transfer (Can et al., 2014). The g-values of several [NiFe]-CODHs, determined by Electron Paramagnetic Resonance (EPR), are shown in Table 10 (Spangler et al., 1996)(Lindahl & Ragsdale, 1990)(Krzycki et al., 1989)(Hadj-Saïd et al., 2015).

Table 10 Electron Paramagnetic Resonance (EPR) data for the CODHs from different sources

Bacteria	B-cluster			C-cluster C_{red1}			C-cluster C_{red2}		
	g-values			g-values			g-values		
<i>R. rubrum</i> ^a	2.04	1.93	1.89	2.03	1.88	1.71	1.97	1.87	1.75
<i>C. hydrogenoformans</i> ^b	2.04	1.93	1.89	2.01	1.89	1.73	1.96	?	1.75
<i>M. thermoacetica</i> ^c	2.04	1.94	1.9	2.01	1.89	1.65	1.97	1.87	1.75
<i>M. barkeri</i> ^d	2.05	1.94	1.9	2.01	1.91	1.76	?	?	1.73
<i>D. vulgaris</i> ^e	2.03	1.94	1.89	2.02	1.9	1.71	1.97	1.87	1.75

a (Spangler et al., 1996), b (Can et al., 2014), c (Lindahl & Ragsdale, 1990), d (Krzycki et al., 1989), e (Hadj-Saïd et al., 2015)

The typical EPR spectra of *Rr*CODH at different redox potentials are shown in Figure 43A (Spangler et al., 1996). The [4Fe4S] clusters also show a characteristic UV-visible absorbance between 350 to 480 nm, as shown in Figure 43B (Ensign et al., 1989).

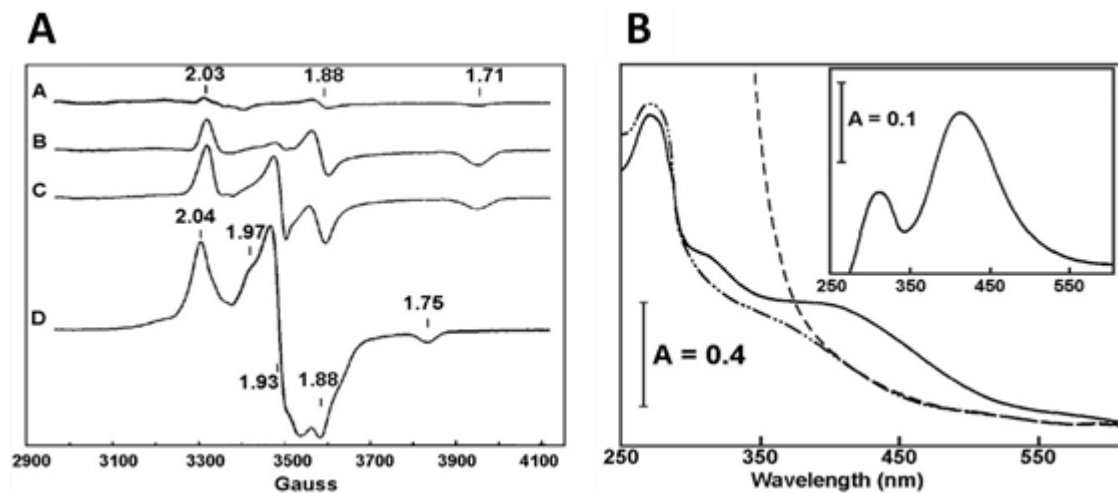


Figure 43 EPR and UV-visible spectra of *R. rubrum* [NiFe]-CODH. (A) Trace A, almost full oxidized FeS clusters. Trace B, 33 % of reduced FeS clusters, C_{red1} state ($g = 2.03, 1.88$ and 1.71). Trace C, 66 % of reduced FeS clusters, $C_{red1} + B_{red}$ ($g = 2.04, 1.97$ and 1.88) states. Trace D, full reduced FeS clusters C_{red2} ($g = 1.97, 1.88$ and 1.75) + B_{red} states. (Spangler et al., 1996) (—) (B) full oxidized [4Fe4S] clusters show the typical absorbance from 350 to 480 nm. (- - -) partially reduced [4Fe4S] clusters by incubation with 100 % CO for 35 minutes. (- - -) full reduced [4Fe4S] clusters by Sodium Dithionite. The inset shows the difference spectrum for oxidized minus CO-reduced enzyme. (Ensign et al., 1989).

Different molecules can act as CODH inhibitors. The attention will be focused on the inhibitors that have contributed to the postulation of the catalytic mechanisms.

Sulfide (S^{2-} , HS^- or H_2S) has been proposed to act both as inhibitors and as activators. Sulfide inhibits the oxidation of CO, but not the reduction of CO_2 , they bind the C_{ox} state by inhibiting catalytic activity at potentials from -50 to -250 mV (Can et al., 2014).

Cyanide, an analogue of CO, is a reversible inhibitor of CO oxidation, which binds the C_{red1} state. But CN^- does not interact with the C_{red2} state and does not inhibit the reduction of CO_2 . As shown above, CN^- has different binding modes, so CN^- can bind Ni in a bent mode like CO and acts as a competitive inhibitor. A subsequent slow rearrangement step can induce the displacement of the water molecule bound to Fe_u and leave room for CN^- relaxation allowing a linear binding mode, in addition to producing a more stable cyanide adduct (Figure 44) (Kung & Drennan, 2011).

Isocyanides (e.g., *n*-BIC) can act both as a substrate and as an inhibitor of CO oxidation. CODH catalyzes the oxidation of *n*-BIC to *n*-BICt 10^5 times slower than CO. In this way, *n*-BIC acts as a competitive Inhibitor of CO (Can et al., 2014).

Cyanate, an analogue of CO_2 , binds the $\text{C}_{\text{red}2}$ state and inhibits the reduction of CO_2 . Conversely it does not interact with the $\text{C}_{\text{red}1}$ state and does not inhibit the oxidation of CO. The binding of NCO^- takes several seconds with millimolar concentrations and inhibition occurs at more positive potentials of -400 mV (Can et al., 2014).

All together this information led to the postulation of the following catalytic mechanism of CODH (Figure 44):

0. **Inactive state:** when the cluster is fully oxidized (C_{ox} state). A first reduction by one electron produces the catalytical ready $\text{C}_{\text{red}1}$ state.
1. **$\text{C}_{\text{red}1} \rightarrow \text{C}_{\text{red}1}\text{-CO}$:** H_2O binds to the Fe(II) ion and the CO binds to the Ni(II) in a bent geometry due to the steric hindrance of a conserved isoleucine.
2. **Fe- H_2O deprotonation:** this step determines the production of the nucleophilic hydroxide. Although binding to Fe should lower the $\text{p}K_a$ of the water molecule, residues surrounding the active site are expected to assist in the formation of nucleophilic hydroxide species. Candidates include a conserved lysine or histidine residues, but this role is not yet clear (Kung & Drennan, 2017).
3. **Nucleophilic attack:** the deprotonation of the Fe-bound water to form hydroxide allows the CO to adopt a linear geometry, which would perfectly position it for the nucleophilic attack of the hydroxide to generate the Fe-Ni-bridging COOH species (carboxylic acid intermediate).
4. **Fe-Ni bridging COOH deprotonation:** a second deprotonation of the reaction intermediate, possibly involving the same residues mentioned above, produces the Ni-Fe bridging COO^- (carboxylate intermediate).
5. **Product releasing:** CO_2 is released, and the cluster is further reduced by two electrons to reach the $\text{C}_{\text{red}2}$ state. A new H_2O binds the Fe(II) ion.
6. **Regeneration ($\text{C}_{\text{red}2} \rightarrow \text{C}_{\text{red}1}$ state):** two electrons are transferred to the B-cluster then the C-cluster goes back to its $\text{C}_{\text{red}1}$ state. The B-cluster then transfers the electrons either to D-cluster, or directly to an external electron acceptor such as the CooF ferredoxin in the biologic WGS complex.

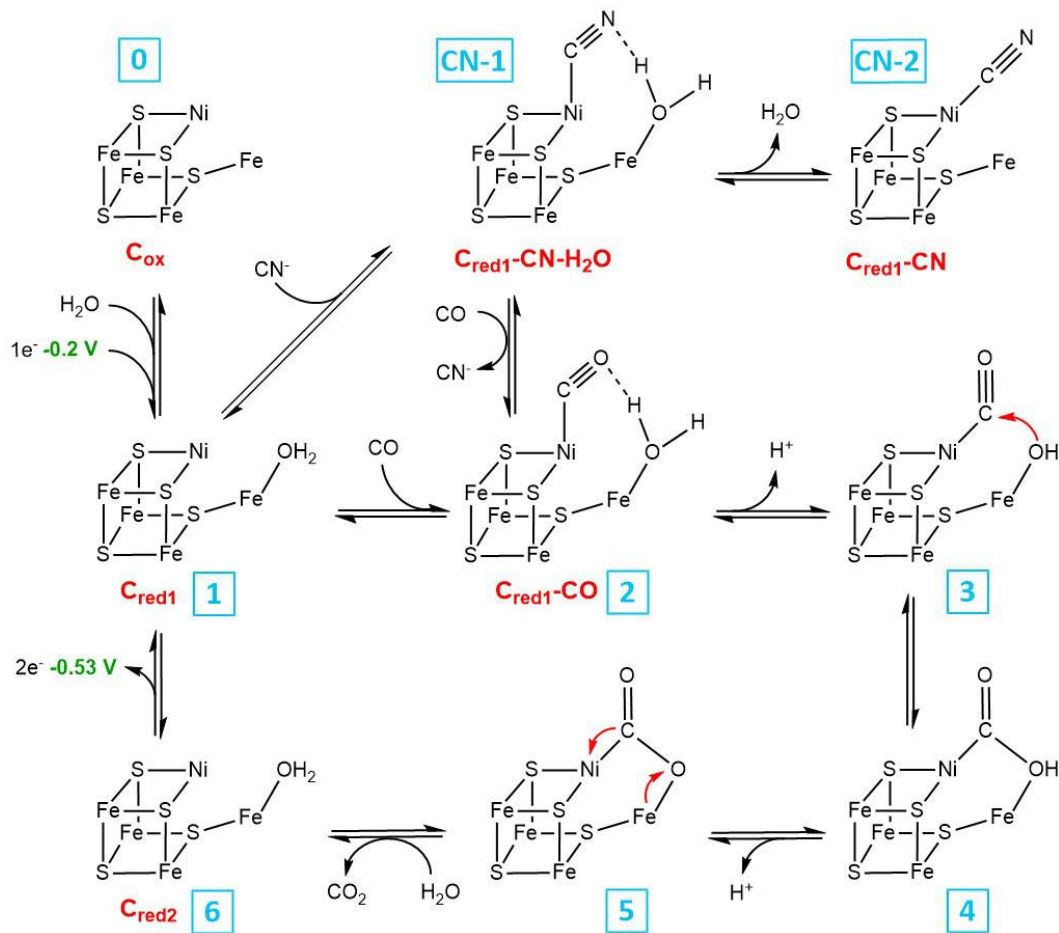


Figure 44 Proposed catalytic and inhibitory mechanisms of the [NiFe]-CODHs C-cluster, consistent with crystal structures containing bound substrate and inhibitor molecules. (Adapted from Kung & Drennan, 2011)

Electrons are transferred from C-cluster to the external acceptor via FeS clusters and vice versa. The access of gaseous substrates, protons and water from the protein surface to the buried active site (and *vice versa*) is made possible through specific gateways. Concerning the gaseous substrate, as shown above, *MtCODH/ACS* displays gas channels for CO/CO₂ transfers from the CODH subunit to the ACS. Furthermore, the *ChCODH* structure co-crystallized with *n*-BIC shows a second *n*-BIC molecule bound to the enzyme which could represent the gateway from the solvent to the C-cluster (Figure 45A). A polar channel is needed to transport the protons to and from the active site. All CODH structures contain a channel of water molecules coated with several ionizable histidine and a lysine residues, the latter being very close to the Fe_u-H₂O (N-Lys at 2.3 Å from O of Fe_u-H₂O) (Figure 45B). Through this gateway, protons can be transferred to C-cluster for CO₂ reduction or to the solvent during CO oxidation. In addition, there is also a gateway for the H₂O substrate, composed of conserved structural water molecules (Figure 45B).

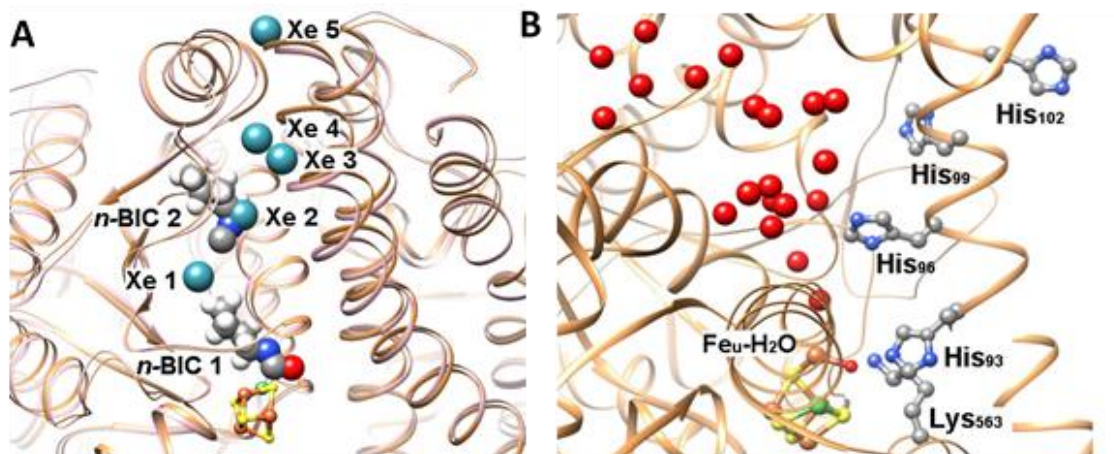


Figure 45 (A) Gaseous substrates channel. Liquorice ribbon diagram of superimposed MtCODH/ACS and ChCODH:n-BIC (PDB codes: 2Z8Y and 2YIV, respectively). Van der Waals representation of n-BIC molecules and Xe atoms. The Xe atoms numeration is the same proposed in Figure 23. Both together n-BIC molecules and Xe atoms show the gas channel from the C-cluster to the solvent which can be used by the CO/CO₂ molecules during the catalysis. **(B)** Protons and water channels. Liquorice ribbon diagram of ChCODH (PDB code: 2YIV). H₂O molecules are show as red spheres, portion of the non-structural water molecules are show as the solvent surface plus the structural water molecules inside the channel which connect the surface to the Fe_u. Polar channel for protons transport in and out of the active site, constituted of conserved histidine residues.

Monofunctional CODHs can catalyze CO/CO₂ interconversion, but there is a significant difference in terms of turnover frequency between CO oxidation and CO₂ reduction (Table 11). Furthermore, the efficiency of CO oxidation varies considerably from one enzyme to another (Table 11).

CO oxidation is characterized either by electrochemistry, usually with an enzyme immobilized on an electrode, or in solution following the CO-dependent reduction of oxidized chemical acceptors. CODHs catalyze the CO-dependent reduction of various electron acceptors, such as methyl- and benzyl-viologen, phenazine metazose, methylene blue, etc. Among them, methyl-viologen (MV) is the most used for the determination of the specific activity of CODHs, by following its reduction over time at 604 nm ($\epsilon = 13.6 \text{ mM}^{-1} \cdot \text{cm}^{-1}$), from colorless to violet.

The reduction of CO₂ is both characterized by electrochemistry and in solution. In solution, the reduction of CO₂ to CO by CODH is measured by monitoring the spectrophotometric absorbance changes upon the binding of CO to reduced hemoglobin (shift of the Soret band from 433 to 419 nm, $\epsilon = 185 \text{ mM}^{-1} \cdot \text{cm}^{-1}$), to form carbonyl-hemoglobin, by using NaHCO₃ as a CO₂ source. CODHs specific activities are expressed in U · mg⁻¹ (μmol of oxidized CO or reduced CO₂ · min⁻¹ · mg⁻¹).

Scheme 1 CO-dependent reduction of oxidized methyl-viologen (MV) and CO₂-dependent formation of carbonyl-hemoglobin (Hb-CO) from hemoglobin (Hb).



The studies on the redox dependence of the reduction of CO₂ by RrCODH confirm that CO₂ is not able to bind the C_{red1} state but is able to bind the C_{red2} state because the activity increase of 2000 times when the potential is less than -500 mV (Heo et al., 2001).

Table 11 Specific activity of CO oxidation and CO₂ reduction from several monofunctional CODHs. The pH buffers and temperatures are reported. Ch is for *Carboxydotherrmus hydrogenoformans*, Rr is for *Rhodospirillum rubrum*, Dv is for *Desulfovibrio vulgaris*, Tc is for *Thermococcus sp. AM4*; r.t. is for room temperature, n.s. is for not specified.

CODH	CO oxidation				CO ₂ reduction			
	pH	T (°C)	U·mg ⁻¹	Ref.	pH	T (°C)	U·mg ⁻¹	Ref.
Ch I	8	70	18900	(Svetlitchnyi et al., 2001)				
Ch II	8	70	14200	(Svetlitchnyi et al., 2001)	n.s.	25	16.9	(T. Inoue et al., 2011)
Rr	7.5	RT	6230	(Jeon et al., 2005)	7.5	25	30.1	(Ensign, 1995)
Dv	10	37	1660	(Hadj-Saïd et al., 2015)	8	n.s.	1.4	(Hadj-Saïd et al., 2015)
Tc I	6	37	10	(Benvenuti et al., 2020)	6	37	0.14	(Benvenuti et al., 2020)
Tc II	6	37	70	(Benvenuti et al., 2020)	6	37	0.3	(Benvenuti et al., 2020)

To date, several electrochemical studies on CODH activities have been conducted. Furthermore, the kinetics properties of the substrates (CO and CO₂) and of the inhibitors (CN⁻ and NCO⁻) were elucidated by electrochemistry. But these results will be presented in the following sections, dedicated to the advantages of bio-electrochemistry for the study of redox metalloenzymes such as CODH.

Oxidoreductase such as CODH, Hydrogenase or Formate Dehydrogenase (FDH), are biocatalysts which during their reactions involve the production and **transfer of electrons**. As presented for the CODH, the activities are closely related to the **electrical potential** of their containing solution. These two common physical phenomena are the foundations of electrochemistry.

Electrochemistry is branch of physical chemistry that studies the relationships between electric potential and chemical reactions involving a flow of electrons between two electrodes separated by a conductive electrolytic solution. Electrochemistry is therefore a technique that allows the study of redox active biomolecules. As shown in the previous sections, homogenous catalysis involves the transfer of electrons to or from an external partner, such as ferredoxin or methyl viologen. In electrochemistry the electrode, cathode or anode, plays the role of final donor or acceptor of these electrons. Redox biomolecules soon sparked interest in electrochemistry (Heyrovsky & Babicka, 1930), and today more and more proteins are being studied by electrochemistry. This is because proteins can act as drugs, early-stage disease biomarkers, targets for drug development and discovery, or as selective catalysts.

Redox proteins can be structurally diverse, from very small proteins (a single chain made up of hundreds of amino acids) to multiprotein complexes, such as mitochondrial complex I (NADH-Ubiquinone oxidoreductase) or photosystem I (plastocyanin-ferredoxin oxidoreductase). As shown above for the [NiFe]-CODH, the active site is frequently buried within the protein scaffold and the electron transfer proceeds *via* prosthetic cofactors (e.g., FeS clusters or FAD) from the active site to an external redox partner, such as ferredoxin or cytochromes. When the aim is to study these biocatalysts by electrochemistry, it is essential to partially reproduce the conditions *in cellulo* to allow the detection of electron flow. Thus, a first difference arises about the **electric connection** between the redox enzymes and the electrode, which will be discussed below, explaining the two main modes of electron transfer: **mediated** or **direct**.

Achieving efficient electron transfer plays a critical role when the goal is to develop new energy conversion devices (such as enzymatic fuel cells and/or electroenzyme reactors) as well as enzymatic biosensors. The latter topic has been extensively studied in the past for medical applications. For instance, different commercial glucose biosensors are available, based on glucose oxidases (Newman & Turner, 2005). Furthermore the biosensors have been studied in order to detect DNA, bacteria, viruses, pollutants, etc. (Holzinger et al., 2014).

In electrochemistry, one of the natural co-substrate/s, cofactor/s or redox partner/s is replaced by an **artificial molecule (mediator)**, or the natural redox partner is electrochemically regenerated by an artificial molecule. This type of electron transfer mechanism is called mediated electron transfer (**MET**) (Figure 47A). Alternatively, if the cofactor is electrochemically regenerated at the electrode, this type of electron transfer mechanism is called direct electron transfer (**DET**) (Figure 47B). The transfer of an electron between two molecules in solution should be thermodynamically favorable and the difference in energy levels is the driving force of the reaction (Rountree et al., 2017). The driving force is expressed in terms of the variation of the Gibbs free energy of the reaction, the distance between the redox centers and the reorganization energy (Vidakovic-Koch, 2019). DET was first demonstrated about 40 years ago (Yaropolov et al., 1978)(Tarasevich et al., 1979)(Armstrong et al., 1988).

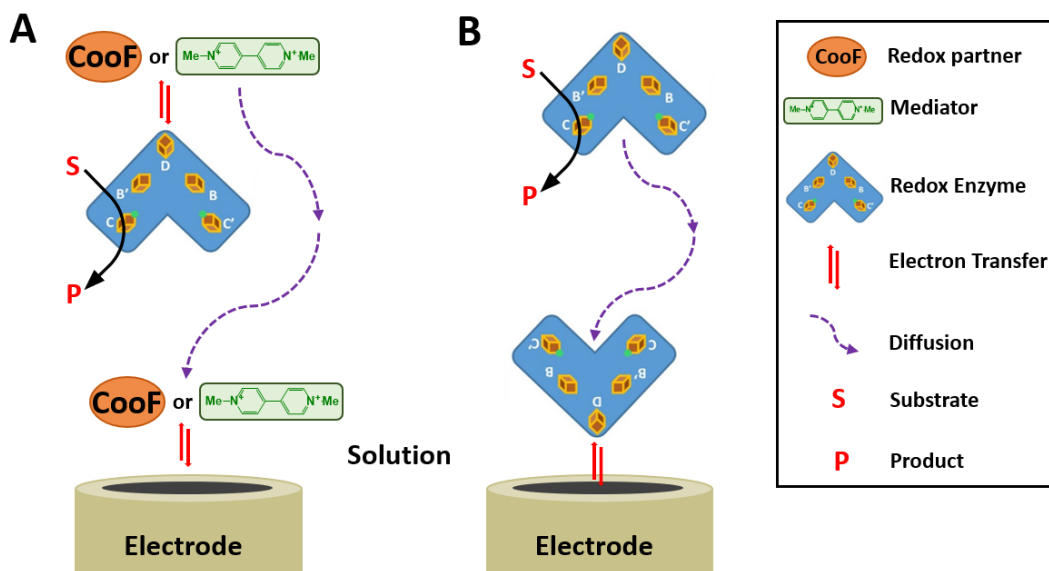


Figure 47 Schematic representation of the two mechanisms of electron transfer between electrode and redox enzyme/partner. **(A)** Mediated electron transfer (MET) by a redox partner or a small redox molecule (mediator). **(B)** Direct electron transfer (DET).

To date, DET has been reported for many enzymes such as peroxidase (horseradish and cytochrome c peroxidases), laccase, bilirubin oxidase and dehydrogenase (cellobiose and fructose dehydrogenases, formate dehydrogenases) (Do et al., 2014)(Andreu et al., 2007)(G. Gupta et al., 2011)(Bollella et al., 2018)(Miller et al., 2019). DET has also been reported for enzymes in which the active site is buried within the protein, such as [NiFe]-Hydrogenases (Léger et al., 2002). This is possible thanks to the presence of FeS clusters which reduces the **distance** between the active center and the surface of the electrode. In fact, the electron transfer rate is inversely proportional to the distance between the enzymatic active site and the electrode surface (Jeuken, 2003). In support of this it has been shown that DET is observable for distances less than 25 Å (Agbo et al., 2014).

It is therefore evident that the **efficiency** of **DET** strongly depends on the **orientation of the enzyme** on the surface of the electrode and on the **electronic and chemical properties** of the **electrode**. The advantage of DET is that it allows the bioelectrocatalysis at the redox potential of the enzyme, which is generally close to the redox potential of the substrate/product involved in the reaction. However, considering that in the enzyme only a small area allows DET, the orientation of the enzyme on the electrode surface is essential to obtain an efficient DET. In fact, in some cases the chemical properties of the protein can favor or disadvantage the DET of the immobilized enzyme and the addition of a redox mediator can improve the quantity of electroactive enzyme and then the catalytic current (Figure 48) (Ciaccafava et al., 2012). The mediator

can be a small molecule (as represented in Figure 48) but also an electroactive polymer or gel in which the enzyme is immobilized. However, in the presence of the mediator, the potential of electrocatalysis is shifted from that of the enzyme to the mediator redox potential. Hence, it is clear that to obtain an efficient DET it is essential to optimize the immobilization of the enzyme on the electrode surface.

1.4.2

Enzyme Immobilization techniques

To date, various enzymatic immobilization techniques have been exploited in order to immobilize and electrically wire enzymes to electrodes, such as: physical adsorption, cross-linking, entrapment or encapsulation, covalent and supramolecular assembly. It is important to consider that immobilization should not affect the stability of the enzyme, such as alteration of the structure or partial unfolding, or modify its catalytic properties. Furthermore, the transport kinetics of the substrate/s and product/s can also be disturbed by immobilization.

Physical adsorption is the simplest immobilization technique, the enzyme is adsorbed on the surface via hydrophobic, electrostatic or Van de Waals interactions (Figure 48A). The advantage is simplicity and the absence of any chemical process that might be detrimental to enzyme activity or accessibility of the substrate. On the other hand, due to the soft interactions, it is possible to observe the desorption of the enzyme, especially under experimental conditions that reduce these interactions.

Cross-linking consists in the use of a bifunctional reagent such as glutaraldehyde, which is the most used reticulant (Migneault et al., 2004)(Sheldon & van Pelt, 2013), which reacts with amines of proteins inducing their reticulation and precipitation on the electrode surface (Figure 48B). Compared to physical adsorption, stability over time is improved, but the cross-linking can induce partial unfolding or a loss of coordination of the cofactors, thereby reducing catalytic performances.

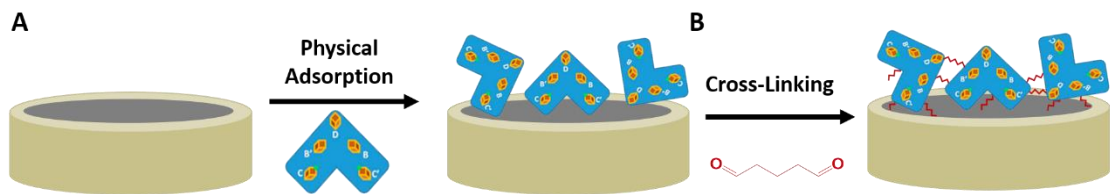


Figure 48 Schematic representation of (A) physical adsorption and (B) cross-linking immobilization of enzyme at the surface of the electrode.

Entrapment or encapsulation consists of compartmentalizing the enzyme in a polymer or in inorganic matrix, such as sol-gels (Figure 49) (Tielmann et al., 2014)(R. Gupta & Chaudhury, 2007). The enzyme can be encapsulated in non-conductive polymers such as chitosan and cellulose (H. Liu et al., 2013)(Krajewska, 2004), with the advantage of preventing direct contact of the enzyme with the environment. Furthermore, conductive polymers such as polypyrrole, polyaniline and polythiophene can be used for the immobilization of enzymes. The electrical wiring of the biocatalysts can be achieved through the modification of the polymer backbone with a redox entity acting as a redox mediator and ensuring charge transport diffusion has been extensively developed for enzyme immobilization and wiring. Polymers can also be produced *in situ* on the electrode surface by electrooxidation of the monomer which produces a matrix with the encapsulated enzyme.

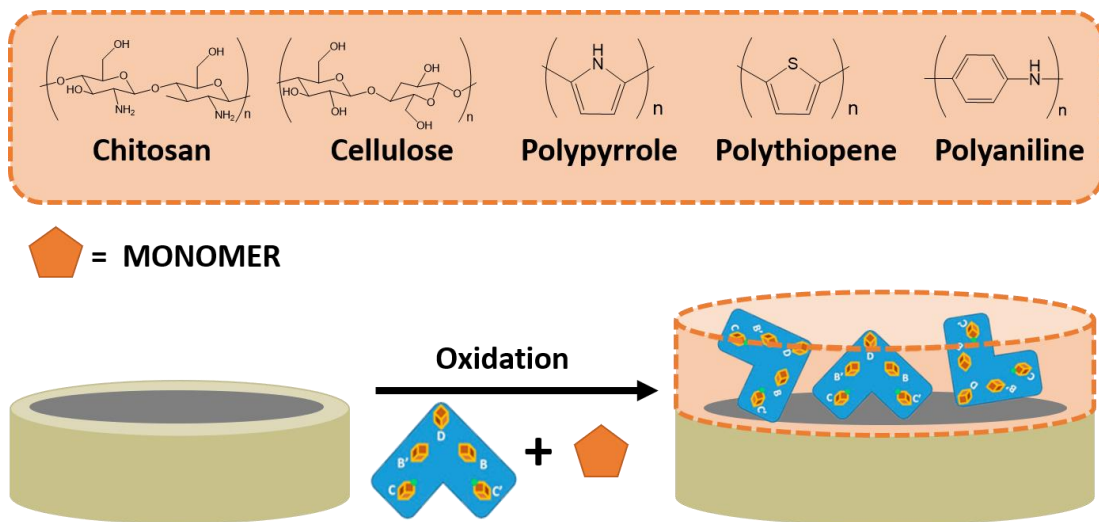


Figure 49 Schematic representation of enzyme encapsulation into conductive or non-conductive polymers, for its immobilization at the surface of the electrode.

More accurate immobilization can be achieved by exploiting bioinspired interactions of molecules, such as between saccharides and lectins or specific chemical groups with specific protein pocket. Particular attention must be paid to the functionalization of the

electrode and/or the enzyme in order to enable affinity interactions. The electrode surface is functionalized with compounds such as polymers, diazonium salts or by forming a self-assembly monolayer (SAM) of enzyme (Samanta & Sarkar, 2011)(Cosnier, 2007). For example, a SAM can be generated by exploiting the biotin/streptavidin chemistry. First the electrode and proteins are functionalized with biotin, then the streptavidin is added to induce the specific interactions (Figure 50A). Another method consists in the use of ferrocene or adamantane cyclodextrin derivatives (Figure 50B) (Villalonga et al., 2007)(Dubacheva et al., 2010)(Cosnier & Holzinger, 2011). A third method is the well-known nitrilotriacetic acid (NTA)-Cu chemistry to provide affinity interactions with histidine tagged proteins (Figure 50C) (Haddour et al., 2005)(Balland et al., 2008).

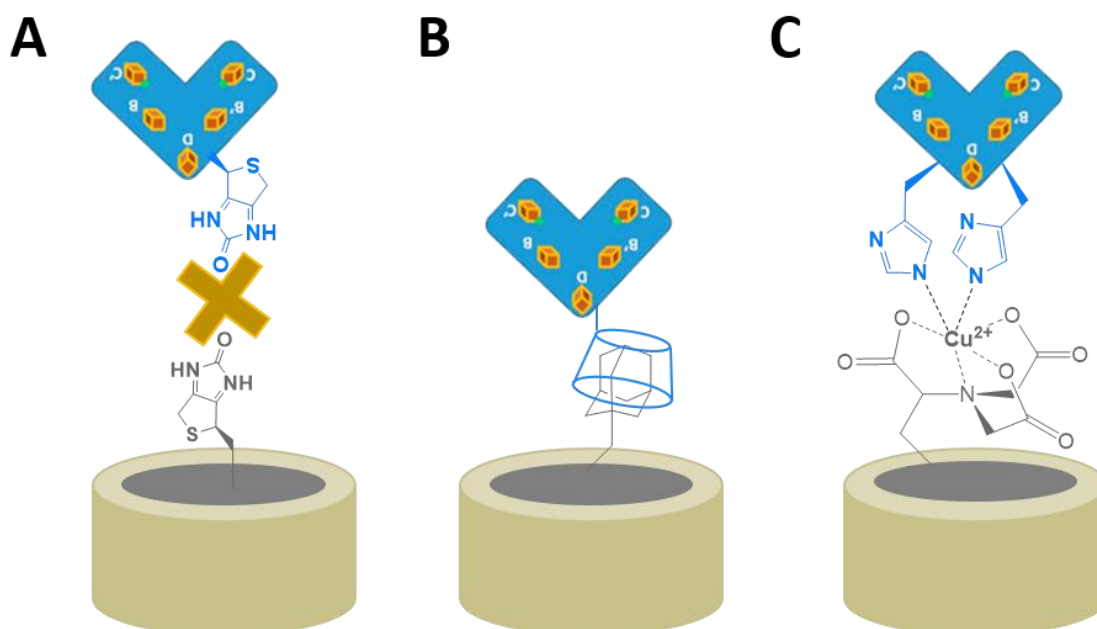


Figure 50 Schematic representation of enzyme immobilization with supramolecular interactions: **(A)** Biotin/Streptavidin, the latter represented as a cross, **(B)** Adamantane/Cyclodextrin functionalized enzyme and **(C)** NTA-Cu(II)-Histidine tagged enzyme.

Other examples are based on electrostatic and hydrophobic interactions (Holzinger et al., 2014). The advantage of these techniques is to provide a specific orientation of the molecules to the electrode surface, but the modification of the proteins can also alter their structure and therefore their catalytic properties.

Finally, a **covalent** immobilization can be used, which required a preliminary functionalization of the electrode surface in order to provide the chemical groups for the covalent immobilization of proteins. Generally, covalent bonding involves

nucleophilic proteins residues such as lysine and cysteine which react with NHS esters or aldehydes, maleimide and epoxides respectively (Figure 51A) (Wong et al., 2009). These techniques provide strong immobilization but do not control orientation, resulting in a mixture of DET-electroactive species. To better control the orientation and maintain the covalently binding of the protein can alternatively be modified with azide to exploit the click chemistry or the Diels-Alder cycloadditions (Figure 51B) (Gentil et al., 2020)(Gentil et al., 2021).

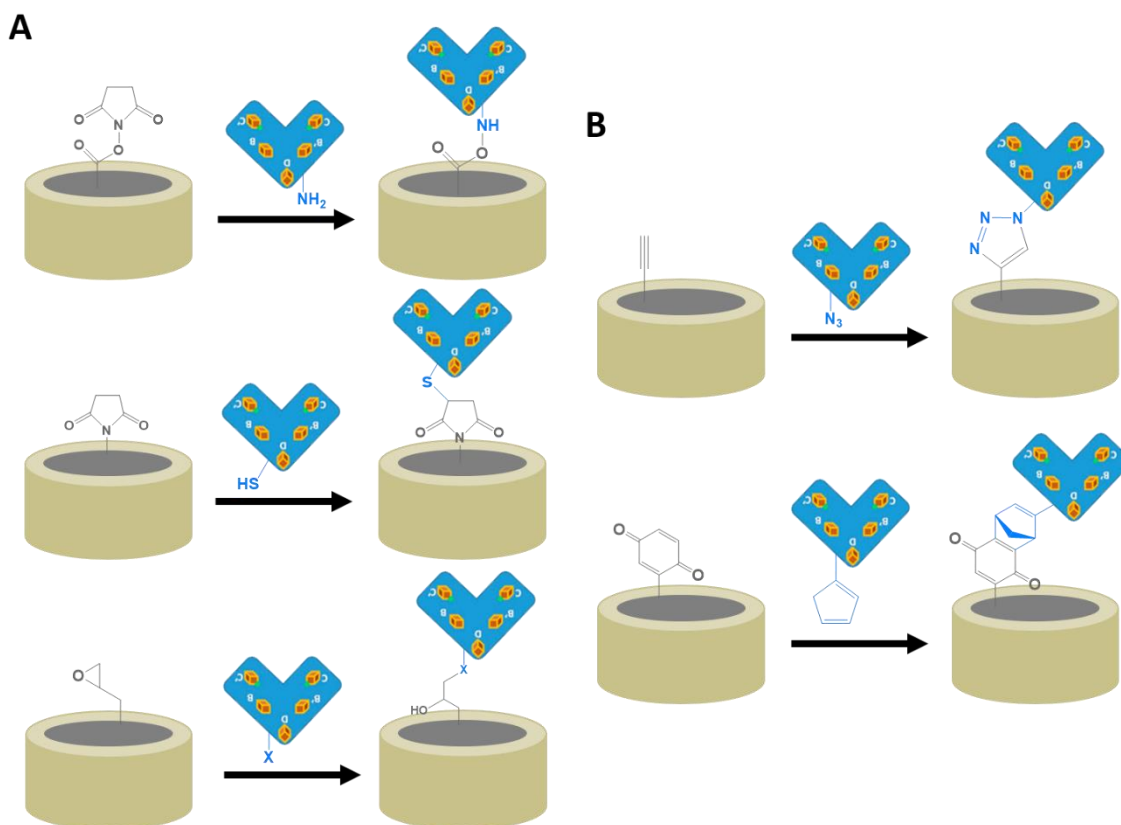


Figure 51 Schematic representation of enzyme covalent immobilization on the electrode surface: **(A)** amidic bond between the amine (lysine) and NHS esters, reactions of thiol (cysteine) with maleimide, reaction of nucleophilic residue with epoxide **(B)** click reaction between the azide functionalized enzyme and alkyne, Diels-Alder cycloaddition between.

Thus, each strategy of enzyme immobilization possesses advantage and drawbacks. For example, the conductive polymers increase the quantity of entrapped enzyme (tridimensional matrix) but does not control its orientation, resulting in portion of non-electroactive enzyme. This is counterbalanced by the modification of the polymer backbone with redox mediators, enabling electron transport throughout the film. On the contrary, the SAM and covalent immobilization favor a specific orientation. However, the amount of enzyme is limited by the bidimensional electrode surface. Then, an ideal electrode should provide a tridimensional conductive surface and allow the

orientated immobilization without interfering with in the catalysis and protein stability. The next section will be focused on the use of **carbon nanotubes (CNT)**-based electrode for enzymatic immobilization.

1.4.3

Carbon Nanotubes and Enzyme Immobilization

Carbon-based nanomaterials such as graphene, carbon black and CNT, are the most suitable materials for enzymatic immobilization for several reasons: they are cheaper than other supports (e.g., gold), afford a good conductivity, a high surface volume ratio and the possibility to easily modify the surface structure. Among these carbon-based nanomaterials, CNTs are particularly attractive because they offer the ideal characteristics to balance the key factors that determine the efficiency of biocatalysts. CNT-based sensors generally have higher sensitivities, lower detection limits and faster electron transfer kinetics than traditional carbon electrodes (W. Feng & Ji, 2011). The performance of the CNT-enzyme based device is influenced by a combination of nanotube chemistry and the immobilization method. It is therefore essential to find optimal methods for CNT functionalization for enzyme immobilization and electric wiring.

CNT are seamless cylinders made of carbon lattice (graphene) with open or closed ends, with diameters typically measured in nanometers. CNT can be made up of a closed wrapped-up graphene layer, called SWCNT discovered independently in 1993 by two research groups (Figure 52) (Iijima & Ichihashi, 1993)(Bethune et al., 1993). On the other hand CNT can consist of nested SWCNT (at least two SWCNT) called MWCNT, discovered in 1991 (Figure 52) (Iijima, 1991). The diameters of SWCNT and MWCNT are generally from 0.4 to 3 nm and 1.4 to 100 nm, respectively, although the MWCNT diameters can exceed the nanoscale (> 100 nm) (Baughman et al., 2002). The lengths of the CNT range from less than 100 nm to several centimeters, covering thus molecular and macroscopic scales (Baughman et al., 2002).

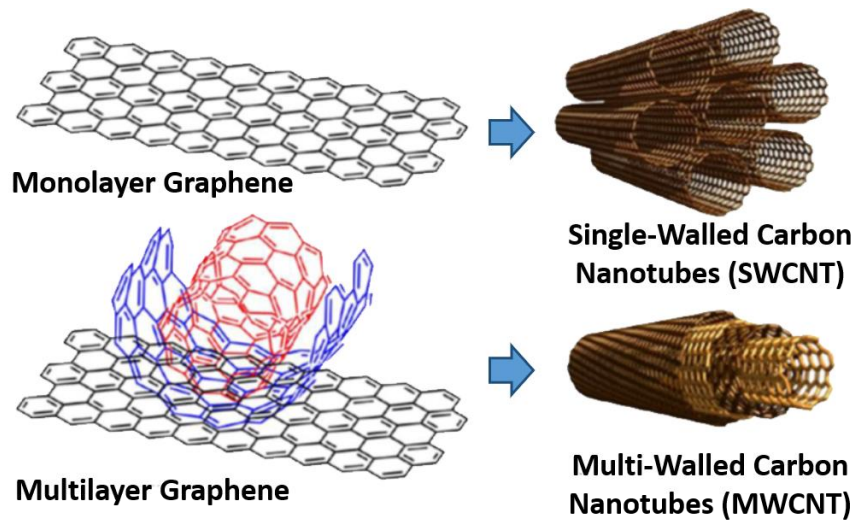


Figure 52 Schematic representation of single walled carbon nanotube (SWCNT) and multi walled carbon nanotube (MWCNT).

The CNT have all the sp^2 carbon atoms bound in a hexagonal lattice except at the extremities. The composition of the lattice can also present defects introducing pentagons, heptagons and other imperfections in the sidewalls, which generally change the properties of the CNT (De Volder et al., 2013). Some carbons are sp^3 which present oxygen-containing functional groups such as alcohols, carbonyl or carboxylic acid.

The CNT show unique properties such as remarkable **electrical conductivity**. The individual CNT walls can be metallic or semiconductor depending on the spatial orientation of the graphene lattice with respect to the axis of the tube, the latter is called CNT chirality. MWCNT are typically metallic and can carry currents of up to $10^9 \text{ A}\cdot\text{cm}^{-2}$ (Wei et al., 2001). CNT also have exceptional **tensile strength**: considering only the cross-sectional area of the CNT walls. An elastic modulus has been measured that approaches 1 TPa and a tensile strength of 100 GPa for individual MWCNT (Peng et al., 2008). This resistance is more than 10 times higher than any industrial fiber. Another interesting property is their **thermal conductivity**. The individual SWCNT shows a thermal conductivity of $3500 \text{ W}\cdot\text{m}^{-1}\cdot\text{K}^{-1}$ at room temperature (Pop et al., 2006), based on the area of the wall, exceeding thus the thermal conductivity of diamond. These properties are expected to be invaluable in many technological areas, such as electronics, optics, composite materials, nanotechnology and other materials science applications (De Volder et al., 2013). The **solubility** of CNT in organic and aqueous solvents has been extensively studied (O'Connell, 2006). Furthermore, the use of surfactants or the

encapsulation into polymers allow the dispersion of CNT. It is important to consider that CNT dispersion should ideally not modify the properties of the CNT (O'Connell, 2006).

Hence, a deposition of **CNT film** on a surface can be obtained with different strategies:

- The Langmuir-Blodgett technique consists in the dispersion of CNT in aqueous solvents and then in the deposition layer-by-layer (up to 100) on the surface, which allow the control of the film thickness (Kim et al., 2003).
- Self-assembly is based on a first surface functionalization with polar (amino or carboxyl) or non-polar (methyl) groups, which drives the self-assembly of the individual CNT (Rao et al., 2003).
- The dip-coating consists in the deposition of a dispersed solution of CNT directly on the surface and subsequently the film is made with high-speed rotation (spin-coating) or drying (drop-casting) (Saran et al., 2004).
- Other methods consists in the pre-formation of the CNT film and then in the transfer to the final surface via soluble membranes or an adhesive surface (Zhuangchun et al., 2004)(M. Zhang et al., 2005) or by means of a micro-contact printing technique (Fuchsberger et al., 2011).

When the goal is the combination of CNT with biological molecules, such as proteins and DNA it is important to consider that CNT can be conveniently functionalized to improve their biocompatibility and biodegradation. Therefore, it is not surprising that the combination of CNT and proteins is a prolific research field, as it has the potential to combine very different properties and surface chemistry of CNT compared to other supports. Several reviews report the uses of these hybrid systems (CNT-proteins) for example in the fields of sensing/detection (Kwon et al., 2019)(Holzinger et al., 2017)(Holzinger et al., 2014)(Vashist et al., 2011) and fuel cells (Cosnier et al., 2014)(Huang et al., 2019)(Le Goff et al., 2015). Two main types of CNT functionalization for the immobilization of different enzymes have been reported: non-covalent and covalent. Non-covalent attachment preserves the unique properties of both enzymes and CNT, but immobilized molecules can be gradually lost during the use of the CNT-enzyme complex. Covalent conjugation provides lasting attachment but modify either the carbon sp^2 of the CNT or CNT defects. Non-covalent functionalization is interesting for the immobilization of biomolecules on CNT because it preserves the intrinsic properties of the CNT electrode and it is simple to implement.

The simplest non-covalent functionalization proceeds through the adsorption of the molecule on the carbon nanotubes by a soaking step.

This technique can be performed by direct physical adsorption on CNT (**non-specific**) or adsorption with the presence of auxiliary (**specific**) molecules such as polymers, surfactants and linking molecules. In the case of non-specific adsorption of enzymes, different interactions are involved, mainly hydrophobic ones. The hydrophobic region in the protein surface allows interaction with the sidewalls of the CNT, such as π - π stacking between the sidewalls of the CNT and the aromatic rings of certain amino acids such as phenylalanine (Matsuura et al., 2006). Electrostatic interaction has also been demonstrated in the adsorption of lysozyme on CNT (Nepal & Geckeler, 2006). In addition, the same work also shows that lysozyme interacts with nanotubes through protonated amino groups with CNT defect sites at pH values lower than the isoelectric point. At pH values higher than the isoelectric point, they interact through amine adsorption. For non-specific adsorption, the quantities of enzymes adsorbed on the CNT are influenced by various factors, such as the nature of the enzyme and the surface chemistry of the CNT. Different enzymes, for example soybean peroxidase, β -glucosidase and chymotrypsin, can be adsorbed on CNT in large quantities of 575, 630 and 670 μg of protein per mg of CNT, respectively (Y. Gao & Kyratzis, 2008)(Gómez et al., 2005)(Karajanagi et al., 2004).

Specific adsorption can be achieved *via* two main types of CNT functionalization: π - π interactions of aromatic molecules with the sidewalls of CNT and by coating with polymers.

Molecules that contain polyaromatic groups or a π -extended network are able to functionalize the CNT by forming specific and directional π - π stacking interactions with the graphite surface of the nanotubes. This interaction might also improve the solubility of the CNT in the solvents (Zhou et al., 2019). Several compounds have been used for the immobilization of biomolecules on CNT for the development of electrochemical bioelectrodes. Among these, the aromatic groups are served by pyrene, naphthalene, and porphyrin derivatives (Figure 53A).

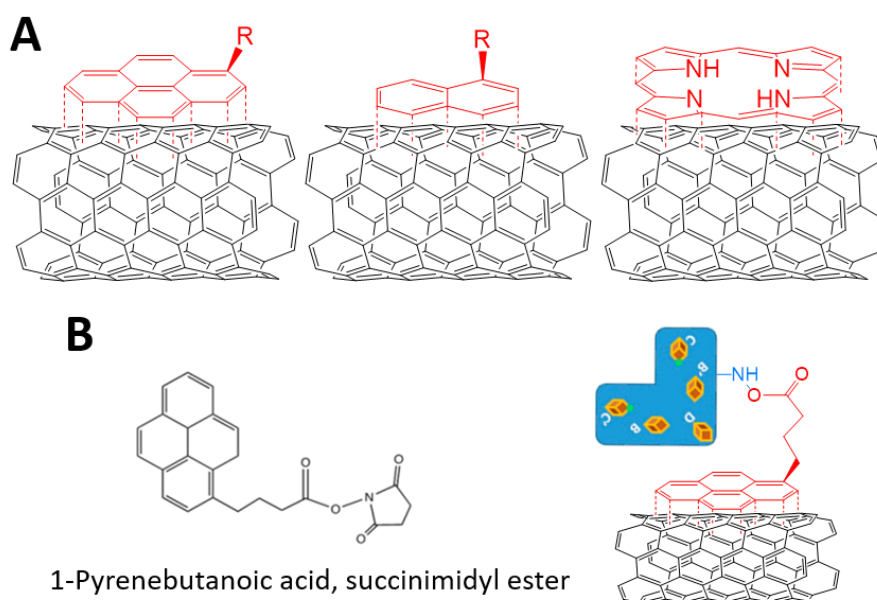
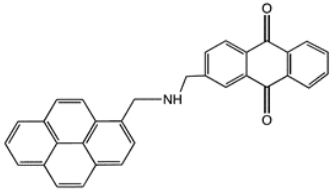
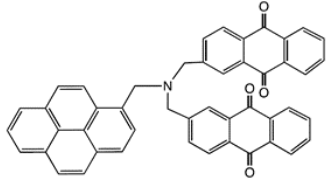
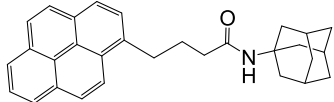
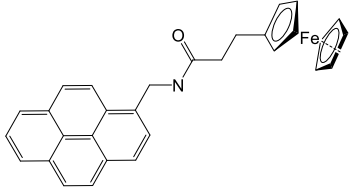
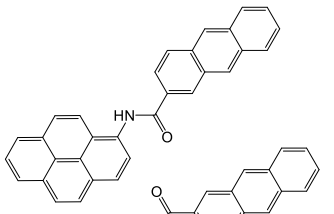
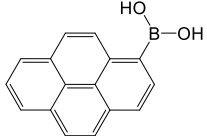


Figure 53 (A) Schematic representation of π - π stacking interactions of pyrene and naphthalene derivatives and porphyrin with CNT **(B)** Schematic representation of enzyme immobilized on 1-Pyrenebutanoic acid, succinimidyl ester functionalized CNT.

In 2001, the possibility of immobilizing a protein via amide bond on π - π stacking functionalized CNT was achieved with 1-Pyrenebutanoic acid, succinimidyl ester, involving the nucleophilic substitution of N-hydroxysuccinimide by an amine group of the protein (Figure 53B) (R. J. Chen et al., 2001). Since this first report of **pyrene-derivate** molecule to date several other molecules have been described for the development of bioelectrodes for enzyme immobilization and wiring (Table 12).

Table 12 List of pyrene-derivate compounds used for non-covalent functionalization of carbon nanotubes bioelectrodes and their applications.

Name and Structure	CNT	Application (enzyme)	Ref.
1-(2-Anthraquinonylamino)methyl)pyrene 	MWCNT	Electrocatalysis of O ₂ (Laccase)	1
[bis(2-anthraquinonyl)-aminomethyl]-pyrene 	MWCNT	Electrocatalysis of O ₂ (Laccase)	1
Adamantane-pyrene 	SWCNT	- H ₂ oxidation ([NiFeSe]-H ₂ ase) - Electrocatalysis of O ₂ (Laccase)	2 6
Ferrocene-pyrene 	SWCNT	Glucose biosensor (GOx)	3
1-pyrenyl anthracene-2-carboxylamide 	MWCNT	Electrocatalysis of O ₂ (Laccase)	4
Boronic acid-pyrene 	MWCNT	Electrocatalysis of O ₂ (GOx and HRP)	5

1 (Bourourou et al., 2013); 2 (Gentil et al., 2018); 3 (Le Goff et al., 2010); 4 (Giroud & Minteer, 2013); 5 (Reuillard et al., 2014); 6 (Lalaoui, David, et al., 2016)

Bourourou et al., in 2013, succeeded in the functionalization of MWCNT with 1-(2-anthraquinonylaminoethyl)pyrene and [bis(2-anthraquinonyl)-aminoethyl]-pyrene to immobilize and orientate laccase. These biocathodes were able to bio-electrochemically reduce oxygen, with an excellent stability over weeks. Holzinger et al., in 2011, achieved the multiple functionalization of SWCNT with three different molecules of pyrene derivatives: adamantane-pyrene, biotin-pyrene, and nitrilotriacetic acid (NTA)-pyrene. This rapid and reproducible procedure was carried out with nanotube-coated electrodes by means of a simple dip coating of the pyrene derivative molecules. The prepared multifunctional electrodes were then immobilized with cyclodextrin modified glucose oxidase, biotinylated glucose oxidase and histidine modified glucose oxidase, to finally develop a glucose biosensor. Adamantane-pyrene was also used for the oriented immobilization of [NiFeSe]-hydrogenase (Gentil et al., 2018). Electrochemistry, quartz crystal microbalance with dissipation monitoring and theoretical calculations show that the enzyme was oriented efficiently to allow direct transfer of electrons from the active site of hydrogenase to CNT. the adamantane-pyrene was also employed for the oriented immobilization of laccase (Lalaoui, David, et al., 2016). Like anthraquinone derivatives, the pyrene moiety was also covalently linked to the anthracene groups to produce a molecule capable of functionalizing the CNT (Giroud & Minter, 2013). These studies showed that anthracene groups are able to orientate the immobilization of the laccase active site near the CNT and allow a rapid direct electron transfer. A pyrene-boronic acid was exploited for the immobilization of glycosylated enzyme, such as the horseradish peroxidase (HRP) *via* the formation of a covalent boronic ester bond (Reuillard et al., 2014). Another example of pyrene derivatives compounds are pyrene-methylammonium and pyrene-carboxylates to introduce negative and positive charges to the surfaces of CNT for the immobilization of hydrogenases or bilirubin oxidases (BOD). Li et al. in 2012, reported an easy functionalization of SWCNT with naphthalen-1-methylphosphoric acid by π - π stacking, the functionalized CNT showed a negative charge from the phosphonate groups which were used for the immobilization of positively charged myoglobin through electrostatic interaction. This biosensor has shown excellent bio-electrocatalytic activity towards the reduction of hydrogen peroxide with a detection limit between micro and nano-molar scale (Li et al., 2012).

The π - π stacking functionalization of CNT sidewalls with porphyrins (protoporphyrin IX and Hemin) was exploited to induce the substrate-mimicking immobilization of bilirubin oxidase (Lalaoui, Le Goff, et al., 2015). The MWCNT/BOD bioelectrode achieved a high current density towards a direct oxygen reduction of $4 \text{ mA}\cdot\text{cm}^{-2}$.

1.4.3.3 Polymer Coating

As previously presented, protein entrapment in a redox polymer offers three main advantages: stable immobilization over time, electronic wiring of the enzymatic active sites to the electrode and enzymatic compartmentalization in the 3D matrix. This can afford in some cases controllable access of the substrate or inhibitors and protection against inhibition, deactivation or denaturation (Le Goff & Holzinger, 2018). Either polyvinyllic or conjugated conductive polymers such as polypyrroles have been extensively studied for enzymatic for biosensors and biofuel cell applications. Pyrrole monomers containing pyrene groups or activated ester groups have been used for the hydrophobic and supramolecular immobilization of Laccase from *Trametes versicolor* (Lalaoui et al., 2013). Another example of a polypyrroles polymer that exploits the advantage of using methyl viologen groups has been described for the immobilization of [NiFe]-Hydrogenase from *D. fructosovorans*. The CNT/polymer bioelectrode displayed a MET-based electrocatalytic current density of $0.3 \text{ mA}\cdot\text{cm}^{-2}$ for H_2 oxidation (Le Goff & Holzinger, 2018). Other widely studied redox polymers are osmium-based hydrogels, based on a polymer backbone that is typically a polyvinyl chain and a redox coordination complex based on osmium (II) bearing groups such as imidazole or pyridine. The redox potential of osmium (III)/osmium (II) can be adjusted to cover the required redox potentials of the biocatalysts in order to enable efficient MET (Le Goff & Holzinger, 2018). Minter and colleagues modified polyethyleneimine with ferrocene for the immobilization of GOx and several dehydrogenases (Aquino Neto et al., 2016)(Aquino Neto, Hickey, et al., 2015)(Knoche et al., 2016)(Aquino Neto, Milton, et al., 2015). It has recently been shown that a methyl viologen based hydrogel can protect oxygen-

sensitive hydrogenases from high potential and oxidative deactivation (Plumeré et al., 2014)(Ruff et al., 2017)(Oughli et al., 2015).

1.4.3.4

Covalently CNT Functionalization

Unlike the non-covalent functionalization, covalent functionalization involves a chemical modification of the CNT, which induces a change in carbon hybridization from sp^2 to sp^3 , changing thus the native properties of the CNT (Mallakpour & Soltanian, 2016). Moreover, as mentioned before, the CNT can already present some defects due to their production and dispersion in solution. Several covalent CNT functionalization techniques are available (Singh et al., 2009)(Georgakilas et al., 2002)(Hirsch, 2002), which can be divided in two main groups: the direct modification of the CNT sidewalls and the indirect modification of previous oxidized CNT, in order to direct the chemical modification on the O-containing groups generated by a first step of oxidation. A first oxidation of the CNT with reagents such as concentrated sulfuric acid, nitric acid and hydrogen peroxide allows the generation of O-containing groups such as carboxy, hydroxyl and epoxy groups or quinones. A commonly used technique is the immersion of the CNT in an oxidizing solution and together with a sonication bath, which allows CNT dispersion. These introduced defects may allow the immobilization of the enzyme through esterification and amide bond (Figure 54).

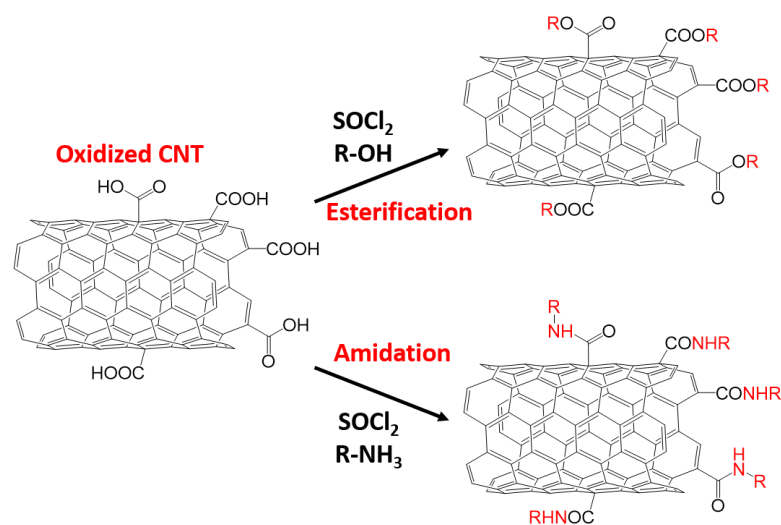


Figure 54 Scheme of indirect oxidized CNT functionalization for enzyme immobilization through esterification and amidation. Only carboxylic groups are represented, other O_2 -containing groups of oxidized CNT are: hydroxy, epoxy groups or quinones.

Furthermore, these defects can be exploited for a subsequent modification with a molecule that allows the supramolecular immobilization of enzymes. For example, Minter and collaborators functionalized defect-containing CNT with anthracene groups for the immobilization of laccases (Figure 55A) (Meredith et al., 2011). Another example is the exploitation of the CNT defect for functionalization with redox mediators, in order to allow MET (Figure 55B) (Callegari et al., 2004)(Nazaruk et al., 2010)(Le Goff et al., 2010).

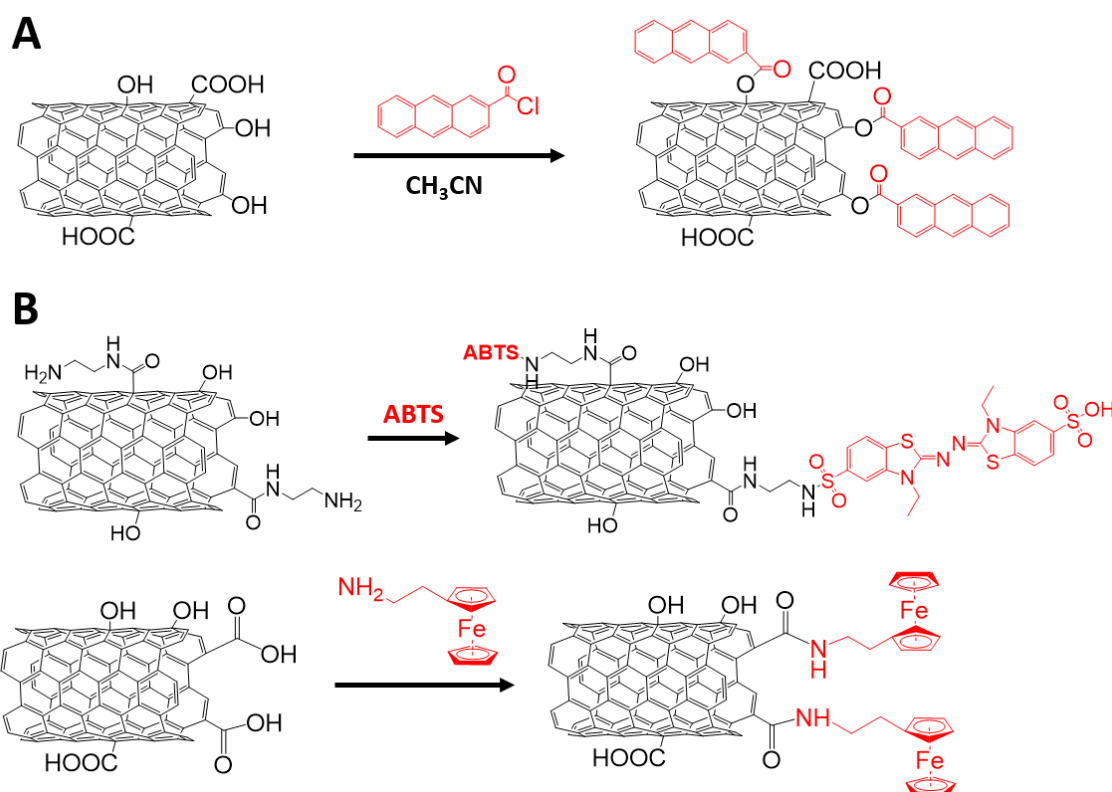


Figure 55 (A) Scheme of covalent functionalization of oxidized CNT with anthracene groups. **(B)** Simplified scheme of co-substrate (ABTS) or mediator functionalization of oxidized CNT (modified from Nazaruk et al., 2010).

On the other hand, the direct functionalization of CNT sidewalls generally proceeds with addition reactions directly on the carbon sp^2 lattice. However, it has been shown that these addition reactions preferably take place at the edge of the tubes or at the defect sites. Therefore, a pre-oxidation step of the CNT is preferable.

Various addition reactions have been described to date, such as carbene or nitrene additions (Figure 56A). Other most exploited methodologies are functionalization with aryldiazonium salts and the Prato reaction. In 1993, Prato first described the 1,3-dipolar cycloaddition for the functionalization of fullerenes and then for CNT in the 2000s. The

reaction is carried out at 130 °C in DMF with an aldehyde derivate and an N-substituted glycine which leads to the formation of substituted pyrrolidine residues. Furthermore, this reaction can be carried out on oxidized or non-oxidized CNTs.

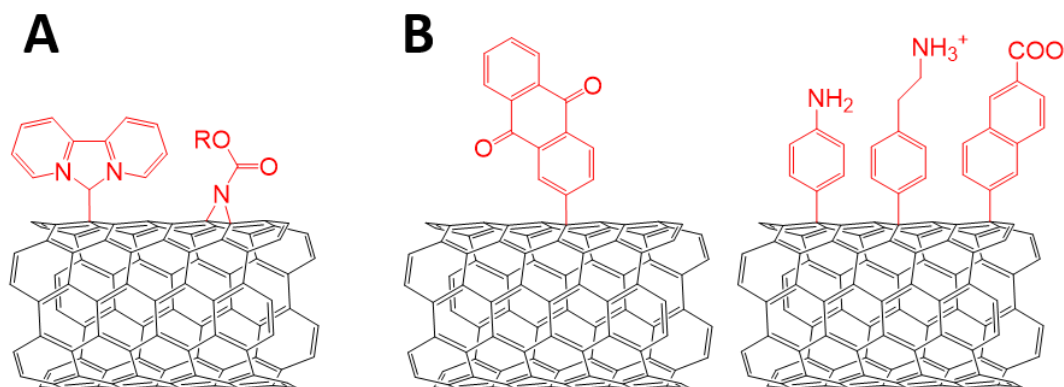


Figure 56 (A) Direct covalent functionalization of CNT sidewall with carbene and nitrene. (B) Direct covalent functionalization of CNT sidewall with diazonium salts in order to expose hydrophobic/hydrophilic and electrostatic interactions or coupling with amino acids or sugar residues.

Described for the first time in 2001, diazonium functionalization has been widely used due to this high functionalization efficiency with different types of phenyl derivatives compounds (Figure 56B). It is generally carried out by electro-grafting of the phenyldiazonium salts on the CNT sidewalls or on the in situ formed phenyldiazonium resulting in a growth of a polyphenylene layer. The diazonium salts can provide hydrophobic functional groups in the para position such as anthraquinone, anthracene, naphthalene or chrysene, as shown for example for the immobilization of laccases (Blanford et al., 2007)(Blanford et al., 2009). The covalent modification of CNTs with other diazonium salts for the immobilization of redox enzymes have been extensively described. Several hydrogenases were immobilized on CNT functionalized with diazonium salts which provided positive, negative or hydrophobic charges (Alonso-Lomillo et al., 2007)(Gentil et al., 2018).

In the next section attention will be focused on the possibility of integrating these nanobio materials in functional devices such as gas diffusion electrodes and biofuel cells.

When the goal is to develop functional devices for biotechnological applications, such as CO₂RR for the production of chemicals, the choice of electrode material has a major impact on the performance of the bioelectrochemical systems. The advantages and disadvantages of biological catalysts and functionalized CNT were discussed above. However, in all the present examples, these nanobio materials were applied in two-phase systems: the solid phase (electrode supported with CNT-biocatalysts) and the liquid phase (electrolyte, substrate(s) and mediator(s)). In this respect, in recent years, **gas diffusion electrodes** (GDEs) have proved to be very attractive electrodes for bioelectrochemical purposes (Figure 57). GDEs avoid major drawbacks when the catalyzed reaction involves gaseous substrates, such as poor gas solubility, mass transport, acidification or basification of electrolytes, and others. GDEs are porous electrodes that have a three-phase boundary: the solid one supports the catalyst and the electrochemical reaction and is located at the interface between the gas and liquid phases. GDEs are typically implemented into conventional fuel cells including **biofuel cells** (Figure 57). The latter are bioelectrochemical devices where a chemical reaction takes place and electrical energy is generated from the conversion of chemical energy (Galvanic Cell, $\Delta G < 0$) or *vice versa* (Electrolysis Cell, $\Delta G > 0$). Generally, a fuel cell consists of an electrolyte chamber in contact with the cathode and the anode. On the anodic side, the oxidation of the fuel is achieved (usually hydrogen from an incoming reservoir is decomposed into protons and electrons) while on the cathodic side the reduction of the oxidant is performed (reduction of O₂ to H₂O) (Le Goff & Holzinger, 2018). Since the first developments of fuel cells (19th century) it has been observed that the main limitation is the need for a significant area between gas, electrolyte and electrode (Segura & Andu, 2009).

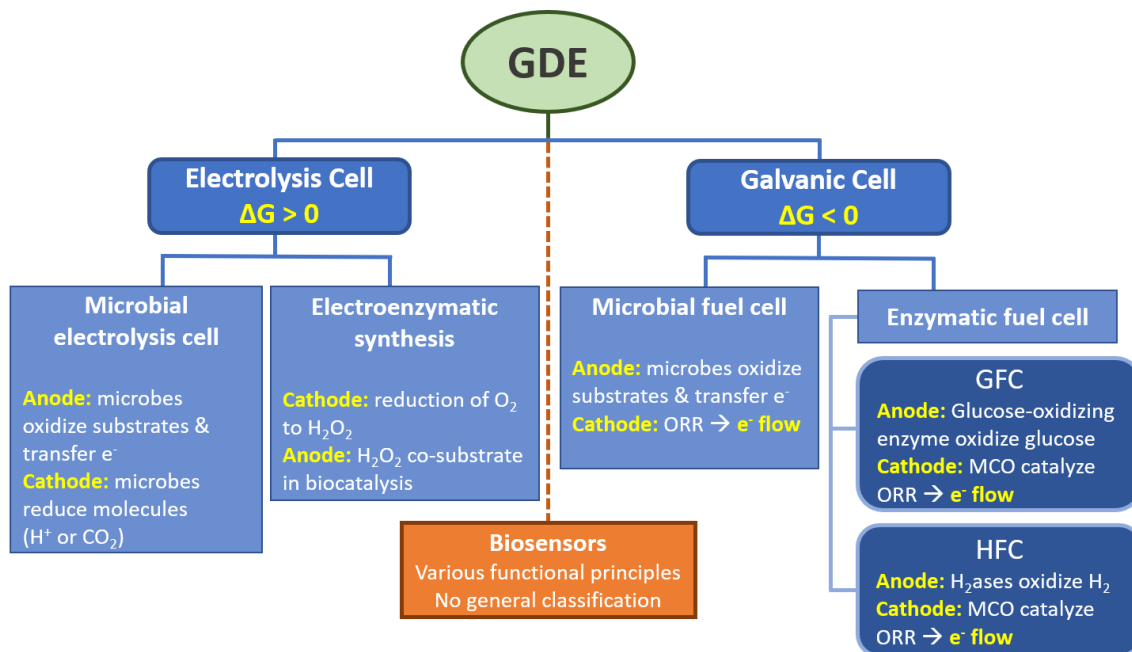


Figure 57 Overview of the different bioelectrochemical application fields for gas diffusion electrodes (GDE). The most typical application method of GDEs is described for the different fields, respectively. GFC and HFC are for Glucose and Hydrogen Fuel Cells, respectively. MCO is for Multi Copper Oxidases. (Modified from Horst et al., 2016).

This limitation has aroused great interest in GDEs and in their implementation in fuel cells, at the interface between the electrolyte and the gas phase.

1.4.4.1 Biofuel Cells

The implementation of GDEs in fuel cells occurs in two configurations: a component of the gas phase intervenes in the electrochemical reaction or the desired gaseous compound is produced at the electrode. In the first case, the cathodic GDE carries out the oxygen reduction reaction (**ORR**), to get around the problem of the low solubility of molecular oxygen in aqueous electrolyte (O_2 concentration is about $250 \mu M$ at room temperature and atmospheric pressure in pure water). ORR in aqueous solutions occurs mainly through two pathways: the direct 4-electrons reduction from O_2 to H_2O and the 2-electrons reduction from O_2 to H_2O_2 (Horst et al., 2016). In non-aqueous aprotic solvents and/or alkaline solutions, a 1-electron reduction pathway from O_2 to O_2^- can also occur (Horst et al., 2016). The second situation is when the anodic GDE performs the hydrogen evolution reaction (**HER**), the electrons from the cathode are used to reduce the protons to form hydrogen, which diffuses through the GDE to a collector. A

standard biofuel cell (Figure 58) contains electrodes where: at the anode a substrate (e.g., glucose) is oxidized by the biocatalysts (enzymes or microbial) to generate electrons and protons. The electrons pass through an outside circuit to the cathode, while the protons pass through an ionic-exchange membrane to reach the cathode where the oxidant such as O_2 is reduced to H_2O . During this redox process, the generated electric current works to continuously operate electrical devices when it is a closed circuit. In biofuel cells biochemical transformations can be performed by either whole cells or enzymes and are called **microbial** or **enzymatic fuel cells**, respectively.

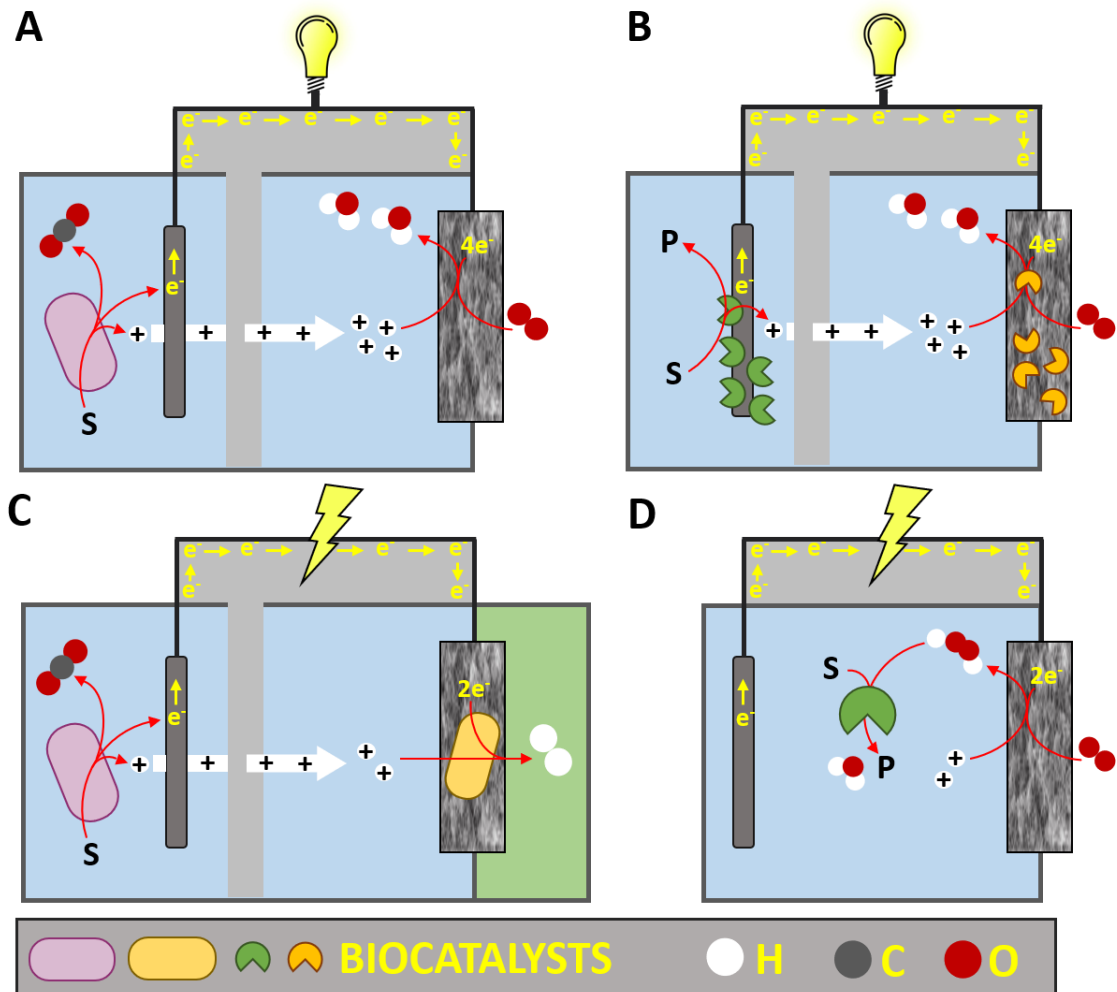


Figure 58 Schematic representations of **(A)** Microbial fuel cell (MFC)- microorganisms oxidize organic substrates (S), produced electrons reduce the anode and are transferred via an external circuit to the cathode. At the cathode ORR takes place, in this case, 4-electrons reduction from O_2 to H_2O . No input in form of electricity is needed but energy is harvested as electrical energy. **(B)** Enzymatic fuel cell (EFC)- enzymes oxidize organic substrates (S) at the anode and transfer electrons to the electrode. At the cathode, oxidases catalyze the ORR to water. Thus, biochemical energy is converted to electrical energy. **(C)** Microbial electrolysis cell (MEC)- microorganisms transfer electrons to the anode and with an energy supply HER takes place at the microbial-based cathode. **(D)** Electroenzymatic synthesis (EES)- oxygen is reduced at the cathode to form hydrogen peroxide. This substance is used as co-substrate for an enzymatic oxidation or halogenation (anodic reaction not shown). (Adapted from Horst et al., 2016)

Microbial fuel cells (MFCs) exploit the metabolism of microbes to oxidize organic matter (anode) and transfer electrons from these reactions to the cathode to carry out a reduction reaction (ORR) and generate current (Figure 58A). The first use of GDE in MFC was reported in 1989, where an oxygen GDE was successfully used as a cathode for ORR with *E. coli* as a catalyst for the oxidation of organic matter and 2-hydroxy-1,4-naphthoquinone as a redox mediator, in the anodic compartment (Sell & Kreysa, 1989). The GDE cathode reached a maximum current density of 1.3 mA·cm⁻². Microorganisms transfer electrons to the anode using several methods, including direct contact of outer membrane cytochromes on the cell surface or on conductive extensions (such as pili which can achieve long-distance electron transfer), through self-produced mediators (such as flavins) which can carry electrons between the cell and the anode (Logan et al., 2020). As an alternative to microorganisms as catalysts for biofuel cells, isolated enzymes can also act as electrochemical catalysts in **enzymatic fuel cells** (EFCs). EFCs use redox enzymes for the oxidation of organic compounds at the anode and redox enzymes for ORR at the cathode to generate electricity (Figure 58B). Apart from applications of EFCs in harvesting energy from oxygen present in extracellular fluids (blood and interstitial fluid), GDEs are often used as cathodes in EFCs based on enzymes capable of reducing oxygen, such as laccases or bilirubin oxidase (multicopper oxidase or MCO) (Osman et al., 2011). The most widely studied EFCs are glucose (**GFCs**) and hydrogen (**HFCs**) EFCs. GFCs are based on MCO at the cathode for ORR and on **glucose oxidizing enzymes** at the anode. GFCs for the development of micro-biosensors have been integrated into living organisms such as rats, rabbits, snails, insects, clams and lobsters (Le Goff & Holzinger, 2018). However, *in vivo* stability is the main bottleneck of GFCs, as they have been reported to be stable for one week, while operating for over one year *in vitro* (Le Goff & Holzinger, 2018). On the other hand, HFCs use **hydrogen oxidizing enzymes**, such as hydrogenases, at the anode and MCO for the ORR at the cathode.

Since the efficiency of electrochemical processes is directly proportional to the electrochemically active area, CNT with their inherently high surface-to-volume ratio have been integrated into GDEs. For example, in 2011, a microbial and enzymatic hybrid fuel cell used an anode consisting of a chitosan-MWCNT 3D macropores matrix

electrode (Figure 59) (Higgins et al., 2011). The microbial anode was inoculated with culture of *Shewanella* MR₁ and lactate as an electron donor. At the cathode, a carbon-based GDE with immobilized laccase was used for ORR by DET. The MFC achieved a power density of 26 W/m³ and an open circuit potential of 1 V. This system was stable for at least 5 days, with a loss of only 4 % of the potential.

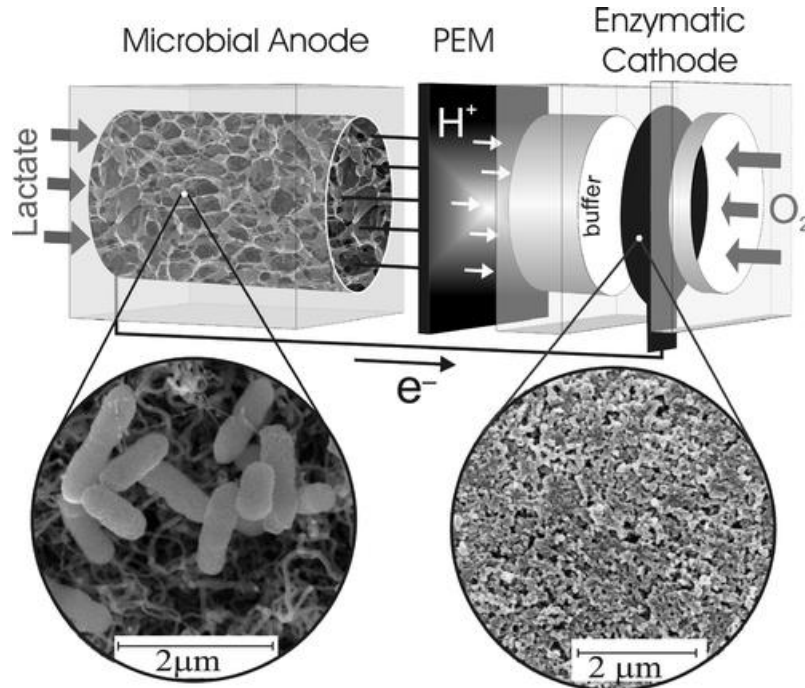


Figure 59 Schematic drawing of 3D Hybrid Fuel Cell. The flow-through anode compartment is filled with a highly porous chitosan-MWCNT composite anode material that was inoculated with *Shewanella* MR₁. The enzymatic cathode is made from teflonized carbon black with adsorbed laccase as the bioelectrocatalysts. High-magnification SEM images show insight into both electrodes: (left) *Shewanella* MR₁ in MWCNT and (right) the porous carbon black gas-diffusion electrode. (Higgins et al., 2011)

In another example, the Copper efflux oxidase from *E. coli* (MCO) was adsorbed on black-modified Ketjen carbon paper (Kontani et al., 2009). This biocathodic GDE was supplemented directly with O₂ from the air and achieved ORR values of 20 mA·cm⁻² at 0.2 V vs. SHE. Lalaoui et al., in 2015 developed an **HFC** based on GDEs and CNT (Lalaoui, Poulpiquet, et al., 2015). CNT were covalently functionalized to enhance the immobilization of bilirubin oxidase (BOD) from *Bacillus pumilus* achieving high current densities up to 3 mA·cm⁻² at 0.2 V vs. SHE for oxygen reduction from air. Then this cathode was used in a membrane-less hydrogen biofuel cell, together with an anode consisting of CNT functionalized for the immobilization of the hydrogenase from *Aquifex aeolicus*. The advantage of this biofuel cell was that the membrane-less design allowed for oxygen reduction at the cathode and oxidation of hydrogen at the anode without inhibition of hydrogenase by O₂. Another example of HFC was reported in 2018 (Figure

60) (Gentil et al., 2018) where the [NiFeSe]-Hydrogenase from *Desulfomicrobium baculatum* was immobilized on covalent functionalized CNT electrodes, through hydrophobic interactions. By exploiting these interactions, the enzyme was able to work efficiently in an H₂/air diffusion HFC, along with the BOD from *Myrothecium verrucaria*.

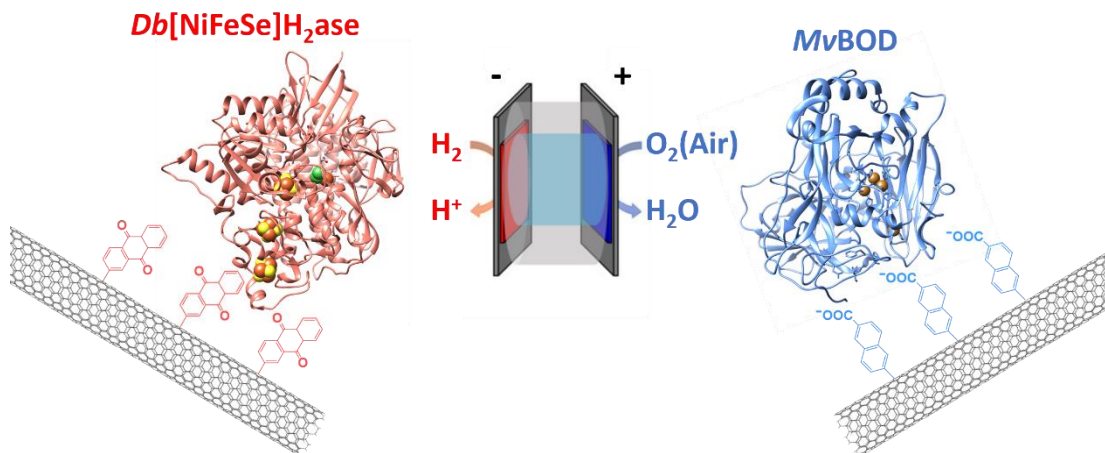


Figure 60 Schematic representation of the H₂/air enzymatic fuel cell. (Adapted from Gentil et al., 2018)

Another example of HFC using [NiFe]-hydrogenases and MCO was reported in 2016. GDE bioelectrodes showed a high current density of approximately 10 mA·cm⁻² as steady state for both the oxidation of H₂ and the reduction of O₂. The integration of the GDE electrodes in a biofuel cell allowed the separation of the gas supply with consequent suppression of the oxidative inhibition of [NiFe]-hydrogenases. The HFC achieved a maximum power density of 8.4 mW·cm⁻² at the cell voltage of 0.7 V under quiescent conditions (So et al., 2016).

1.4.4.2

Microbial Electrolysis Cells

Microbial Electrolysis Cells (**MECs**) work according to the same principle as MFCs. Microbes oxidize organic substrates at the anode and molecules are electrochemically reduced at the cathode (such as CO₂ and H⁺) by microbes. Unlike MFCs, the flow of electrons, from the anode to the cathode, generally is supplied by an external power source ($\Delta G > 0$) (Figure 58C). Cathodic reduction reactions are typically for Hydrogen Evolution Reaction (HER) and different hydrocarbons synthesis processes (such as CH₄ and EtOH). MECs cathodes are generally microbial community (biofilm) which in

addition to the desired reaction can carry out the synthesis of by-products. For example, in the case of HER it was shown that in the biofilm the hydrogenogens *Desulfovibrio* species were predominant (Aulenta et al., 2012). However, side reactions such as the reduction of CO₂ to CH₄ can be observed, in this the use of cathodic GDE is very useful, especially in single chamber MEC, facilitating the rapid removal and recovery of the produced H₂, in order to minimize its microbial metabolism (Horst et al., 2016).

Tartakovsky et al., built and optimized a MEC for HER, based on the microbial oxidation of acetate, which operated continuously and electrically supplemented (1.16 V) (Tartakovsky et al., 2008) (Tartakovsky et al., 2009). The optimized MEC displayed a volumetric selective production of hydrogen was improved to 6.3 L per liter of anode chamber and day and the presence of methane in the outgoing gas was only 2.1 %.

The possibility of using MECs to perform CO₂RR processes was first demonstrated in 2010, here the biofilm included acetogenic bacteria, such as *Sporomusa* spp. and *Clostridium* spp. This graphite cathode supported biofilms were able to reduce CO₂ to acetate and small amount of 2-oxobutyrate (Nevin et al., 2010).

1.4.4.3

Electroenzymatic Synthesis

Electroenzymatic synthesis (EES) mostly refers to the possibility of functionalizing H₂O₂-driven organic compounds such as selective epoxidation, hydroxylation and heteroatom oxygenation. These reactions are catalyzed by enzymes such as peroxygenases and peroxidases. The main problem for the industrial-scale applications of EES is the enzymatic instability towards the H₂O₂ co-substrate. Which should be generated electrochemically at a low but sufficient concentration (Figure 58D). Also, in EES the GDEs are fundamental for the availability of O₂, an example of a cathode GDE-based for the conversion of phenolic monoterpenes (such as thymol and carvacrol), into antimicrobials has been described (Getrey et al., 2014). To date, it has never been developed an electrochemical cell for the H₂ evolution from CO based on Hydrogenase and [NiFe]-CODH. Only one work shows the proof of concept where the enzymatic WGSR was tested in a narrow anaerobic condition in a glass tube filled with a suspension

of *Ch*CODH-I and Hydrogenase 2 from *E. coli* adsorbed on a graphite platelets. The reaction was started by injecting aliquots of CO into the gas phase of the glass tube, the CO and H₂ concentrations were monitored over time by gas chromatography. The WGSR TOF was estimated to be at least 2.5 s⁻¹ at 30 °C, which is based on the less active enzyme (Hydrogenase 2) and is much lower than the rate at which the hydrogenase can work (Lazarus et al., 2009).

EES processes have been exploited to carry out various reactions such as dehydrogenation, oxygenation, disproportion and formation of oxidative bonds (Schmitz & Rosenthal, 2017). Furthermore, EES are still limited in terms of stability and final product yield (Schmitz & Rosenthal, 2017), this is mainly due to the fact that combining promising reaction engineering concepts with the required catalytic conditions of the enzyme is a high task. In the context of this project, attention will now be focused on the electrochemistry of [NiFe]-CODHs.

1.4.5 Electrochemistry of [NiFe]-CODHs

The first time that the methyl viologen mediated electroreduction of CO₂ into CO by a [NiFe]-CODH has been demonstrated was in 2003. The bifunctional enzyme (CODH/ACS) from *Moorella thermoacetica* reduces CO₂ at -0.57 V vs. SHE, with a Faradaic efficiency (see Annex) of almost 100 % at pH 6.3 (Shin et al., 2003). After this work, the other studies focused on the monofunctional CODHs from *C. hydrogeniformans*, conducted by Armstrong and co-workers.

In 2013, they investigated the inhibition of the two *Ch*CODHs (I and II) by protein film electrochemistry (PFE, see Annex). In general, enzymes were adsorbed nonspecifically on a PGE electrode or by using molecules that improve the stability of the protein film, such as polymyxin (V. C.-C. Wang, Can, et al., 2013)(V. C.-C. Wang, Ragsdale, et al., 2013). In addition to improving the surface coverage of the enzyme, the PGE electrodes were also functionalized with MWCNT by dip-coating a solution of 1 mg·mL⁻¹ of MWCNT dispersed in DMF. The MWCNT were further functionalized with polymyxin (V. C.-C. Wang et al., 2015).

First, both *Ch*CODHs were shown to direct electrocatalyze the interconversion of CO₂/CO. Thus, they investigated the potentials threshold of the known [NiFe]-CODH inhibitors: sulfide (C_{ox} state), cyanide (C_{red1} state), cyanate (C_{red2} state) and O₂ (Figure 61).

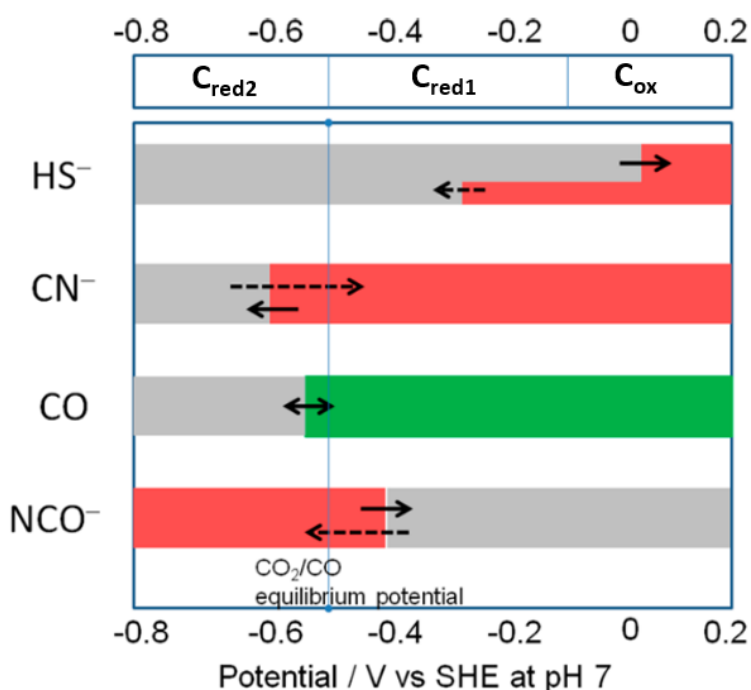


Figure 61 Potential dependence of binding of inhibitors to *Ch*CODH I. Red refers to the potential region over which the enzyme is inhibited, gray indicates no binding, and green indicates that binding leads to turnover. The dashed arrows indicate reactions that are slow compared to those indicated by full arrows. (Adapted from V. C.-C. Wang, Ragsdale, et al., 2013).

Since cyanide (CN⁻) inhibits exclusively the C_{red1} state, it acts as an inhibitor a potential below -300 mV. The addition of cyanide (1mM) into the electrochemical cell during the oxidation of CO at -280 and +80 mV resulted in both cases in the drop of current for the two *Ch*CODHs. Cyanide inhibition was also tested under CO₂ by its injection at more negative potential (-760 mV) during the second scan. The CO₂ reduction current decreases at each scan due to the binding of cyanide in the C_{red1} range of potentials. Chronoamperometry experiments were performed to evaluate the rate of inactivation and reactivation at low potential (release of CN⁻ while C_{red1} state is converted to C_{red2} state) of cyanide inhibited *Ch*CODHs. In figure 62AB the current is due to the respective oxidation of CO (-460 mV) and the reduction of CO₂ (-560 mV). The injections of CN⁻ were performed to reach a final concentration of 0.5 mM. These experiments were performed at different potentials to calculate the half-time inhibition, which is stable (all around 1-

5 minutes) until very reductive potentials (-760 mV) (V. C.-C. Wang, Ragsdale, et al., 2013).

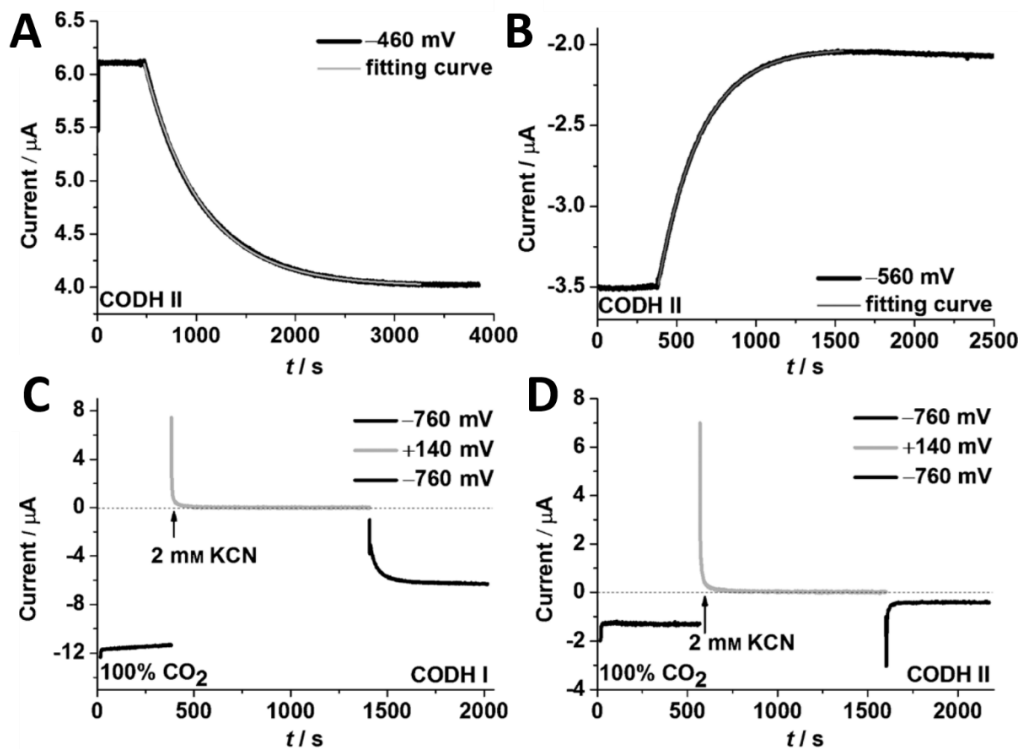


Figure 62 Chronoamperometric measurements of the inactivation rates, (A) and (B), and the reactivation rates, (C) and (D), of cyanide-inhibited ChCODH I and II, respectively. The inactivation rate of ChCODH II by cyanide was measured at (A) -460 mV under 100% CO and (B) -560 mV under 100% CO₂. A final concentration of 0.5 mM KCN in the electrochemical cell was used to measure the half-time for inactivation. (D) Cyanide release at -760 mV is much faster than the instrumental response. Experimental conditions: 25 °C, 0.2 M MES pH 7, rotation at 3500 rpm. (V. C.-C. Wang, Ragsdale, et al., 2013)

Concerning the reactivation tests (Figure 62CD), a high potential was previously applied for 10 minutes in the presence of 2 mM CN⁻, in order to completely inhibit the enzyme. The authors stated that, up to -560 mV, there was no reactivation, while, at -760 mV, the half-time reactivation was 19 seconds for ChCODH I and spontaneous for ChCODH II (V. C.-C. Wang, Ragsdale, et al., 2013). On the other hand, cyanate (NCO⁻) inhibiting exclusively the C_{red2} state, exhibits the opposite behavior of cyanide by binding and inhibiting the enzyme at potentials below -500 mV and being released at high potentials. The addition of 6.67 mM NCO⁻ was tested at -760 mV under either 100 % CO₂ and a mixture of 50 % CO₂ and 50 % CO. The injection of cyanate resulted in a rapid full inhibition of CO₂ reduction while the inhibition of CO oxidation was negligible under 100 % CO₂ and 50 % CO₂ and 50 % CO, respectively. The exclusive binding of cyanate to the C_{red2} state was also confirmed by EPR.

In figure 63 it is possible to observe the spectra of an oxidized sample (benzyl viologen) (A), reduced to the C_{red1} state by CO (D) and dithionite reduced to the C_{red2} state (F). The addition of 1 and 20 mM cyanate did not affect the spectra of oxidized samples (BC), while the addition of 1 mM cyanate to the CO-reduced sample induces the conversion of C_{red1} state ($g = 2.01, 1.89, 1.73$) to the C_{red2} state (increase of $g = 1.96, 1.77$ and loss of the C_{red1} g values). Similarly, for the dithionite-reduced sample the intensity of the C_{red2} state increases in the presence of 20 mM cyanate (G).

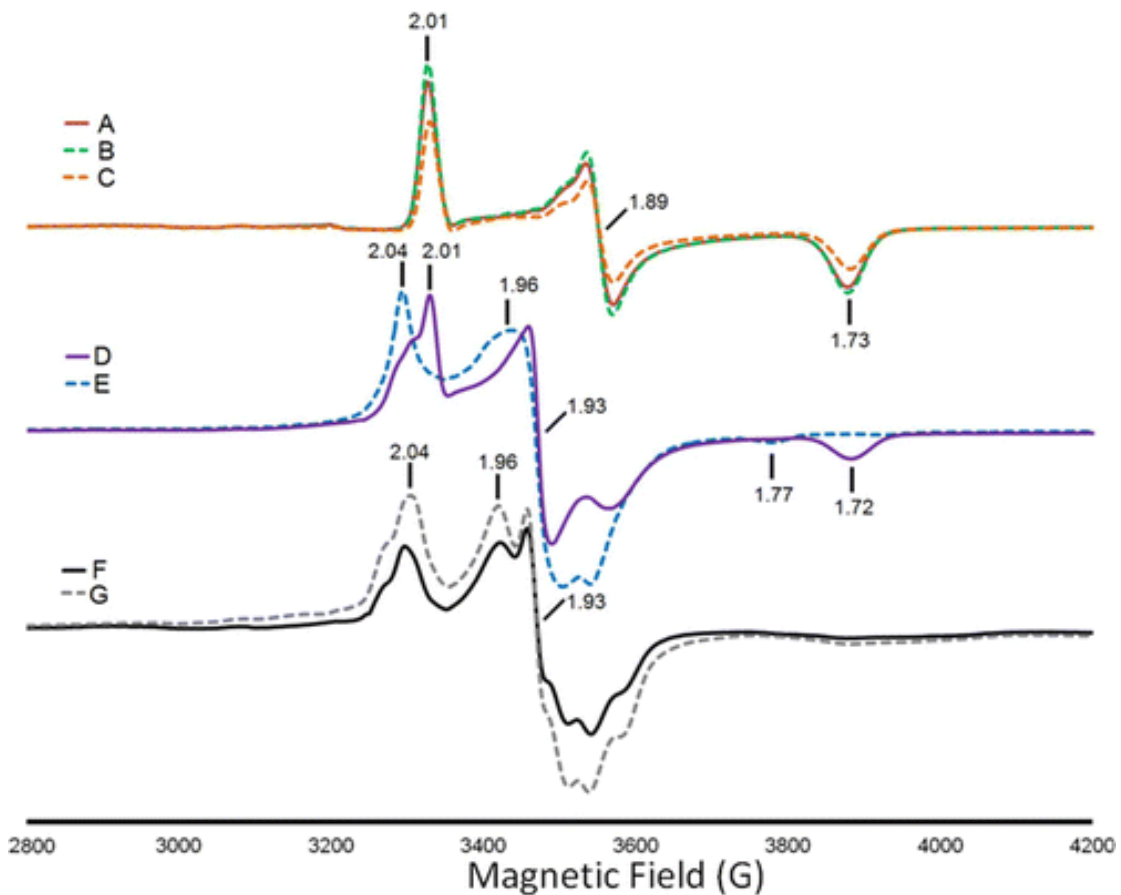


Figure 63 EPR spectra of ChCODH I (A) oxidized with benzyl viologen (B) oxidized with benzyl viologen and in presence of 1 mM or 20 mM (C) cyanate (D) reduced with CO (E) reduced with CO and in presence of 1 mM cyanate (F) reduced with dithionite (G) reduced with dithionite and in presence of 20 mM cyanate (A) 12 K, 41.2 mW, 9.38 GHz (B) 12 K, 41.18 mW, 9.38 GHz (C) 12 K, 41.2 mW, 9.383 GHz (D) 12 K, 41.22 mW, 9.382 GHz (E) 12 K, 41.21 mW, 9.379 GHz (F) 12 K, 41.21 mW, 9.38 GHz (G) 12 K, 41.21 mW, 9.381 GHz (V. C.-C. Wang, *Can, et al.*, 2013)

Finally, the inhibition of the C_{ox} state by sulfide was also confirmed by electrochemistry (V. C.-C. Wang, Ragsdale, et al., 2013). Sulfide acts as an inhibitor at potential above -50 mV and at -260 mV is fast released due to full conversion of C_{ox} to C_{red1} .

O_2 inhibition of ChCODH II was also investigated by chronoamperometry (Figure 64) (V. C.-C. Wang et al., 2015). The reaction with O_2 was tested at +140 mV and -260 mV under 100 % CO. Before and after O_2 injection, steps of prereduction were carried out a -760 mV. The results show that raising the potential from -260 to +140 mV protects the

*Ch*CODH II towards O₂ inhibition, because at +140 mV the residual catalytic current was approximately 70 % compared to that observed -260 which retained only 1 % of electrocatalytic activity. From these experiments, the C_{red1} state appears to be more prone to O₂ inhibition/damage than C_{ox} state.

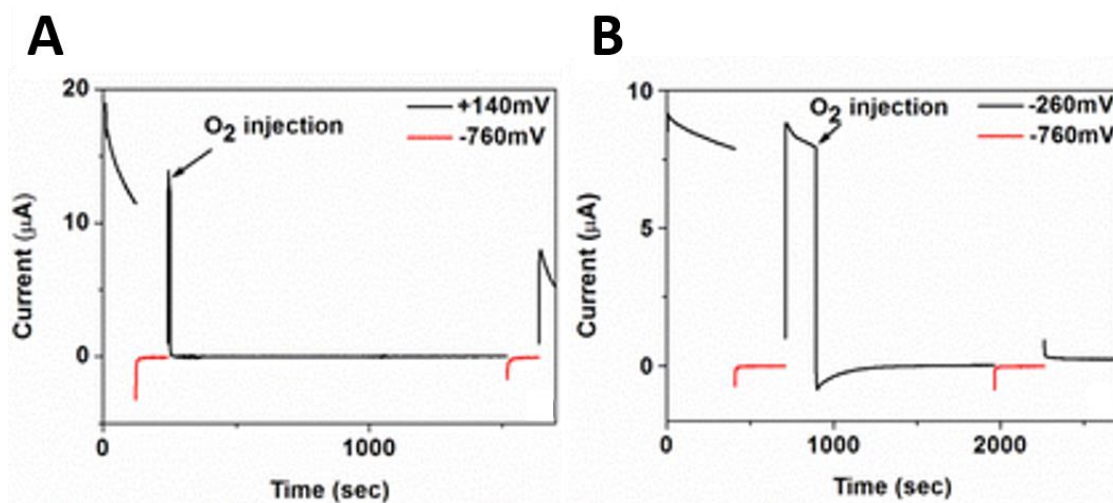


Figure 64 Effect on *Ch*CODH II electrocatalysis of injecting O₂-saturated buffer (0.5 mL) into the electrochemical cell (3 mL) under different conditions. The black line indicates times during which the electrode potential was poised at (A) +140 mV or (B) -260 mV, and red lines indicates times during which the electrode potential was poised at -760 mV for reductive reactivation. Experimental conditions: 25 °C, 0.2 M MES pH 7, 2500 rpm under 100 % CO atmosphere. Experimental conditions: 10 °C, 0.2 M MES pH 7, 2500 rpm, 100 % CO. (V. C.-C. Wang et al., 2015)

To better understand the irreversible inactivation of O₂, similarly to experiments Figure 64B further experiments were conducted with a cyanide fully-inhibited *Ch*CODH II. The injection of CN⁻ before O₂ resulted in a protection from O₂ inhibition at -260 mV with a remaining electroactivity of approximately 50 % versus 1 % in Figure 64B. Taken together, these results confirms that the O₂ inhibition occurs from its binding to the Ni of the C-cluster, but that the decomposition of FeS clusters can also contribute, resulting in reduced DET as well as reduced electrocatalytic current. The oxygen inhibition of CODHs was further investigated by electrochemistry for *Dv*CODH, *Ch*CODH IV, *Tc*CODH I and II, through similar approaches (Merrouch et al., 2015)(Domnik et al., 2017)(Benvenuti et al., 2020). For the chronoamperometry experiments the potential was switched between -310 mV (catalysis and inhibition) and -560 mV (pre-reduction) and short transient exposition to a range of O₂ concentration were tested for the different CODHs. From these first studies the *Dv*CODH was shown to be more resistant to O₂ compared to *Ch*CODH II. For example, in the case of injection 1 µM of O₂, the *Dv*CODH recovers all the activity while only 20 % at most was restored for *Ch*CODH II (Merrouch et al., 2015). The same research group also characterized the O₂ inhibition of

*Ch*CODH IV. This enzyme shows a very high affinity for CO and is able to oxidize it at the diffusion limit over a wide range of temperatures (K_m for CO at 25 °C of $8 \pm 1 \mu\text{M}$ and $47 \pm 3 \text{ nM}$ for *Ch*CODH II and *Ch*CODH IV, respectively) (Domnik et al., 2017). Indeed, its role in defense against oxidative stress has been proposed, which support the theory that CODHs can be different in terms of activity and physiological roles (Domnik et al., 2017). The results shows that the high affinity of *Ch*CODH IV for CO protects the enzyme from O₂ inhibition. The two *Tc*CODHs displayed behaviors similar to that of *Ch*CODH IV (Benvenuti et al., 2020). The results about these two different behaviors of O₂ competition with CO reinforce the previous proposed theory on the different possible functions of CODHs.

Table 13 summarizes the best electrocatalytic activities reported for mononuclear [NiFe]-CODHs, currently available. To date, no literature data are available on the direct or mediated electrocatalytic activities of CODH from *Rhodospirillum rubrum*, while for *Dv*CODH and *Ch*CODH IV, only mechanistic data are reported.

Table 13 Best electrocatalytic mononuclear [NiFe]-CODHS activities for CO oxidation and CO₂ reduction

CODH	CO oxidation			CO ₂ reduction current			T (°C)	pH	Ref
	I (mA·cm ⁻²)	E vs. SHE (mV)	Overp. (mV)	I (mA·cm ⁻²)	E vs. SHE (mV)	Overp. (mV)			
<i>Tc</i> I	0.0027	-160	300	-0.0046	-760	300	37	6	1
<i>Tc</i> II	0.03	-160	300	-0.048	-760	300	37	6	1
<i>Ch</i> I	2.86	250	770	-0.4	-760	240	25	7	2
<i>Ch</i> II	1.75	250	770	-0.16	-760	240	25	7	3

1 PFE on PGE electrodes (Benvenuti et al., 2020); 2 PFE on Polymyxin coated PGE electrodes (V. C.-C. Wang, Can, et al., 2013); 3 PFE on Polymyxin coated PGE electrodes (V. C.-C. Wang, Ragsdale, et al., 2013)

These works have highlighted the possibility of using CODH in bio-electrocatalytic CO₂RR processes, in mild conditions, but also in bifunctional devices allowing the reduction of CO₂ to CO coupled to H₂ oxidation by a Hydrogenase. However, improvements are needed, such as the compartmentalization of the two enzymes on GDE electrodes, for example to prevent the CO inhibition of hydrogenases or improve direct electron transfer by co-immobilizing the two enzymes on the CNT. After the presentation of [NiFe]-CODHs, the comparison with catalysts currently used in CO₂RR processes such as Formate Dehydrogenase, metal-based catalysts and molecular catalysts will be presented in the next section.

To date, five oxidoreductases are described using naturally CO₂ as substrate: Formate Dehydrogenase (FDH), Carbon dioxide reductase, remodeled nitrogenase, Pyruvate:Ferredoxin oxidoreductase (PFOR) and CODH. Some *in vitro* catalytic properties and products of these enzymes are shown in Table 14.

Table 14 Some products obtained from *in vitro* CO₂ conversion with different enzymes (Modified from Ünlü et al., 2021)

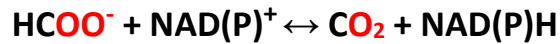
Enzyme	Products	Advantages	Disadvantages
Formate Dehydrogenase (FDH)	Formate	<ul style="list-style-type: none"> Value-added product 	<ul style="list-style-type: none"> Forward reaction is favorable for most FDHs Requirement of improvement for long-term covalent immobilization Expensive cofactor (NADH)
Multiple Dehydrogenases (FDH + FaldDH + ADH)	Methanol	<ul style="list-style-type: none"> Value-added product 	<ul style="list-style-type: none"> Unstable for long-term activity Requirement of immobilization for industrial applications Expensive cofactor
Carbon Dioxide Reductase	Formate	<ul style="list-style-type: none"> No requirement of cofactor Reaction direction can easily drive by substrate concentration 	<ul style="list-style-type: none"> In cascade system, CO can easily inhibit the reaction
Remodeled Nitrogenase	Methane	<ul style="list-style-type: none"> No inhibition by H₂ 	<ul style="list-style-type: none"> Improvement required for turnover numbers and frequency Oxygen-sensitive enzyme
Pyruvate:Ferredoxin Oxidoreductase (PFOR)	Pyruvate		<ul style="list-style-type: none"> Forward reaction is strongly favorable
Carbon Monoxide Dehydrogenase (CODH)	Carbon Monoxide	<ul style="list-style-type: none"> CO easily convertible to value-added products 	<ul style="list-style-type: none"> Oxygen-sensitive enzyme

Only two enzymes are capable of directly catalyzing the CO₂ reduction: the CODH, already presented above, and the FDH.

1.4.6.1

Formate Dehydrogenase

Formate dehydrogenase catalyze the reversible oxidation of formate to CO₂. Typically, FDHs require redox/co-substrate such as NAD(P)⁺/NAD(P)H.



FDHs are attractive enzymes for the production of formate through CO₂ reduction. However, CO₂ reduction being on unfavorable endergonic reaction, most FDH catalyze the oxidation of formate (Crabbe et al., 2011)(Førgaard et al., 2019). But under appropriate thermodynamic conditions (notably a high substrate concentration) CO₂ is reduced to formate. FDHs can be divided into metal independent (Type 1) and metal dependent (Type 2) catalysts. The latter can adopt different molecular organization, such as monomers, heterodimers or heterotrimers, while Type 1 are found as monomers. Type 1 FDHs usually catalyze the reduction of formate to CO₂ using NAD⁺ as a cofactor, while Type 2 possess active sites based on Molybdenum or Tungsten, Mo(VI) or W(VI) as part of a pyranopterin guanosine dinucleotide cofactor and is coordinated to the proteins *via* cysteine or selenocysteine residues. Furthermore they also possess FeS clusters for the electron transfer (Førgaard et al., 2019). Metal-dependent enzyme are mostly O₂ sensitive but are the most active FDH ($K_{\text{cat}} > 1000 \text{ s}^{-1}$) compared to the O₂ insensitive low active metal independent ones ($K_{\text{cat}} < 1 \text{ s}^{-1}$) for formate oxidation. Soluble NADH & metal-independent FDHs can exhibit CO₂ reduction activities ($K_{\text{cat}} = 10 \text{ s}^{-1}$), which is 10 times higher than metal-independent enzymes. Unlike CODHs, FDHs need more attention to electrode immobilization to achieve direct electron transfer, e.g., graphite-epoxy electrodes, CNT-coated graphite electrodes, TiO₂ or polymyxin coated PGE electrodes (Meneghello et al., 2020).

Enzyme-assisted Photoreduction of CO₂

Electrocatalytic activity of FDHs has been studied in depth over the past decade by Reisner's research group with the aim of using light as a sole source of energy and water as a sole source of electrons for driving the CO₂ reduction to formate (photoreduction of CO₂). In 2018 an electroenzymatic synthesis was developed system using a photoanode capable of catalyzing the oxidation of water to O₂ and a cathode with FDH adsorbed on a hierarchically structured inverse opal titanium dioxide scaffold (Figure 65) (Sokol et al., 2018). This system achieves the light-guided CO₂ conversion to formate with a selectivity of 80 % and the FDH-functionalized cathode retain approximately 83 % of the initial activity after 2 hours.

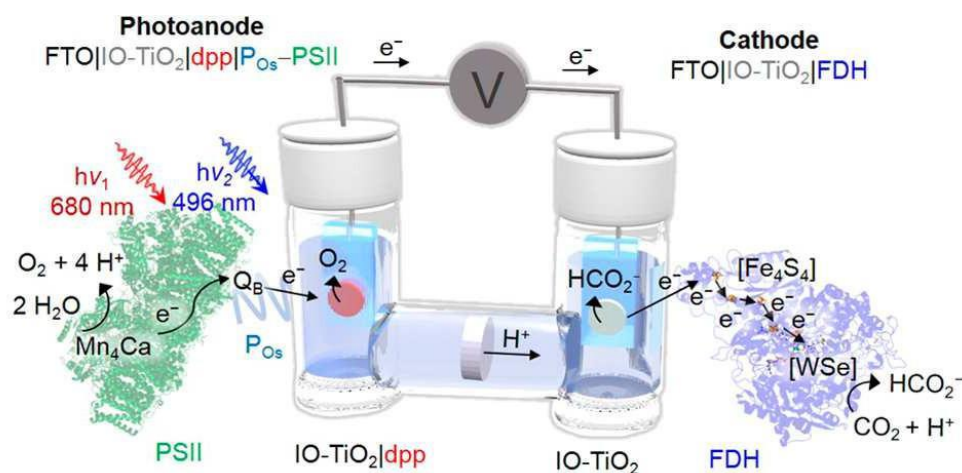


Figure 65 Schematic representation of the semi-artificial photosynthetic tandem PEC cell coupling CO₂ reduction to water oxidation. A blend of POs and PSII adsorbed on a dpp-sensitized photoanode (IO-TiO₂|dpp|POs-PSII) is wired to an IO-TiO₂|FDH cathode (species size not drawn to scale) (Sokol et al., 2018)

Based on the same principle, they used metal oxide electrodes (TiO₂) for the immobilization of an FDH and RuP or diketopyrrolopyrrole (DPP) as photosensitizers (Figure 66). The latter injects photoexcited electrons into the conductive TiO₂ which are transferred to the FDH which carries out the reduction of CO₂ to formate with a TOF of 11 s⁻¹ (Miller et al., 2019). This system shows a stable formate production for about 6 hours and after 24 hours of continuous photocatalysis the residual enzymatic activity was about 36 % (Miller et al., 2019).

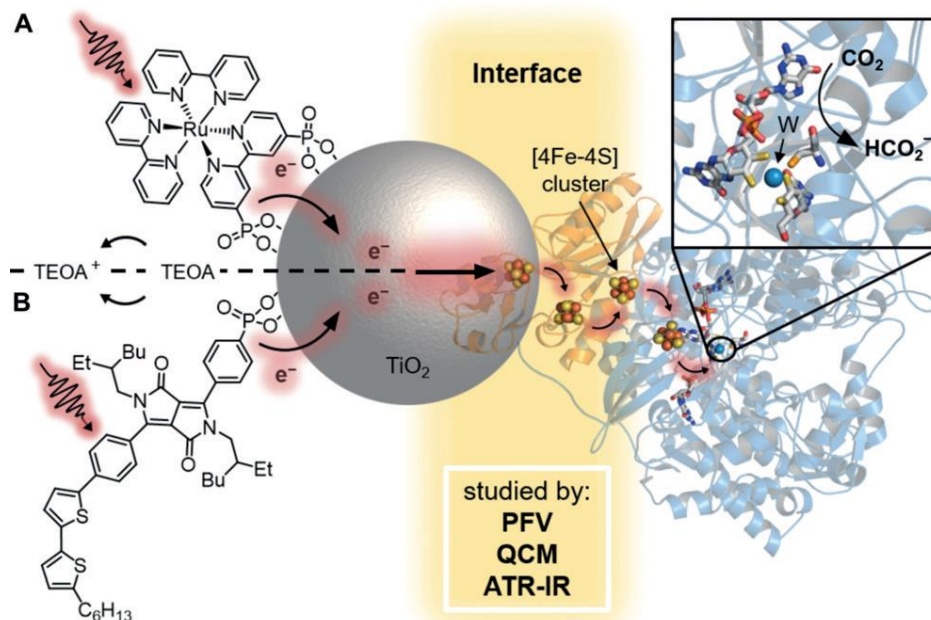


Figure 66 Schematic CO_2 conversion with a dye–semiconductor–FDH photocatalyst system. Photoexcited electrons from the dye, RuP in (A) or DPP in (B), are transferred via the conduction band (CB) of TiO_2 across the enzyme–material interface through the intraprotein [4Fe–4S] relays to the active site of FDH for the reduction of CO_2 to formate. The oxidized dye is regenerated by triethanolamine (TEOA). (Miller et al., 2019)

The same group also used a conductive indium tin oxide (ITO) as an electron relay to connect the active sites of FDH and Hydrogenase (Figure 67B) (Sokol et al., 2019). This system was bioinspired by the formate hydrogenlyase complex (FHL), which naturally catalyzes the oxidation of formate (FDH subunit) to the production of H_2 (Hydrogenase subunit) (Figure 67A). This system shows reversibility and good stability for 24 hours with a selectivity for formate and H_2 production of 76 and 77 %, respectively.

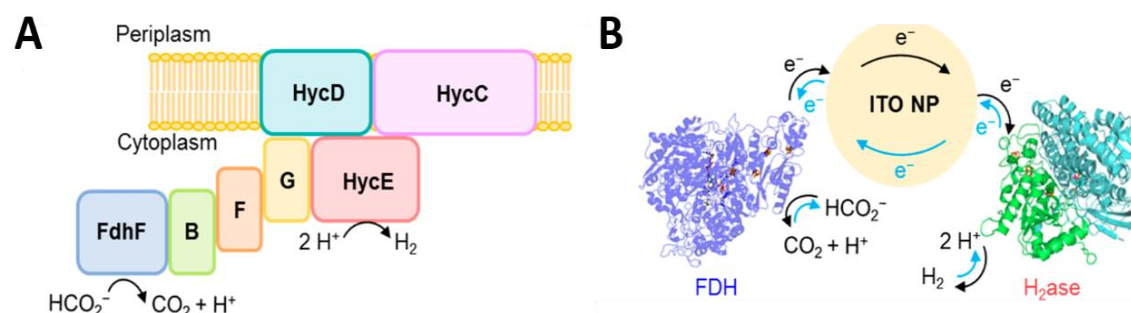


Figure 67 (A) Biological *E. coli* FHL-1 complex. FdhF, FDH; B/F/G, Fe–S cluster-containing proteins; HycE, [NiFe]– H_2 ase; HycD/C, membrane proteins. (B) FDH–ITO– H_2 ase nanoparticle (NP) system with enzymes immobilized onto ITO NP in solution. Species size not drawn to scale (Sokol et al., 2019)

In 2007, Armstrong and collaborators developed a model system for the photoreduction of CO_2 to CO using visible light (Figure 68) (Woolerton et al., 2010)(Woolerton et al., 2011). They adsorbed *Ch*CODH-I, as a catalyst, and a RuP, as a photosensitizer, on n-type MOx semiconductor nanoparticles (such as TiO_2 , ZnO, anatase, etc.). The working

principle is as follows: visible light excites the RuP which injects electrons into the semiconductor, electrons are finally transferred through the FeS cluster of the CODH to the active site where the CO₂ is reduced to CO. They also managed to regenerate the photosensitizer, through a sacrificial electron donor. This system in the best configuration achieved a TOF of 0.14 s⁻¹ and TON of 2 000. This low TOF was improved using a RuP free system, where CODH was assembled on CdS nanocrystals with visible light harvesting capability, which offered sufficient driving force to reduce CO₂ to CO. This system achieved an average TOF of 1.23 s⁻¹ and a TON of 2 200 (Benniston et al., 2012).

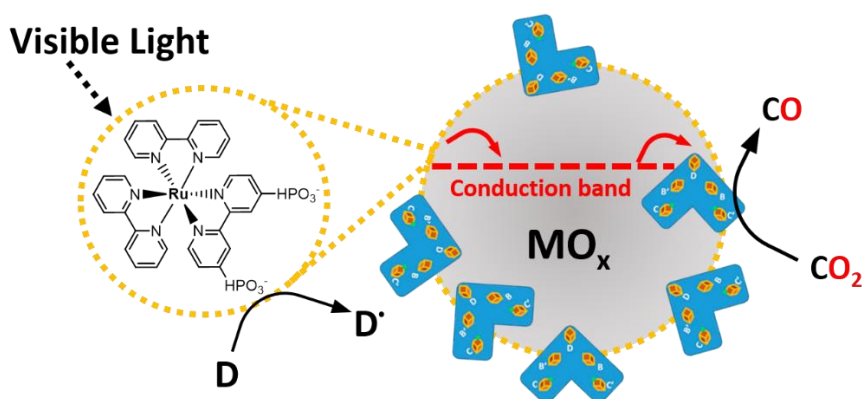


Figure 68 Schematic representation of the photoreduction of CO₂ to CO system based on ChCODH-I and RuP.

1.4.6.3

CO₂ Electrolyzers

As previously mentioned, CO₂RR is an important strategy to generate valuable chemicals from CO₂. In recent years, CO₂ to formate electrolysis cells have been reported based on FDHs. Mo-FDH was immobilized and electrically wired to a redox polymer consisting of cobaltocene grafted onto polyallylamine. The bioelectrode achieved the reduction of CO₂ to formate with a Faradaic efficiency of 99 % at -0.66 V vs. SHE (Yuan et al., 2018). K. Kano and colleagues reported earlier the immobilization of W-FDH on Ketjen Black electrode functionalized with polytetrafluoroethylene groups in order to promote the immobilization of W-FDH through hydrophobic interactions. The bioelectrode reached a current density of about 20 mA·cm⁻² under atmospheric pressure and ambient temperature in neutral pH (Sakai et al., 2016).

CO₂-to-CO electrolyzers with high efficiency and high specificity is an important strategy for CO₂ valorization. This type of electrolyzers must operate at high current density of several hundreds of mA cm⁻². Nowadays, this types of electrolyzers are based on gold and silver catalysts operating in gas-diffusion electrolyzers (Torbensen et al., 2020). To date, several non-biological catalysts have been combined with CNT-based electrodes, demonstrating CO₂RR activity with high specificity towards aqueous CO/CO₂ interconversion. Several cobalt-based compounds have been synthesized as: Co-phthalocyanine (CoPc) or Co-quaterpyridine complexes (CoQpy) (Figure 69AB) (Kramer & McCrory, 2016)(X. Zhang et al., 2017)(Takanabe & Rodionov, 2016)(M. Wang et al., 2018).

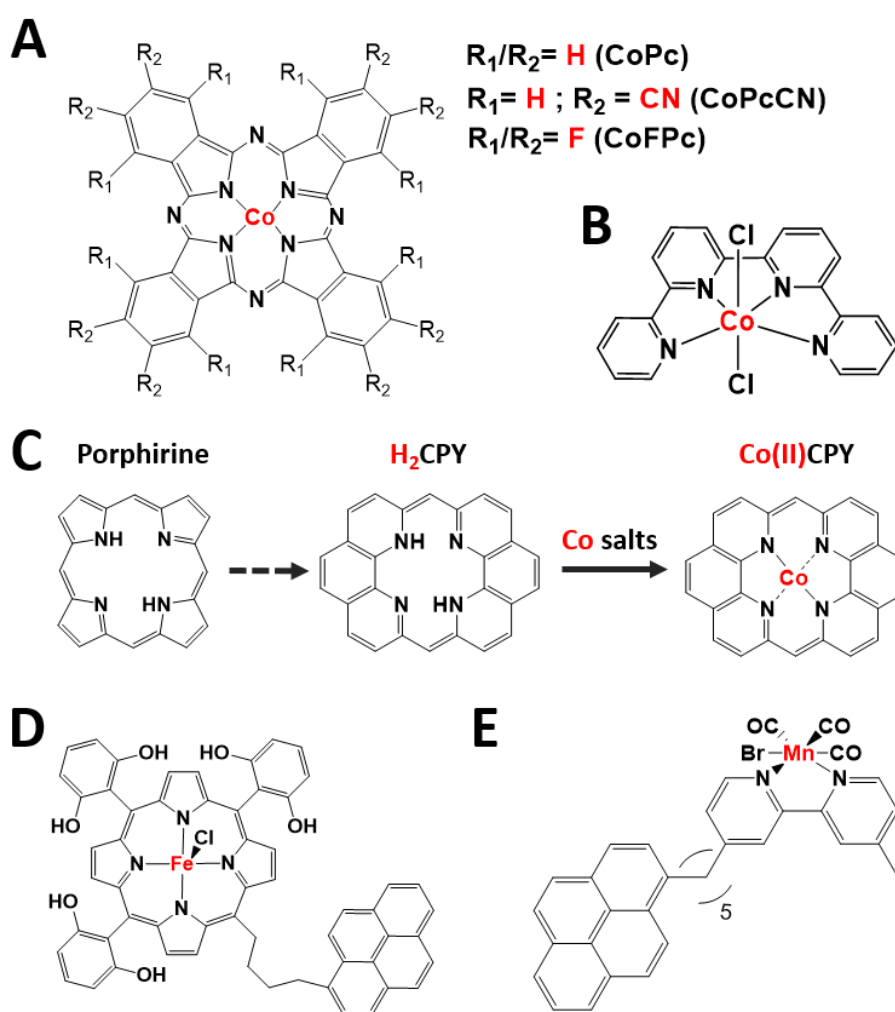


Figure 69 Structures of some metal-based molecular catalysts for CO₂/CO interconversion: (A) Co-phthalocyanine (CoPc), (B) Co-quaterpyridine complex, (C) N₄-macrocyclic Co complex (Co-CPY) (Adapted from Sun et al., 2020), (D) pyrene-substituted iron porphyrin (E) pyrene substituted [MnBr(2,2'-bipyridine)(CO)₃].

In another example, a cobalt porphyrin catalyst was used as a building block to synthesize a covalently-linked macrostructure (Covalent organic framework or COF) (Lin

et al., 2015). Another Co-based complex has recently been reported, derived from phenanthroline subunits an N4-macrocyclic Co complex (Co-CPY) has been synthesized (Figure 69C) (Sun et al., 2020). Other molecular catalysts based on earth-abundant metals have also been synthesized and have demonstrated selective CO₂RR such as a pyrene-substituted iron porphyrin (FePhpyr) (Figure 69D) (Maurin & Robert, 2016) and a pyrene-substituted manganese-bipyridine-CO complex [MnBr(2,2'-bipyridine)(CO)₃] (Figure 69E) (Reuillard et al., 2017).

Among these catalysts which have been implemented in pre-industrial flow cells operating in alkaline media at CO₂-diffusing electrodes, several CNT-supported cobalt phthalocyanine have reached current densities >150 mA·cm⁻² with near to 100% CO Faradaic efficiency (Ren et al., 2019)(M. Wang et al., 2019). Furthermore, stability and Faradaic efficiency were kept for at least 8-10 hours at lower current densities (20-75 mA·cm⁻²). In addition, other metal-based catalysts have been synthesized such as: Copper polyphthalocyanine (CupolyPc)(Karapinar et al., 2020), gold nanoneedles or nanowires (M. Liu et al., 2016)(Zhu et al., 2014), palladium nanoparticles (D. Gao et al., 2015), and nanoporous silver (Lu et al., 2014). The performances of several best metal-based catalysts are summarized in Table 15.

Table 15 Metal-based catalysts for aqueous CO₂/CO interconversion.

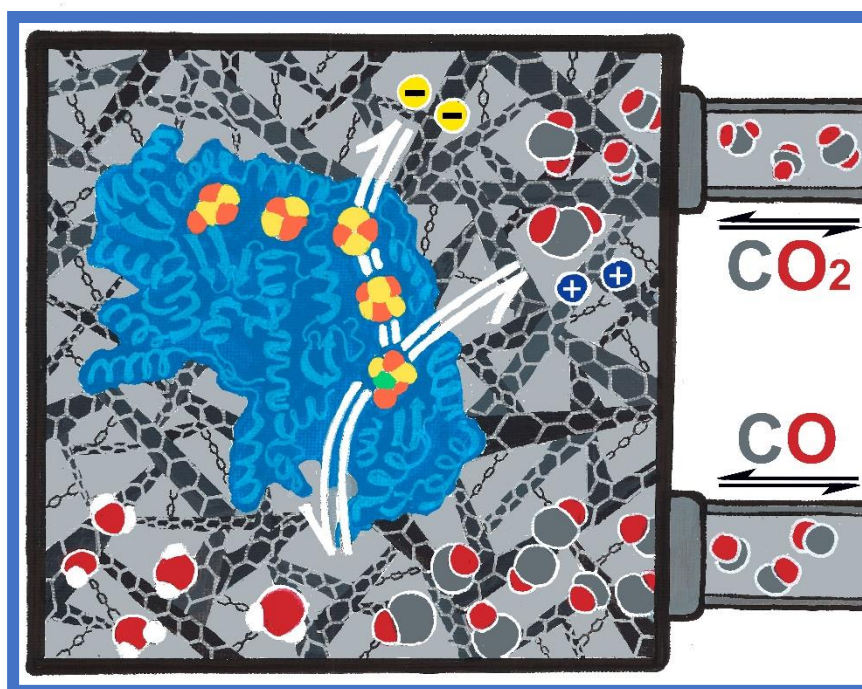
Catalyst	J _{co} (mA·cm ⁻²)	TOF (s ⁻¹)	TON	Overpot. (mV)	CO selectivity (%)	pH	Ref.
CoPc2	165	3.9	ND	400	94	14	1
CoPc	175	0.21	125	1910	95	14	2
CoPc-P4VP	2	4.8	34,000	610	89	4.7	3
CoFPc	4.4	1.6	ND	280	93	7.2	4
CoPcCN/CNT	15	4.1	97,000	520	98	7.2	5
CoQpy/CNT	19.9	12	89,905	440	99	7.3	6
Co-COF	3.3	0.53	290,000	550	90	7	7
CupolyPc/CNT	6.9	ND	ND	590	80	ND	8
Au nanoneedles	22	ND	ND	240	95	ND	9
Au nanowires	8.16	0.02	ND	ND	94	7.2	10
Pd nanoparticles	9.76	0.16	ND	390	91	6.8	11
Nanoporous Ag	8.7	0.002	ND	390	92	7.2	12
FePhpyr/CNT	0.24	0.04	432	480	93	7.3	13
Mn-bipy/CNT	5	0.04	2000	550	34	7.4	14

*Mn-bipy = [MnBr(2,2'-bipyridine)(CO)₃]; **1** (M. Wang et al., 2019); **2** (Ren et al., 2019); **3** (Kramer & McCrory, 2016); **4** (Takanabe & Rodionov, 2016); **5** (X. Zhang et al., 2017); **6** (M. Wang et al., 2018); **7** (Lin et al., 2015); **8** (Karapinar et al., 2020); **9** (M. Liu et al., 2016); **10** (Zhu et al., 2014); **11** (D. Gao et al., 2015); **12** (Lu et al., 2014); **13** (Maurin & Robert, 2016); **14** (Reuillard et al., 2017)

Article 1:

Efficient electrochemical CO₂/CO Interconversion by an Engineered Carbon Monoxide Dehydrogenase on a Gas-Diffusion Carbon Nanotube Based Bioelectrode

Graphical Abstract



The understanding of complex Ni enzymes and the development of bio-inspired systems for CO₂ reduction were the two major driving forces that led us to start the study of the [NiFe]-CODH from *Rhodospirillum rubrum* (*RrCODH*) and allowed us to obtain the following results. The choice of *RrCODH* is based on the following criteria: the enzyme has been thoroughly characterized by a combination of approaches, its X-ray structure has been solved in 2001, the Ni chaperones involved in its maturation are well known and characterized, and finally, its specific activity for CO oxidation in solution is the highest under ambient conditions compared to that of the other described CODHs.

When I started my PhD three years ago, several aims were raised. The first was to provide a novel simple and efficient protocol for the heterologous production of an active recombinant *RrCODH* with a high production and purification yields, in order to facilitate both its detailed characterization and the development of its use in CO₂RR processes.

The second objective was to provide insights on the maturation processes of [NiFe]-CODHs. For this reason, before this work our group together with international collaborations, has already characterized the two Ni chaperones CooT and CooJ. These latter proteins are widely spread in the genome of several microorganism that also possess the CODH and CooC genes (Darrouzet et al., 2021)(Alfano et al., 2018)(Timm et al., 2017). The ultimate goal was to show whether *RrCODH* could be electrochemically connected to an electrode, since almost no other electrochemical studies on *RrCODH* had been performed prior to this study. Furthermore, with the aim of a future development of functional CO₂RR devices based on *RrCODH*, we have investigated the best electrode surface immobilization technique to obtain electrochemical performances at least comparable to non-biological CO₂RR catalysts. In support of this last point, our laboratories have already succeeded in the efficient electrochemical immobilization of other redox enzymes (Hydrogenase, Peroxidase, Glucose Oxidase, exc.) on carbon nanotubes, exploiting the advantages of using these nanomaterials.

- Providing a novel method for the heterologous production of a fully active recombinant *Rr*CODH with high yields.

The protocol provided for the aerobic production of Rec-*Rr*CODH in *E. coli* has been extensively studied and validated prior to publication. I spent about a year of this PhD project discovering the best conditions and problems related to aerobic production and anaerobic purification, with the aim of keeping a stable and fully active enzyme without protein or metallic co-factors damages, such as proteolysis, oxidative reactions, due to the interaction of reducing agents (DTT and DTH) with O₂.

Regarding the production yield, the following table summarizes the reported growth conditions of the host bacteria together with the yields of crude microbial culture and pure CODH enzymatic preparations.

CODH	Host bacteria	Growth conditions	Cells Yield (g L ⁻¹)	Purification yield (mg L ⁻¹)	Reference
<i>Ch</i> II	<i>E. coli</i>	Fully anaerobic expression, N ₂ gas supply.	3	1.76	(J.-H. Jeoung & Dobbek, 2007)
<i>Ch</i> II	<i>E. coli</i>	Aerobic before IPTG induction Anaerobic expression in 10L Fermenter with N ₂ gas supply, About 1 day at 28 °C.	3.6	2.61	(T. Inoue et al., 2011)
<i>Dv</i>	<i>D. fructosovorans</i>	Fully anaerobic expression in 10L Fermenter with N ₂ gas supply.	ND	0.1-0.2	(Hadj-Saïd et al., 2015)
<i>Dv</i> ^{CooC}		5 days at 37 °C.	ND	0.3-0.6	
<i>Rr</i> from native <i>R. rubrum</i>		Fully anaerobic expression in 80L Fermenter light and gas (N ₂ and CO) supply.	7.5	0.3-3	(Bonam & Ludden, 1987)
<i>RecRr</i>	<i>E. coli</i>	Fully aerobic auto induced expression in standard Erlenmeyer, 3 and 21 hours respectively at 37 and 15 °C.	12-20	14-17	This work
<i>RecRr</i> ^{CooCTJ}				4-6	

Our expression system requires no specific precautions for *E. coli* growth, such as fermenter or gas supply. The *E. coli* cells yield is approximately 4-7 times higher than that reported for *Ch*CODH II, while the yield of pure enzyme (Rec*Rr*CODH) is approximately 28-170 and 7-10 times higher than *Dv*CODH and *Ch*CODH II preparations, respectively.

These high yields of Rec*Rr*CODH preparations allowed for several fine biochemical, spectroscopic and electrochemical characterizations presented above, in particular the EPR titrations, that is notoriously expensive in proteins. The latter, were performed at the EPR facilities of the CNRS in Marseille under the supervision of Pr. Bruno Guigliarelli. We also performed a spectroscopic full characterization of the enzymatic properties such as pH and temperature dependence of the CO oxidation activity in solution, the pH and the temperature stability of the Rec-*Rr*CODH and stability over time (91 % of remaining CO oxidation activity after at least 140 hours under anaerobic conditions at 21 °C).

- **Insight into [NiFe]-CODHs metallochaperones dependent maturation.**

The differences between Rec-*Rr*CODH and Rec-*Rr*CODH^{CTJ} in terms of specific activities in solution and MWCNT-immobilized, DTH-dependent redox activation in solution and Ni content strongly supports what was previously observed *in vivo* for the native enzymes (Kerby et al., 1997): the three metallo-chaperones CooC, CooT and CooJ are fundamental for the correct and full maturation of *Rr*CODH. However, further studies are needed to fully understand the maturation mechanism of Rec*Rr*CODH and compare it already described mechanisms for other CODH.

- **First determination of DET for *Rr*CODH.**

Before the DET for the CODH from *R. rubrum* has never been shown. As for the other [NiFe]-CODHs, an efficient DET was obtained by immobilizing the Rec-*Rr*CODH on a functionalized MWCNT electrode, as previously shown in the lab for other nickel enzymes such as the [NiFeSe]-Hydrogenase from *D. baculatum* (Gentil et al., 2018).

- **Integration of RecRrCODH^{CTJ} functionalized MWCNT^{ADA} in GDE.**

Finally, we were able to integrate the RecRrCODH functionalized MWCNT into a functional device. This first shows that a [NiFe]-CODH can catalyze the interconversion of CO₂/CO at the gas/liquid interface. Secondly, the potential of [NiFe]-CODHs as robust biocatalysts for CO₂RR was shown for the first time. This is because, unlike other previous electrochemical works on [NiFe]-CODHs, the GDE CODH-based electrode achieved electrochemical performances comparable to other catalysts for CO₂/CO interconversion (See 2.3, Table S1 Supporting Information).

Efficient Electrochemical CO₂/CO Interconversion by an Engineered Carbon Monoxide Dehydrogenase on a Gas-Diffusion Carbon Nanotube-Based Bioelectrode

Umberto Contaldo, Bruno Guigliarelli, Julien Perard, Clara Rinaldi, Alan Le Goff,* and Christine Cavazza*



Cite This: *ACS Catal.* 2021, 11, 5808–5817



Read Online

ACCESS |



Metrics & More

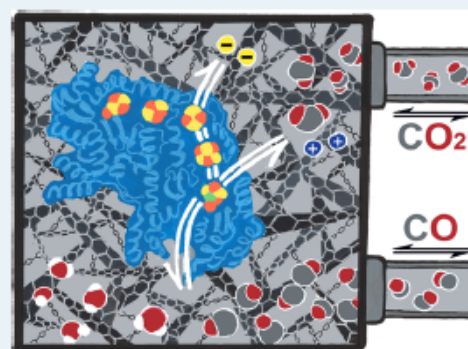


Article Recommendations



Supporting Information

ABSTRACT: Carbon monoxide dehydrogenase catalyzes the reversible oxidation of CO to CO₂. The monofunctional enzyme from *Rhodospirillum rubrum* (RrCODH) has been extensively characterized in the past, although its use and investigation by bioelectrochemistry have been limited. Here, we developed a heterologous system yielding a highly stable and active recombinant RrCODH in one-step purification, with CO oxidation activity reaching a maximum of 26 500 U·mg⁻¹, making RrCODH the most active CODH under ambient conditions described so far. Electron paramagnetic resonance was used to precisely characterize the recombinant RrCODH, demonstrating the integrity of the active site. Selective CO₂/CO interconversion with maximum turnover frequencies of 150 s⁻¹ for CO oxidation (1.5 mA cm⁻² at 250 mV overpotential) and 420 s⁻¹ for CO₂ reduction (4.2 mA cm⁻² at 180 mV overpotential) is catalyzed by the recombinant RrCODH immobilized on MWCNT electrodes modified with 1-pyrenebutyric acid adamantyl amide (MWCNT^{ADA}), either in a classic three-electrode cell or in specifically designed CO₂/CO-diffusing electrodes. This functional device is stable for hours with a turnover number of at least 800 000. The performances of recombinant RrCODH-modified MWCNT^{ADA} are close to the best metal-based and molecular-based catalysts. These results greatly increase the benchmark for bioelectrocatalysis of reversible CO₂ conversion.



KEYWORDS: nickel enzymes, carbon monoxide dehydrogenase, carbon nanotubes, bioelectrocatalysis, CO₂ RR, EPR

INTRODUCTION

Ni-dependent carbon monoxide dehydrogenase (CODH) plays a central role in carbon metabolism in anaerobic microorganisms by reversibly catalyzing the oxidation of CO to CO₂ for a variety of metabolic purposes. It is able to produce CO from CO₂ to synthesize diverse products (ethanol, acetate, methane, formate, etc.). In the reverse direction, the enzyme catalyzes the oxidation of CO into CO₂, with CO serving thus as a source of energy and fixed carbon. Enzyme performances result from billion years of evolution and selection, giving highly efficient catalysts with high substrate and function specificity in response to environmental demands. In the case of CODH, the enzyme evolved as the most proficient catalyst in terms of activity, selectivity, and ability to operate under mild conditions with CO and CO₂, known to be difficult to activate. X-ray structures of CODH from *Rhodospirillum rubrum* (RrCODH) and CODH-II from *Carboxydotherrmus hydrogenoformans* (ChCODH-II) both revealed a homodimer conformation with one active site per monomer, namely, C-cluster.^{1,2} Three additional FeS clusters per dimer (two B-clusters and one intermolecular D-cluster) are present, mediating the electron transfer between the active

site and the protein surface. The C-cluster, unique in biology, is constituted of a Fe₃S₄Ni cluster, linked to a mononuclear Fe site (Fe1). Four different oxidation states have been proposed for the C-cluster: a catalytically inactive and EPR-silent C_{ox} state; a one-electron reduced C_{red1} state, which binds CO; a two-electron-reduced EPR-silent C_{int} intermediate state; and a three-electron-reduced form, C_{red2}, which binds CO₂ with C_{red1} and C_{red2} being the two catalytically important oxidation states (Scheme 1).⁴

The reaction mechanism of CODH has been extensively studied in the past decades, and even if details are still discussed,⁵ this allowed to propose a common mechanistic model, postulating that CO binds to nickel and H₂O binds to Fe1. After deprotonation of water, a nucleophilic attack of OH⁻ on CO gives a Fe1-Ni-bridging COOH intermediate. A

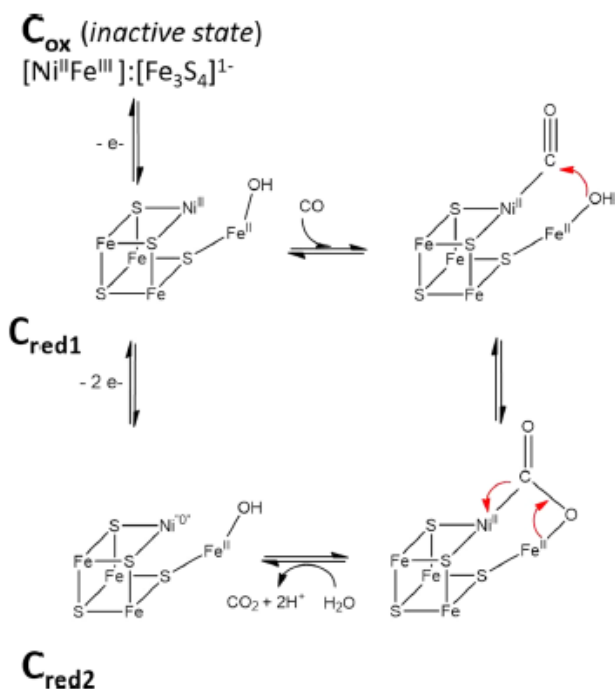
Received: December 11, 2020

Revised: April 16, 2021

Published: April 27, 2021



Scheme 1. Proposed Mechanism of Action of Ni-Dependent CODH



second deprotonation yields a FeI-Ni-bridging COO^- species, before the release of CO_2 and the reduction of the cluster by two electrons (Scheme 1). Electrons are subsequently transferred to an external electron acceptor via Fe_4S_4 clusters. CODHs are mostly inactive at redox potentials higher than -300 mV vs SHE.³ The $\text{C}_{\text{ox}}/\text{C}_{\text{red1}}$ redox couple and the $\text{C}_{\text{red1}}/\text{C}_{\text{red2}}$ redox couple potential were reported to be -200 and -530 mV, respectively, the latter matching well with the CO/CO_2 redox potential.

In the field of catalysis for sustainable chemistry, interest in CODH has dramatically increased in recent years to develop new methods for CO_2 sequestration. Direct bioelectrochemistry of CODH has been deeply investigated by protein film voltammetry by Armstrong et al.^{6–9} or Léger et al.,^{10–12} showing the ability of this enzyme to behave as reversible electrocatalysts and catalyze selective CO oxidation and CO_2 reduction with minimal overpotential. As in other types of metalloenzymes, this ability is achieved owing to low reorganization energies through multiple electron transfer, proton-coupled electron transfer, and close values for redox potentials of the active site and the CO_2/CO couple. Several attempts have also been made to integrate CODH in functional devices. When immobilized at silver-nanoparticle-coated TiO_2 surfaces, CODH achieves fast photocatalytic CO_2 -to-CO reduction.¹³ Its mixing with graphite pellets along with the hydrogenase Hyd-2 from *Escherichia coli* allowed the development of an enzymatic water-gas shift reaction (WGSR).¹⁴ However, the achievement of stable and high electrocatalytic activity toward CO_2/CO interconversion has never been optimized in these systems, both in terms of CODH activity and interfacing with nanomaterials.

Despite the undeniable performances and specificities of CODH, several challenges still need to be addressed to make their exploitation practical. Firstly, microorganisms that naturally produce this complex enzyme often require specific

growth conditions (anaerobiosis, specific substrates and media, toxic gases, etc.).^{15,16} Secondly, given its complexity, the biosynthesis and insertion of the multimetallic active sites into the target enzyme is extremely challenging. It requires the identification of all of the protein partners involved in the intracellular metal trafficking and maturation machinery, as well as the understanding of the synchronization and the sequence of the different events leading to the biosynthesis of the active enzyme.¹⁷ Thirdly, while in nature, enzymes are spatially and temporally controlled by intracellular conditions and physiological partners, once purified and isolated, they become more sensitive to their environment (pH, temperature, oxygen, solvents, etc.). To consider the relevance of complex redox metalloenzymes such as CODH for future biotechnological applications, the development of easy methods for their large-scale production is necessary. The possibility to produce CODH in easy-to-grow bacteria facilitates also mechanistic studies at the molecular level.

In the last decades, *C. hydrogenoformans* has represented a model organism for the study of monofunctional CODH. This thermophilic bacterium, able to use CO as a sole energy and carbon source, possesses four CODH (I to IV) with distinct functions.¹⁸ Among them, fully active recombinant monofunctional ChCODH-II and -IV have been successfully purified from anaerobic *E. coli* cultures,^{10,19} and thoroughly structurally, electrochemically, and spectroscopically characterized. However, in terms of performances, the catalytic efficiencies of these thermophilic enzymes are optimal at temperatures above 70°C . On the other hand, CODH from the mesophile bacterium *R. rubrum* has been largely characterized since the late 1980s,^{20–23} although studies have been limited in the last decade. *R. rubrum* possesses a single monofunctional CODH (homologue to ChCODH-I), involved in the WGSR ($\text{CO} + \text{H}_2\text{O} \rightarrow \text{CO}_2 + \text{H}_2$), enabling the bacterium to use CO as the sole energy source. The reaction is catalyzed by a multiprotein complex involving CODH, converting CO into CO_2 , a ferredoxin CooF transferring the electrons produced to an energy-conserving-[NiFe]-hydrogenase (ECH).²⁴ In *R. rubrum*, the structural gene of CODH, namely, *cooS*, belongs to the ωoFSCTJ operon, where *cooF* encodes the ferredoxin CooF,²⁵ ωoC , a Ni-dependent ATPase,²⁶ and *cooT* and *cooJ*, two nickel-binding proteins.^{27–30} *In vivo*, the three chaperones CooC, CooT, and CooJ are required for the correct insertion of nickel into the active site, shown to be a key step in the enzyme activation.^{31,32}

Wiring of metalloenzymes at electrodes requires rational strategies aimed at minimizing electrode-active site distances as well as maximizing catalyst loading. In this respect, carbon nanotubes (CNTs) possess a set of abilities, which make them an ideal material for such a purpose: thin nanowire morphology, biocompatibility, high conductivity, high electroactive surface, and ease of functionalization.^{33–36} Furthermore, these biofunctionalized nanomaterials can be further integrated in operational devices such as gas-diffusion electrodes of fuel cells.^{34,36,37} Specific functionalization of CNTs has taken advantage of noncovalent interactions such as enzyme dipolar moment or hydrophobic/hydrophilic interactions to enhance the immobilization of enzymes such as hydrogenases or laccases and influence their orientation at CNTs.³⁵

In the present study, we developed a novel heterologous system allowing the easy production of highly active recombinant RrCODH (Rec-RrCODH) in good yields, which was biochemically and spectroscopically characterized

in detail. Multiwalled CNT (MWCNT) electrodes were modified with 1-pyrenebutyric acid adamantyl amide to optimize Rec-RrCODH direct electrochemistry as well as enzyme loading at electrodes for CO/CO₂ interconversion, either in a classic three-electrode cell or in specifically designed CO₂/CO-diffusing electrodes.

RESULTS AND DISCUSSION

Metallated RrCODH Is Produced in *E. coli* under Aerobic Conditions. The structural gene of RrCODH (*RrcooS*) from *Rhodospirillum rubrum* was expressed in *E. coli*. Two forms of the recombinant enzyme were produced by transforming *E. coli* with either *cooS* alone or with the three *cooC*, *cooT*, and *cooJ* genes, yielding Rec-RrCODH and Rec-RrCODH^{CTJ}, respectively. One-step purification led to pure and homogeneous enzymes as shown by sodium dodecyl sulfate polyacrylamide gel electrophoresis (SDS-PAGE) (Figure S1A). The two enzymes were routinely purified with a yield of 14–17 mg of Rec-RrCODH and 4–6 mg of Rec-RrCODH^{CTJ} per liter of culture. SEC-MALLS experiments showed the homogeneity and the homodimeric organization (Figure S1B).

In addition, both CODH displayed typical brown coloration due to the presence of Fe₄S₄ clusters. This was also supported by the UV–visible absorption spectra of the oxidized enzymes. The typical broad shoulder from 350 to 480 nm (Figure S1C) and a purity coefficient (A420/A280) of 0.37–0.38 are comparable to those of wild-type RrCODH.³⁸ Metal content determination on Rec-RrCODH and Rec-RrCODH^{CTJ} revealed that iron content is similar in both enzymes with approximately 9–10 atoms of iron per monomer, in agreement with the expected 10 Fe atoms per monomer found in the wild-type enzyme. As previously described for CODH I, II, and IV from *C. hydrogenoformans*,^{39,19} the ISC machinery from *E. coli* appeared then to be able to build the B- and D-clusters and deliver the FeS moiety of the C-cluster in RrCODH. In *R. rubrum*, the ISC machinery is not present but is likely replaced by the SUF machinery,⁴⁰ suggesting that ISC and SUF machineries are interchangeable for FeS insertion into the C-cluster.

The nickel content was about 0.7 ± 0.1 and 0.8 ± 0.1 of Ni(II) per monomer for Rec-RrCODH and Rec-RrCODH^{CTJ}, respectively, corresponding to about 70 and 80% of the expected content in a fully metallated enzyme. Consequently, supplementing 500 μM Ni(II) salt to the growth medium seems to be sufficient to allow partial nickel insertion into RrCODH *in cellulo*, without the requirement of the three chaperone CooCTJ. This is in agreement with previous studies showing that a Ni excess can compensate for the absence of the chaperones. More surprisingly, aerated culture of *E. coli* in the absence of reducing agents except L-cysteine and Fe(II) salts would allow Ni insertion into RrCODH. This was not expected since the redox potential of *E. coli* cytoplasm is estimated to be about −0.22 V, while C-cluster biosynthesis and especially Ni insertion mechanism have been shown to require a reducing step at a low redox potential (below −0.3 V). Besides, the production of all active recombinant CODH produced in *E. coli* described so far requires anaerobic conditions in the presence of highly reducing agents, such as sodium sulfide.

CO Oxidation Activity of Rec-RrCODH and Rec-RrCODH^{CTJ} in Solution. To determine their specific activity, the enzymes were first diluted in 50 mM Tris-HCl, pH 8.5, and

5 mM DTT with dithionite (DTH) at 21 °C prior to measurement. Interestingly, Rec-RrCODH activity is strictly dependent on DTH concentration, with the enzyme requiring a reducing preactivation step by adding at least 15 mM DTH to reach a maximum specific activity of 2500 U·mg^{−1} (Figure S2). In contrast, Rec-RrCODH^{CTJ} did not require any reducing preactivation and reached a specific activity of 10 508 U·mg^{−1} in the presence of 1 mM DTH (Table 1). Moreover, the latter

Table 1. Specific Activities of Monofunctional CODH

	CO oxidation		
	1 U: 1 μmol of CO oxidized·min ^{−1}		
	pH	T (°C)	U·mg ^{−1}
native RrCODH ⁴¹	7.5	25	7700
rec-RrCODH ^{CTJ}	7.5	25	5685
	8.5	25	10 508
	9.5	50	26 016
native ChCODH-I ⁴²	8.0	20	1300
		70	15 756
		95	37 949
recombinant ChCODH-I (+Ni(II) & CooC) ³⁹	8.0	70	8060
native ChCODH-II ⁴²	8.0	20	1000
		70	14 200
		105	40 666
recombinant ChCODH-II (+Ni(II)) ³⁹	8.0	70	12 229
recombinant TspCODH-1 (+Ni(II) & CooC) ⁴³	8.0	37	62
recombinant TspCODH-2 (+Ni(II) & CooC) ⁴³	8.0	37	262
recombinant DrCODH (+Ni(II) & CooC) ⁴⁴	10.0	37	1660

enzyme remains active for several days at room temperature without the requirement of any additional reactivation (91% of maximum specific activity after 140 h). While the Fe and Ni contents are comparable in both enzymes, the co-production of Rec-RrCODH with the three CooCTJ proteins seems to play a significant role in the stability and activity of the produced enzyme, although their role at the molecular level has been not yet elucidated. This is in agreement with previous studies on the CODH from *Desulfovibrio vulgaris*, highlighting the plasticity of the C-cluster and the identification of different reduced active or oxidized inactive C-cluster states.⁴⁵ Moreover, with a specific activity of 5685 U·mg^{−1} at pH 7.5 (corresponding to 75% of the native enzyme one purified from *R. rubrum*⁴¹), Rec-RrCODH^{CTJ} appears roughly as active as the native enzyme (Table 1), considering a Ni content of about 0.8 Ni atom per monomer. Therefore, we consider that the expression system developed in this study allows the production of a fully active and stable recombinant RrCODH.

pH and Temperature Dependence of Rec-RrCODH^{CTJ} CO Oxidation in Solution. Several monofunctional CODH have been thoroughly characterized over the last decades. Although CODH from the thermophile *C. hydrogenoformans* have often been described as the most active enzymes, there are many discrepancies about optimum temperature and pH of CODH activity in the literature (Table 1). We therefore decided to perform a pH and temperature dependence study of CO oxidation activity displayed by Rec-RrCODH^{CTJ}. First, the effect of pH and temperature on the kinetics was evaluated (Figure 1A,B). Second, the enzyme stability according to pH and temperature was measured (Figure 1C,D). We determined

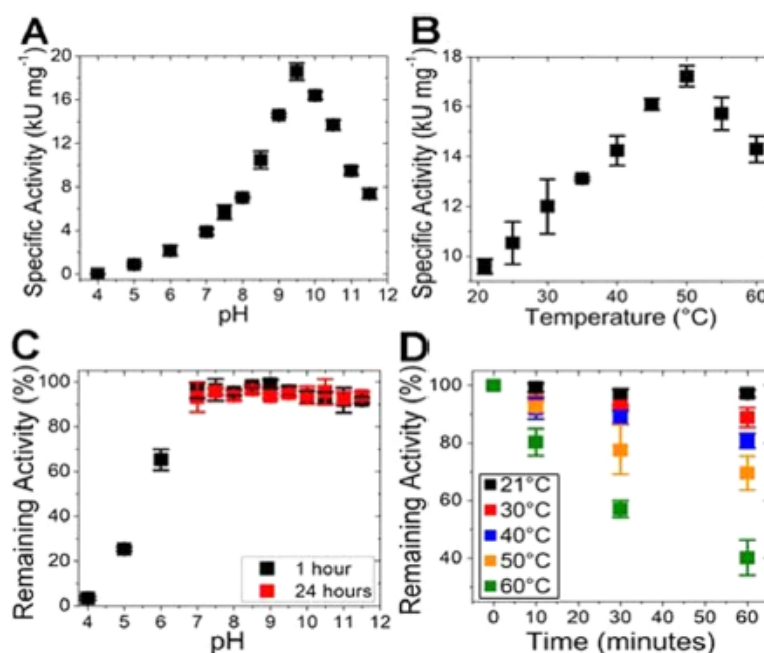


Figure 1. CO oxidation activity of Rec-RrCODH^{CTJ} in solution (4 nM dimer) A: pH titration from 4.0 to 11.5, with a maximum activity of 18 567 U·mg⁻¹ reached at pH 9.5 and 21 °C. B: Temperature dependence from 21 to 60 °C, with a maximum activity of 17 221 U·mg⁻¹ reached at 50 °C, pH 8.5. C: Rec-RrCODH^{CTJ} stability according to pH. D: Rec-RrCODH^{CTJ} stability according to temperature.

optimum pH and temperature of 9.5 and 50 °C, respectively. Under these conditions, Rec-RrCODH^{CTJ} reaches a CO oxidation activity of 26 016 U·mg⁻¹.

By comparison with other CODH, we observed that CO oxidation activities of Rec-RrCODH^{CTJ}, wild-type *Ch*CODH-I, and wild-type or recombinant *Ch*CODH-II are comparable at their optimum temperature (50 and 70 °C, respectively) (Table 1). In contrast, recombinant CODH from *Desulfovibrio vulgaris* (*Dv*CODH) and recombinant CODH from *Thermococcus Sp.* (*Tsp*CODH-1 and -2) are much less active (Table 1), suggesting that under these conditions, the enzyme may not be fully and correctly matured. The low activity of recombinant *Tsp*CODH produced in *Desulfovibrio* (Table 1) strongly suggests that aside from *CooC*, other missing partners are likely required for CODH maturation. In the latter case, we observed that two nonannotated genes present downstream *CooC2* actually encodes two *CooT* proteins. Their presence in a common cluster gene with *cooS* and *cooC* strongly suggests their implication in the C-cluster biosynthesis. Another possibility would be that some CODH are not directly involved in CO/CO₂ interconversion catalysis but would have other functions, as illustrated by *Ch*CODH-IV, a CO scavenger in defense against oxidative stress.¹⁰ The different specific activities of recombinant *Ch*CODH-I and *Ch*CODH-II when produced in *E. coli* in the presence or absence of *CooC* and/or Ni salts (Table 1) also suggest fundamental differences in their maturation pathways and nickel-dependent enzyme activation. All of these studies point out that the mechanism of nickel insertion into the C-cluster appears to be not straightforward and not common for all CODH.

EPR Characterization of Rec-RrCODH^{CTJ}. To further examine and characterize the metal cluster integrity of Rec-RrCODH^{CTJ}, redox titration of the recombinant enzyme was performed and monitored by EPR spectroscopy at a low temperature (10 K). After buffer exchange, the enzyme

solution was prepared anaerobically in 100 mM MOPS buffer pH 8.0 and titrated in a glovebox with DTH.

Upon reduction of Rec-RrCODH^{CTJ}, no significant signal was observed above -250 mV. Below this value, a rhombic signal develops at $g = 2.029, 1.886, \text{ and } 1.710$ (Figure 2A-a). This signal is characteristic of the C_{red1} state of the C-cluster^{46,47} and reaches a maximum amplitude at about -450 mV (Figure S3). Concomitantly, a second rhombic signal appears below -350 mV with g values of 2.041, 1.931, and 1.882. This signal is typical of a reduced $[4\text{Fe-4S}]^{1+}$ center and increases progressively upon reduction with a significant broadening below -500 mV and broad lateral bands around $g = 2.09$ (Figure 2A-c,d) likely due to intercluster magnetic couplings.^{48,49} Interestingly, below -500 mV, the C_{red1} signal decreases and additional features appear at $g = 1.757$ and 1.970, which reveals the redox conversion of the C_{red1} state into the C_{red2} one ($g = 1.970, 1.887, 1.757$), a conversion reported as a two-electron redox process.⁴⁷ All of these signals exhibit fast relaxation properties typical of CODH metal centers, the FeS signal being not saturated at 10 K with 1 mW microwave power, while C_{red1} and C_{red2} are not saturated up to 10 mW. Spin intensity measurements performed at 10 K by double integration of the EPR spectra recorded under nonsaturating conditions indicate that C_{red1} signal corresponds to 0.6 spin/dimer (0.3 spin/monomer) at its maximum intensity (around -450 mV) and that the EPR spectrum of the most reduced sample represents 3.0 spins/dimer (1.5 spin/monomer). Although the C_{red2} signal overlaps FeS and C_{red1} signals, it has been possible to estimate its spin intensity by performing spectral differences between samples taken at different potentials. In the more reduced state of the enzyme, it corresponds to 0.34 spin/dimer (0.17 spin/monomer), suggesting that, within experimental error, all of the C_{red1} state is converted into C_{red2} during redox titration. Moreover, by weighing the spin intensity of C_{red1} and C_{red2} signals by the

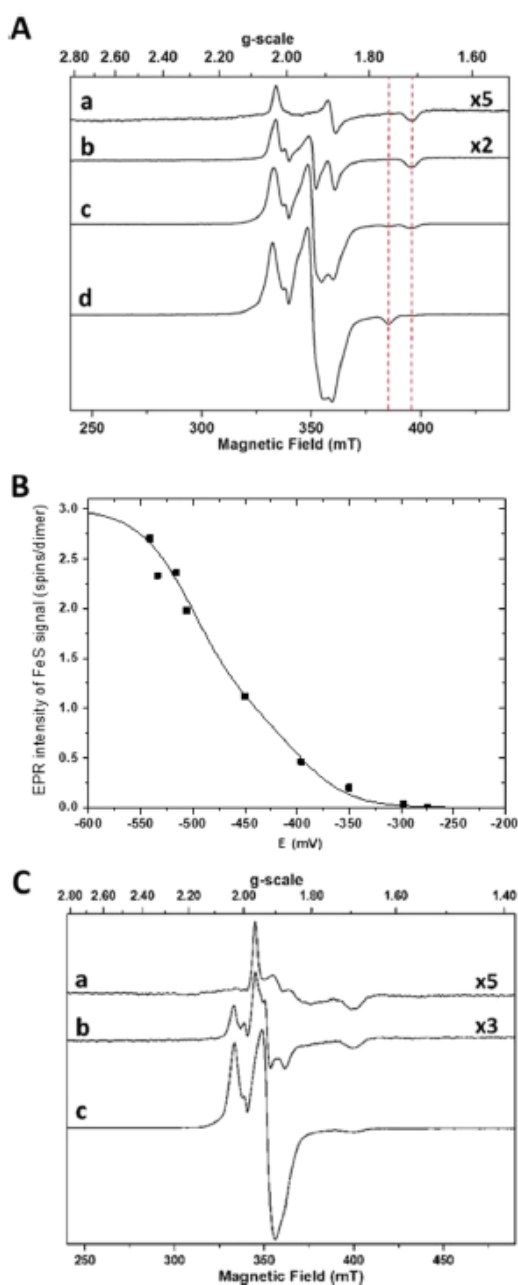


Figure 2. EPR titration of Rec-RrCODH^{CTJ}. **A:** EPR spectra of Rec-RrCODH^{CTJ} poised at different potentials: (a) -275 mV, (b) -396 mV, (c) -506 mV, (d) -541 mV. Experimental conditions: temperature, 10 K; microwave power, 10 mW at 9480 GHz; modulation amplitude, 1 mT at 100 kHz. Red vertical dashed lines indicate the position of the negative peaks of the C_{red1} and C_{red2} signals at $g = 1.710$ and 1.757 , respectively. **B:** Redox behavior of the FeS signal spin intensity. For each sample, the spin intensity of the FeS signal (black squares) was obtained by subtracting the C_{red1} and C_{red2} signal contributions (see text). The curve is the sum of two Nernst processes centered at $E_1^\circ = -400$ mV and $E_2^\circ = -500$ mV weighed by spin intensity one and two, respectively. EPR conditions are as in (A) except microwave power of 1 mW. **C:** EPR titration of Rec-RrCODH^{CTJ} in the presence of cyanide: (a) -297 mV, (b) -416 mV, (c) -592 mV.

amplitude of the lines at $g = 1.71$ and 1.757 , respectively, their contributions to the total spin intensity of each sample could be subtracted to deduce that of the FeS signal alone.

The redox behavior of the FeS signal intensity so obtained is well fitted by the superimposition of two Nernst curves centered at $E_1^\circ = -400$ mV (± 10 mV) and $E_2^\circ = -500$ mV (± 10 mV), corresponding to one and two spins/dimer (Figure 2B). This result is in good agreement with the FeS cluster content of RrCODH dimer, which is composed of one intermonomer bridging D-cluster and two B-clusters. All of these results clearly indicate that the metal cofactor content and properties of the Rec-RrCODH^{CTJ} enzyme are similar to that of the native enzyme.

Cyanide is a well-known inhibitor of CODH, which binds directly on the catalytic C-cluster of the enzyme.⁴ To address the ability of this inhibitor to interact with C-clusters of the Rec-RrCODH^{CTJ} enzyme, EPR titration of the enzyme was also performed anaerobically in the presence of an excess of NaCN (~ 100 equiv). Below -250 mV, a complex EPR signal can be observed with a sharp peak at $g = 1.969$ and major features at $g = 1.898$, 1.848 , and 1.70 . Additionally, a broad line is also detected at a high field around $g = 1.57$ (Figure 2C-a). This signal is characterized by fast relaxation properties, being not saturated at 10 K and 10 mW. This signal is reminiscent of other EPR signals obtained upon treatment of other CODH with cyanide.⁵⁰ Upon more pronounced reduction, its amplitude remains approximately unchanged, while the signatures of FeS center develop at $g = 2.039$, 1.932 , and 1.88 (Figure 2C-b).

At a very low potential, the FeS signal is similar to that detected in the absence of cyanide (Figure 2C-c). In contrast to the titration without cyanide, no C_{red1} or C_{red2} signal was observed in the whole potential range investigated, which confirms that Rec-RrCODH^{CTJ} is fully inhibited by cyanide as the native enzyme.

In view of its characteristics, Rec-RrCODH^{CTJ} appears in our opinion as the best compromise for future studies and applications, considering on the one hand its easy production and purification and on the other hand its high activity under ambient conditions (physiological pH and room temperature) and its stability (several months at 4°C). These encouraging results urged us to investigate its electrocatalytic properties toward both CO oxidation and CO₂ reduction in a specifically designed gas-diffusion enzymatic system.

Direct Electrochemistry of Rec-RrCODH. We have recently investigated the use of direct electron transfer (DET) promoters for metalloenzymes to favor their immobilization and orientation at the surface of MWCNT electrode. The adamantane moiety has proven its ability to strongly interact with well-defined hydrophobic patches at the surface of several metalloenzymes such as laccase⁵¹ and NiFeSe hydrogenases.³⁶ In this respect, Rec-RrCODH and Rec-RrCODH^{CTJ} were immobilized at MWCNT electrodes modified with 1-pyrenebutyric acid adamantyl amide. The electrochemistries of pristine MWCNT and adamantane-modified MWCNT (MWCNT^{ADA}) were compared under Ar, CO, or CO₂ after incubation of the electrode in an enzyme solution at $38\ \mu\text{M}$ monomer concentration for 4 h.

Figure 3 displays CV performed under argon at pH 8.5 for MWCNT and MWCNT^{ADA} electrodes. A reversible redox system was observed at $E_{1/2} = -0.595$ V vs SHE (pH 8.5) for both types of electrodes, corresponding to the $C_{\text{red1}}/C_{\text{red2}}$ redox system. A potential/pH dependence was observed

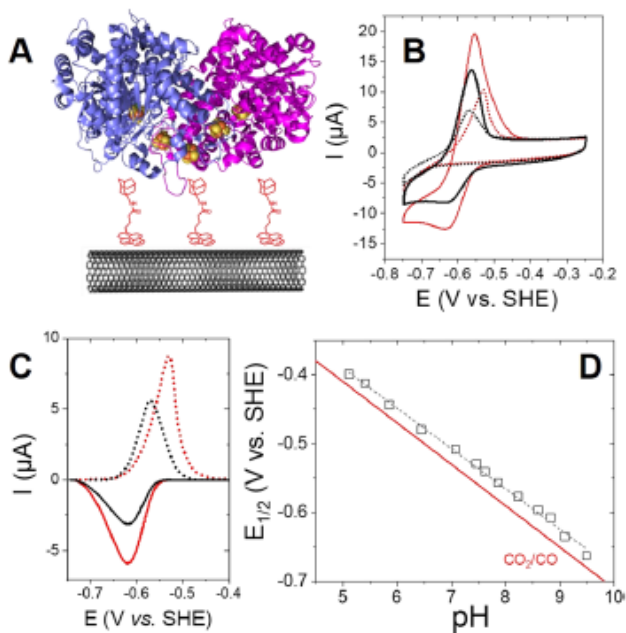


Figure 3. A: Schematic representation of CODH-modified MWCNT^{ADA}. B: CVs of the Rec-RrCODH^{CTJ}-functionalized (black) pristine MWCNT and (red) MWCNT^{ADA} electrodes under Ar at pH 8.5 before (straight line) and after (dotted line) addition of 2 mM NaCN (50 mM Tris-HCl, pH 8.5, $\nu = 5 \text{ mV s}^{-1}$). C: Background-subtracted oxidation peak (in the presence of NaCN) and reduction peak for Rec-RrCODH^{CTJ}-functionalized (black) pristine MWCNT and (red) MWCNT^{ADA} electrodes under Ar. D: potential/pH dependence of $E_{1/2}$ for the Rec-RrCODH^{CTJ}-functionalized MWCNT electrodes accompanied with linear fit (gray dashed line) and standard CO/CO₂ redox couple pH dependence (red line).

between pH 5.0 and 9.5. A 58.4 mV, the slope per pH unit is consistent with a proton/electron ratio of 1. Considering the fact that the observed redox potential is consistent with the redox potential of the $C_{\text{red1}}/C_{\text{red2}}$ redox system (see above), this pH dependence likely accounts for a two-proton/two-electron system. This is further confirmed by the potential width of $\Delta E_{p1/2} = 55 \text{ mV}$ at half-height, close to the theoretical value of $90.6/2 = 45.3 \text{ mV}$ accounting for a surface-confined bielectronic system.⁵²

Compared to the reduction peak current, a higher oxidation peak current indicates the presence of residual catalytic activity from the reduction of dissolved CO₂ traces and the oxidation of as-formed CO at this highly porous electrodes. CVs were performed in the presence of 2 mM NaCN to inhibit the catalytic activity corresponding to CO oxidation by forming the $C_{\text{red1}}\text{-CN}$ adduct. As expected from EPR studies (see above), the oxidation peak current decreases, leaving the response of the electrochemically irreversible $C_{\text{red1}}\text{-CN}$ inactive species. On the contrary, catalytic CO₂ reduction does not contribute significantly to the cathodic peak, as confirmed by CV performed in the presence of 5 mM KOCN (Figure S4). Having confirmed the nonturnover redox signal of the immobilized Rec-RrCODH^{CTJ}, a surface coverage of $\Gamma_{\text{CODH}} = 35 (\pm 2)$ and $52 (\pm 2) \text{ pmol cm}^{-2}$ was estimated for MWCNT and MWCNT^{ADA} electrodes respectively, calculated from the integration of the charge under both the reduction peak and the oxidation peak. For comparison, NiFeSe hydrogenase from *Desulfomicrobium baculatum* has also been immobilized on similar MWCNT electrodes with maximum

surface coverages in the order of 10 pmol cm^{-2} .³⁶ Considering the fact that the amount of MWCNT is approximately $40 \mu\text{g}$ per electrode, this corresponds to mass loadings of 0.17 and $0.25 \mu\text{g}$ of enzyme per mg of MWCNT for MWCNT and MWCNT^{ADA} electrodes, respectively. As far as we know, no reversible system has ever been observed on electrodes for CODH, further underlining the excellent direct wiring of Rec-RrCODH^{CTJ} on both MWCNT and MWCNT^{ADA} electrodes.

Rec-RrCODH and Rec-RrCODH^{CTJ} were then investigated under CO and CO₂. Figure 4 displays CV performed in

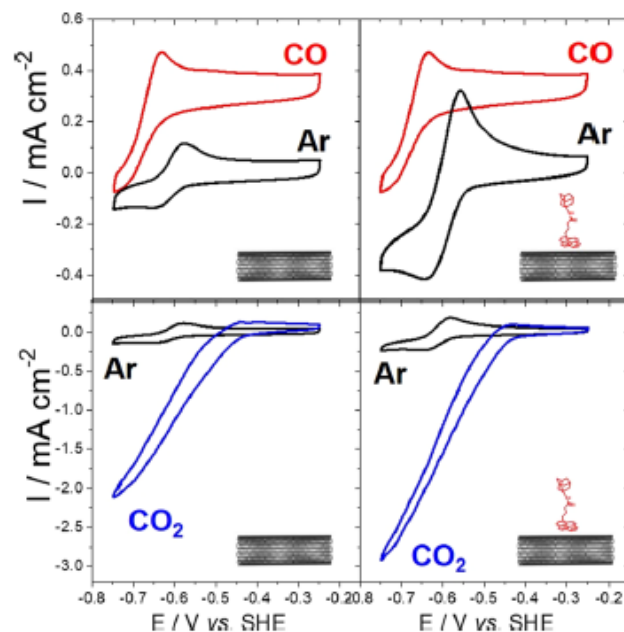


Figure 4. CVs of the Rec-RrCODH^{CTJ}-functionalized (black) pristine MWCNT and (red) MWCNT^{ADA} electrodes under Ar, CO, and CO₂ (50 mM Tris-HCl, pH 8.5, $\nu = 5 \text{ mV s}^{-1}$).

saturated solutions of CO and CO₂ under quiescent conditions for MWCNT and MWCNT^{ADA} electrodes. Control experiments were also performed on nonfunctionalized MWCNTs (Figure S5). Neither redox activity nor electrocatalytic activity toward both CO₂ reduction and CO oxidation were observed.

Under CO, an irreversible oxidation peak with a maximum current density of 0.35 mA cm^{-2} at -0.3 V vs SHE was observed for both MWCNT and MWCNT^{ADA}. Two main factors are responsible for the fact that electrocatalytic waveshapes exhibit a residual slope instead of reaching a plateau: the diffusion limitations of gas at these highly porous nanostructured electrodes and the presence of a statistical distribution of enzyme orientation immobilized at the surface of the electrode.^{37,53,54} It is important to note that lower current under CO atmosphere is mostly due to the low solubility of CO at atmospheric pressure. Furthermore, substrate diffusion limitations are commonly observed at these highly porous MWCNT electrodes. Nonetheless, high electrocatalytic current densities under CO₂ of 2.1 and 2.9 mA cm^{-2} at -0.75 V vs SHE were measured for MWCNT and MWCNT^{ADA} electrodes, respectively.

Electrocatalytic activities were tested for both Rec-RrCODH and Rec-RrCODH^{CTJ}. Higher maximum electrocatalytic currents were observed for Rec-RrCODH^{CTJ}, compared to the Rec-RrCODH, which shows 1.2 and 2.1 mA cm^{-2} toward

CO₂ reduction for MWCNT and MWCNT^{ADA} electrodes, respectively (Figure S6). This likely accounts for the higher enzymatic activity and stability of Rec-RrCODH^{CTJ}. As expected from surface coverage measurements, the MWCNT^{ADA} electrode exhibits the highest electrocatalytic activity for CO₂ reduction, due to the high amount of CODH immobilized on these modified MWCNTs. A study of RrCODH surface hydrophobicity (Figure S7) indicates that the D-cluster is surrounded by two well-defined hydrophobic patches, which may contribute to the enzyme affinity for adamantane, previously shown to interact with proteins via hydrophobic interactions.³⁶ In this regard, adamantane would play a significant role in the enzyme immobilization and orientation, explaining the improvement of the Rec-RrCODH^{CTJ}-functionalized MWCNT^{ADA} activity.

pH dependence measurements were performed and showed that the immobilized enzyme follows the trend of the enzyme in solution, with the best performances observed above pH 8.5, reaching maximum current densities of 3.15 mA cm⁻² at pH 9.5 (Figure S8). Chronoamperometric measurements were performed to estimate the operating stability and the turnover number (TON) of the immobilized Rec-RrCODH^{CTJ}. TON was measured by the integration of the total charge passed during the chronoamperometry taking into account the estimated enzyme surface coverage. A TON of 800 000 was measured by a 1 h chronoamperometry (Figure S9) performed at a fixed potential of -0.75 V vs SHE (overpotential of 0.13 V). This corresponds to an average TOF of 224 s⁻¹ over 1 h. TOF value was calculated using the equation $TOF = I_{MAX}/(2 \times F \times \Gamma_{CODH})$. A partial deactivation after 1 h (35%) likely arises from the leaking of loosely adsorbed CODH or the presence of O₂ traces in a CO₂ gas bottle (10 ppm).

CO₂/CO Interconversions in Gas-Diffusion Bioelectrodes. To optimize the electrocatalytic performances of these bioelectrodes and to test their ability to operate in a functional device, a specific gas-diffusion electrode was designed, allowing the constant flow of CO or CO₂ at CODH-modified gas-diffusion MWCNT electrode. This type of electrode allows the (bio)catalyst to operate at a three-phase boundary, circumventing gas substrate solubility and diffusion issues. This is especially challenging for enzymes, which requires the presence of a surrounding buffer solution with optimal pH.^{34,36,37,55} An MWCNT film was deposited at the surface of a microporous gas-diffusion layer and subsequently modified with 1-pyrenebutyric acid adamantyl amide and Rec-RrCODH^{CTJ} (Figure 5A,B). A graphite plate with a serpentine flow design

ensures a homogeneous gas flow at the back of the bioelectrode where the enzyme is in contact with a degassed 50 mM Tris-HCl pH 8.5. Laser scanning microscopy (LSM) measurements were performed showing a homogeneous MWCNT film with an average thickness of 3 μm on the microporous layer (Figure S10A,B). Scanning electron microscopy of the surface of the electrode underlines the high porosity of these functionalized bioelectrodes (Figure S10C). CVs were performed with a constant flow of CO, CO₂, or Ar (Figure 5C). Owing to the gas-diffusion electrode, the electrocatalytic current density for CO oxidation reaches 1.5 mA at -0.38 V, while the maximum current density for CO₂ reaches 4.2 mA cm⁻² at -0.8 V. This corresponds to TOF values of 420 s⁻¹ for CO₂ reduction at 180 mV overpotential and 150 s⁻¹ for CO oxidation at 250 mV overpotential. Comparing gas-diffusion electrode performances with previous experiments with solubilized gas, an increase in terms of current density is observed for both CO oxidation and CO₂ reduction. While CO oxidation is mostly limited by low CO solubility in solution, both catalyst loading and substrate diffusion are the limiting factors at these porous 3D MWCNT films for gas-diffusion electrode experiments.

The products of the electrocatalysis were analyzed by gas chromatography. As expected, the immobilized enzyme produces 100% CO from CO₂ reduction and 100% CO₂ from CO oxidation, either at MWCNT-modified GC electrodes or at gas-diffusion MWCNT electrodes (Figure S11).

For comparison, the state-of-the-art performances for molecular-based catalysts toward CO₂-to-CO conversion have been reported for CNT-modified azamacrocyclic cobalt complexes.^{56–58} A cobalt quaterpyridine hybrid catalyst reaches 19.9 mA cm⁻² at an overpotential of 440 mV with a catalyst loading of 8.5 nmol cm⁻², a TOF of 12 s⁻¹, and a maximum estimated TON of 89 095.

This work represents the first example of a CODH-based electrode working at a gas-diffusion electrode. For comparison, the only other CODH studied at the nanostructured electrode toward the electrocatalytic CO₂ reduction is ChCODH-I, which was immobilized at nanostructured silver-nanocluster-modified TiO₂ electrodes and achieved a maximum current density of 0.26 mA cm⁻².¹² Other types of metal-based nanomaterials such as CNT-supported copper phthalocyanines⁵⁹ reach 6.9 mA cm⁻² at 300 mV overpotential, while, in the case of mesoporous gold-based electrodes,⁶⁰ 22 mA cm⁻² can be reached at 240 mV overpotential. These results show that Rec-RrCODH^{CTJ}-modified MWCNT^{ADA} electrodes are close to the best metal-based and molecular-based catalysts in terms of current densities. In addition, Rec-RrCODH-modified MWCNT^{ADA} outperforms state-of-the-art catalysts for CO₂ to CO reduction in terms of overpotential and exhibits higher TON values compared to molecular catalysts for CO₂ reduction (Table S1).

CONCLUSIONS

The design of efficient electrocatalysts holds the promise to offer new attractive strategies in sustainable energy. In this field, anaerobic gas-processing metalloenzymes suffer from their complexity and stability. However, bioelectrocatalysis affords several advantages such as highly selective catalytic efficiencies under mild conditions (pH, temperature, aqueous solvent, etc.) at low overpotentials and using non-noble metals. In this study, the easy production of a stable and fully active recombinant RrCODH with a CO oxidation activity reaching

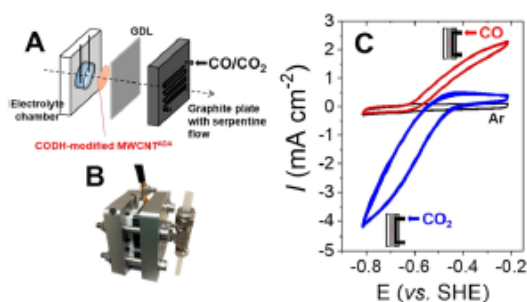


Figure 5. A: Schematic representation and B: photograph of the gas-diffusion electrochemical cell. C: CVs (three cycles) of the Rec-RrCODH^{CTJ}-functionalized MWCNT^{ADA} gas-diffusion bioelectrodes under Ar, CO, and CO₂ (50 mM Tris-HCl, pH 8.5, $\nu = 5$ mV s⁻¹).

up to 26500 U·mg⁻¹ in solution makes it an interesting candidate for future applications. The electrocatalytic activity of Rec-RrCODH^{CTJ}-immobilized MWCNT^{ADA} electrodes for CO/CO₂ interconversion, either in a classic three-electrode cell or in specifically designed CO₂/CO-diffusing electrodes surpasses those reported earlier, when graphite or TiO₂ was used. Remarkably, the high performances of Rec-RrCODH^{CTJ}-modified MWCNT^{ADA} are fully demonstrated, with stability over several hours and a TON of at least 800 000. Its competitiveness with molecular-based catalysts used in electrochemical CO₂ reduction paves the way for the development of new functional enzymatic devices. Furthermore, taking into account the high sensitivity of these enzymes toward oxygen, oxygen deactivation has to be tackled, through diverse approaches such as specific electrode engineering,^{36,55,61} screening of CODH biodiversity, site-directed mutagenesis,¹² or enzyme immobilization. Furthermore, the ability of Rec-RrCODH^{CTJ} to, reversibly, oxidize CO at low overpotentials with similar high electrocatalytic activity under mild conditions makes this type of biofunctionalized nanostructured electrode a potent catalyst for applications such as WGS.

■ ASSOCIATED CONTENT

Supporting Information

The Supporting Information is available free of charge at <https://pubs.acs.org/doi/10.1021/acscatal.0c05437>.

Methods: cloning, enzyme production, purification, and characterization, EPR, electrochemistry, and preparation and functionalization of MWCNT (PDF)

■ AUTHOR INFORMATION

Corresponding Authors

Alan Le Goff – University Grenoble Alpes, DCM UMR 5250, BEA, F-38000 Grenoble, France; orcid.org/0000-0002-6765-5859; Email: alan.le-goff@univ-grenoble-alpes.fr

Christine Cavazza – Univ. Grenoble Alpes, CEA, CNRS, IRIG, CBM, F-38000 Grenoble, France; orcid.org/0000-0002-3657-1302; Email: christine.cavazza@cea.fr

Authors

Umberto Contaldo – Univ. Grenoble Alpes, CEA, CNRS, IRIG, CBM, F-38000 Grenoble, France; University Grenoble Alpes, DCM UMR 5250, BEA, F-38000 Grenoble, France

Bruno Guigliarelli – Aix Marseille Univ., CNRS, BIP UMR 7281, F-13009 Marseille, France

Julien Perard – Univ. Grenoble Alpes, CEA, CNRS, IRIG, CBM, F-38000 Grenoble, France

Clara Rinaldi – Univ. Grenoble Alpes, CEA, CNRS, IRIG, CBM, F-38000 Grenoble, France

Complete contact information is available at: <https://pubs.acs.org/doi/10.1021/acscatal.0c05437>

Funding

This work was supported by the Agence Nationale de la Recherche through the LabEx ARCANÉ program (ANR-11-LABX-0003-01) and the Graduate School on Chemistry, Biology and Health of Univ Grenoble Alpes CBH-EUR-GS (ANR-17-EURE-0003). The authors acknowledge support from the plateforme de Chimie NanoBio ICMG FR 2607 (PCN-ICMG). This work was partially funded by CNRS via Mission pour les Initiatives Transverses et Interdisciplinaires

(MITI) and Cellule Energie of CNRS through the project EGreenSyn.

Notes

The authors declare no competing financial interest.

■ ACKNOWLEDGMENTS

The authors are grateful to the EPR facilities available at the French EPR network (RENARD, IR CNRS 3443) and the Aix-Marseille University EPR center. They acknowledge support from the plateforme de Chimie NanoBio ICMG FR 2607 (PCN-ICMG). The authors also thank Gregory Cwickdinski for his help in GC measurements.

■ REFERENCES

- (1) Drennan, C. L.; Heo, J.; Sintchak, M. D.; Schreiter, E.; Ludden, P. W. Life on Carbon Monoxide: X-Ray Structure of Rhodospirillum Rubrum Ni-Fe-S Carbon Monoxide Dehydrogenase. *Proc. Natl. Acad. Sci. U.S.A.* **2001**, *98*, 11973–11978.
- (2) Dobbek, H.; Svetlichnyi, V.; Gremer, L.; Huber, R.; Meyer, O. Crystal Structure of a Carbon Monoxide Dehydrogenase Reveals a [Ni4Fe5S] Cluster. *Science* **2001**, *293*, 1281–1285.
- (3) Jeoung, J. H.; Martins, B. M.; Dobbek, H. Carbon Monoxide Dehydrogenases. In *Metalloproteins; Methods in Molecular Biology*; Humana Press: New York, NY, 2019; Vol. 1876, pp 37–54.
- (4) Can, M.; Armstrong, F. A.; Ragsdale, S. W. Structure, Function, and Mechanism of the Nickel Metalloenzymes, CO Dehydrogenase, and Acetyl-CoA Synthase. *Chem. Rev.* **2014**, *114*, 4149–4174.
- (5) Breglia, R.; Arrigoni, F.; Sensi, M.; Greco, C.; Fantucci, P.; De Gioia, L.; Bruschi, M. First-Principles Calculations on Ni,Fe-Containing Carbon Monoxide Dehydrogenases Reveal Key Stereoelectronic Features for Binding and Release of CO₂ to/from the C-Cluster. *Inorg. Chem.* **2021**, *60*, 387–402.
- (6) Wang, V. C.-C.; Can, M.; Pierce, E.; Ragsdale, S. W.; Armstrong, F. A. A Unified Electrocatalytic Description of the Action of Inhibitors of Nickel Carbon Monoxide Dehydrogenase. *J. Am. Chem. Soc.* **2013**, *135*, 2198–2206.
- (7) Wang, V. C.-C.; Islam, S. T. A.; Can, M.; Ragsdale, S. W.; Armstrong, F. A. Investigations by Protein Film Electrochemistry of Alternative Reactions of Nickel-Containing Carbon Monoxide Dehydrogenase. *J. Phys. Chem. B* **2015**, *119*, 13690–13697.
- (8) Wang, V. C.-C.; Ragsdale, S. W.; Armstrong, F. A. Investigations of Two Bidirectional Carbon Monoxide Dehydrogenases from Carboxydotherrus Hydrogenofomans by Protein Film Electrochemistry. *ChemBioChem* **2013**, *14*, 1845–1851.
- (9) Parkin, A.; Seravalli, J.; Vincent, K. A.; Ragsdale, S. W.; Armstrong, F. A. Rapid and Efficient Electrocatalytic CO₂/CO Interconversions by Carboxydotherrus Hydrogenofomans CO Dehydrogenase I on an Electrode. *J. Am. Chem. Soc.* **2007**, *129*, 10328–10329.
- (10) Domnik, L.; Merrouch, M.; Goetzl, S.; Jeoung, J.-H.; Léger, C.; Dementin, S.; Fourmond, V.; Dobbek, H. CODH-IV: A High-Efficiency CO-Scavenging CO Dehydrogenase with Resistance to O₂. *Angew. Chem., Int. Ed.* **2017**, *56*, 15466–15469.
- (11) Merrouch, M.; Hadj-Saïd, J.; Domnik, L.; Dobbek, H.; Léger, C.; Dementin, S.; Fourmond, V. O₂ Inhibition of Ni-Containing CO Dehydrogenase Is Partly Reversible. *Chem. – Eur. J.* **2015**, *21*, 18934–18938.
- (12) Wittenborn, E. C.; Guendon, C.; Merrouch, M.; Benvenuti, M.; Fourmond, V.; Léger, C.; Drennan, C. L.; Dementin, S. The Solvent-Exposed Fe–S D-Cluster Contributes to Oxygen-Resistance in Desulfovibrio Vulgaris Ni–Fe Carbon Monoxide Dehydrogenase. *ACS Catal.* **2020**, *10*, 7328–7335.
- (13) Zhang, L.; Can, M.; Ragsdale, S. W.; Armstrong, F. A. Fast and Selective Photoreduction of CO₂ to CO Catalyzed by a Complex of Carbon Monoxide Dehydrogenase, TiO₂, and Ag Nanoclusters. *ACS Catal.* **2018**, *8*, 2789–2795.

- (14) Lazarus, O.; Woolerton, T. W.; Parkin, A.; Lukey, M. J.; Reisner, E.; Seravalli, J.; Pierce, E.; Ragsdale, S. W.; Sargent, F.; Armstrong, F. A. Water–Gas Shift Reaction Catalyzed by Redox Enzymes on Conducting Graphite Platelets. *J. Am. Chem. Soc.* **2009**, *131*, 14154–14155.
- (15) Robb, F. T.; Techtmann, S. M. Life on the Fringe: Microbial Adaptation to Growth on Carbon Monoxide. *Frontiers in Microbiology* **2018**, *9*, 1981.
- (16) Kerby, R. L.; Ludden, P. W.; Roberts, G. P. Carbon Monoxide-Dependent Growth of *Rhodospirillum rubrum*. *J. Bacteriol.* **1995**, *177*, 2241–2244.
- (17) Alfano, M.; Cavazza, C. Structure, Function, and Biosynthesis of Nickel-Dependent Enzymes. *Protein Sci.* **2020**, *29*, 1071–1089.
- (18) Wu, M.; Ren, Q.; Scott Durlin, A.; Daugherty, S. C.; Brinkac, L. M.; Dodson, R. J.; Madupu, R.; Sullivan, S. A.; Kolonay, J. F.; Nelson, W. C.; Tallon, L. J.; Jones, K. M.; Ulrich, L. E.; Gonzalez, J. M.; Zhulin, I. B.; Robb, F. T.; Eisen, J. A. Life in Hot Carbon Monoxide: The Complete Genome Sequence of *Carboxythermus hydrogenoformans* Z-2901. *PLoS Genet.* **2005**, *1*, e65.
- (19) Jeoung, J.-H.; Dobbek, H. Carbon Dioxide Activation at the Ni₂Fe-Cluster of Anaerobic Carbon Monoxide Dehydrogenase. *Science* **2007**, *318*, 1461–1464.
- (20) Spangler, N. J.; Meyers, M. R.; Gierke, K. L.; Kerby, R. L.; Roberts, G. P.; Ludden, P. W. Substitution of Valine for Histidine 265 in Carbon Monoxide Dehydrogenase from *Rhodospirillum rubrum* Affects Activity and Spectroscopic States. *J. Biol. Chem.* **1998**, *273*, 4059–4064.
- (21) Craft, J. L.; Ludden, P. W.; Brunold, T. C. Spectroscopic Studies of Nickel-Deficient Carbon Monoxide Dehydrogenase from *Rhodospirillum rubrum*: Nature of the Iron-Sulfur Clusters. *Biochemistry* **2002**, *41*, 1681–1688.
- (22) Bonam, D.; Ludden, P. W. Purification and Characterization of Carbon Monoxide Dehydrogenase, a Nickel, Zinc, Iron-Sulfur Protein, from *Rhodospirillum rubrum*. *J. Biol. Chem.* **1987**, *262*, 2980–2987.
- (23) Jeon, W. B.; Singer, S. W.; Ludden, P. W.; Rubio, L. M. New Insights into the Mechanism of Nickel Insertion into Carbon Monoxide Dehydrogenase: Analysis of *Rhodospirillum rubrum* Carbon Monoxide Dehydrogenase Variants with Substituted Ligands to the [Fe₃S₄] Portion of the Active-Site C-Cluster. *J. Biol. Inorg. Chem.* **2005**, *10*, 903–912.
- (24) Alfano, M.; Cavazza, C. The Biologically Mediated Water–gas Shift Reaction: Structure, Function and Biosynthesis of Monofunctional [NiFe]-Carbon Monoxide Dehydrogenases. *Sustainable Energy Fuels* **2018**, *2*, 1653–1670.
- (25) Singer, S. W.; Hirst, M. B.; Ludden, P. W. CO-Dependent H₂ Evolution by *Rhodospirillum rubrum*: Role of CODH:Coof Complex. *Biochim. Biophys. Acta, Bioenerg.* **2006**, *1757*, 1582–1591.
- (26) Jeon, W. B.; Cheng, J.; Ludden, P. W. Purification and Characterization of Membrane-Associated CooC Protein and Its Functional Role in the Insertion of Nickel into Carbon Monoxide Dehydrogenase from *Rhodospirillum rubrum*. *J. Biol. Chem.* **2001**, *276*, 38602–38609.
- (27) Alfano, M.; Veronesi, G.; Musiani, F.; Zambelli, B.; Signor, L.; et al. A Solvent-Exposed Cysteine Forms a Peculiar Ni II -Binding Site in the Metallochaperone CooT from *Rhodospirillum rubrum*. *Chem. – Eur. J.* **2019**, *25*, 15351–15360.
- (28) Alfano, M.; Pérard, J.; Cavazza, C. Nickel-Induced Oligomerization of the Histidine-Rich Metallochaperone Coof from *Rhodospirillum rubrum*. *Inorganics* **2019**, *7*, 84.
- (29) Alfano, M.; Pérard, J.; Carpentier, P.; Basset, C.; Zambelli, B.; Timm, J.; Crouzy, S.; Ciurli, S.; Cavazza, C. The Carbon Monoxide Dehydrogenase Accessory Protein Coof Is a Histidine-Rich Multidomain Dimer Containing an Unexpected Ni(II)-Binding Site. *J. Biol. Chem.* **2019**, *294*, 7601–7614.
- (30) Timm, J.; Brochier-Armanet, C.; Pérard, J.; Zambelli, B.; Ollagnier-de-Choudens, S.; Ciurli, S.; Cavazza, C. The CO Dehydrogenase Accessory Protein CooT Is a Novel Nickel-Binding Protein. *Metallomics* **2017**, *9*, 575–583.
- (31) Kerby, R. L.; Ludden, P. W.; Roberts, G. P. In Vivo Nickel Insertion into the Carbon Monoxide Dehydrogenase of *Rhodospirillum rubrum*: Molecular and Physiological Characterization of CooCTJ. *J. Bacteriol.* **1997**, *179*, 2259–2266.
- (32) Ensign, S. A.; Campbell, M. J.; Ludden, P. W. Activation of the Nickel-Deficient Carbon Monoxide Dehydrogenase from *Rhodospirillum rubrum*: Kinetic Characterization and Reductant Requirement. *Biochemistry* **1990**, *29*, 2162–2168.
- (33) Le Goff, A.; Holzinger, M. Molecular Engineering of the Bio/Nano-Interface for Enzymatic Electrocatalysis in Fuel Cells. *Sustainable Energy Fuels* **2018**, *2*, 2555–2566.
- (34) Lau, C.; Adkins, E. R.; Ramasamy, R. P.; Luckarift, H. R.; Johnson, G. R.; Atanassov, P. Design of Carbon Nanotube-Based Gas-Diffusion Cathode for O₂ Reduction by Multicopper Oxidases. *Adv. Energy Mater.* **2012**, *2*, 162–168.
- (35) Meredith, M. T.; Minson, M.; Hickey, D.; Artyushkova, K.; Glatzhofer, D. T.; Minter, S. D. Anthracene-Modified Multi-Walled Carbon Nanotubes as Direct Electron Transfer Scaffolds for Enzymatic Oxygen Reduction. *ACS Catal.* **2011**, *1*, 1683–1690.
- (36) Gentil, S.; Che Mansor, S. M.; Jamet, H.; Cosnier, S.; Cavazza, C.; Le Goff, A. Oriented Immobilization of [NiFeSe] Hydrogenases on Covalently and Noncovalently Functionalized Carbon Nanotubes for H₂/Air Enzymatic Fuel Cells. *ACS Catal.* **2018**, *8*, 3957–3964.
- (37) Gentil, S.; Lalaoui, N.; Dutta, A.; Nedelec, Y.; Cosnier, S.; Shaw, W. J.; Artero, V.; Le Goff, A. Carbon-Nanotube-Supported Bio-Inspired Nickel Catalyst and Its Integration in Hybrid Hydrogen/Air Fuel Cells. *Angew. Chem., Int. Ed.* **2017**, *56*, 1845–1849.
- (38) Ensign, S. A.; Bonam, D.; Ludden, P. W. Nickel Is Required for the Transfer of Electrons from Carbon Monoxide to the Iron-Sulfur Center(s) of Carbon Monoxide Dehydrogenase from *Rhodospirillum rubrum*. *Biochemistry* **1989**, *28*, 4968–4973.
- (39) Inoue, T.; Takao, K.; Fukuyama, Y.; Yoshida, T.; Sako, Y. Over-Expression of Carbon Monoxide Dehydrogenase-I with an Accessory Protein Co-Expression: A Key Enzyme for Carbon Dioxide Reduction. *Biosci. Biotechnol. Biochem.* **2014**, *78*, 582–587.
- (40) Roche, B.; Aussel, L.; Ezraty, B.; Mandin, P.; Py, B.; Barras, F. Iron/sulfur proteins biogenesis in prokaryotes: formation, regulation and diversity. *Biochim. Biophys. Acta, Bioenerg.* **2013**, *1827*, 923–937.
- (41) Ensign, S. A.; Ludden, P. W. Characterization of the CO Oxidation/H₂ Evolution System of *Rhodospirillum rubrum*: Role of a 22-KDa Iron-Sulfur Protein in Mediating Electron Transfer between Carbon Monoxide Dehydrogenase and Hydrogenase. *J. Biol. Chem.* **1991**, *266*, 18395–18403.
- (42) Svetlitchnyi, V.; Peschel, C.; Acker, G.; Meyer, O. Two Membrane-Associated NiFeS-Carbon Monoxide Dehydrogenases from the Anaerobic Carbon-Monoxide-Utilizing Eubacterium *Carboxythermus hydrogenoformans*. *J. Bacteriol.* **2001**, *183*, 5134–5144.
- (43) Benvenuti, M.; Meneghello, M.; Guendon, C.; Jacq-Bailly, A.; Jeoung, J. H.; Dobbek, H.; Léger, C.; Fourmond, V.; Dementin, S. The Two CO-Dehydrogenases of *Thermococcus* sp. AM4. *Biochim. Biophys. Acta, Bioenerg.* **2020**, *1861*, No. 148188.
- (44) Hadj-Saïd, J.; Pandelia, M. E.; Léger, C.; Fourmond, V.; Dementin, S. The Carbon Monoxide Dehydrogenase from *Desulfovibrio vulgaris*. *Biochim. Biophys. Acta, Bioenerg.* **2015**, *1847*, 1574–1583.
- (45) Wittenborn, E. C.; Merrouch, M.; Ueda, C.; Fradale, L.; Léger, C.; Fourmond, V.; Pandelia, M.-E.; Dementin, S.; Drennan, C. L. Redox-Dependent Rearrangements of the NiFeS Cluster of Carbon Monoxide Dehydrogenase. *Elife* **2018**, *7*, No. e39451.
- (46) Hu, Z.; Spangler, N. J.; Anderson, M. E.; Xia, J.; Ludden, P. W.; Lindahl, P. A.; Münck, E. Nature of the C-Cluster in Ni-Containing Carbon Monoxide Dehydrogenases. *J. Am. Chem. Soc.* **1996**, *118*, 830–845.
- (47) Spangler, N. J.; Lindahl, P. A.; Bandarian, V.; Ludden, P. W. Spectroelectrochemical Characterization of the Metal Centers in Carbon Monoxide Dehydrogenase (CODH) and Nickel-Deficient CODH from *Rhodospirillum rubrum*. *J. Biol. Chem.* **1996**, *271*, 7973–7977.

- (48) Guigliarelli, B.; Guillaussier, J.; More, C.; Sétif, P.; Bottin, H.; Bertrand, P. Structural Organization of the Iron-Sulfur Centers in Synechocystis 6803 Photosystem I: EPR Study of Oriented Thylakoid Membranes and Analysis of the Magnetic Interactions. *J. Biol. Chem.* **1993**, *268*, 900–908.
- (49) Bertrand, P.; Camensuli, P.; More, C.; Guigliarelli, B. A Local Spin Model To Describe the Magnetic Interactions in Biological Molecules Containing [4Fe–4S]⁺ Clusters. Application to Ni–Fe Hydrogenases. *J. Am. Chem. Soc.* **1996**, *118*, 1426–1434.
- (50) Anderson, M. E.; DeRose, V. J.; Hoffman, B. M.; Lindahl, P. A. Identification of a Cyanide Binding Site in CO Dehydrogenase from *Clostridium thermoaceticum* Using EPR and ENDOR Spectroscopies. *J. Am. Chem. Soc.* **1993**, *115*, 12204–12205.
- (51) Lalaoui, N.; David, R.; Jamet, H.; Holzinger, M.; Le Goff, A.; Cosnier, S. Hosting Adamantane in the Substrate Pocket of Laccase: Direct Bioelectrocatalytic Reduction of O₂ on Functionalized Carbon Nanotubes. *ACS Catal.* **2016**, *6*, 4259–4264.
- (52) Bard, A. J.; Faulkner, L. R. *Electrochemical Methods: Fundamentals and Applications*; Wiley-VCH Verlag GmbH & Co. KGaA, 2001.
- (53) Léger, C.; Jones, A. K.; Albracht, S. P. J.; Armstrong, F. A. Effect of a Dispersion of Interfacial Electron Transfer Rates on Steady State Catalytic Electron Transport in [NiFe]-Hydrogenase and Other Enzymes. *J. Phys. Chem. B* **2002**, *106*, 13058–13063.
- (54) Lalaoui, N.; Le Goff, A.; Holzinger, M.; Cosnier, S. Fully Oriented Bilirubin Oxidase on Porphyrin-Functionalized Carbon Nanotube Electrodes for Electrocatalytic Oxygen Reduction. *Chem. – Eur. J.* **2015**, *21*, 16868–16873.
- (55) Lalaoui, N.; de Poulpiquet, A.; Haddad, R.; Le Goff, A.; Holzinger, M.; Gounel, S.; Mermoux, M.; Infossi, P.; Mano, N.; Lojou, E.; Cosnier, S. A Membraneless Air-Breathing Hydrogen Biofuel Cell Based on Direct Wiring of Thermostable Enzymes on Carbon Nanotube Electrodes. *Chem. Commun.* **2015**, *51*, 7447–7450.
- (56) Wang, M.; Chen, L.; Lau, T.-C.; Robert, M. A Hybrid Co Quaterpyridine Complex/Carbon Nanotube Catalytic Material for CO₂ Reduction in Water. *Angew. Chem., Int. Ed.* **2018**, *57*, 7769–7773.
- (57) Zhang, X.; Wu, Z.; Zhang, X.; Li, L.; Li, Y.; Xu, H.; Li, X.; Yu, X.; Zhang, Z.; Liang, Y.; Wang, H. Highly Selective and Active CO₂ Reduction Electrocatalysts Based on Cobalt Phthalocyanine/Carbon Nanotube Hybrid Structures. *Nat. Commun.* **2017**, *8*, No. 14675.
- (58) Wang, X.; Libo, S.; Huang, Z.; Reddu, V.; Su, T.; Fisher, A. A Planar, Conjugated N₄-Macrocyclic Cobalt Complex for Heterogeneous Electrocatalytic CO₂ Reduction with High Activity. *Angew. Chem.* **2020**, *132*, 17252–17257.
- (59) Karapinar, D.; Zitolo, A.; Huan, T. N.; Zanna, S.; Taverna, D.; Galvão Tizei, L. H.; Giaume, D.; Marcus, P.; Mougél, V.; Fontecave, M. Carbon-Nanotube-Supported Copper Polyphthalocyanine for Efficient and Selective Electrocatalytic CO₂ Reduction to CO. *ChemSusChem* **2020**, *13*, 173–179.
- (60) Liu, M.; Pang, Y.; Zhang, B.; De Luna, P.; Voznyy, O.; Xu, J.; Zheng, X.; Dinh, C. T.; Fan, F.; Cao, C.; de Arquer, F. P. G.; Saefi, T. S.; Mepham, A.; Klinkova, A.; Kumacheva, E.; Filleter, T.; Sinton, D.; Kelley, S. O.; Sargent, E. H. Enhanced Electrocatalytic CO₂ Reduction via Field-Induced Reagent Concentration. *Nature* **2016**, *537*, 382–386.
- (61) Plumeré, N.; Rüdiger, O.; Oughli, A. A.; Williams, R.; Vivekananthan, J.; Pöller, S.; Schuhmann, W.; Lubitz, W. A Redox Hydrogel Protects Hydrogenase from High-Potential Deactivation and Oxygen Damage. *Nat. Chem.* **2014**, *6*, 822–827.

Supporting information for

**Efficient electrochemical CO₂/CO interconversion by an
engineered carbon monoxide dehydrogenase on a gas-
diffusion carbon nanotube-based bioelectrode**

Umberto Contaldo^{1,2}, Bruno Guigliarelli³, Julien Perard¹, Clara Rinaldi¹, Alan Le Goff^{2*} and Christine Cavazza^{1*}

¹Univ. Grenoble Alpes, CEA, CNRS, IRIG, CBM, F-38000 Grenoble, France

²University Grenoble Alpes, DCM UMR 5250, BEA, F-38000, Grenoble, France

³Aix Marseille Univ, CNRS, BIP (Bioenergetics and Protein Engineering Laboratory), Marseille, France.

*Corresponding Authors: christine.cavazza@cea.fr; alan.le-goff@univ-grenoble-alpes.fr

Cloning and expression

The *Rhodospirillum rubrum cooS* gene was obtained from DNA 2.0 in pET15b as a codon-optimized gene for expression in *E. coli* (640 residues, 66911 Da). The *cooS* gene was subcloned in a modified version of the vector pCDFDuet-1, namely pCDF-Duet1-LIC1 (Structural Genomics Consortium, Toronto) which contains a TEV cleavage site downstream the histidine tag at the N-terminus (662 residues, 69547 Da).

MGSSMHHHHHHSSGRENLYFQGHMTHHDCAHCSSDACATEMLNLAEANSIET
AWHRYEKQQPQCGFGSAGLCCRICLKGPCRIDPFGEGPKYGVCGADRDTIVAR
HLVRMIAAGTAAHSEHGRHIALAMQHISQGELHDYSIRDEAKLYAIAKTLGVA
TEGRGLLAIVGDLAAITLGFQNDYDKPCAWLAASLTPRRVKRLGDLGLLPH
NIDASVAQTMSRTHVGCADPTNLILGGLRVAMADLDGSMLATELSDALFGTP
QPVVSAANLGVMKRGAVNIAVNGHNPMLSDIICDVAADLRDEAIAAGAAEGIN
IIGICCTGHEVMMRHGVPLATNYLSQELPILTGAEAMVVVDVQCIMPSPRIAEC
FHTQIITTDKHNKISGATHVPFDEHKAVETAktiIRMAIAAFGRRDPNRVAIPAF
KQKSIVGFSAEAVVAALAKVNADDPLKPLVDNVVNGNIQGIVLFGVCNTTKVQ
QDSAYVDLAKSLAKRNVLVLATGCAAGAFKAGLMTSEATTQYAGEGLKGV
LSAIGTAAGLGGPLPLVMHMGSCVDNSRAVALATALANKLGVDLSDLPLVAS
APECMSEKALAIGSWAVTIGLPTHVGSVPPVIGSQIVTKLVTETAKDLVGGYFIV
DTDPKSAGDKLYAAIQERRAGLGL

The *Rhodospirillum rubrum cooCTJ* genes, manually codon optimized genes for expression in *E. coli* were obtained from Genscript in pBAD24 vector (NcoI/HindIII): *pBAD_cooCTJ*. The *cooCTJ* genes were subcloned into pRSFDuet1 (NcoI/HindIII) to give the *pRSF_RrcooCTJ* construction.

E. coli BL21 (DE3) cells transformed with pCDF-Duet1-LIC1_*RrcooS* alone or co-transformed with pRSF_*RrCooCTJ* were cultured under aerobic conditions in auto-induction medium, supplemented with appropriate antibiotics, 1 mM Fe(II)SO₄ (Sigma Aldrich), 2 mM L-Cysteine (Sigma Aldrich) and 500 μM NiSO₄ (ACROS ORGANICS) for 3 hours at 37 °C and 180 rpm (OD₆₀₀ 0.8-1.5) and subsequently transferred for 21 hours at 15 °C and 180 rpm (OD₆₀₀ 9-14). Cultures were centrifuged and cell pellets collected under argon flow before being stored in liquid nitrogen.

Protein purification

All the following steps were carried out in a glove box under controlled atmosphere ($O_2 < 2$ ppm, Jacomex), excepted for the centrifugation step. Bacterial pellets from 2 L culture were thawed directly inside the glove box and resuspended in buffer A (50 mM TrisHCl, pH 8.5, 150 mM NaCl) supplemented with one complete Protease Inhibitors cocktail tablet (Roche), 20 mM imidazole, 9 mM sodium dithionite (DTH) (Merck) and 9 mM dithiothreitol (DTT) (Euromedex) and lysed by sonication. The cell debris were removed by centrifugation at 25000 rpm for 25 minutes at 4 °C. The cleared lysate was diluted 3 times with buffer A and loaded onto a 25 mL Ni-NTA Agarose resin in batch (Qiagen). After washing with 250 mL of buffer B (buffer A + 3 mM DTT) supplemented with 20 mM imidazole, and 300 mL of buffer B supplemented with 50 mM Imidazole, protein was eluted with buffer B supplemented with 300 mM Imidazole. The fractions were analysed by SDS-PAGE, and those containing Rec-RrCODH were pooled and buffer exchanged with buffer C (50 mM TrisHCl, pH 8.5, 5 mM DTT, 5 mM DTH) by desalting using a Sephadex® G-25 (GE Healthcare). The Rec-RrCODH and Rec-RrCODH^{CTJ} fractions were concentrated to 75 μ M dimer and stored at 4 °C under anaerobic conditions.

UV-visible spectra of oxidized CODH

Protein samples were dialyzed in two successive baths of 500 mL of 50 mM TrisHCl pH 8.5 in an anaerobic glove box ($O_2 < 2$ ppm, Jacomex). The UV-visible spectra of oxidized Rec-RrCODH and Rec-RrCODH^{CTJ} were recorded on a UV-1800 spectrophotometer (Shimadzu Corporation).

Size-exclusion chromatography coupled to multi-angle laser light scattering with on-line refractive index (SEC-MALLS-RI)

Purified Rec-RrCODH and Rec-RrCODH^{CTJ} samples were injected manually into a SEC-MALLS system (Wyatt Dawn HELEOS-II 18-angle light scattering detector and Wyatt Optilab rEX refractive index monitor linked to a Shimadzu HPLC system comprising a LC-20AD pump and SPD20A UV/Vis detector) using a Superdex 200 10/300 Increase size exclusion column eluted with buffer containing 50 mM TrisHCl, pH 8.5, 150 mM NaCl, 1 mM TCEP. An in-line refractive index detector (Optirex, Wyatt Instruments) was used to follow the differential refractive index relative to the solvent. The data were analyzed using the ASTRA software (version 6) and the molecular masses were

calculated for each sample. Protein concentration in all samples was determined by integration of the differential refractive index (dRI) peak after injection of 20 μ L protein.

Metal content determination

Bathophenanthroline assay was used for the determination of Fe(II) by following a previous published protocol.¹ Ammonium iron(II) sulfate (Sigma Aldrich) was used for made the calibration curve between 0 to 215 μ M Fe(II). RecRrCODH and RecRrCODH^{CTJ} were diluted between 2.8 to 0.36 μ M of dimer and each dilution was measured in triplicate. The absorbance 535-680 nm was measured by using Varian Cary® 50 UV-Vis Spectrophotometer (Agilent Technologies).

4-(2-pyridylazo)resorcinol (PAR) assay was used for the determination of Ni(II) by following a previous published protocol.² Nickel(II) sulfate heptahydrate (Sigma Aldrich) was used for the calibration curve between 0 to 40 μ M Ni(II). RecRrCODH and RecRrCODH^{CTJ} in buffer C (see above) were preincubated 15 minutes with 1 mM EDTA to remove aspecific Ni(II) traces, after the buffer was exchanged with 50 mM TrisHCl buffer pH 8.5 by using Micro BioSpin® 6 columns (Bio-Rad). The CO oxidation activity was tested before and after the EDTA treatment to verify the integrity of the enzyme. RecRrCODH and RecRrCODH^{CTJ} were diluted between 9.6 to 1.1 μ M of dimer and each dilution was measured in triplicate. The absorbance was measured at 495 nm by using Varian Cary® 50 UV-Vis Spectrophotometer (Agilent Technologies).

CO oxidation activity measurements

Rec-RrCODH and Rec-RrCODH^{CTJ} were diluted to about 20 and to about 5 nM of monomer, respectively. CO oxidation activity was assayed at 25 °C by following the reduction of methyl viologen at 604 nm [$\epsilon=13.6 \text{ mM}^{-1} \text{ cm}^{-1}$] in CO-saturated solutions containing 12 mM methyl viologen and 1 mM DTT (standard conditions). CODH specific activity unit is expressed as micromoles of CO oxidized per minute per milligram of protein. The standard buffer used to dilute the enzyme prior to measurements was 50 mM TrisHCl pH 8.5, 5 mM DTT, 1 mM DTH (buffer A). For pH dependence measurements (Figure 2 A), Rec-RrCODH^{CTJ} was diluted in buffer A at 21 °C. CO oxidation activity was measured in standard conditions, except that the following range of pH and buffers were used: 100 mM NaAcetate for pH 4.0 or 5.0 and 50 mM BisTris Propane from pH 6.0 to pH 11.5. For temperature dependence measurements (Figure 2 B), Rec-RrCODH^{CTJ} was diluted in solution A at 21 °C and the activity was measured in standard

conditions except that the following range of temperatures was used: 21, 25, 30, 35, 40, 45, 50, 55 and 60 °C. For stability experiments (Fig. 2 CD), Rec-RrCODH^{CTJ} was diluted in buffer A, except that the range of pH and buffers described above was used at 21 °C. The activity was measured at t_0 and t_{24h} . Rec-RrCODH^{CTJ} was diluted in solution A and incubated at different temperatures (from 21 to 60°). The activity was measured at t_{10} , t_{30} and $t_{60 \text{ min}}$.

Redox titration by Electron Paramagnetic Resonance

Purified Rec-RrCODH^{CTJ} at 108 μM was oxidized by buffer exchange with 0.1 M MOPS pH 8.0 using a desalting a NAPTM-10 column (GE Healthcare) and diluted to 70 μM (dimer concentration).

Enzyme preparations were titrated in glove box in the presence of the following mediators (10 μM concentration each): methylene blue, indigo carmine, phenosafranine, neutral red and methyl viologen. Redox potentials were measured with an Ag/AgCl/KCl (3 M) electrode. In the text, all potential values are given with respect to standard hydrogen electrode. After addition of a small amount of dithionite solution, potential stabilization was achieved in a few minutes, and sample was transferred into calibrated EPR tube and immediately frozen in the glove box in a cold ethanol bath. EPR experiments were performed on a Bruker ELEXSYS E500 spectrometer equipped with an ER4102ST standard rectangular Bruker EPR cavity fitted to an Oxford Instruments ESR 900 helium flow cryostat. Spin intensity measurements were performed by double integration of EPR spectra recorded in non-saturating conditions and compared to a 1mM Cu(II)EDTA standard.

Electrochemical measurements

1-pyrenebutyric acid adamantyl amide was prepared as previously described.³ All reagents were purchased from Sigma Aldrich. Commercial grade thin Multi-Walled Carbon Nanotubes (MWCNT, 9.5 nm diameter, purity > 99%). Carbon nanomaterials were used as received without any purification. When not used, the enzymes were stored at 4 °C. All the reagents were used without further purification. All solvents were of analytical grade. Distilled water was passed through a Milli-Q water purification system. The electrochemical experiments were carried out in a three-electrode electrochemical gas thig cell using a Biologic VMP3 Multi Potentiostat inside an anaerobic glove box ($\text{O}_2 < 2 \text{ ppm}$, Jacomex). The MWCNT bioelectrodes were used as working electrodes. Pt

wire was used as counter electrode and the Saturated Calomel served as reference electrode. Potentials are referred to the Standard Hydrogen Electrode according to $E_{SHE} = E_{SCE} + 0.242$ V. Current densities are normalized towards the geometrical surface of the glassy carbon electrode or the gas-diffusion electrode (0.071 cm^2). The experiments were conducted at glove box temperature, 21°C . The electrolyte was 50 mM TrisHCl buffer pH 8.5, 50 mM Bis-Tris propane pH 5.5, 6.5, 7.5, 8.5 and 9.5 and 54 mM Britton-Robinson buffer pH 5.0. For information, CO solubility in water is 3.3 mL and 2.3 mL per 100 mL at 0°C and 20°C , respectively. CO_2 solubility in water is 171 mL and 88 mL per 100 mL at 0°C and 20°C , respectively.

Preparation of the glassy carbon- and gas diffusion- modified MWCNT electrode and enzyme immobilization

The working electrodes were glassy carbon and gas diffusion electrodes (3 mm diameter). N-methyl-2-pyrrolidinone (NMP) dispersion of MWCNTs were prepared by 30 minutes sonication of 5 mg MWCNTs dispersed in 1 mL NMP until homogeneous black suspension was obtained. Then 20 μL of the MWCNTs solution were drop-casted on a GCE/GDE and NMP was removed under vacuum leaving a 5- μm -thick film on the GCE. The functionalised electrodes were then incubated for 4 hours with 25 μL of the enzymatic Rec-RrCODH and Rec-RrCODH^{CTJ} solutions (19 μM dimer concentration pH 8.5) which were pre-reduced in presence of 5 mM DTH and 5 mM DTT. The latter step was carried out inside an anaerobic glove box ($\text{O}_2 < 2$ ppm, Jacomex). The electrodes were finally washed with buffer TrisHCl 50 mM pH 8.5. When not used the electrodes were kept in buffer TrisHCl 50 mM pH 8.5.

Functionalisation of MWCNT with 1-pyrenebutyric acid adamantyl amide and enzyme immobilization

MWCNT-modified electrodes were soaked for 30 minutes in DMF solution containing 10 mM 1-pyrenebutyric acid adamantyl amide and after rinsed in DMF solution and two times in water. The functionalised electrodes were then incubated for 4 hours with 25 μL of the enzymatic Rec-RrCODH and Rec-RrCODH^{CTJ} solutions (19 μM dimer concentration pH 8.5) which were pre-reduced in presence of 5 mM DTH and 5 mM DTT. The latter step was carried out inside an anaerobic glove box ($\text{O}_2 < 2$ ppm, Jacomex). The electrodes were finally washed with buffer TrisHCl 50 mM pH 8.5.

Gas Chromatography products analysis of MWCNT^{ADA} immobilized RecRrCODH^{CTJ}
RecRrCODH^{CTJ} immobilized on either MWCNT^{ADA} glassy carbon- or gas diffusion-electrodes were used to analyze the electrocatalysis products. The production of CO and CO₂, from CO₂ and CO, respectively were analyzed with a PerkinElmer Clarus 500 gas chromatography (GC). Chronoamperometry experiments were performed under a saturated and continuous flow of each substrate. Regarding the glassy carbon electrode, an aliquot of the gas phase from the gas-tight electrochemical cell was taken and injected into the GC. While for the gas diffusion electrode the outgoing gas was taken and directly injected into the GC. Controls experiments were performed with injections of CO (10 μ L of 100 % CO) and CO₂ (50 μ L of a mixture 20 % CO₂ 80% N₂) gasses.

Figure S1. A: SDS/PAGE of pure Rec-RrCODH (left) and Rec-RrCODH^{CTJ} (right). Marker 150; 100; 80; 60; 40; 30; 20; 10 kDa. **B:** SEC-MALLS of pure Rec-RrCODH (23 μ M dimer concentration) and Rec-RrCODH^{CTJ} (24.3 μ M dimer concentration), 50 mM TrisHCl buffer 150 mM NaCl 1 mM TCEP. **C:** UV-vis. spectra of oxidized pure preparation of Rec-RrCODH (1.1 μ M dimer concentration) and Rec-RrCODH^{CTJ} (1 μ M dimer concentration).

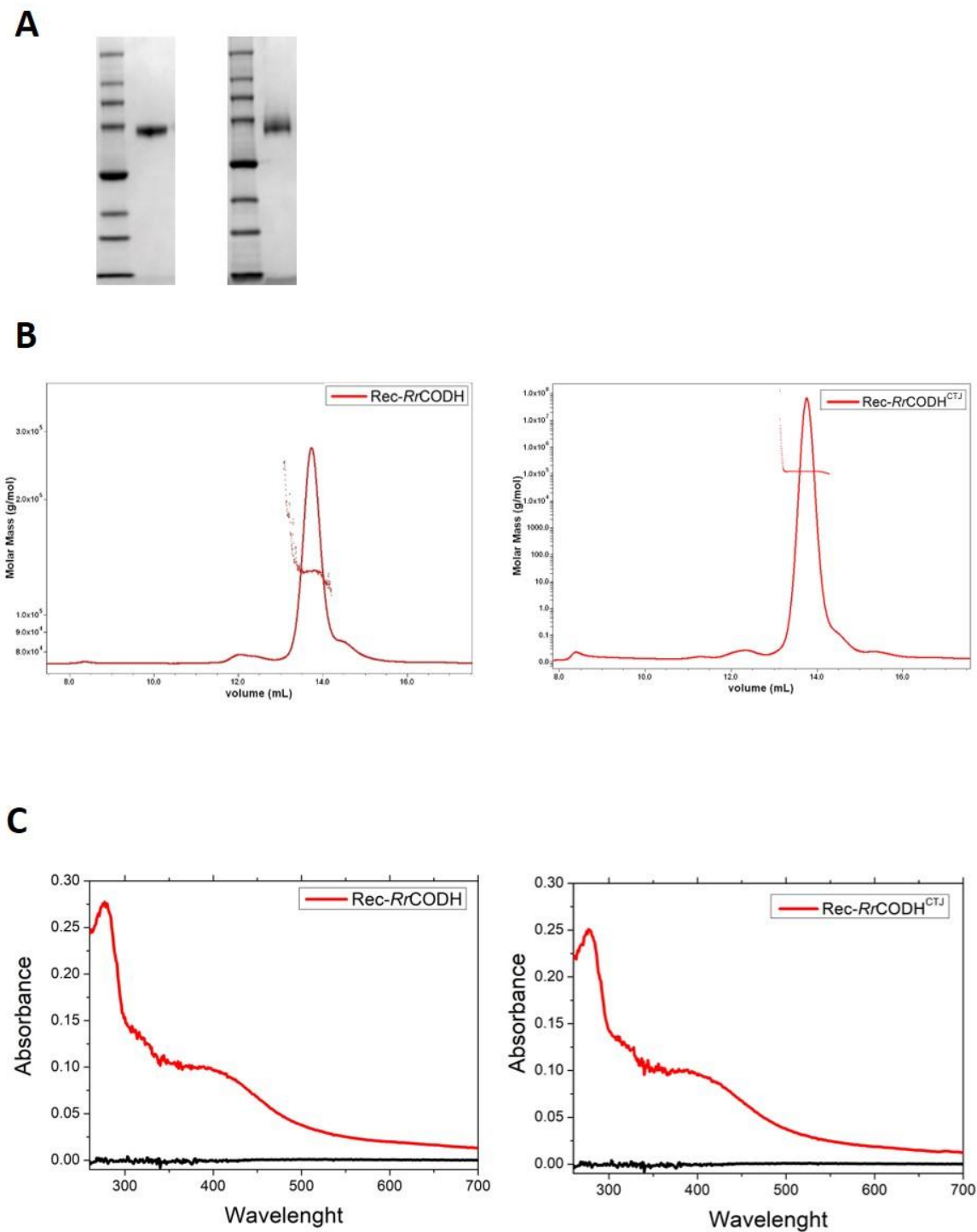


Figure S2. Dithionite-dependent specific activity of Rec-RrCODH compared to Rec-RrCODH^{CTJ}

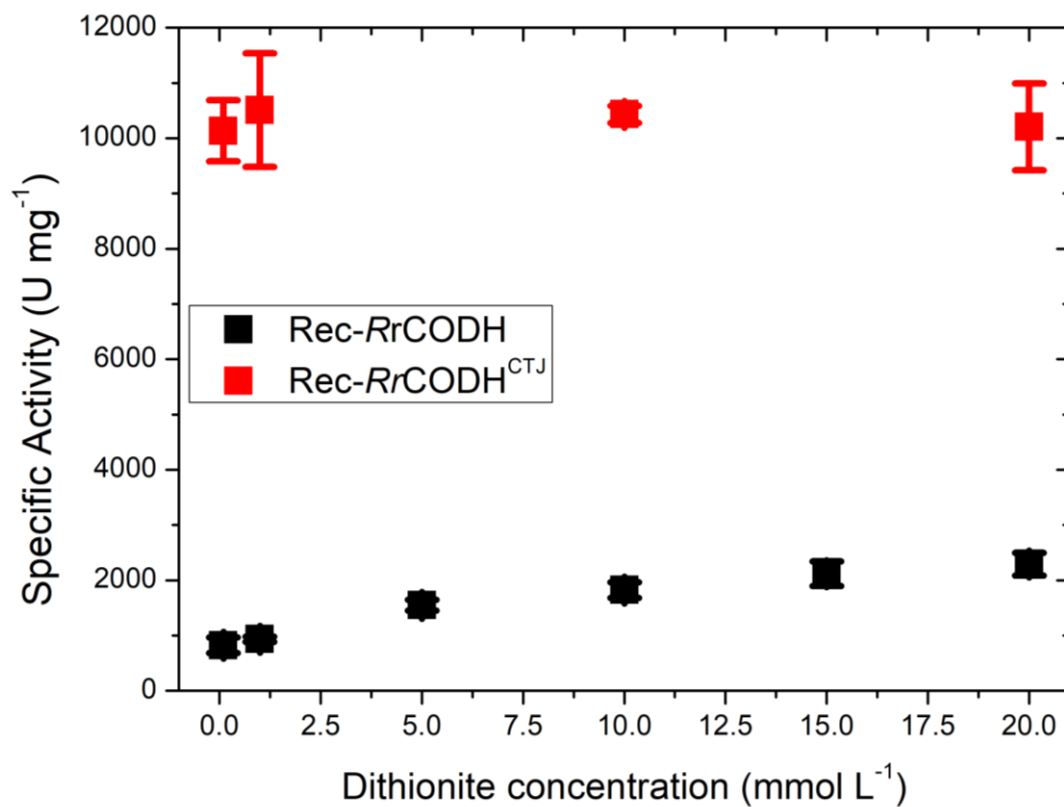


Figure S3. Variation of EPR signal amplitudes with redox potential: black square, peak to peak amplitude of the $g=1.93$ line of the FeS signal, red circle, amplitude of the $g=1.71$ line of C_{red1} signal; blue circle, amplitude of the $g=1.757$ line of C_{red2} signal. EPR conditions: Temperature, 10 K; microwave power, 10 mW; modulation amplitude, 1 mT. For sake of clarity, the normalization of signal amplitudes is different for each signal.

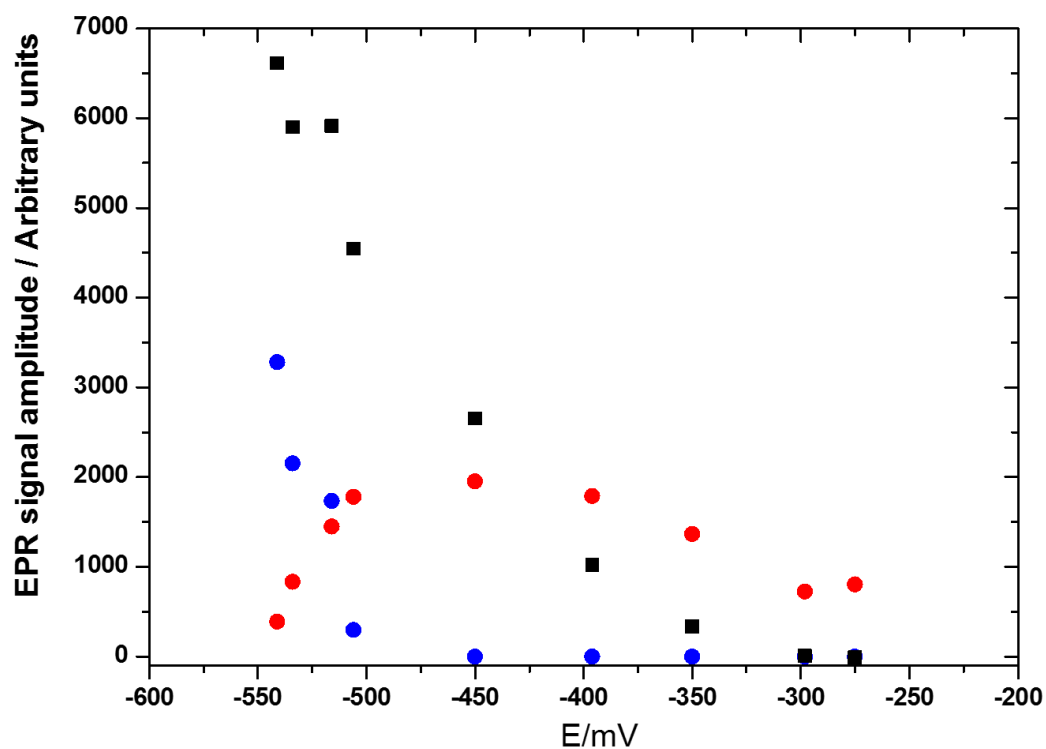


Figure S4. CVs of the Rec-RrCODH^{CTJ}-functionalized MWCNT^{ADA} electrode under Ar before (black) and after (blue) addition of 5 mM KOCN (50 mM TrisHCl, pH 8.5, $v = 5 \text{ mV s}^{-1}$)

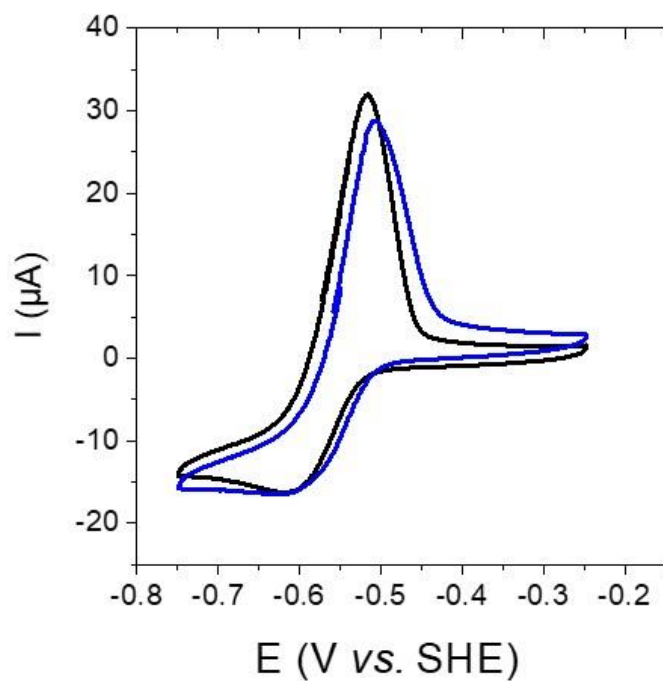


Figure S5. CVs of a non-modified MWCNT electrode under Ar (black), CO (red) and CO₂ (blue), in 50 mM Tris-HCl, pH 8.5, $v = 5 \text{ mV s}^{-1}$.

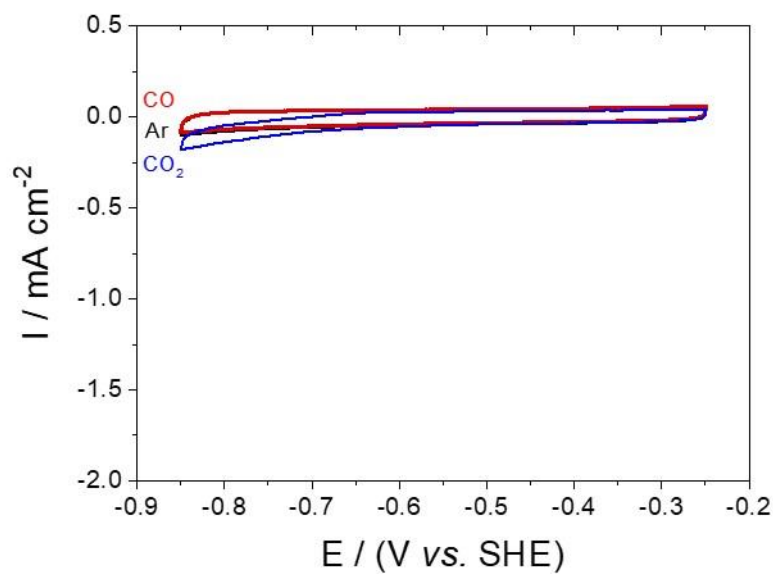


Figure S6. CVs of the Rec-RrCODH-functionalized (black) pristine MWCNT, (red) MWCNT^{ADA} electrodes under Ar, CO and CO₂ (50 mM Tris-HCl, pH 8.5, $\nu = 5 \text{ mV s}^{-1}$)

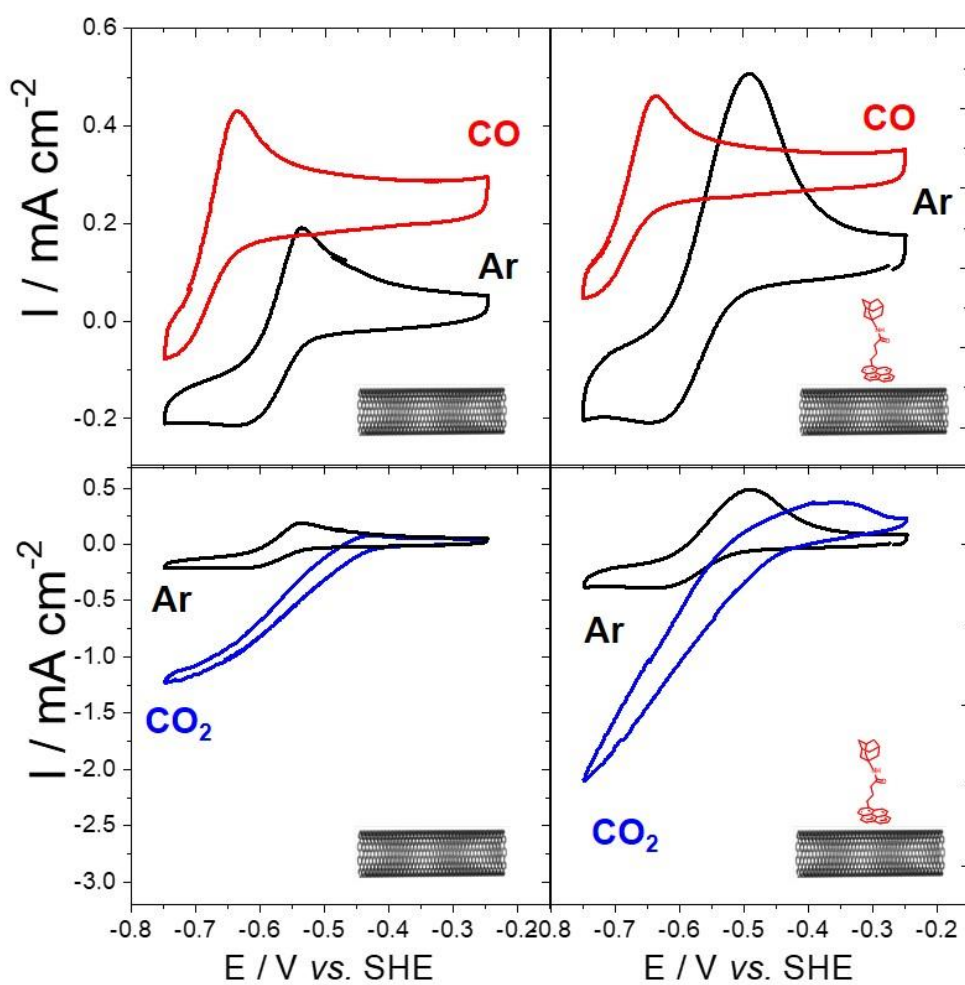
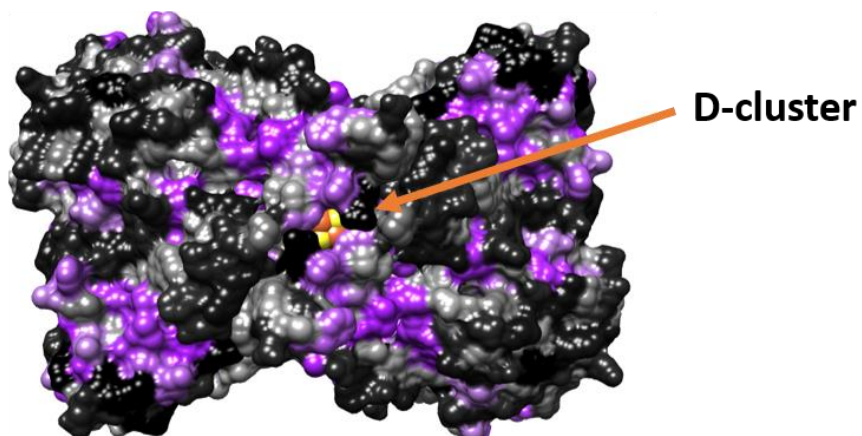
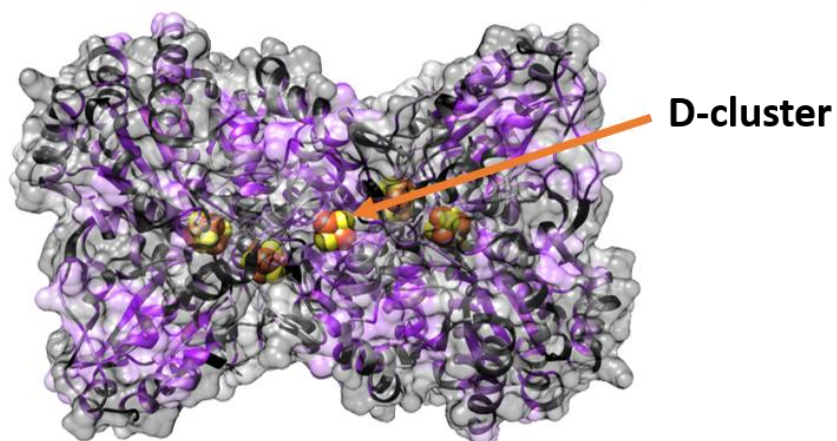


Figure S7. *Rr*CODH (1JQK) hydrophobic surface analysis. Surface and ribbon diagram are coloured from hydrophilic (black) to hydrophobic (purple) residues. **A:** upper view, **B:** upper view (transparency), **C:** side view (transparency).

A



B



C

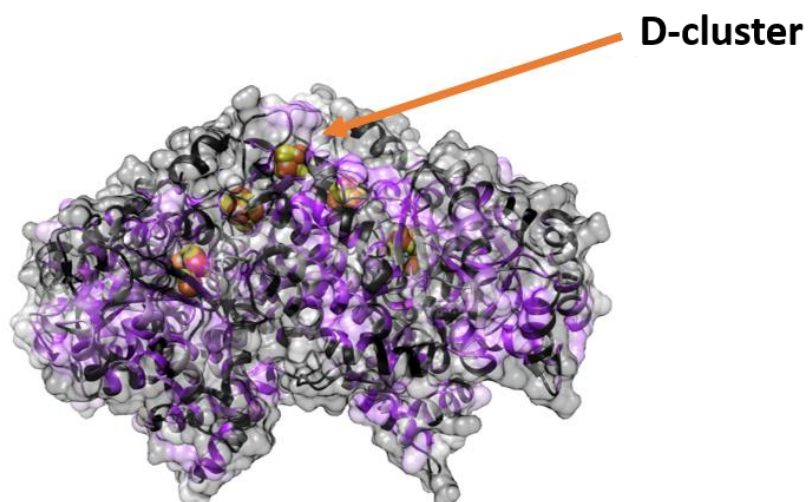


Figure S8. pH dependence of the maximum current density measured at $E = -0.8$ V vs SHE by CV performed under CO_2 (50 mM Bis-Tris propane pH 5.5, 6.5, 7.5, 8.5 and 9.5, $v = 5 \text{ mV s}^{-1}$)

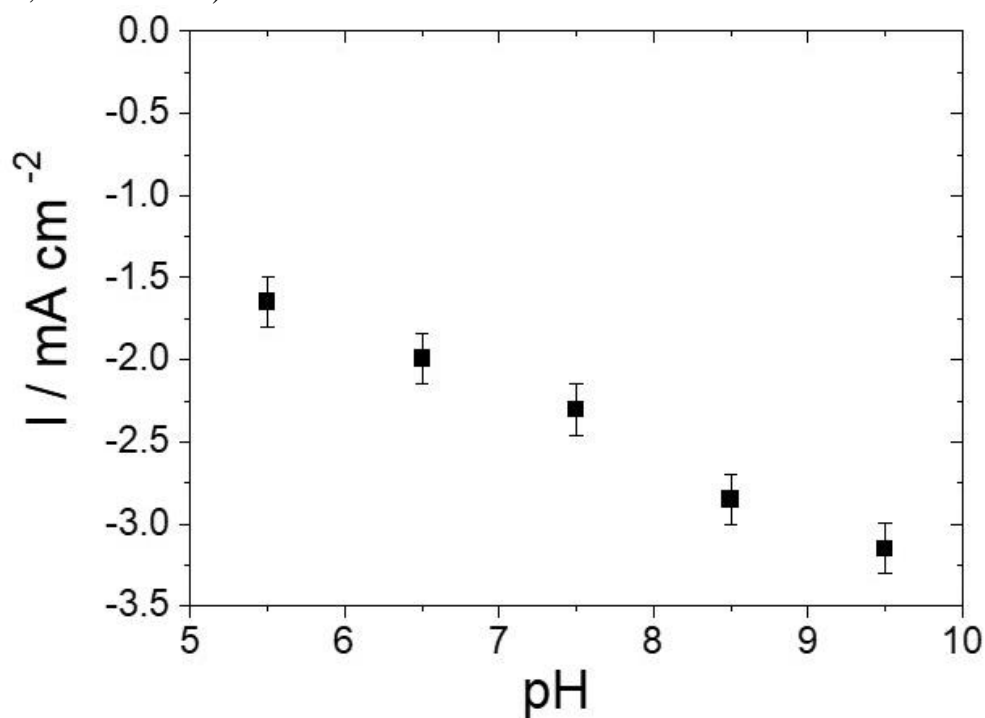


Figure S9. One-hour chronoamperometry of the Rec-*Rr*CODH^{CTJ}-functionalized MWCNT^{ADA} electrode in a stirred CO_2 -saturated 50 mM TrisHCl, pH 8.5 at -0.75 V vs. SHE.

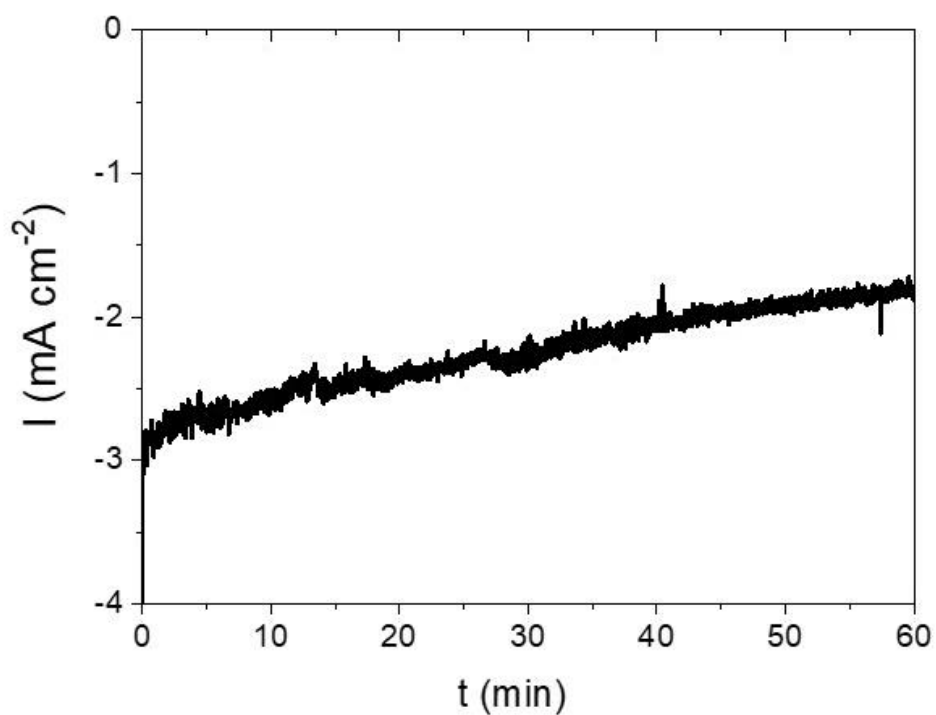


Figure S10. (A) 3D image, (B) profile measurement performed by Laser Scanning microscopy and (C) Scanning Electron Microscopy image on a *Rec-RrCODH^{CTJ}*-functionalized MWCNT^{ADA} gas-diffusion bioelectrodes.

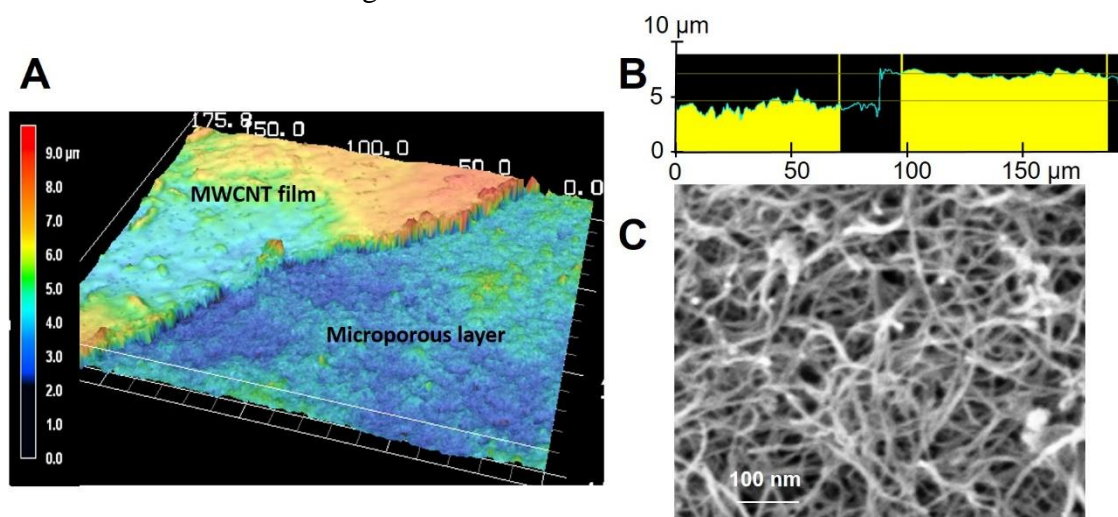


Figure S11. Electrocatalysis products analysed by Gas Chromatography. CO/CO₂ production by of Rec-*Rr*CODH^{CTJ}-functionalized MWCNT^{ADA} electrodes (A, B) and Gas Diffusion-Electrode (C, D). References: CO 100% (black) 0.59 min and CO₂ (violet) 1.79 min (20 % CO₂ 80% N₂). Aliquots of gas from the gas-tight electrochemical cell (10-50 μL) saturated with CO (A) or CO₂ (B). Outgoing gas of gas diffusion electrode (10-50 μL) saturated with CO (C) or CO₂ (D). Since a continuous flow of CO or CO₂ was applied during the experiments, the saturated major peaks correspond to the substrates.

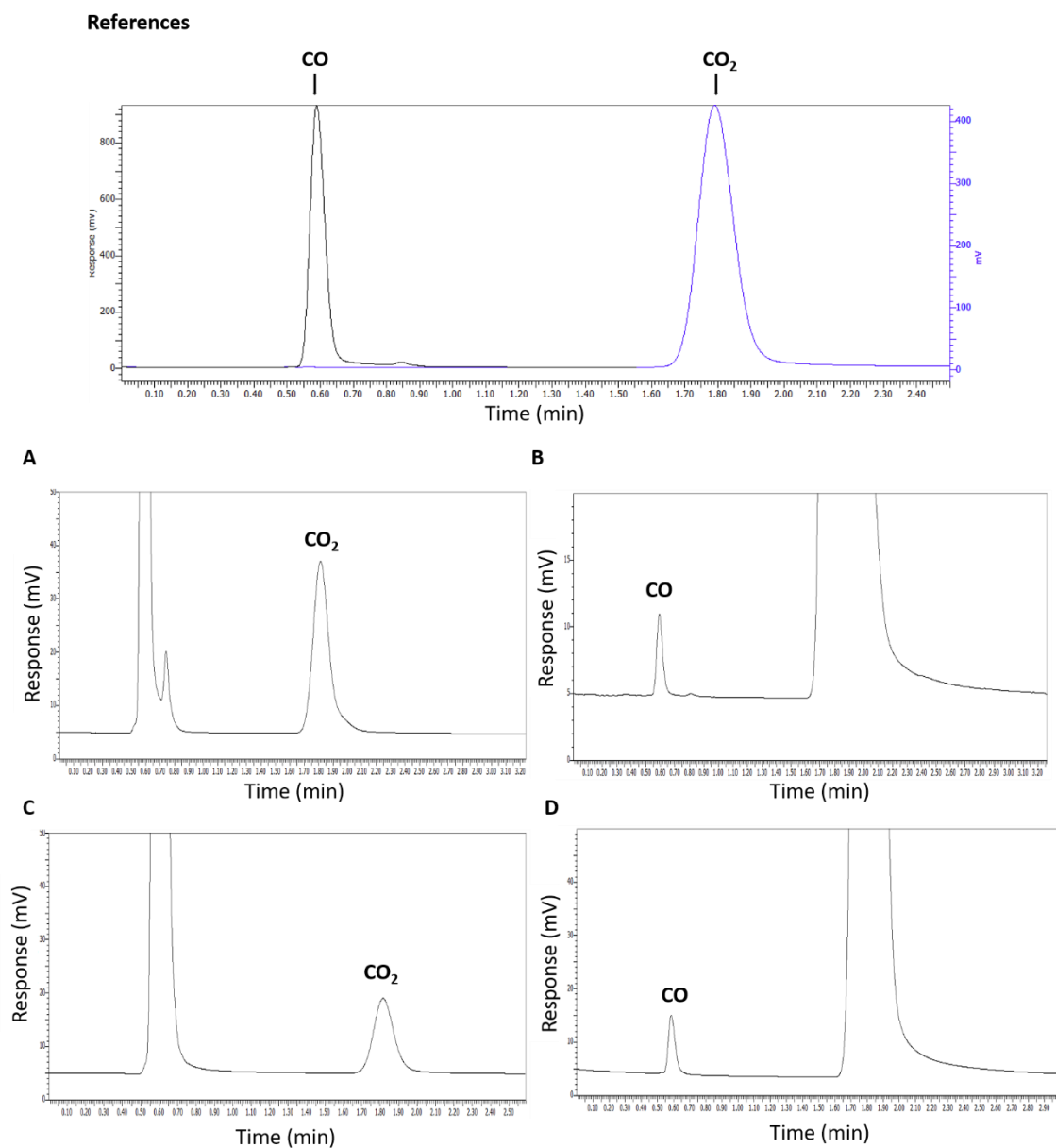


Table S1. State-of-the art catalysts for CO₂ reduction

Catalyst	Overpotential (mV)	Current density (mA cm ⁻²)	CO ₂ selectivity (%)	Catalyst Loadings (nmol cm ⁻²)	TOF (s ⁻¹)	TON	Ref.
Rec-RrCODH ^{CTJ} /MWCNT ^{ADA}	180	4.2	100	0.052	420	800,000	This work
Cobalt quaterpyridine/CNT	440	19.9	99	8.5	12	89,095	4
CN-substituted phtalocyanin cobalt/CNT	520	15	98	18	4.1	97,000	5
Cobalt phenanthroline/CNT	590	10.7	96	59	9.6	nd	5
[MnBr(2,2'-bipyridine)(CO) ₃ on CNT	550	5	34	50	0.04	2,000	6
Iron porphyrin on CNT	500	ca 5.5	90	6.4	0.05	750	7
Poly-CuPc	300	6.9	80	-	-	-	8
Gold nanoneedles	240	22	95	-	-	-	9

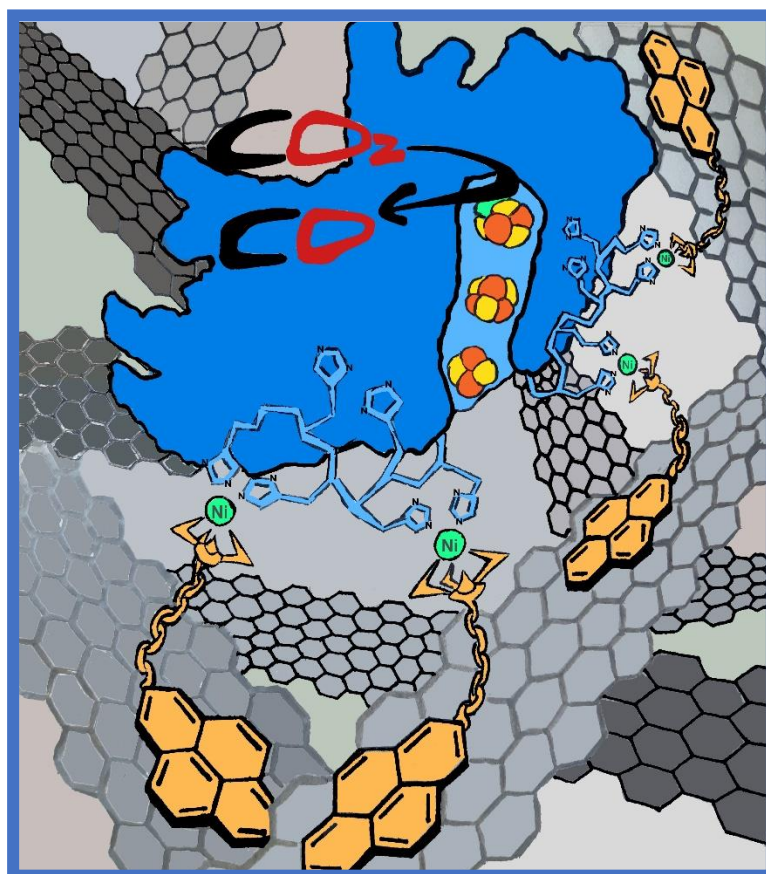
References

- (1) Ghosh, M. M.; O'Connor, J. T.; Engelbrecht, R. S. Bathophenanthroline Method for the Determination of Ferrous Iron. *J. Am. Water Works Assoc.* 1967, 59 (7), 897–905.
- (2) Mccall, K. A.; Fierke, C. A. Colorimetric and Fluorimetric Assays to Quantitate Micromolar Concentrations of Transition Metals 1. 2000, 315, 307–315.
- (3) Haddad, R.; Holzinger, M.; Villalonga, R.; Neumann, A.; Roots, J.; Maaref, A.; Cosnier, S. Pyrene-Adamantane- β -Cyclodextrin: An Efficient Host–guest System for the Biofunctionalization of SWCNT Electrodes. *Carbon N. Y.* 2011, 49 (7), 2571–2578.
- (4) Wang, M.; Chen, L.; Lau, T.-C.; Robert, M. A Hybrid Co Quaterpyridine Complex/Carbon Nanotube Catalytic Material for CO₂ Reduction in Water. *Angew. Chemie Int. Ed.* 2018, 57 (26), 7769–7773.
- (5) Sun, L.; Huang, Z.; Reddu, V.; Su, T.; Fisher, A. C.; Wang, X. A Planar, Conjugated N₄-Macrocyclic Cobalt Complex for Heterogeneous Electrocatalytic CO₂ Reduction with High Activity. *Angew. Chemie Int. Ed.* 2020, 59 (39), 17104–17109.
- (6) Reuillard, B.; Ly, K. H.; Rosser, T. E.; Kuehnel, M. F.; Zebger, I.; Reisner, E. Tuning Product Selectivity for Aqueous CO₂ Reduction with a Mn(Bipyridine)-Pyrene Catalyst Immobilized on a Carbon Nanotube Electrode. *J. Am. Chem. Soc.* 2017, 139 (41), 14425–14435.
- (7) Maurin, A.; Robert, M. Catalytic CO₂-to-CO Conversion in Water by Covalently Functionalized Carbon Nanotubes with a Molecular Iron Catalyst. *Chem. Commun.* 2016, 52 (81), 12084–12087.
- (8) Karapinar, D.; Zitolo, A.; Huan, T. N.; Zanna, S.; Taverna, D.; Galvão Tizei, L. H.; Giaume, D.; Marcus, P.; Mougél, V.; Fontecave, M. Carbon-Nanotube-Supported Copper Polyphthalocyanine for Efficient and Selective Electrocatalytic CO₂ Reduction to CO. *ChemSusChem* 2020, 13 (1), 173–179.
- (9) Liu, M.; Pang, Y.; Zhang, B.; De Luna, P.; Voznyy, O.; Xu, J.; Zheng, X.; Dinh, C. T.; Fan, F.; Cao, C.; de Arquer, F. P. G.; Safaei, T. S.; Mepham, A.; Klinkova, A.; Kumacheva, E.; Filleter, T.; Sinton, D.; Kelley, S. O.; Sargent, E. H. Enhanced Electrocatalytic CO₂ Reduction via Field-Induced Reagent Concentration. *Nature* 2016, 537 (7620), 382–386.

Article 2:

A pyrene-triazacyclononane anchor affords high operational stability for CO₂RR by a CNT-supported histidine-tagged CODH

Graphical Abstract



The results presented in Chapter 2 strongly encouraged us to continue to improve the electrochemical performances of recombinant *RrCODH*. As presented in Chapter 1, non-specific enzymatic immobilization on the electrode surface is useful for starting to study a redox enzyme and avoid drawbacks such as partial unfolding of the biocatalyst.

However, the “soft” immobilization of the enzyme often results in poor stability over time, as shown in Chapter 2 for the Rec*RrCODH*^{CTJ} by chronoamperometry under CO₂. Another bottleneck of non-specific immobilization is the inability to control the orientation of the catalysts on the electrode surface.

For these reasons we decided to study the possibility of immobilizing the recombinant *RrCODH* *via* affinity interactions in order to improve its stability over time and to better control the orientation of the enzyme at the electrode surface. Our strategy was based on the affinity immobilization provided by the nitrilotriacetic acid (NTA) chemistry, as previously shown for glucose oxidase, laccase and nitrate reductase (Campbell et al., 2013)(Sosna et al., 2013)(Holzinger et al., 2011)(Balland et al., 2008)(Haddour et al., 2005). This electrode functionalization strategy allows the formation of oriented and fully electroactive enzymatic monolayer. Initially, NTA was developed for the purification of engineered proteins *via* the formation of specific metal coordination interactions between NTA and histidine-tagged recombinant proteins.

We have already successfully exploited the NTA-Ni to obtain a pure Rec*RrCODH* preparation, thus our idea was to use the same technology to immobilize the *RrCODH* to the MWCNT-based electrode. Our strategy also involved the use of an alternative to the NTA ligand by studying the triazaciclone-Ni complex at the electrode to provide increased stability towards enzyme immobilization. Another purpose of this study was to provide insights on the O₂ resistance or inhibition of CODH from *R. rubrum*, based on the observed differences in terms of catalytic activities and O₂ reactivity of the different monofunctional [NiFe]-CODHs.

A pyrene-triazacyclononane anchor affords high operational stability for CO₂RR by a CNT-supported histidine-tagged CODH

Umberto Contaldo,^[a,b] Mathieu Curtil,^[a] Christine Cavazza,^{*[b]} and Alan Le Goff^{ff[a]}

[a] U. Contaldo, M. Curtil, Dr A. Le Goff
Univ. Grenoble Alpes, DCM UMR 5250, BIOECN, F-38000, Grenoble, France
E-mail: alan.le-goff@univ-grenoble-alpes.fr

[b] U. Contaldo, C. Cavazza
Univ. Grenoble Alpes, CEA, CNRS, IRIG, CBM, F-38000 Grenoble, France
E-mail: christine.cavazza@cea.fr

Supporting information for this article is given via a link at the end of the document.

Abstract: An original 1-acetato-4-(1-pyrenyl)-1,4,7-triazacyclononane (AcPyTACN) was synthesized for the immobilization of the his-tagged recombinant CODH from *Rhodospirillum rubrum* (RrCODH) on carbon-nanotube electrodes. The strong binding of the enzyme at the Ni-AcPyTACN complex affords high current density of 4.9 mA cm⁻² towards electro-enzymatic CO₂ reduction and high stability of more than 3 × 10⁶ TON when integrated in a gas-diffusion bioelectrode.

Great efforts have been devoted to synthesize catalysts for the CO₂ reduction reaction (CO₂RR) into valuable chemicals or fuels such as CO, HCOOH or CH₃OH with 100% selectivity. In particular, synthesizing rare-metal-free catalysts for the CO₂-to-CO reduction reaction is aimed at designing the next generation of cost-effective and industrially-viable CO₂ electrolyzers.^[1–6] In this matter, many efficient molecular catalysts have been recently developed based on iron, nickel, molybdenum or cobalt complexes.^[2,7–11] However, many of these catalysts possess substantial overpotential towards CO₂RR, associated with competing H₂ evolution and, often, require the use of organic solvents, high temperature or alkaline media. In nature, Ni-dependent carbon monoxide dehydrogenase (CODH) is responsible for the reversible reduction of CO₂ to CO and the concomitant biosynthesis of chemicals such as ethanol, acetate, methane or formate. Owing to billion years of evolution, CODHs achieve the CO₂RR with a high catalytic activity, at near neutral pHs and with minimal overpotential.^[12–17] However, their inactivation by O₂ is a limiting factor for their use in operational devices either for CO oxidation or CO₂ reduction.^[12] Studies of CO oxidation in the presence of O₂ have demonstrated that an inactive state is formed which can only be partially reactivated. Furthermore, this reactivation is highly dependent of the nature of the CODH and its mechanism is mostly unknown.^[13,18,19] Beyond that point, competitive inhibition of CO₂RR by oxygen is also a major challenge in the global design of CO₂RR catalyst. O₂ can either directly inhibit catalysts or its reduction into H₂O₂ can compete with CO₂ reduction or produce highly reactive species such hydroxide radicals or H₂O₂, especially when catalysts do not meet minimal overpotential requirement.^[20] The high catalytic efficiency of CODH has been further evidenced when the enzyme is immobilized at the surface of an electrode, CODH behaving as a reversible electrocatalyst towards both electro-enzymatic CO₂RR and CO oxidation.

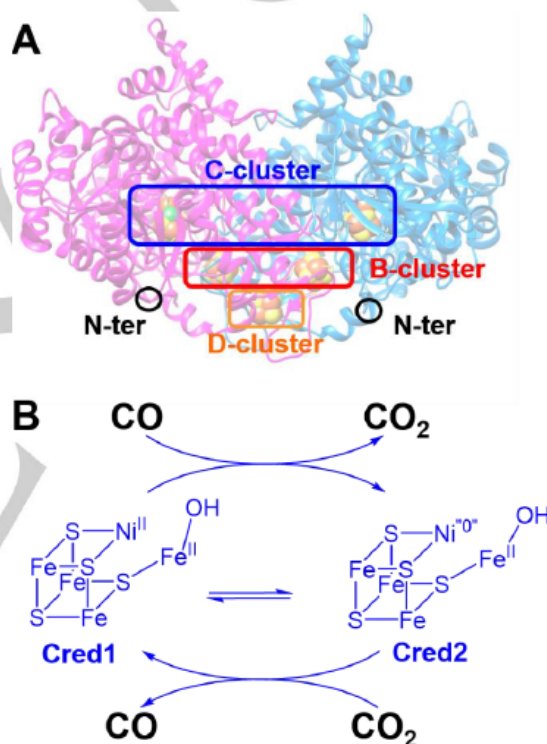


Figure 1. (A) Schematic representation of RrCODH dimer indicating C-clusters, B-clusters, D-cluster and N-terminal positions. (B) simplified mechanism for the reversible CO₂ reduction at the C-cluster involving Cred1 and Cred2 states

We have recently developed the engineering of one of the most efficient CODH towards CO₂RR.^[16]

The recombinant CODH from *Rhodospirillum rubrum* (Rec-RrCODH) was combined with functionalized carbon-nanotube-based electrodes, achieving high performance towards CO₂RR. However, the immobilization of this Rec-RrCODH relied on hydrophobic interactions owing to a Direct-Electron-Transfer (DET) promoter, 1-pyrenebutyric acid adamantyl amide. Thus, stability up to 8 × 10⁵ TON were observed over one hour. The immobilization of biomolecules on surfaces and nanomaterials via specific interactions is a powerful tool in

bioanalytical sciences.^[21] To do that, a variety of tags can be easily and reproducibly introduced at the surface or at the terminal positions of biomolecules without any loss of their biological activity. Such immobilization strategies are mostly based on supramolecular interactions, favoring self-assembly of the bioentities on surfaces. These strategies provide many advantages over covalent chemistry or polymer since biological activity is barely affected by the immobilization process. One of the most well-known approaches is the modification of surfaces with the chelating ligand nitrilotriacetic acid (NTA) followed by the complexation of a divalent metal ion such as Cu^{2+} , Ni^{2+} or Co^{2+} .^[21,22] This metal complex has a strong affinity towards poly-histidine sequences and this tool is largely used in protein analysis, notably for the purification of histidine tagged enzymes. This strategy was therefore successfully adapted at the surface of electrodes for biosensor and biofuel cell applications.^[21,23–25] through the synthesis of pyrene-NTA (PyNTA) molecules.^[26] Pyrene is a soft and stable way of functionalization of CNT sidewalls by π - π interactions between pyrene and graphene walls for the immobilization of enzymes.^[27–32] This type of bifunctional molecule allows the subsequent immobilization of biomolecules via the Ni-NTA anchoring group. Recently L. Martin and colleagues developed the use of self-assembled monolayer on gold using a thiol modified with a 1-acetato-4-benzyl-triazacyclononane, (AcbzTacn) moiety.^[33] This moiety possesses a similar 4-atom metal-binding site, but with an increase in the stabilization of the metal/ligand interaction via a macrocycle effect^[33–35]. This type of ligand, whose synthesis has been previously developed by Spiccia et al.^[36] have shown superior selectivity and stability towards the immobilization of simple redox his-tagged proteins such as thioredoxin, plastocyanin and Green Fluorescent Protein.^[33] In this work, we synthesized an original 1-acetato-4-(1-pyrenyl)-1,4,7-triazacyclononane (AcPyTACN). We took advantage of this TACN moiety for the immobilization of his-tagged redox enzymes at CNT sidewalls. We demonstrate the efficient functionalization of CNTs via the AcPyTACN and the achievement of highly-stable low overpotential CO_2RR at gas-diffusion bioelectrodes, accompanied with improved oxygen tolerance.

AcPyTACN was synthesized as a hydrochloride salt in 4 steps starting from 1,4,7 triazatricyclo[5.2.1.0^{4,10}]decane (figure 2).

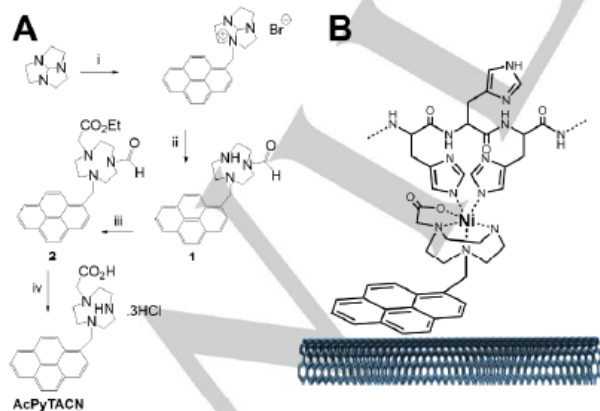


Figure 2. (A) Synthesis of AcPyTACN: (i) $\text{BrCH}_2\text{pyrene}/\text{THF}$; (ii) NaOH ; (iii) $\text{BrCH}_2\text{CO}_2\text{Et}/\text{Na}_2\text{CO}_3/\text{CH}_3\text{CN}$; (iv) HCl/reflux ; (B) Ni complexes formed from the MWCNT sidewalls modified with AcPyTACN for the binding of histidine tagged enzymes

This starting derivative was prepared from the commercially available 1,4,7-triazacyclononane as previously described.^[37,38] This derivative reacts with 1-pyrenylmethyl bromide in THF affording the corresponding monoamidinium bromide salt. Hydrolysis of this derivative gave access to the formyl derivative (1) in 87% yield. Reaction of 1 with ethylbromoacetate in MeCN yielded the ester derivative 2 in 63% yield after chromatography. This product was characterized by ^1H NMR and ^{13}C NMR. Characteristic ^1H NMR signals (figure S1) confirm the presence of pyrenyl, formyl and ester residues. As many compounds bearing the TACN moiety, this derivative exists as two conformational isomers in a two-third/one-third ratio, arising from a rotation allowed around the C-N amide bond^[36,39]. This product was further deprotected (removal of formyl and ester groups) in refluxing 5 M HCl, giving access to the final AcPyTACN zwitterionic derivative as a highly insoluble green solid.

The His-tagged Rec-RrCODH (Rec-RrCODH^{His}) was immobilized at MWCNT electrodes modified with AcPyTACN according to Figure 3A. MWCNT were functionalized by successive incubation steps with the pyrene solution in DMF and a solution of NiCl_2 in water. The MWCNT electrodes were finally modified by incubation of 38 μM (dimer) of Rec-RrCODH^{His} for 4 hours. Electrochemistry of pristine MWCNT and AcPyTACN-functionalized MWCNT electrodes were compared under Ar and CO_2 at pH 8.5 (Figure 3).

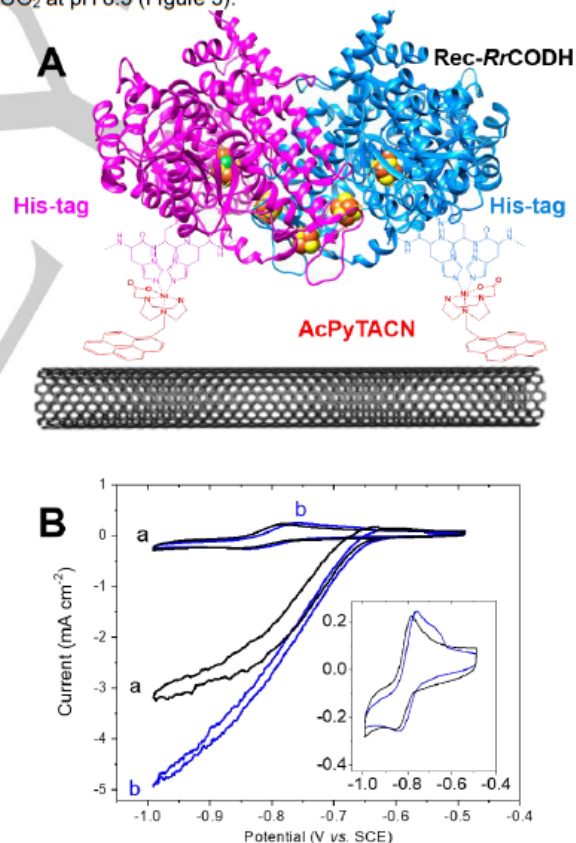


Figure 3. (A) Schematic representation of AcPyTACN-modified MWCNT for the immobilization of Rec-RrCODH^{His}. (B) CVs of Rec-RrCODH^{His}-functionalized (a, black) pristine MWCNT electrode and (b, blue) Ni-AcPyTACN-modified MWCNT electrodes under Ar and CO_2 (50 mM Tris-HCl, pH 8.5, $v = 5 \text{ mV s}^{-1}$).

A reversible redox system is observed at $E_{p1/2} = -0.59$ V vs. NHE for all electrodes, corresponding to the C_{red1}/C_{red2} bielectronic redox couple. It is noteworthy that a partial contribution to the current response is likely attributed to the reduction of traces of CO_2 in the experimental buffer. Under CO_2 , an irreversible electrocatalytic wave is observed for all electrodes with a half-wave potential of $E_{red} = -0.54$ V vs. NHE. Maximum current density of 4.9 (± 0.2) $mA\ cm^{-2}$ was measured for AcPyTACN-functionalized MWCNT electrodes while nonmodified MWCNT electrodes exhibits maximum current density of 3.1 (± 0.2) $mA\ cm^{-2}$. These results show the superior performances of AcPyTACN to immobilize Rec-RrCODH^{His}, underlining the fact that histidine tag is involved in the immobilization of the enzyme on electrodes. As previously investigated, the fact that MWCNT electrodes exhibits fairly high electrocatalytic activity mostly arises from excellent hydrophobic interactions between CODH and MWCNTs. Experiments were also performed on CODH after removal of the histidine tag (Figure S2). Surprisingly, electrocatalytic performances, as well as catalyst loadings, exhibits very similar performances with maximum current density of 4.8 $mA\ cm^{-2}$ for the AcPyTACN-functionalized MWCNT electrode. When closely looking at the N-terminal amino-acid sequence of RrCODH (where the histidine tag is introduced), the presence of three histidines and two cysteines in the first ten residues might be involved in the binding of the N-terminal domain at the Ni-AcPyTACN sites of the electrode. These results underline the ability of these sites to accommodate histidine-rich domains and further confirms their efficiency in enzyme immobilization.

In order to confirm the nature of the interactions between functionalized MWCNT and Rec-RrCODH^{His}, bio-functionalized MWCNT electrodes were incubated in the presence of increasing concentration of imidazole, a well-known competing ligand towards Ni-NTA-histidine binding. As expected, the CO_2RR is reduced after incubation with increasing concentration of imidazole. Figure 4A displays the loss of CO_2RR activity at pH 8.5 as a function of the incubating imidazole concentration. The curves exhibit a typical Langmuir-type evolution towards imidazole concentration. Upon increasing concentration of imidazole, immobilized Rec-RrCODH^{His} is progressively replaced by imidazole at TACN sites. The curves follow an apparent Langmuir-Freundlich isotherm model (see ESI for full details).^[40,41] The introduction of the Freundlich parameter is caused by the heterogeneity of the MWCNT surface towards imidazole binding. In the case of the his-tagged enzyme, it is noteworthy that no complete loss of CO_2RR activity is observed at high imidazole concentrations. The functionalized electrode exhibits only a 25 % decrease at 100 mM and a maximum decrease of 43 (± 2) % according to the Langmuir-Freundlich isotherm (i.e. at infinite imidazole concentration). For the tag-free enzyme, a decrease of 38 % is observed at 100 mM of imidazole and a maximum decrease of 94 (± 11) is given by the model. Furthermore, low affinity constants of 4 (± 1) and 12 (± 3) $L\ mol^{-1}$, for immobilized Rec-RrCODH^{His} and Rec-RrCODH respectively, confirm the strong attachment of the enzymes at the AcPyTACN-functionalized electrode. The high stability of the AcPyTACN-functionalized MWCNT electrode towards imidazole might arise from the possible binding of the Rec-RrCODH^{His} via at least four histidine groups per dimer in the best conditions, as depicted in figure 3A.

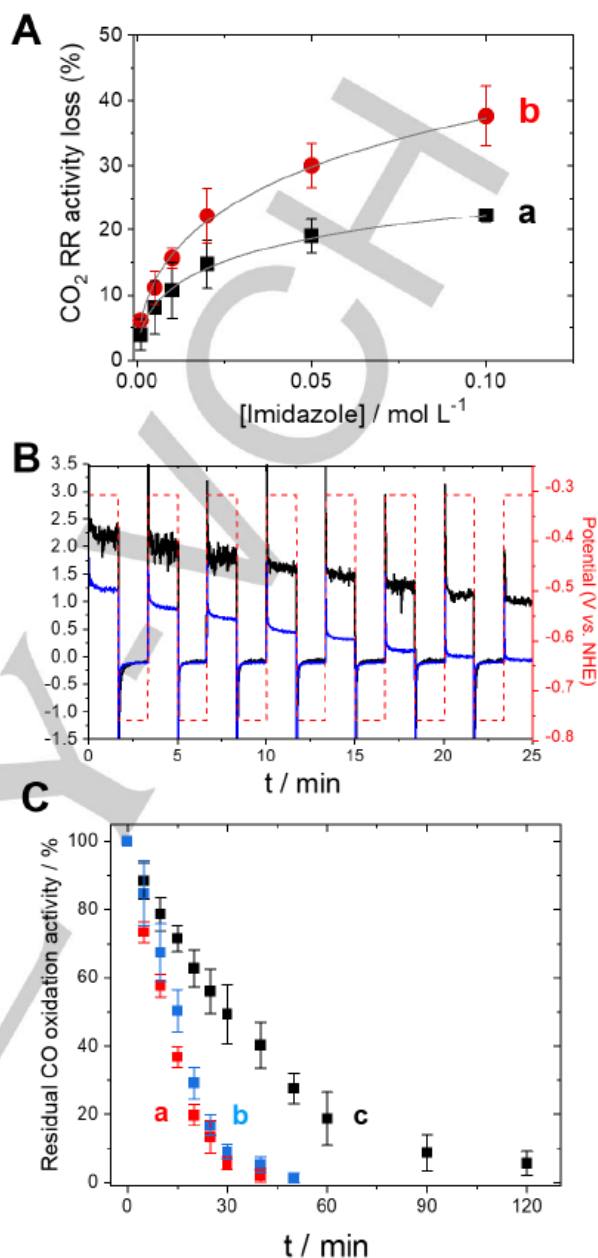


Figure 4. (A) Plot of the CO_2RR activity loss towards incubation (5 min) of imidazole with AcPyTACN-modified MWCNT electrodes with (■) Rec-RrCODH^{His} and (●) Rec-RrCODH (under CO_2 , 50 mM Tris-HCl, pH 8.5, $v = 5$ $mV\ s^{-1}$) and corresponding simulated curves using a Langmuir-Freundlich isotherm model (gray line, see ESI for details); (B) Chronoamperometry performed at E_p in CO -saturated pH 8.5 phosphate buffer for his-tagged Rec-RrCODH immobilized at (a) AcPyTACN-modified MWCNT electrode and (b) nonmodified electrode after increasing time exposure to air and reactivation at E_p for 100 seconds; (C) Plot of the residual CO oxidation activity towards increasing time exposure to air for (a) Rec-RrCODH^{His} in solution, (b) Rec-RrCODH^{His} immobilized at non modified MWCNT electrode and (c) Rec-RrCODH^{His} immobilized at AcPyTACN-modified MWCNT electrode

AcPyTACN provides a homogenous attachment of enzymes as it has already been observed for the immobilization of simple proteins on TACN-based SAM on gold electrodes.^[33]

After confirming the immobilization of CODH at AcPyTACN-functionalized MWCNT electrodes, we investigated the oxygen tolerance of immobilized CODH at these functionalized electrodes. First, the electrocatalytic CO₂RR for AcPyTACN-functionalized MWCNT electrodes and nonmodified electrodes were compared towards increasing time exposure to air. Figure 4B displays the remaining electrocatalytic activity measured by chronoamperometry under CO performed at -0.31 V vs. SHE. CO oxidation was chosen in order to compare heterogeneous CO oxidation with CO oxidation measured in solution in the presence of DDT/DTH/MV redox partners. After each exposure to air, a reduction step is performed at -0.79 V for 100 s in order to reactivate the enzyme towards CO oxidation. As it has been demonstrated before, irreversible deactivation is observed for CODH after exposure to air.^[18,19] Rec-RrCODH^{His} exhibits similar stability towards air exposure either in solution or immobilized on nonmodified MWCNTs retaining only 5 % of activity after 30 min. On the contrary, Rec-RrCODH^{His} still retains almost 10 % of activity (220 $\mu\text{A cm}^{-2}$) after 90 min exposure to air. These experiments show that the AcPyTACN anchors not only provide stable immobilization of CODH but also improve oxygen tolerance of the enzyme. This likely arises from the high biocatalyst surface coverage offered by the nanostructured MWCNT, making substrate diffusion the limiting step of the catalysis. A favorable orientation of the enzyme at the surface of MWCNTs might also protect either the D/B-cluster or C-cluster from oxygen deactivation. Another aspect of this improved stability might also be increased by the presence of two His-tags in the enzyme, one per monomer. It is noteworthy that CO oxidation is also inhibited by the presence of oxygen in the solution. If an oxygen-saturated buffer is added in the solution, complete deactivation of the electrocatalytic signal is observed when oxygen is added at a concentration of 178 μM . On the contrary, no inhibition is observed for CO₂ reduction when similar amounts of oxygen are added (figure S3). Although CODH have better affinity for CO than CO₂ (K_m in the μM range vs. mM range), this is consistent with the fact that O₂, such as other inhibitors of CODH (CN⁻ for instance) binds to the Cred1 state of the enzyme, likely at the Ni centre, and can be reversibly reactivated upon reduction.^[13] The existence of this reactivation upon reduction indicates that oxygen has negligible reactivity towards the C_{red2} state at the potential at which CO₂RR is performed, i.e. -0.8 V vs. SHE.

We recently developed a CO₂-diffusion bioelectrochemical cell where the enzyme is able to operate at a three-phase boundary.^[16] This type of cell allows the integration of CODH at a gas-diffusion electrode, ensuring efficient CO₂ flux towards CODH, while maintaining the enzyme in its optimal buffer. Furthermore, no stirring of the solution is required and negligible acidification of the electrolyte is observed since CO₂ is not directly purged in the electrolyte. Figure 5A displays a typical CV performed at a gas-diffusion electrode modified with Ni-AcPyTACN-functionalized MWCNT and Rec-RrCODH^{His}. A maximum current density of 3.2 mA cm⁻² is obtained. It is noteworthy that current density is lower as compared to MWCNT electrodes in solution. In addition to the absence of stirring, this arises from non-optimized three-phase boundary where gas accessibility needs to be optimized at immobilized enzymes in contact with the electrolyte. The stability

of different type of electrode were compared under constant applied potential of for 6 hours, corresponding to an overpotential of 180 mV (Figure 5B).

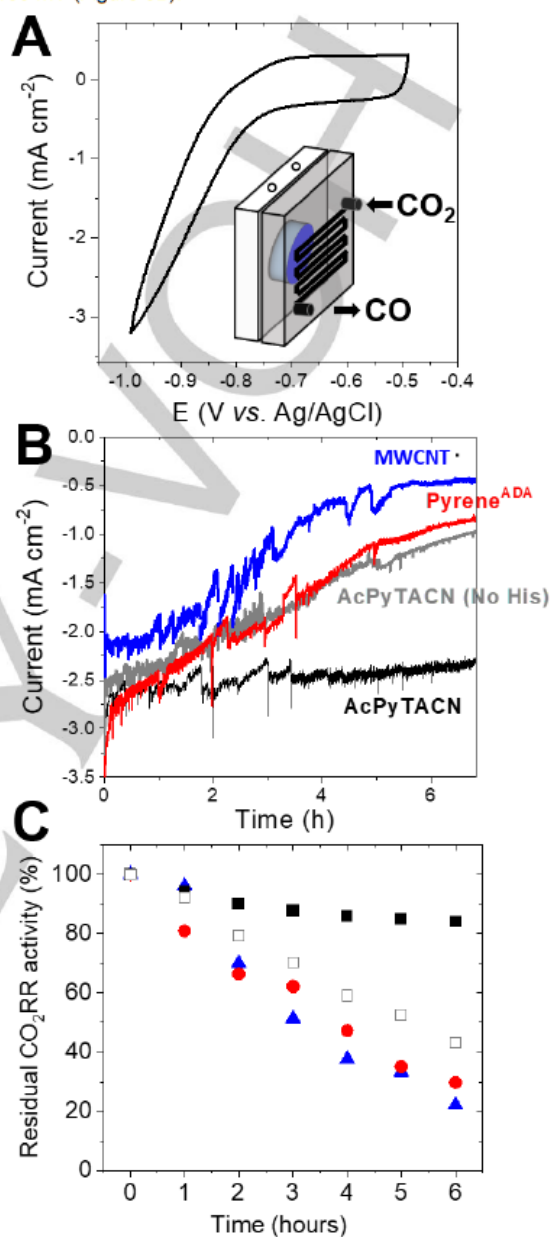


Figure 5. (A) CVs of the Rec-RrCODH^{His}-functionalized Ni-TACN-modified gas-diffusion bioelectrode under Ar, CO and CO₂ (50 mM Tris-HCl, pH 8.5, $\nu = 5 \text{ mV s}^{-1}$). (inset) Schematic representation of the gas-diffusion electrochemical cell; (B) Chronoamperometry performed at -0.8 V vs. NHE under CO₂ for 6 hours under CO₂ for (black) Rec-RrCODH^{His} immobilized at nonmodified MWCNT electrode, (red) Rec-RrCODH^{His} immobilized at pyrene^{ADA}-modified MWCNT electrode, (gray) Rec-RrCODH immobilized at AcPyTACN-modified MWCNT electrode and (blue) his-tagged Rec-RrCODH immobilized at AcPyTACN-modified MWCNT electrode. (C) Residual CO₂RR activity measured each hour for (▲) Rec-RrCODH^{His} immobilized at nonmodified MWCNT electrode, (●) Rec-RrCODH^{His} immobilized at pyrene^{ADA}-modified MWCNT electrode, (□) Rec-RrCODH immobilized at AcPyTACN-modified MWCNT electrode and (◆) Rec-RrCODH^{His} immobilized at AcPyTACN-modified MWCNT electrode.

On nonmodified MWCNT electrode, CO₂RR current density rapidly decreases over time, showing a residual activity of 22 % of the starting CO₂RR current density after 6 hours. Despite higher enzyme surface coverage and starting current density, MWCNT electrodes modified with pyrene^{ADA} exhibit a residual activity of 29 %. Rec-RrCODH immobilized at AcPyTACN-modified electrodes shows higher stability with residual activity of 43%. For the immobilization of Rec-RrCODH^{His} at Ni-AcPyTACN-modified MWCNT electrode, a small decrease is observed after 6 hours and a residual activity of 85 % is measured corresponding to current density of 2.3 mA cm⁻². This corresponds to a TON of 3 10⁶ and an average TOF of over 6 hours. These results unambiguously demonstrate the high stability of the enzyme binding at these electrodes, outperforming stability performances in any other configurations. These performances are in line with the best catalysts for CO₂RR which are either based on highly efficient gold-based nanomaterials^[42] or based on CNT-supported molecular catalysts such as cobalt azamacrocycles.^[43–45]

This work shows the combination of a high-performance CODH and an original pyrene anchor to achieve efficient and stable CO₂ reduction at near-zero overpotential with improved stability towards air exposure and negligible inhibition of oxygen during catalysis. The use of such original TACN-based anchor molecules for the immobilization of high-performance metalloenzymes open new perspectives in enzyme immobilization for electrocatalytic applications. Next developments towards enzymatic CO₂RR will aim at understanding and improving irreversible oxidative inactivation by this family of enzymes to improve their further integration in operational devices such as CO₂ electrolyzers.

Acknowledgements

This work was supported by the Agence Nationale de la Recherche through the LabEx ARCANÉ program (ANR-11-LABX-0003-01) and the Graduate School on Chemistry, Biology and Health of Univ Grenoble Alpes CBH-EUR-GS (ANR-17-EURE-0003). The authors acknowledge support from the plateforme de Chimie NanoBio ICMG FR 2607 (PCN-ICMG) and Plateau Synthèse Organique (PSO-DCM).

Keywords: carbon monoxide dehydrogenase • pyrene • carbon nanotubes • CO₂ reduction • azamacrocycle

- [1] T. R. Cook, D. K. Dogutan, S. Y. Reece, Y. Surendranath, T. S. Teets, D. G. Nocera, *Chem. Rev.* **2010**, *110*, 6474–6502.
- [2] K. Torbensen, B. Boudry, D. Joulié, N. von Wolff, M. Robert, *Current Opinion in Electrochemistry* **2020**, *24*, 49–55.
- [3] C. Costentin, M. Robert, J.-M. Savéant, *Chem. Soc. Rev.* **2013**, *42*, 2423–2436.
- [4] K. Torbensen, D. Joulié, S. Ren, M. Wang, D. Salvatore, C. P. Berlinguette, M. Robert, *ACS Energy Lett.* **2020**, *5*, 1512–1518.
- [5] R. I. Masel, Z. Liu, H. Yang, J. J. Kaczur, D. Carrillo, S. Ren, D. Salvatore, C. P. Berlinguette, *Nat. Nanotechnol.* **2021**, *16*, 118–128.
- [6] S. Jin, Z. Hao, K. Zhang, Z. Yan, J. Chen, *Angewandte Chemie International Edition* **2021**, *60*, 20627–20648.
- [7] S. Ren, D. Joulié, D. Salvatore, K. Torbensen, M. Wang, M. Robert, C. P. Berlinguette, *Science* **2019**.
- [8] L. Sun, V. Reddu, A. C. Fisher, X. Wang, *Energy Environ. Sci.* **2020**, *13*, 374–403.
- [9] D.-C. Liu, D.-C. Zhong, T.-B. Lu, *EnergyChem* **2020**, *2*, 100034.
- [10] P. Gotico, Z. Halime, A. Aukauloo, *Dalton Trans.* **2020**, *49*, 2381–2396.
- [11] S. Amanullah, P. Saha, A. Nayek, M. Estak Ahmed, A. Dey, *Chemical Society Reviews* **2021**, *50*, 3755–3823.
- [12] M. Can, F. A. Armstrong, S. W. Ragsdale, *Chem. Rev.* **2014**, *114*, 4149–4174.
- [13] V. C.-C. Wang, S. T. A. Islam, M. Can, S. W. Ragsdale, F. A. Armstrong, *J. Phys. Chem. B* **2015**, *119*, 13690–13697.
- [14] A. Parkin, J. Seravalli, K. A. Vincent, S. W. Ragsdale, F. A. Armstrong, *J. Am. Chem. Soc.* **2007**, *129*, 10328–10329.
- [15] V. C.-C. Wang, S. W. Ragsdale, F. A. Armstrong, *ChemBioChem* **2013**, *14*, 1845–1851.
- [16] U. Contaldo, B. Migliarelli, J. Perard, C. Rinaldi, A. Le Goff, C. Cavazza, *ACS Catal.* **2021**, 5808–5817.
- [17] M. Alfano, C. Cavazza, *Sustainable Energy & Fuels* **2018**, *2*, 1653–1670.
- [18] L. Domnik, M. Merrouch, S. Goetzl, J.-H. Jeoung, C. Leger, S. Dementin, V. Fourmond, H. Dobbek, *Angew. Chem.-Int. Edit.* **2017**, *56*, 15466–15469.
- [19] M. Merrouch, J. Hadj-Said, L. Domnik, H. Dobbek, C. Leger, S. Dementin, V. Fourmond, *Chem.-Eur. J.* **2015**, *21*, 18934–18938.
- [20] B. Mondal, P. Sen, A. Rana, D. Saha, P. Das, A. Dey, *ACS Catal.* **2019**, *9*, 3895–3899.
- [21] M. Holzinger, A. L. Goff, S. Cosnier, *New J. Chem.* **2014**, *38*, 5173–5180.
- [22] C. Ley, D. Holtmann, K.-M. Mangold, J. Schrader, *Colloids and Surfaces B: Biointerfaces* **2011**, *88*, 539–551.
- [23] N. Haddour, S. Cosnier, C. Gondran, **2005**, 5752–5753.
- [24] W. H. Campbell, J. Henig, N. Plumeré, *Bioelectrochemistry* **2013**, *93*, 46–50.
- [25] W. Yao, A. Le Goff, N. Spinelli, M. Holzinger, G.-W. Diao, D. Shan, E. Defranco, S. Cosnier, *Biosens. Bioelectron.* **2013**, 556–562.
- [26] M. Holzinger, J. Baur, R. Haddad, X. Wang, S. Cosnier, *Chem. Commun.* **2011**, 2450–2452.
- [27] A. Le Goff, K. Gorgy, M. Holzinger, R. Haddad, M. Zimmerman, S. Cosnier, *Chem. Eur. J.* **2011**, *17*, 10216–10221.
- [28] L. Fritea, A. J. Gross, B. Reuillard, K. Gorgy, S. Cosnier, A. Le Goff, *ChemElectroChem* **2019**, *6*, 3621–3626.
- [29] N. Lalaoui, R. David, H. Jamet, M. Holzinger, A. Le Goff, S. Cosnier, *ACS Catal.* **2016**, *6*, 4259–4264.
- [30] B. Reuillard, A. Le Goff, M. Holzinger, S. Cosnier, *J. Mater. Chem. B* **2014**, *2*, 2228–2232.
- [31] B. Reuillard, A. Le Goff, S. Cosnier, *Chem. Commun.* **2014**, *50*, 11731–11734.
- [32] N. Lalaoui, P. Rousselot-Pailley, V. Robert, Y. Mekmouche, R. Villalonga, M. Holzinger, S. Cosnier, T. Tron, A. Le Goff, *ACS Catal.* **2016**, *6*, 1894–1900.
- [33] D. L. Johnson, L. L. Martin, *J. Am. Chem. Soc.* **2005**, *127*, 2018–2019.
- [34] D. K. Cabbiness, D. W. Margerum, *J. Am. Chem. Soc.* **1969**, *91*, 6540–6541.
- [35] F. P. Hinz, D. W. Margerum, *Inorg. Chem.* **1974**, *13*, 2941–2949.
- [36] A. Warden, B. Graham, M. T. W. Hearn, L. Spiccia, *Org. Lett.* **2001**, *3*, 2855–2858.
- [37] T. J. Atkins, *J. Am. Chem. Soc.* **1980**, *102*, 6364–6365.
- [38] G. R. Weisman, V. Johnson, R. E. Fiala, *Tetrahedron Letters* **1980**, *21*, 3635–3638.
- [39] A. J. Blake, I. A. Fallis, S. Parsons, S. A. Ross, M. Schröder, *J. Chem. Soc., Dalton Trans.* **1996**, 525–532.
- [40] F. Haddache, A. Le Goff, B. Reuillard, K. Gorgy, C. Gondran, N. Spinelli, E. Defranco, S. Cosnier, *Chem. Eur. J.* **2014**, *20*, 15555–15560.
- [41] S. Sharma, G. P. Agarwal, *Anal. Biochem.* **2001**, *288*, 126–140.
- [42] M. Liu, Y. Pang, B. Zhang, P. De Luna, O. Voznyy, J. Xu, X. Zheng, C. T. Dinh, F. Fan, C. Cao, F. P. G. de Arquer, T. S. Safaei, A. Mepham, A. Klinkova, E. Kumacheva, T. Filletier, D. Sinton, S. O. Kelley, E. H. Sargent, *Nature* **2016**, *537*, 382–386.
- [43] M. Wang, L. Chen, T.-C. Lau, M. Robert, *Angewandte Chemie International Edition* **2018**, *57*, 7769–7773.
- [44] X. Zhang, Z. Wu, X. Zhang, L. Li, Y. Li, H. Xu, X. Li, X. Yu, Z. Zhang, Y. Liang, H. Wang, *Nature Communications* **2017**, *8*, 14675.
- [45] L. Sun, Z. Huang, V. Reddu, T. Su, A. C. Fisher, X. Wang, *Angewandte Chemie International Edition* **2020**, *59*, 17104–17109.

Supporting Information for:

A pyrene-triazacyclononane anchor affords high operational stability for CO₂RR by a CNT-supported histidine-tagged CODH

Umberto Contaldo,^[a,b] Mathieu Curtil,^[a] Christine Cavazza,^{*[b]} and Alan Le Goff^{*[a]}

[a] U. Contaldo, M. Curtil, Dr A. Le Goff
Univ. Grenoble Alpes, DCM UMR 5250, BIOCEM, F-38000, Grenoble, France
E-mail: alan.le-goff@univ-grenoble-alpes.fr

[b] U. Contaldo, C. Cavazza
Univ. Grenoble Alpes, CEA, CNRS, IRIG, CBM, F-38000 Grenoble, France
E-mail: christine.cavazza@cea.fr

1. Materials and methods

Materials and Instruments. 1-pyrenebutyric acid adamantyl amide was prepared as previously described.^[1] All reagents were purchased from Sigma Aldrich. Commercial grade thin Multi-Walled Carbon Nanotubes (MWCNT, 9.5 nm diameter, purity > 99%). Carbon nanomaterials were used as received without any purification. RecRrCODH was co-produced in presence of the three Ni-chaperones (*RrCooC*, *RrCooT* and *RrCooJ*) and isolated as previously described.^[2] When not used, the enzymes were stored at 4 °C. All the reagents were used without further purification. All solvents were of analytical grade. Distilled water was passed through a Milli-Q water purification system. Acetonitrile (HPLC) grade used for electrochemistry was obtained from VWR chemicals and used after drying on 4 Å molecular sieves. NMR spectra were recorded on a Bruker AM 300 (¹H at 300 MHz, ¹³C at 75 MHz) or a Bruker Avance 400 (¹H at 400 MHz, ¹³C at 100 MHz). Chemical shifts are given relative to solvent residual peak. Mass spectra were recorded on a Bruker Esquire 3000 (ESI/Ion Trap) equipment.

Electrochemical analysis. The electrochemical experiments in aqueous media were performed in 50 mM TrisHCl buffer pH 8.5 in a three-electrode electrochemical cell, using a Biologic VMP3 Multi Potentiostat, inside an anaerobic glove box (O₂ <2 ppm, Jacomex). The surface of GC electrodes was polished with a 2 μm diamond paste purchased from Presi (France) and rinsed successively with water, acetone, and ethanol. A Pt wire placed was used as counter electrode, and the SCE or Ag/AgCl served as reference electrodes.

2. Synthesis of the ligands

Synthetic procedures for compound 1 and 2:

Addition of **1-Pyrenylmethyl bromide** (555mg, 1.87mmol) to a solution of tacn orthoamide (260 mg, 1.87 mmol) in tetrahydrofuran (6 ml) produced a precipitate almost immediately. Stirring was continued for another 30 minutes after which the product was filtered and washed with absolute ethanol (2 x 2 ml) and ether (3 x 2 ml). The green solid was then dissolved in water (6 mL) and heated at reflux for 4 hours. The solution pH was adjusted to 12 with NaOH, the product was extracted into chloroform (4 x 10 ml), the extracts dried over magnesium sulfate and the solvent removed under reduced pressure to give **1** (411 mg, 87 % yield). **1** (411mg, 1.1 mmol) was then dissolved in acetonitrile (30 mL), sodium carbonate (3 g) and ethyl bromoacetate (252 μ L, 2.3 mmol) were added. The mixture was stirred at reflux for 6 h. Solvents were removed under reduced pressure. The crude product was dissolved in a 5M aqueous solution of NaOH (pH=12) extracted into chloroform (3 x 10 ml). The gathered extracts were dried over magnesium sulfate and the solvent removed under reduced pressure to give a viscous, yellow/orange oil. The product was purified by column CH_2Cl_2 /Acetone affording a white powder (255mg, 63% yield). ^1H NMR (400 MHz, CDCl_3), δ (ppm): 1.14 and 1.25 (3H, t, OEt, two resonance forms), 2.41 – 3.41(12H, m, CH_2 from macrocycle, two resonance forms), 3.27 and 3.39 (2H, s, NCH_2COOEt , from two resonance forms), 4.05 and 4.15 (2H, OEt, two resonance forms), 4.32 and 4.33 (2H, s, CH_2 -pyrene, from two resonance forms), 7.76-8.21 (9H, ms, CH from pyrene), 8.48 and 8.50 (1H, s, NCHO, from two resonance forms). ^{13}C NMR (100 MHz, CDCl_3) δ (ppm): 14.18 and 14.32 (CH₃), 46.72 (CH₂), 47.43 (CH₂), 50.14(CH₂), 51.12(CH₂), 53.84(CH₂), 53.94(CH₂), 54.60(CH₂), 54.80(CH₂), 54.88(CH₂), 55.56(CH₂), 57.94(CH₂), 58.08(CH₂), 58.39(CH₂), 58.47(CH₂), 60.37(CH₂), 60.43(CH₂), 61.18(CH₂), 61.71(CH₂), 76.83(CH₂), 77.09(CH₂), 77.34(CH₂), 124.04 (CH) 124.40 (CH), 124.42 (CH), 124.45 (CH), 124.76 (Cq), 124.82 (Cq), 125.01 (Cq), 125.08(CH), 125.10(CH), 125.18(CH), 125.33(CH), 125.91(CH), 126.01(CH), 127.09(CH), 127.16(CH), 127.29(CH), 127.40(CH), 127.49(CH), 128.13(CH), 128.31(CH), 129.81(Cq), 129.87(Cq), 130.88(Cq), 130.89(Cq), 130.93(Cq), 131.28(Cq), 131.33(Cq), 132.74(Cq), 133.16(Cq), 163.84 (CH), 171.78 (Cq), 172.10 (Cq)

Synthetic procedures for AcPyTACN:

Compound 2 (225 mg 0.49 mmol) was dissolved in 5M HCl (5 ml) and the solution refluxed for 3h. Removal of the solvent gave the deprotected **AcPyTACN** as a green solid.

3. Preparation of the electrodes

The working electrodes were glassy carbon and gas diffusion electrodes (3 mm diameter). N-methyl-2-pyrrolidinone (NMP) dispersion of MWCNTs were prepared by 30 minutes sonication of 5 mg MWCNTs dispersed in 1 mL NMP until homogeneous black suspension was obtained. Then 20 μ L of the MWCNTs solution were drop-casted on a GCE/GDE and NMP was removed under vacuum leaving a 5- μ m-thick film on the GCE.

Functionalisation of MWCNT with AcPyTACN or 1-pyrenebutyric acid adamantyl amide and enzyme immobilization

MWCNT-modified electrodes were soaked for 30 minutes in DMF solution containing 10 mM 1-pyrenebutyric acid adamantyl amide and after rinsed in DMF solution and two times in MilliQ water. MWCNT-modified electrodes were soaked for 30 minutes in DMF solution containing 10 mM AcPyTACN and after rinsed in DMF solution and two times in MilliQ water. The AcPyTACN functionalised MWCNT electrodes were further soaked in 10 mM NiCl₂ (MilliQ) for 30 minutes and then rinsed two times in MilliQ water.

The functionalised electrodes were then incubated for 4 hours with 25 μ L of the enzymatic His-tagged-Rec-RrCODH and Rec-RrCODH solutions (38 μ M dimer concentration pH 8.5). The latter step was carried out inside an anaerobic glove box (O₂ <2 ppm, Jacomex). The electrodes were finally washed with buffer TrisHCl 50 mM pH 8.5. When not used the electrodes were kept in buffer TrisHCl 50 mM pH 8.5.

CO oxidation activity measurements after air exposure

CO oxidation activity was assayed at 25 °C by following the reduction of methyl viologen at 604 nm [$\epsilon=13.6 \text{ mM}^{-1} \text{ cm}^{-1}$] in CO-saturated solutions containing 12 mM methyl viologen and 1 mM DTT. CODH specific activity unit is expressed as micromoles of CO oxidized per minute per milligram of protein. CODH 115 μ M (monomer) in 50 mM

TrisHCl pH 8.5, 5 mM DTT, 5 mM DTH was diluted to 23 nM (monomer) in 50 mM TrisHCl pH 8.5, remaining 1 μ M of DTT and DTH. Then, the enzyme was exposed to the air for several times (0-40 minutes) at 25 °C. The enzyme was further diluted to 5 nM (monomer) in anaerobic 50 mM TrisHCl pH 8.5, 5 mM DTT, 1 mM DTH and incubated 5 minutes in this buffer in order to pre-activate the enzyme before measuring the remaining specific activity.

4. Electrochemical analysis

The Langmuir-Freundlich model was employed to fit the experimental data, according to equation 1:^[3,4]

$$\%Loss_{eq} = \frac{\%loss_{max} \times (K_{Imid}^{app} \times [imidazole])^n}{1 + (K_{Imid}^{app} \times [imidazole])^n}$$

Where %Loss_{eq} is the percentage of CO activity loss at the equilibrium, %loss_{max} is the maximum percentage of CO activity loss at maximum imidazole concentration, K_{Imid}^{app} is the apparent association constant in water between imidazole and AcPyTACN sites at the modified electrode and n is Langmuir-Freundlich coefficient number. Table 1 shows the Langmuir-Freundlich model parameters obtained from fitting curves from Figure 4A.

Table 1. Fitting parameters for the Langmuir-Freundlich isotherm model from figure 4A.

	%Loss_{max}	K_{Imid}^{app} (L mol⁻¹)	n	R²
Rec-RrCODH	94 (+/-12)	4 (+/- 1)	0.5	0.995
His-tagged Rec-RrCODH	43 (+/-2)	12 (+/-3)	0.5	0.999

5. Figures and Tables

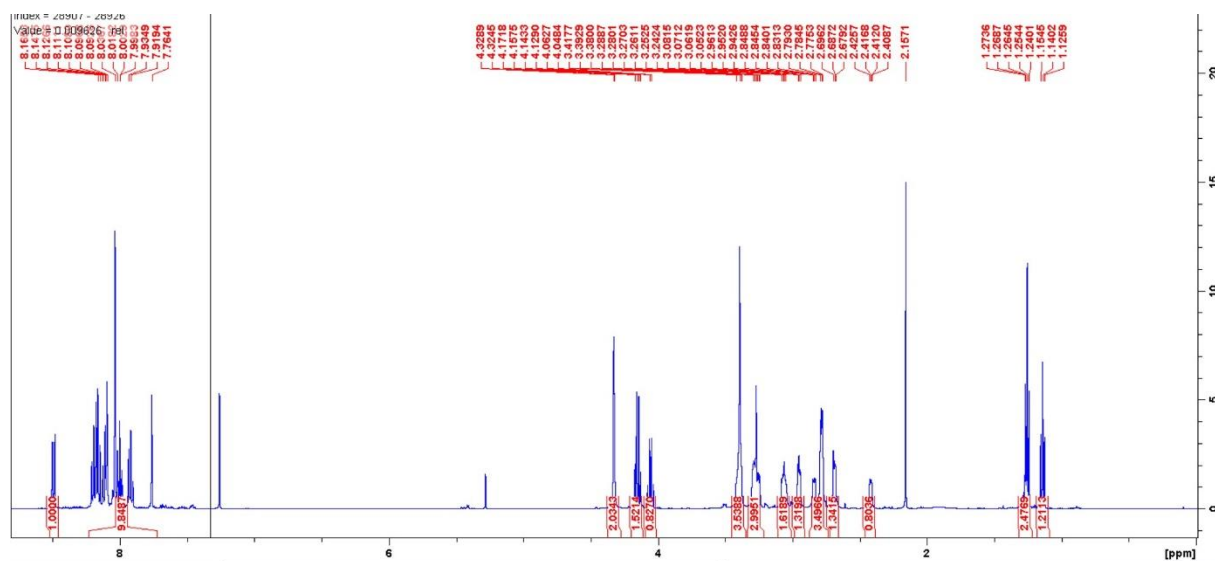


Figure S1. ^1H NMR spectrum of compound 2 in CDCl_3

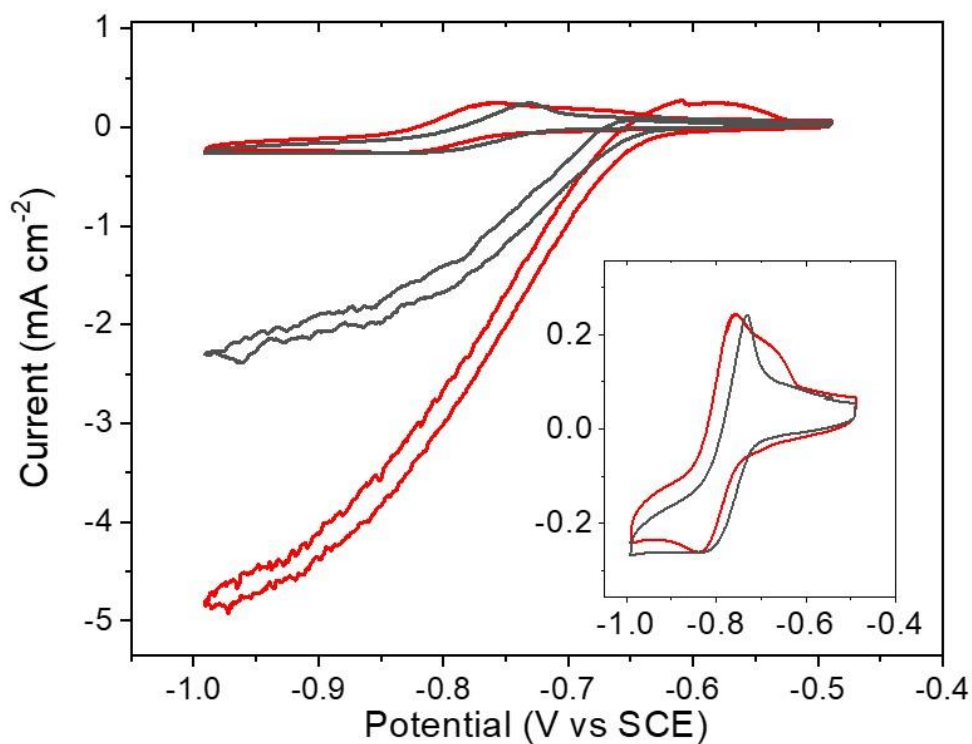


Figure S2. CVs of the Rec-*Rr*CODH-functionalized (a, black) pristine MWCNT electrode and (b, blue) Ni-AcPyTACN-modified MWCNT electrodes under Ar and CO_2 (50 mM Tris-HCl, pH 8.5, $v = 5 \text{ mV s}^{-1}$).

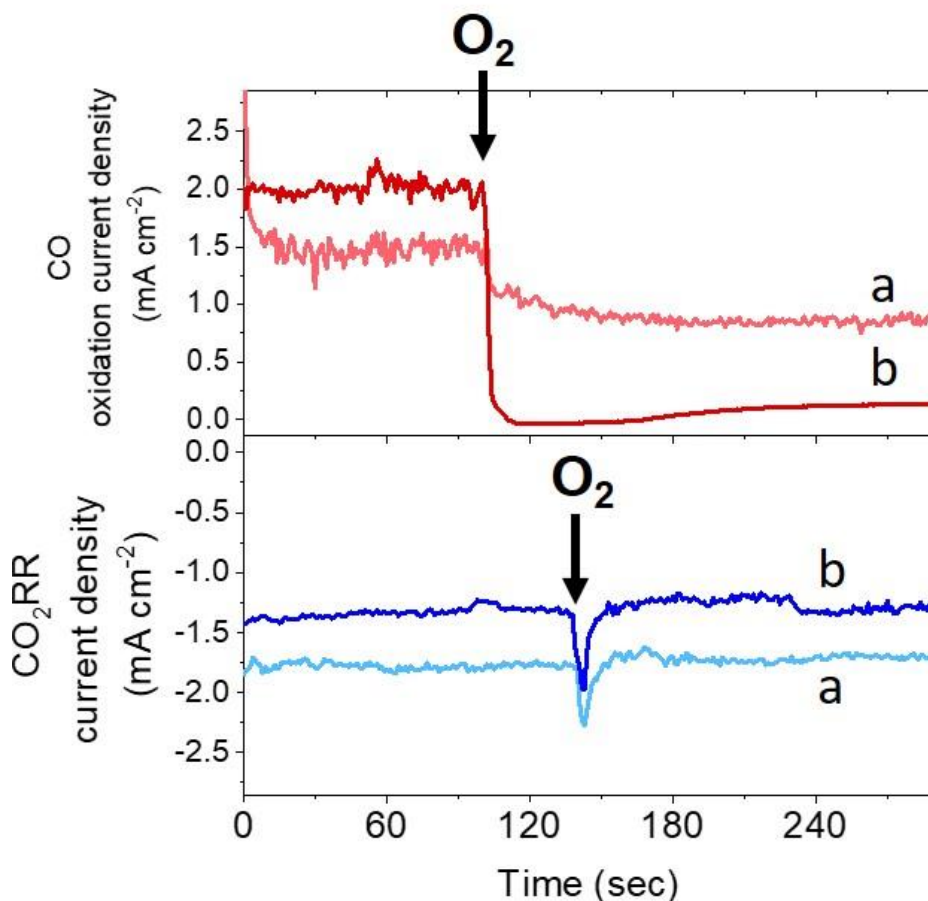


Figure S3. (up) Chronoamperometry performed at $E_p = -0.009$ V vs. SHE in CO-saturated pH 8.5 phosphate buffer for his-tagged Rec-RrCODH immobilized at **AcPyTACN**-modified MWCNT electrode after addition of (a) 95 and (b) 178 μM O₂; (down) Chronoamperometry performed at $E_p = -0.8$ V vs. SHE in CO₂-saturated pH 8.5 phosphate buffer for his-tagged Rec-RrCODH immobilized at **AcPyTACN**-modified MWCNT electrode after addition of (a) 105 and (b) 178 μM O₂ (50 mM Tris-HCl, pH 8.5)

6. References

- [1] R. Haddad, M. Holzinger, R. Villalonga, A. Neumann, J. Roots, A. Maaref, S. Cosnier, *Carbon* 2011, 49, 2571–2578.
- [2] U. Contaldo, B. Guigliarelli, J. Perard, C. Rinaldi, A. Le Goff, C. Cavazza, *ACS Catal.* 2021, 5808–5817.
- [3] F. Haddache, A. Le Goff, B. Reuillard, K. Gorgy, C. Gondran, N. Spinelli, E. Defrancq, S. Cosnier, *Chem. Eur. J.* 2014, 20, 15555–15560.
- [4] S. Sharma, G. P. Agarwal, *Anal. Biochem.* 2001, 288, 126–140.

NTA can coordinate different metal ions such as Ni^{2+} , Co^{2+} , Cu^{2+} and Fe^{3+} . In biochemistry, commercial resins based on NTA-Ni and NTA-Co are widely used for the isolation of biomolecules with histidine tags. A pyrene derivate of the NTA-Cu has also been exploited for the immobilization of biomolecules on the electrode surface (Holzinger et al., 2011). Based on these observations, we were interested in confirming that the 1,4,7-triazonane-1-carboxylic acid (TACN) moiety can also chelate different metals and retain its property for specific immobilization of the histidine-tagged RecRrCODH.

The immobilization of RecRrCODH was tested on MWCNT-based electrodes functionalized with AcPyTACN-Co and AcPyTACN-Cu, furthermore for comparison, the immobilization was also tested with pyrene derivatives of NTA-Ni, NTA-Co and NTA-Cu. The experimental procedures were performed as described above (Supporting information), except for the chelation of metal ions where 10 mM of Cobalt Sulphate or Copper Chloride was used. Cyclic voltammetry was used to characterize the electrocatalytic CO_2 reduction activity for all types of bioelectrodes in a CO_2 saturated buffer under quiescent conditions (Figure A1).

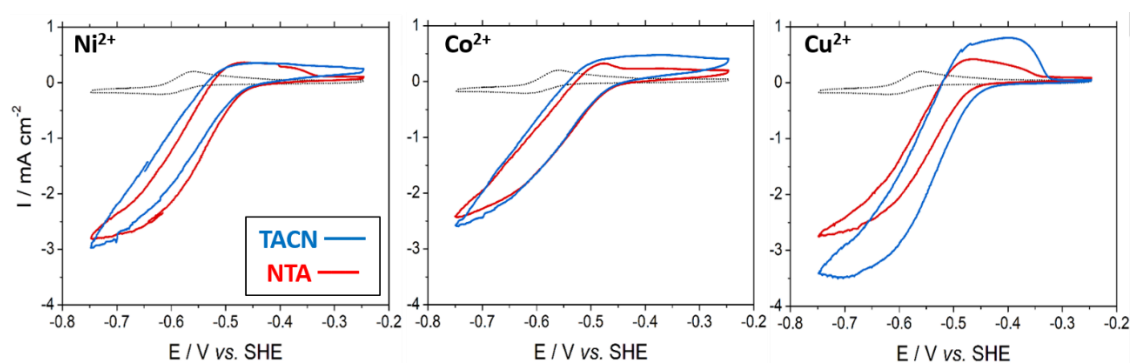


Figure A1 CVs of the RecRrCODH immobilized on AcPyTACN and NTA-pyrene MWCNT functionalized electrodes under argon (dotted) and CO_2 (solid). Experimental conditions: 50 mM Tris-HCl, pH 8.5, $\nu = 5 \text{ mV s}^{-1}$.

The achieved current densities for CO_2 reduction showed no major differences (Table A1), confirming that the TACN moiety can chelate other metal ions and maintain its specificity for His-RecRrCODH immobilization.

Table A1 Maximum current density for CO₂ reduction at -0.75 V vs. SHE achieved by RecRrCODH immobilized on different functionalized MWCNT electrodes.

MWCNT Functionalization	I / mA·cm ⁻²
NTA-Ni	2.82
TACN-Ni	2.93
NTA-Co	2.45
TACN-Co	2.61
NTA-Cu	2.76
TACN-Cu	3.38

Furthermore, based on the fact that recombinant histidine-tagged proteins are isolated from the entire cell lysate using an NTA-Ni/Co resin, we tested the possibility of directly immobilizing the RecRrCODH on an AcPyTACN-Ni functionalized MWCNT electrode from the *E. coli* cell lysate. The extract was prepared as described in Chapter 2 (Supporting information), aliquots of 50 µL were incubated 4 hours with AcPyTACN-Ni functionalized MWCNT electrode. Then, the electrode was tested by cyclic voltammetry under argon and CO₂ (Figure A2).

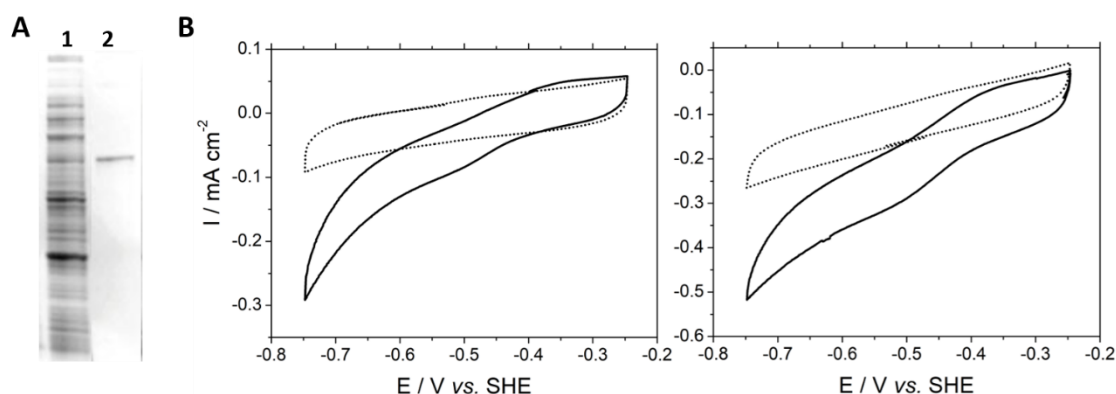


Figure A2 (A) SDS/PAGE of pure Rec-RrCODH, 0.175 µg (2) and *E. coli* whole proteins extract (1). The amount of Rec-RrCODH in the whole proteins extract can be approximate to 0.2 mg·mL⁻¹, based on the same intensity of the pure. (B) CVs of AcPyTACN-Ni-MWCNT electrodes under argon (dotted) and CO₂ (solid). Experimental conditions: 50 mM Tris-HCl, pH 8.5, $\nu = 5 \text{ mV s}^{-1}$.

The modified electrodes exhibit electrocatalytic activity even if in very diluted (about 0.2 mg·mL⁻¹). However, current densities are not high enough to conclude on a positive effect of the TACN-Ni anchoring sites towards specific immobilization of the CODH from the cell lysate. There might be competition between the histidine tagged RecRrCODH and other proteins which naturally possess a histidine tag, such as the co-expressed CooJ. The electrodes showed an average current density for CO₂ reduction of $0.44 \pm 0.11 \text{ mA}\cdot\text{cm}^{-2}$ (triplicate). These results confirm the strong affinity of the TACN-Ni moiety towards histidine-tagged proteins. To further confirm the strong affinity of AcPyTACN-Ni with histidine-tagged proteins, we also tested the immobilization of commercial

Horseradish Peroxidase (HRP). HRP was obtained from Sigma Aldrich. The enzyme is a 44 kDa monomer that contains 18% glycosylated amino acids. HRP was post-translational modified in order to chemically attach histidine residues to the carbohydrates surrounding the protein, as previously described (Blankespoor et al., 2005). The chemical modification consists in a first oxidation of the carbohydrates in aldehyde groups and then by Schiff base condensation with the amino groups of histidines. From the original work, approximately 5-6 histidine residues were added to the surface of the protein after this chemical modification without affecting enzymatic performances. Therefore, without further characterization, we tried the immobilization of His-HRP on non-functionalized MWCNT or TACN/NTA functionalized electrodes. 20 μL of His-HRP at $2 \text{ mg}\cdot\text{mL}^{-1}$ were drop casted on the functionalized electrodes and incubated 4 hours at room temperature. The results of CVs under air or in the presence of 10 mM H_2O_2 are shown in Figure A3.

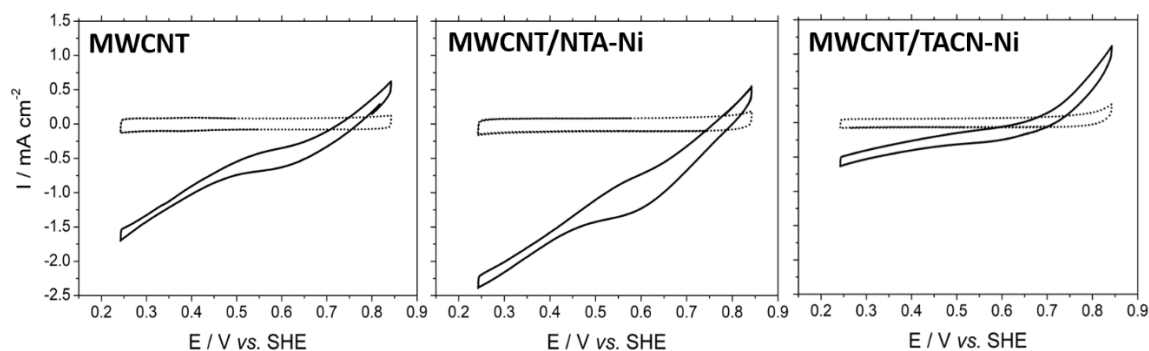


Figure A3 CVs of histidine added-HRP immobilized on different functionalized electrodes, under air (dotted) and in presence of 10 mM H_2O_2 (solid). Experimental conditions: 0.1 M PBS, pH 7.0, $\nu = 10 \text{ mV s}^{-1}$.

As expected, the current density for H_2O_2 reduction is higher in the case of NTA-Ni ($2.4 \text{ mA}\cdot\text{cm}^{-2}$) functionalized MWCNT as compared to non-functionalized MWCNT ($1.5 \text{ mA}\cdot\text{cm}^{-2}$). However, the current density of the TACN-Ni functionalized bioelectrode ($0.6 \text{ mA}\cdot\text{cm}^{-2}$) is four-times lower as compared to NTA-Ni. This was not expected since this behavior was not observed in the case of RecRrCODH immobilized on TACN-Ni electrodes. However, the fact that histidines are located at multiple and nonspecific locations at the surface of HRP, on the contrary of CODH, might have a deleterious effect on the stable immobilization of HRP as well as its integrity at the surface of the electrode. To conclude these first experiments did not confirm the strong affinity of the TACN-Ni moiety for other histidine tagged proteins. Further experiments are needed to confirm this hypothesis with other engineered proteins.

■ **Improved RecRrCODH orientation on the electrode surface.**

The ability to precisely control the orientation of the RecRrCODH on the surface of the MWCNT-based electrode was achieved by promoting self-assembly of the enzyme at the electrode surface *via* supramolecular interactions. Our results are in agreement with what was observed by L. Martin et al. and Spiccia et al. The electrocatalytic performances of the AcPyTACN-MWCNT bioelectrode exceed the previous reported for the CODH functionalized pyrene^{ADA}-modified MWCNT electrode (Chapter 2).

Bioelectrode	TON CO ₂ reduction (6 hours)	CO ₂ reduction		CO oxidation	
		I / mA·cm ⁻²	TOF (s ⁻¹)	I / mA·cm ⁻²	TOF (s ⁻¹)
AcPyTACN	3 000 000	4.9	531	2.02	211
pyrene ^{ADA}	2 300 000	2.9	289	0.35	16

■ **Original non-covalently functionalization of CNT for supramolecular enzyme immobilization.**

We provided an original MWCNT functionalization for histidine-tagged enzymes immobilization which provide enhanced electrocatalytic performances. However, in this first work it was not possible to further confirm the behavior of AcPyTACN-MWCNT electrode with other histidine tagged biomolecules such as His-HRP. At this point, it is possible to hypothesize that the strong affinity of the RecRrCODH is due to its homodimeric organization which provides two histidine tags, differently from the post-translational modified HRP. The synthesis of 1-acetato-4-(1-pyrenil)-1,4,7-triazacyclononane and NMR characterization was performed by Mathieu Curtil (*Plateau Synthèse Organique*, PSO-DCM).

- **Improved stability under aerobic conditions.**

One of the biggest bottlenecks for the development of nanodevices based on O_2 sensitive biocatalysts is their instability under aerobic conditions. In particular, [NiFe]-CODHs, unlike Hydrogenases, are irreversibly inactivated for long periods of exposure to oxidative conditions, and can be slightly reactivated even in highly reductive conditions. Our results show that achieving accurate immobilization of biocatalysts can also provide better O_2 tolerance.

- **Insight into redox dependent O_2 Inhibition of [NiFe]-CODHs.**

The dependent redox reactivity of [NiFe]-CODHs towards substrates and inhibitors has been investigated in the last decades. Regarding the reactivity of O_2 , it has been shown that C_{red1} state is the most prone to O_2 -inhibition and C_{ox} state can reduce its reactivity. Here, we showed that under catalytic conditions as well as in the C_{red2} state the enzyme is slightly affected by O_2 in the sense of CO_2 reduction. However, further characterizations are needed to confirm the reactivity of O_2 toward the C_{red2} state.

The role of D-cluster in [NiFe]-CODH from *R. rubrum*

4.1 - Introduction

As discussed in the previous chapters, the two essential parameters required for the development of biocatalytic CO₂RR nanodevices to take advantages of low overpotentials and high catalytic activity of enzymes are: I) an **efficient DET** between the active site of the enzyme and the electrode surface and II) a **stability in time** towards experimental conditions, such as temperature, pH or O₂ for oxygen-sensitive enzymes. Although several electrochemical studies, have demonstrated that *Ch*CODH-I and -II, *Dv*CODH, the two *Tc*CODHs and *Rr*CODH are able to establish a DET, the precise characterization of the electron transfer pathway in these enzymes has never been clearly understood. In particular, it is not clear if the electrons pass from C- to B-cluster and then from B- to D-cluster or directly from B-cluster to the physiological partner (Figure 1A). Indeed, the B-cluster is at a distance of 11.5 Å from the surface, which is compatible with a direct electron transfer without the requirement of the D-cluster. On the other hand, concerning their stability towards O₂, it has been shown that O₂ can inhibit the enzymes either via its direct binding to Ni atom, or via the oxidative damage of the FeS clusters impacting thus the electron relay. As show in Chapter 3, efficient anchoring of the *Rr*CODH to the MWCNT can improve the catalytic performances but also the stability towards O₂ inhibition. In support of this last result, the role of the D-cluster in O₂ resistance has recently been demonstrated in *Dv*CODH (Wittenborn et al., 2018)(Wittenborn et al., 2020). It is worth mentioning that the D-cluster in *Dv*CODH is made of a [2Fe2S] cluster instead of a [4Fe4S] cluster as observed in other described CODH (Figure 1A). In CODH, the nature of the D-cluster depends on its binding motif: C-X₂-C in the *Dv*CODH sequence instead of C-X₇-C in other CODHs (Figure 1B).

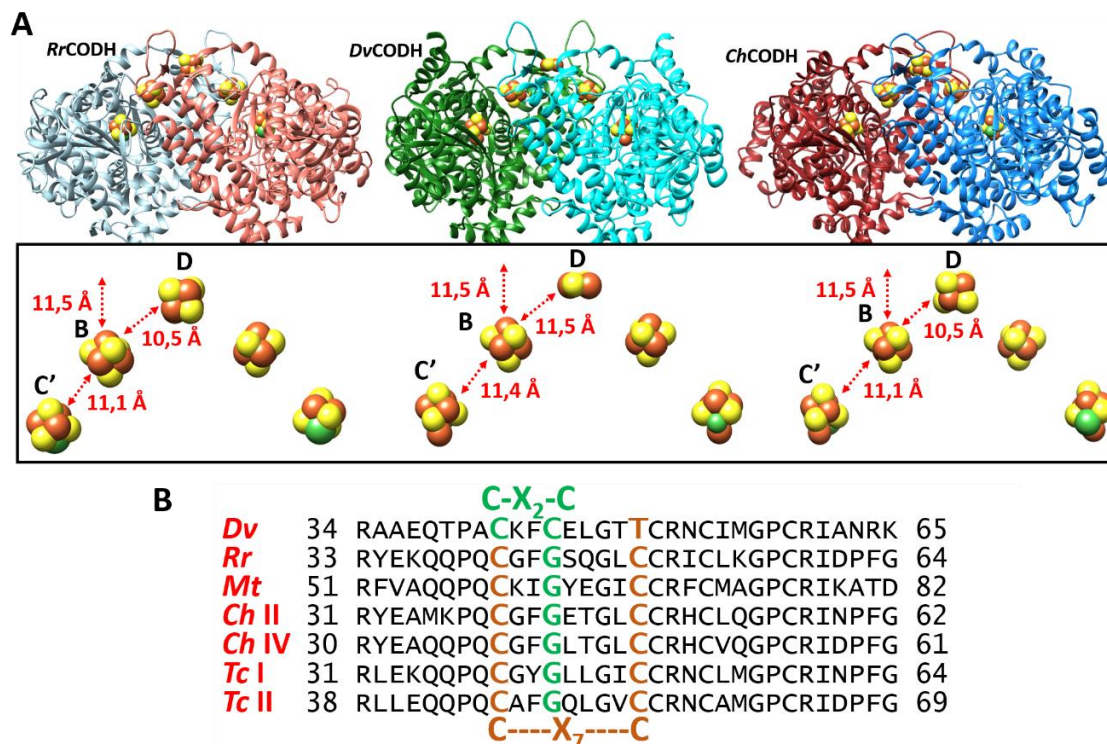


Figure 1 (A) Ribbon diagrams of monofunctional CODHs (PDB codes: *Rr* 1JQK, *Dv* 6B6V, *Ch* 6ELQ). Inset: relative cluster distances indicate in Angstrom. **(B)** CODHs amino acids sequences alignment and D-cluster motif binding.

The prolonged exposure to air (2 days) of *Dv*CODH crystals induces the formation of a catalytically inactive C-cluster in an oxidized conformation (as shown in Chapter 1 section 3.3.1) (Wittenborn et al., 2018).

However, the [2Fe2S] D- and the [4Fe4S] B-clusters are not affected by oxidative damage (Wittenborn et al., 2018). To support the hypothesis of an increase in O₂ tolerance in *Dv*CODH, a C₄₅G/T₅₀C mutant, corresponding to the replacement of the C-X₂-C motif by a C-X₇-C motif, was constructed. The crystal structure of the C₄₅G/T₅₀C mutant, solved at 1.84 Å, revealed a canonical [4Fe4S] D-cluster (Figure 2B) although its overall structure is nearly identical to that of the WT enzyme (with an rmsd of 0.27 Å for 1250 their C α atoms) and the region surrounding the D-cluster is not affected by the amino acid substitution (Figure 2A). The impact of O₂ on WT and C₄₅G/T₅₀C enzymes on the catalysis as well as the protein structure and metal center were studied. Anaerobically grown crystals of the anaerobically purified C₄₅G/T₅₀C mutant were exposed to air as a function of time.

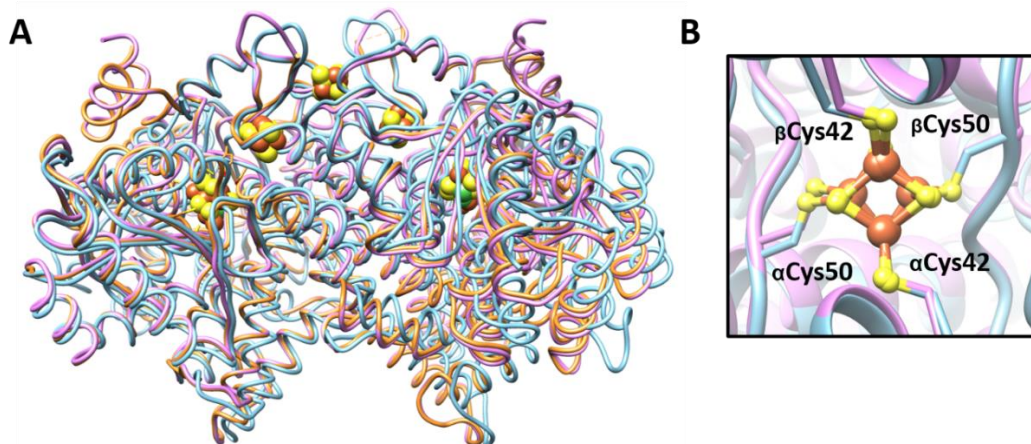


Figure 2 (A) Licorice diagram of superimposed CODHs: Rr is cyan (1JQK), Dv WT is orange (6B6Y) and C₄₅G/T₅₀C (6VWY). (B) [4Fe4S] D-cluster of Rr and Dv C₄₅G/T₅₀C CODHs coordination by Cys42 and Cys50 residues (Dv numeration).

The crystal structure collected immediately after exposure to air showed an intact [4Fe4S] D-cluster (Figure 3A), while after 2 hours, the D-cluster begins to decay as shown by the electron density which probably corresponds to a mixture of conformational states and result in the poor fit of the [4Fe4S] cluster with 30% occupancy (Figure 3B) (Wittenborn et al., 2020). After 2 days under air, the crystal structure does not longer show any electron density related to the presence of a FeS cluster (Figure 3C) (Wittenborn et al., 2020). These results show that the C₄₅G/T₅₀C mutant is less stable towards air than the WT with a complete decomposition of the D-cluster in 2 days, although the B- and C-clusters are still intact (Figure 3DE).

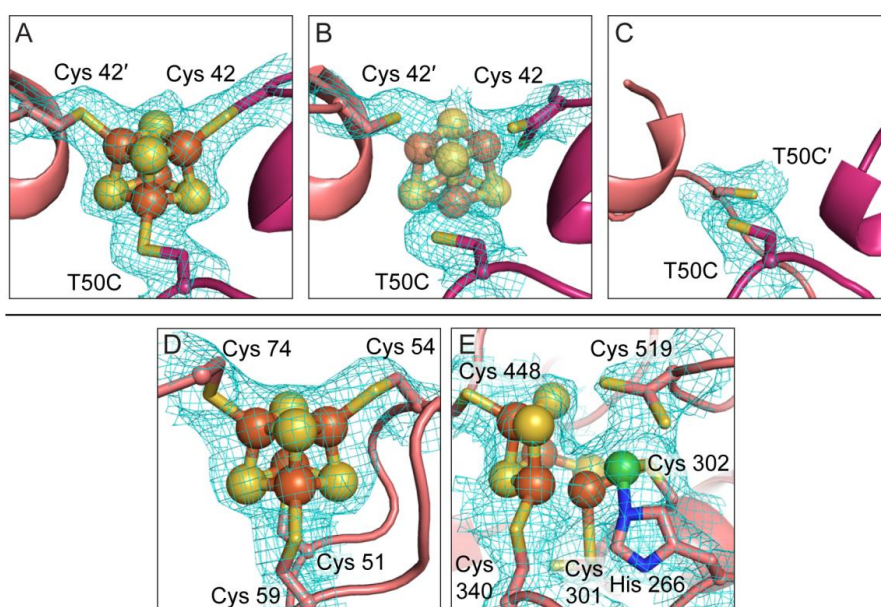


Figure 3 The [4Fe-4S] D-cluster in C₄₅G/T₅₀C Dv CODH crystals decays over time in air, whereas the B- and C-clusters remain intact. (A) 2Fo-Fc electron density at the D-cluster for crystals harvested immediately after removal from the anaerobic chamber; (B) 2Fo-Fc electron density for the D-cluster 2 hours or 2 days (C) after the crystal was removed from the anaerobic chamber; 2Fo-Fc electron density for the B-cluster (D) or C-cluster (E) 2 days after the crystal was removed from the anaerobic chamber. (Wittenborn et al., 2020).

The differences between the WT enzyme and the C₄₅G/T₅₀C mutant were further investigated at the catalytic level via electrochemical and biochemical approaches. First, the O₂ inhibition tests were performed by direct electrochemistry as described for the other CODHs (Chapter 1 section 4.4.3). However, the results revealed no major differences between the two enzymes. Then, the behavior of the WT and the C₄₅G/T₅₀C mutant produced anaerobically and purified anaerobically or aerobically was studied. Several differences were observed when the WT and the C₄₅G/T₅₀C mutant were purified aerobically, and compared to the WT enzyme purified anaerobically. Firstly, the metal content is 20% and 10% Ni/monomer and 75 % and 60 % of Fe, respectively. Secondly, the WT and C₄₅G/T₅₀C mutant purified aerobically retained only 30 % (~130 U·mg⁻¹) and 10 % (~40 U·mg⁻¹) of specific CO oxidation activity, respectively.

Furthermore, these two aerobically prepared enzyme samples were stored at 4 °C under aerobic conditions and their activity was controlled over time. After 1 day, The C₄₅G/T₅₀C mutant retains only 5 % (~20 U·mg⁻¹) of specific CO oxidation activity, while the WT in the same conditions maintain 25 % of activity (~100 U·mg⁻¹) after 8 days.

Taken together, these results strongly suggest a role of the [2Fe2S] D-cluster in *Dv*CODH in O₂ protection.

Interestingly, several functions could therefore be attributed to the D-cluster:

- A role in electron transfer.
- Due to its position at the dimer interface, the D-cluster could help with dimer stabilization.
- Depending on its nature, this cluster would provide to the enzyme a better resistance towards O₂.

We then decided to start to investigate the role of the D-cluster in *Rr*CODH, with the aim of improving its catalytic performances. During the studies, I had the opportunity to supervise a Master student Emma Colombari (this internship is about 2 months and have to be done at the end of the first year of the master program). A part of her results are presented in this chapter.

4.2 - Results

First, we designed the G₄₄C/C₄₉T *RrCODH* mutant (G₄₄C/C₄₉T) as a mimic of the WT *DvCODH* to change the C-X₇-C binding motif to a C-X₂-C one (Figure 4). We also designed single and double mutants of the two cysteines that coordinate the D-cluster: C₄₁S, C₄₉S, C₄₉T, C₄₁A/C₄₉S and C₄₁S/C₄₉S (Figure 4).

	41	44	49	
WT				33 RYEKQQPQCGFGSAGLCCRICKGPCRIDPFG 64
C ₄₉ S				33 RYEKQQPQCGFGSAGLSCRICKGPCRIDPFG 64
C ₄₉ T				33 RYEKQQPQCGFGSAGLTCRICKGPCRIDPFG 64
C ₄₁ S				33 RYEKQQPQSGFGSAGLCCRICKGPCRIDPFG 64
C ₄₁ A/C ₄₉ S				33 RYEKQQPQAGFGSAGLSCRICKGPCRIDPFG 64
C ₄₁ S/C ₄₉ S				33 RYEKQQPQSGFGSAGLSCRICKGPCRIDPFG 64
G ₄₄ C/C ₄₉ T				33 RYEKQQPQCGFCSAGLTCRICKGPCRIDPFG 64

Figure 4 Amino acids sequences of designed *RrCODH* D-cluster mutants.

4.2.1 - *RrCODH* D-cluster mutants are produced in *E. coli* under Aerobic and Anaerobic conditions.

The designed *RrCODH* mutants and the *RrCooC*, *RrCooT*, and *RrCooJ* accessory proteins were co-produced aerobically in *E. coli* following our previous established protocol (Chapter 2). Our standard anaerobic protocol was used for the purification of all mutants and led to pure enzymes in one step, with the exception of G₄₄C/C₄₉T which was difficult to concentrate, suggesting a loss of the homodimeric organization. For this mutant, several protocols were then tested in order to optimize its purification. G₄₄C/C₄₉T expression was then tested in the Rosetta2 Δ iscR strain ($_{a}G_{44}C/C_{49}T^{\Delta$ iscR), where the *isc* operon is constitutively expressed to ensure the optimum biogenesis of FeS clusters. Furthermore G₄₄C/C₄₉T was produced under anaerobic conditions namely $_{an}G_{44}C/C_{49}T$, following a method previously described for the recombinant *ChCODHs* (J. H. Jeoung & Dobbek, 2007)(Domnik et al., 2017). However, despite these optimizations, G₄₄C/C₄₉T still remains difficult to produce and purify, in comparison to the other mutants.

4.2.2 - SEC-MALLS-RI.

SEC-MALLS-RI experiments were performed to determine the homogeneity and oligomerization state of the produced *RrCODH* mutants (Figure 5). The percentage of homodimer and monomer were determined by comparison of each concentration versus the total concentration of injected sample. The results are reported in Table 1.

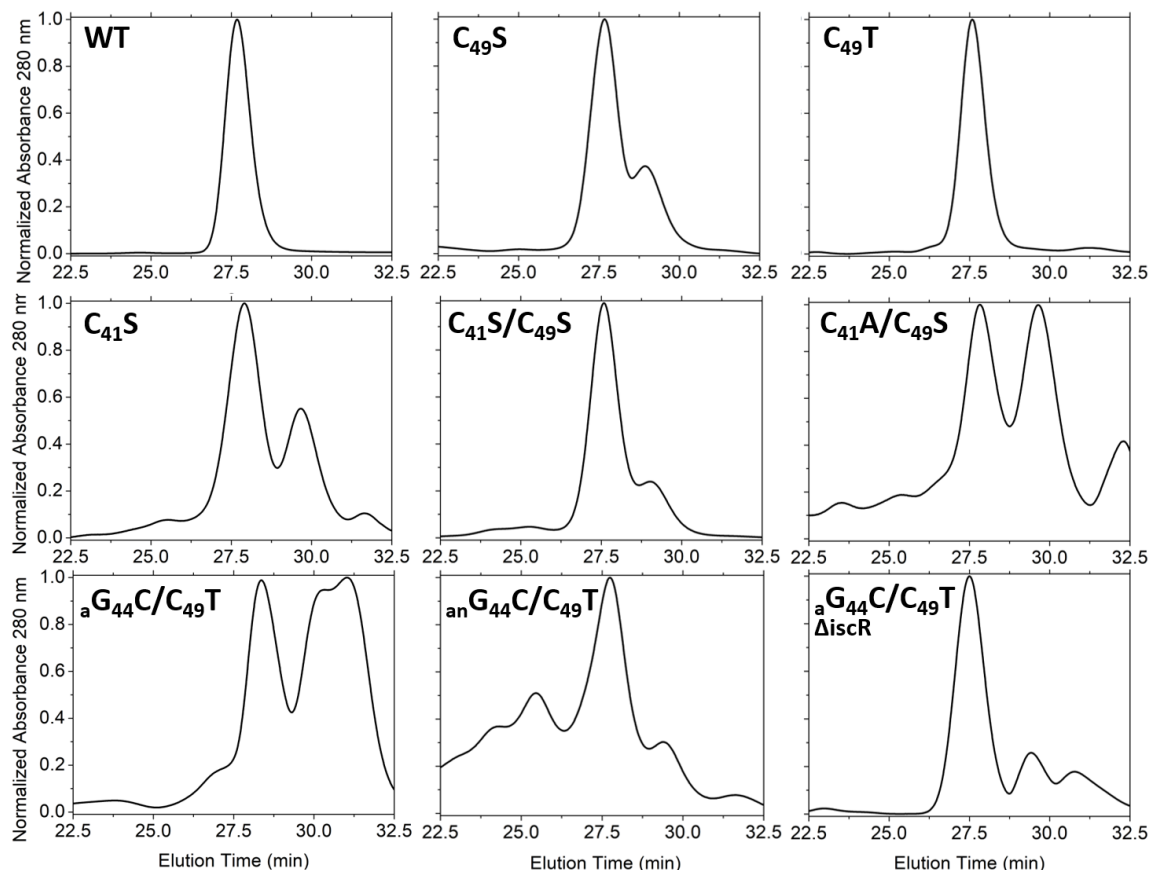


Figure 5 SEC-MALLS-RI of *RrCODH* D-cluster mutants and WT, 50 mM TrisHCl, pH 8.5, 150 mM NaCl (oxygenated buffer).

Table 1 Oligomerization percentage of *RrCODH* D-cluster mutants and WT calculated by integration of the dRI peaks from the results reported in Figure 5. The low resolution of ${}^aG_{44}C/C_{49}T$ and ${}^{an}G_{44}C/C_{49}T$ does not allow the calculations.

<i>RrCODH</i>	Tetramer/Trimer (%)	Homodimer (%)	Monomer (%)
WT	0.0	100.0	0.0
C ₄₁ S	0.2	40.0	59.8
C ₄₉ S	0.0	97.9	2.1
C ₄₉ T	0.0	100.0	0.0
C ₄₁ A/C ₄₉ S	1.2	71.3	27.5
C ₄₁ S/C ₄₉ S	1.1	87.9	10.9
${}^aG_{44}C/C_{49}T$	ND	ND	ND
${}^{an}G_{44}C/C_{49}T$	ND	ND	ND
${}^aG_{44}C/C_{49}T^{\Delta iscR}$	0.0	78	12

These results revealed an unexpected behavior of the different mutants: First in the case of Cys₄₉ mutants, the mutation of Cys into Thr (corresponding to the replacement of the thiol group by a methyl group) seems to have a greater impact on the enzyme stability than the mutation of Cys to Ser (corresponding to the replacement of the thiol group by a OH group). Second, the removal of all coordinating-cysteines in C₄₁S/C₄₉S does not impact the dimerization, while the single C₄₉S mutation does. Third, the G₄₄C/C₄₉T stability seems to be greatly increased by its expression in Rosetta2 ΔiscR strain.

To go further, we investigated the possible role of oxygen on the oligomerization state of the enzyme. Indeed, in SEC-MALLS-RI experiments, each sample was exposed to air for about 30 minutes (corresponding to the duration of the experience), which could have a great impact on the conformation of the enzyme. To answer this hypothesis, SEC-MALLS-RI experiments were used to study the behaviour of both WT and C₄₉T enzymes exposed to air for different incubation times (Figure 6).

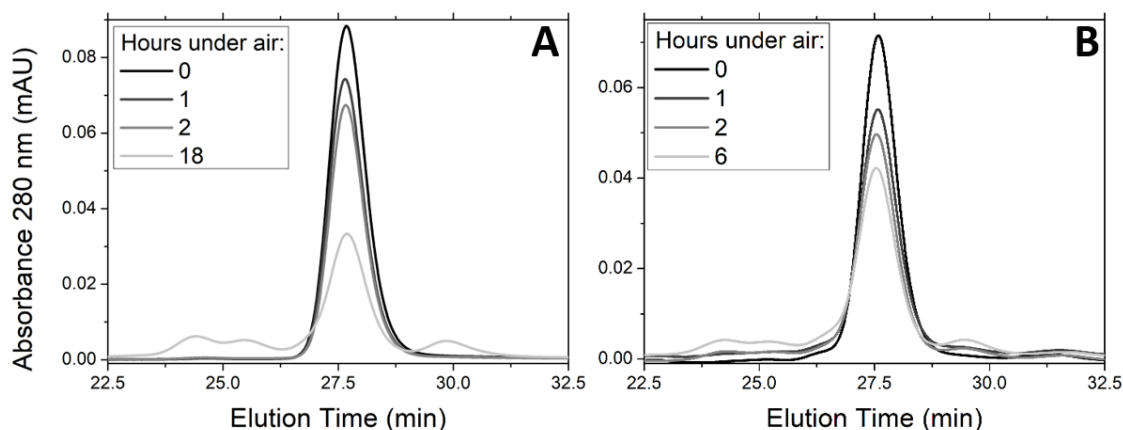


Figure 6 SEC-MALLS-RI absorbance traces of WT (A) and C₄₉T (B) RrCODHs incubated under air for different time scales prior to be manually injected.

From the chromatograms in Figure 6, different oligomerization peaks can be observed: 279-220 ± 2 kDa tetramer/trimer, 139.6 ± 2 kDa dimer, 71.8 ± 4 kDa monomer. The oligomerization percentage results from Figure 6 are shown in Table 2. In both WT and C₄₉T, the homodimeric state does not appear to be greatly impacted by air exposure and does not lead to the dissociation into monomers. However, some precipitation starts to appear at 1 h and increase with time.

Table 2 RrCODH WT and C₄₉T oligomerization incubated under air at different time scale. Percentage calculations refers to time 0 hour.

Time (Hours)	Tetramer/Trimer	Dimer	Monomer (%)	Precipitated/Aggregated
WT				
0	0.0	100.0	0.0	0.0
1	0.0	82.1	0.0	17.9
2	0.0	72.6	0.0	27.4
18	7.7	35.2	3.5	53.6
C ₄₉ T				
0	2.2	97.5	0.3	0.0
1	2.9	74.1	0.5	22.5
2	4.5	63.4	1.4	30.6
6	7.1	58.7	3.0	31.1

Therefore, the presence of mixture of monomers and dimers in the different mutants does not seem to be related to their O₂ sensitivity. However, these experiments have to be conducted on the other mutants.

4.2.3 - UV-visible spectroscopy.

All mutants displayed the typical brown color due to the presence of [4Fe4S] clusters, with the exception of the three G₄₄C/C₄₉T samples which were colorless compared to the others enzymes at the same concentration. The presence of [4Fe4S] clusters was also investigated by UV-visible spectroscopy performed on oxidized enzymes (Figure 7). The typical shoulder of the [4Fe4S] clusters and the purity coefficient (A_{420}/A_{280}) are shown in Table 3. The purity coefficient relative to the native enzyme can be used to estimate the percentage of [4Fe4S] clusters together with the determination of the iron content (Table 3). A single mutation appears then to be sufficient to lead to the loss of the coordination of the D-cluster, based on the lower than expected Fe(II) content of all mutants. In addition, the lower purity coefficient and Fe(II) content of C₄₉S, C₄₁S, C₄₁S/C₄₉S also suggest that even B- or C-clusters could be lost or converted to [2Fe2S] clusters. In the case of G₄₄C/C₄₉T and C₄₁A/C₄₉S, the UV-visible spectra revealed the total loss of [4Fe4S] clusters and the observed peaks can be rather attributed to [2Fe2S] clusters (322 and 455 nm). Further EPR experiments are required to clearly characterize the FeS clusters present in the different mutants. However, these results shows that the

absence of the D-cluster direct impacts the enzyme stability and the integrity of the B- and C-clusters.

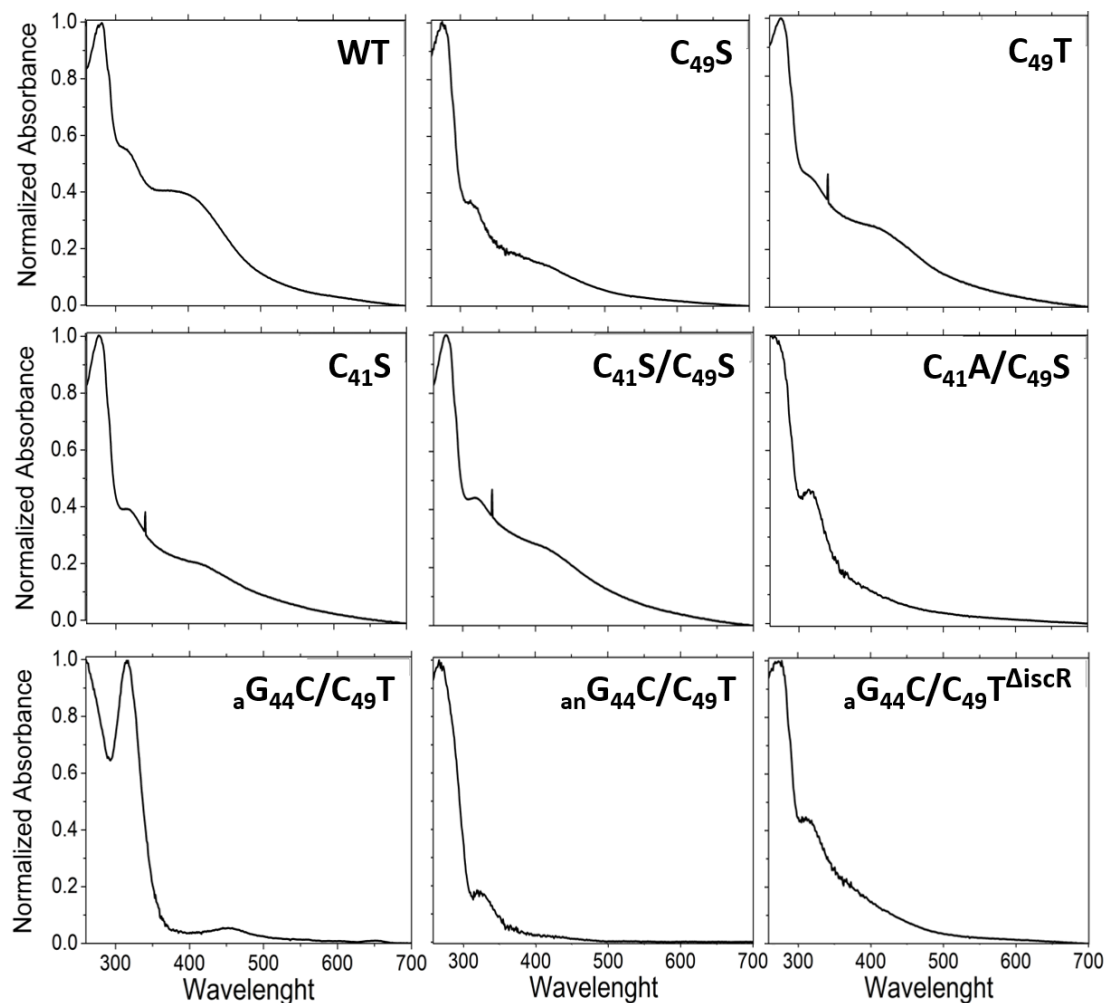


Figure 7 Normalized UV-visible absorbance spectra of oxidized pure preparations of RrCODH WT and mutants.

Table 3 RrCODH mutants purity coefficient (A_{420}/A_{280}), percentage of [4Fe4S] relative to native RrCODH and Fe(II) dosage.

Enzyme	A_{420}/A_{280}	[4Fe4S] (%)	Fe/Dimer
WT	0.38 ± 0.01	100	19.0 ± 1.0
C ₄₉ S	0.21 ± 0.05	55 ± 13	9.4 ± 1.5
C ₄₉ T	0.27 ± 0.04	75 ± 8	13.5 ± 2.5
C ₄₁ S	0.23	60	11.2 ± 1.8
C ₄₁ A/C ₄₉ S	ND	ND	6.5 ± 1.7
C ₄₁ S/C ₄₉ S	0.28 ± 0.02	74 ± 5	14.2 ± 2.7
^a G ₄₄ C/C ₄₉ T	ND	ND	4 ± 1
^{an} G ₄₄ C/C ₄₉ T	ND	ND	9.4 ± 1.11
^a G ₄₄ C/C ₄₉ T ^{ΔiscR}	ND	ND	9.4 ± 1.12

The values with error are referred to at least 2 different preparations

The stability of the different mutants towards O₂ was investigated by UV-visible spectroscopy. Samples of oxidized WT, C₄₉T, C₄₁S and C₄₁S/C₄₉T were anaerobically prepared and then exposed to air over time and UV-visible spectra were recorded every 15 minutes, in order to characterize the degradation kinetics of FeS clusters (Figure 8A).

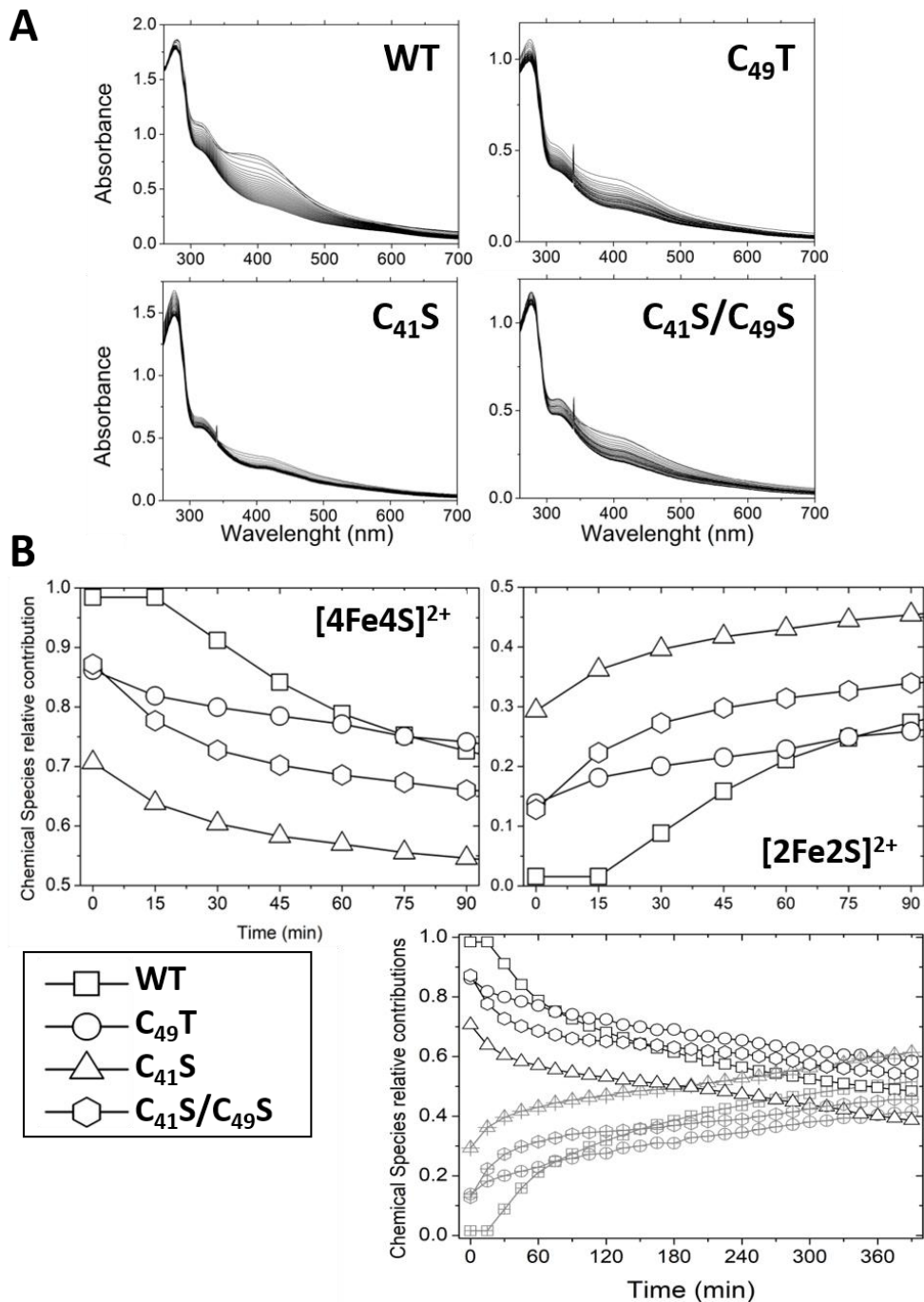


Figure 8 (A) UV-visible spectra of oxidized WT and mutants of RrCODH over time under air incubated, each spectrum was recorded every 15 minutes. **(B)** Fit-FeS v 1.1.1 spectra decomposition analysis. First 90 minutes (Up) under air time-dependent [4Fe4S] clusters decomposition (left) and [2Fe2S] clusters formation (right). And complete analysis until 390 minutes (below).

Then, semiquantitative analyses of the UV-visible spectra were performed using the software Fit-FeS v 1.1.1 (Figure 8B) (Betinol et al., 2021). As predicted by the Fe(II)

content, the mutants showed an initial [4Fe4S] content lower than the WT enzyme, but in all cases the degradation kinetics after 90 minutes under air are comparable between WT, C₄₁S and C₄₁S/C₄₉S, although WT is stable during the first 15 minutes. Surprisingly C₄₉T appeared to behave differently starting from a lower initial [4Fe4S] content and reaching the same content of WT at the end of the experiment. Similar results were also obtained for the [2Fe2S] clusters formation, a well described intermediate in the degradation process of [4Fe4S] clusters. From these first results, we can conclude that the removal of S-donors ligands induces as expected the loss of the coordination of D-cluster leading to an instability of the other FeS clusters and affecting the dimerization state of some mutants.

4.2.4 - In Solution and Electrochemical CO oxidation and CO₂ reduction activities.

To determine whether these mutants are still able to catalyze the CO-to-CO₂ interconversion, their catalytic efficiencies were investigated in solution and electrochemically. First, the activity in solution was measured for all enzymatic preparations. The enzymes were diluted in 50 mM TrisHCl, pH 8.5, 5 mM DTT and 1 mM DTH at 21 °C, then the CO oxidation activity was assayed in CO saturated 50 mM TrisHCl, pH 8.5, 1 mM DTT 12 mM methyl viologen at 25 °C (Table 4).

Table 4 Methyl Viologen-Mediated CO oxidation activity in solution and metals content of WT and D-cluster mutants of RrCODH. Theoretical specific activities are calculated relative to the WT Ni amount per dimer and specific activity.

Enzyme	Fe/Dimer	Ni/Dimer	Specific Activity (U·mg ⁻¹)	
			Measured	Theoretical
WT ¹	19.0 ± 1.0	1.6 ± 0.2	10,508	10,508
C ₄₉ S	9.4 ± 1.5	0.4 ± 0.2	6.2 ± 5	2,627
C ₄₉ T	13.5 ± 2.5	1.2 ± 0.1	4,271 ± 220	7,881
C ₄₁ S	11.2 ± 1.8	0.3 ± 0.1	514 ± 35	1,970
C ₄₁ A/C ₄₉ S	6.5 ± 1.7	0.2 ± 0.1	368 ± 17	1,313
C ₄₁ S/C ₄₉ S	14.2 ± 2.7	1.0 ± 0.2	7.8 ± 2	6,567
_a G ₄₄ C/C ₄₉ T	4 ± 1	0.2 ± 0.1	< 1	1,313
_{an} G ₄₄ C/C ₄₉ T	9.4 ± 1.11	0.2 ± 0.1	< 1	1,313
_a G ₄₄ C/C ₄₉ T ^{ΔiscR}	9.4 ± 1.12	0.4 ± 0.2	1.7 ± 0.5	2,627

¹ (Chapter 1)

As expected, _aG₄₄C/C₄₉T and _{an}G₄₄C/C₄₉T did not show any measurable activity, supported by their global instability. Surprisingly, the other RrCODHs preparations retained partial CO oxidation activity. However, the activities are lower than the theoretical expected, calculated from the linear correlation between the amount of Ni

and specific activity of the WT enzyme in the same experimental conditions. To further characterize their catalytic properties, these enzymatic preparations were studied electrochemically. *Rr*CODH D-cluster mutants were immobilized on 1-pyrenebutyric acid adamantyl amide (ADA) modified MWCNT electrodes (MWCNT^{ADA}). All enzymes preparations were diluted to 38 μ M monomer and incubated 4 hours with MWCNT^{ADA} electrodes. An investigation of the C_{red1}/C_{red2} reversible redox system was first performed under argon (Figure 9).

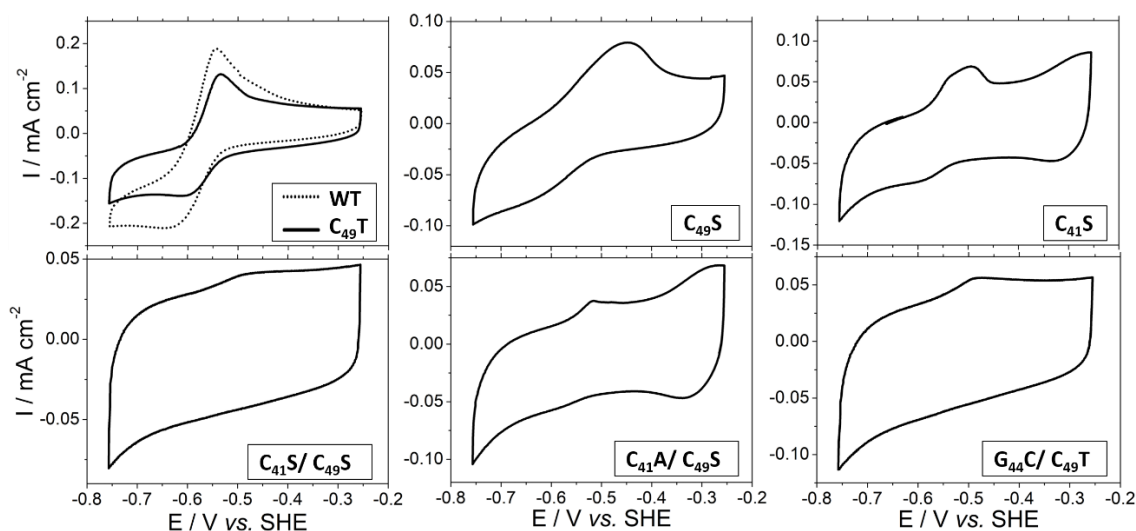


Figure 9 CVs of the D-cluster mutants and WT *Rr*CODH-functionalized MWCNT^{ADA} electrodes under Argon at pH 8.5. Experimental conditions: 50 mM TrisHCl, pH 8.5, $\nu = 5 \text{ mV s}^{-1}$.

It is interesting to note that for all mutants it was possible to observe the non-turnover redox signal and also to estimate the surface coverage (Γ_{max}) (Table 5). Due to the low Ni content, it is difficult to interpretate CV in non-turnover conditions, C_{49T} exhibits similar midpotentials as compared to WT. Despite the high Ni content of C_{41S}/C_{49S} , the non-turnover signal is negligible, indicating that electron relays and/or C clusters are non-conserved or damaged in the protein.

Table 5 Surface coverage Γ_{max} ($\text{pmol}\cdot\text{cm}^{-2}$), potentials of oxidation, reduction and half wave potentials ($E_{1/2}$) of the C_{red1}/C_{red2} redox system.

Enzyme	Γ_{max} ($\text{pmol}\cdot\text{cm}^{-2}$)	Potential (V vs. SHE)		
		Oxidation	Reduction	$E_{1/2}$
WT(Chapter 2)	52 ± 2			-0.59
WT	60	-0.54	-0.65	-0.59
C_{49S}	24	-0.45	-0.60	-0.52
C_{49T}	38	-0.54	-0.61	-0.57
C_{41S}	13	-0.49	-0.61	-0.55
C_{41A}/C_{49S}	3.2	-0.52	-0.58	-0.55
C_{41S}/C_{49S}	1.5	ND	-0.48	ND
$^aG_{44C}/C_{49T}^{\Delta\text{iscR}}$	3.5	ND	-0.47	ND

Figure 10 shows CVs of the mutant-functionalized $\text{MWCNT}^{\text{ADA}}$ under CO_2 atmosphere. Almost all enzymatic preparations showed electrocatalytic current toward the CO_2 reduction. Interestingly, for C_{49}T and C_{41}S , it was possible to observe a reversible catalysis, due to the oxidation of the CO produced from the CO_2 reduction when the potential is closed to $C_{\text{red}2}/C_{\text{red}1}$ one, showing that the enzymes are still able to catalyze the reaction in both directions.

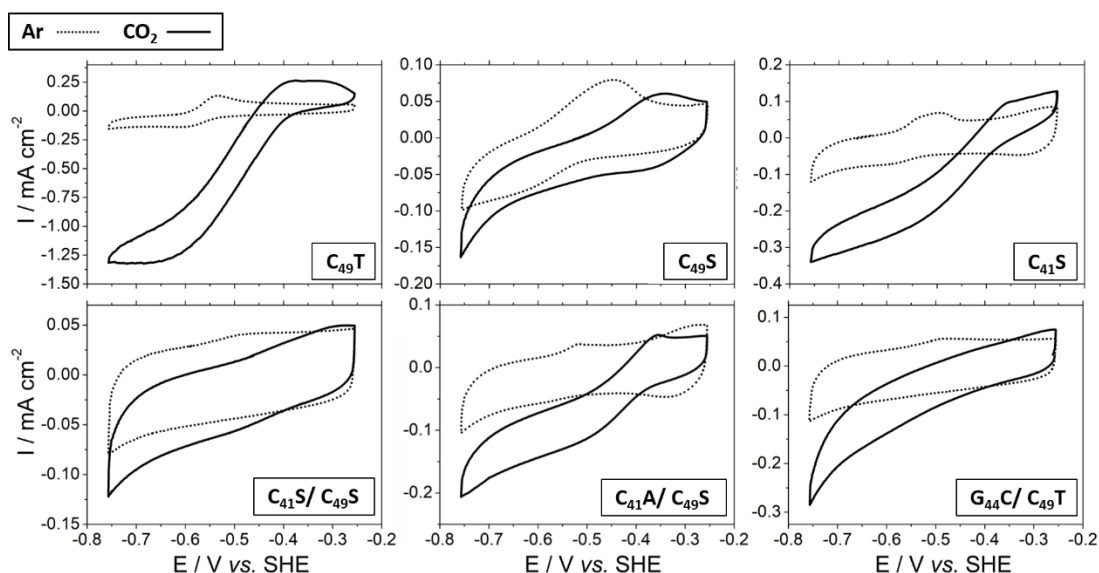


Figure 10 CVs of the D-cluster mutants RrCODH-functionalized $\text{MWCNT}^{\text{ADA}}$ electrodes under Argon (dotted) and CO_2 . Experimental conditions: 50 mM TrisHCl, pH 8.5, $\nu = 5 \text{ mV s}^{-1}$.

To further confirm this, a $\text{MWCNT}^{\text{AcPyTACN}}$ electrode was functionalized with C_{49}T following our previous described protocol (Chapter 3). The CVs were performed in CO and CO_2 saturated solutions under continuous gas flow and agitation (Figure 11).

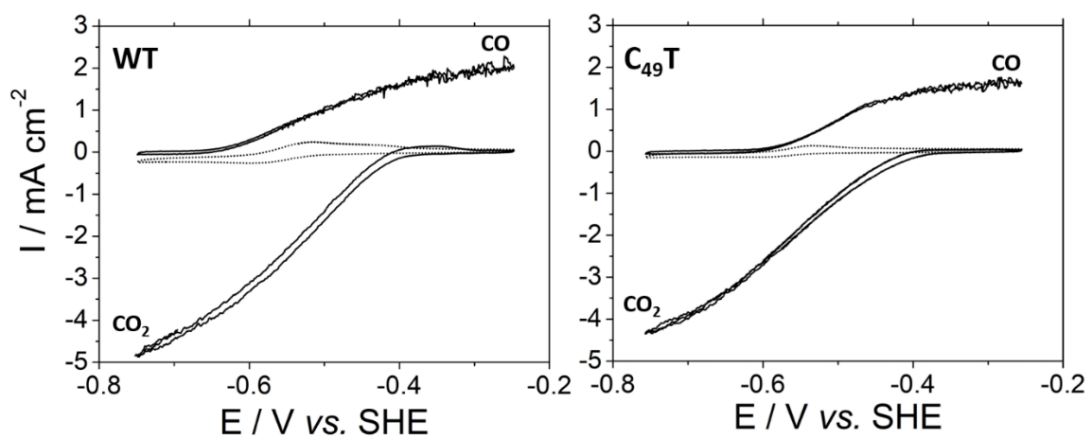


Figure 11 CVs of the WT and C_{49}T D-cluster mutant RrCODH-functionalized $\text{MWCNT}^{\text{AcPyTACN}}$ electrode under Argon (dotted) and continuous flow of CO or CO_2 . Experimental conditions: 50 mM TrisHCl, pH 8.5, $\nu = 5 \text{ mV s}^{-1}$, 1100 rpm.

C_{49}T supports well the histidine tag-induced covalent immobilization on the $\text{MWCNT}^{\text{AcPyTACN}}$ electrode, indicating that the loss of D-cluster did not affect the N-

terminus of the recombinant enzyme, as further confirmed by SEC-MALLS-RI oligomerization. Furthermore, current densities and TOF shows a similar trend to that of the C₄₉T immobilized on the MWCNT^{ADA} electrode (Table 6).

Table 6 Electrocatalytic properties and specific activities comparison between in solution and immobilized WT and D-cluster mutants of RrCODH.

RrCODH	Γ_{\max} ($\mu\text{mol}\cdot\text{cm}^{-2}$)	Electroactivity				CO oxidation in solution ($\text{U}\cdot\text{mg}^{-1}$)
		CO ₂ reduction		CO oxidation		
		i / $\text{mA}\cdot\text{cm}^{-2}$	TOF (s^{-1})	i / $\text{mA}\cdot\text{cm}^{-2}$	TOF (s^{-1})	
² WT ^{AcPyTACN}	49.8	4.9 ± 2	531	2.02 ± 1.3	211	10,430
C ₄₉ T ^{AcPyTACN}	41	4.3	542	1.65	208	4,271
¹ WT ^{ADA}	52 ± 2	2.9	289			10,508
C ₄₉ T ^{ADA}	38	1.3	177			4,271
C ₄₉ S	24	0.17	36.7			2.2
C ₄₁ S	13	0.24	ND			514
C ₄₁ A/C ₄₉ S	3.2	0.21	ND			380
C ₄₁ S/C ₄₉ S	1.5	0.12	ND			10
^a G ₄₄ C/C ₄₉ T ^{DiscR}	3.5	0.28	ND			1

¹(Chapter 2); ²(Chapter 3);

From these results we can conclude that all D-cluster mutants achieved DET once immobilized on functionalized MWCNT. Furthermore, electrocatalytic currents for each mutant follow the same trend observed with the activities measured in solution. It is noteworthy that, despite having negligible activity in solution the ^aG₄₄C/C₄₉T^{DiscR} mutant still exhibit electrocatalytic current density of 0.28 mA·cm⁻² towards CO₂RR, although the efficiency of DET seems compromised as confirmed by lower current densities and TOF compared to WT enzyme, which is in agreement with the activities measured in solution. The functionalized C₄₉T-MWCNT^{AcPyTACN} electrode was also tested in CA experiment under CO₂ saturated condition with injection of O₂ saturated (Figure 12). As demonstrated for the WT enzyme, a favorable immobilization of the RrCODH on the MWCNT surface could also improve oxygen deactivation under CO₂ catalysis (Chapter 3). The same type of experiment was performed for C₄₉T which showed a similar result, allowing to suggest that AcPyTACN anchor could improve the O₂ tolerance of the C-cluster, even in the absence of the D-cluster.

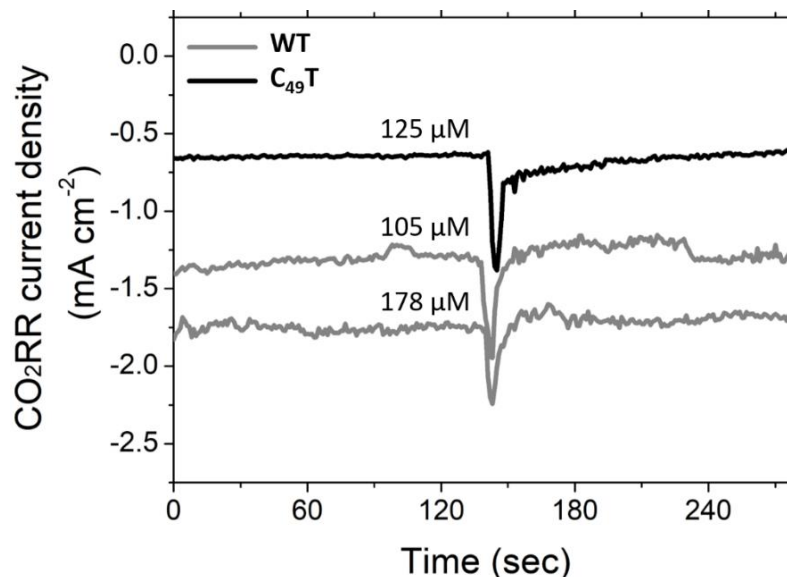


Figure 12 Chronoamperometry performed at $E_p = -0.8$ V vs. SHE in CO_2 saturated 50 mM TrisHCl, pH 8.5, of C_{49}T D-cluster mutant and WT RrCODH immobilized at AcPyTACN-modified MWCNT electrode after addition of O_2 . (WT are referred at Rec-RrCODH from Chapter 3).

4.2.5 - Crystallization of RecRrCODH.

In order to further characterize the D-cluster mutants of the RrCODH we begin a crystallographic study of the WT RecRrCODH. The only structure of RrCODH available to date (at 2.8 Å resolution) has been obtained by microcapillary batch diffusion method under argon with precipitating agents: 10 % polyethylene glycol 8000 (PEG 8k), 0.1 M TrisHCl, pH 7.5, 0.4 M calcium chloride (CaCl_2), 5 % 2-methyl-2,4-pentenediol (MPD). The RrCODH was about $20 \text{ mg}\cdot\text{mL}^{-1}$ in a first approach, we screened similar crystallization conditions by using the hanging drop vapor diffusion method under argon in a glove box (Jacomex, $\text{O}_2 < 2$ ppm) for RecRrCODH with or without His tag. However, the histidine-tagged enzyme did not yield any nucleation. Thus, only the results obtained with the enzyme where the His tag was removed will be presented. Table 7 shows the results of the first crystallization test. These first results show that for almost all tested conditions, fast protein precipitation occurred. Then in order to slow down the protein precipitation, we decided to decrease the concentration of PEG 8k and CaCl_2 as shown in Table 8.

Table 7 Crystallization conditions tested for RecRrCODH at 25 mg·mL⁻¹, mixed 50/50 with the crystallization solution.

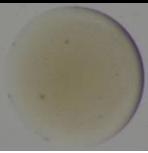
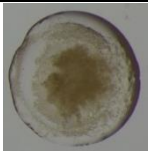
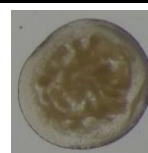
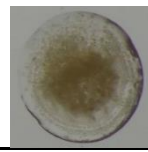
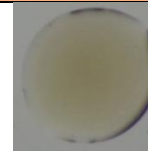
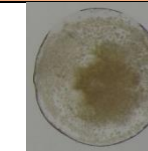
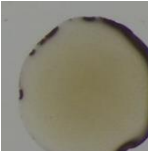
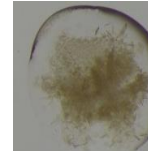
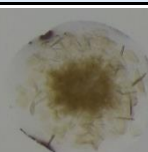
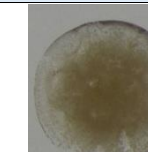
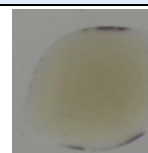
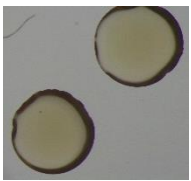
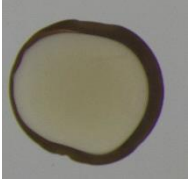
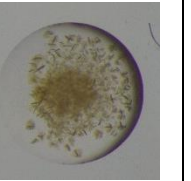
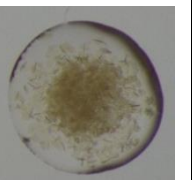
0.1 M TrisHCl, pH 7.5, 1 mM DTT, 0.4 M CaCl ₂				
PEG 8k 6 %	10 %	14 %	18 %	22 %
A1	A2	A3	A4	A5
2.5 % MPD				
				
B1	B2	B3	B4	B5
5 % MPD				
				
C1	C2	C3	C4	C5
7.5 % MPD				
				

Table 8 Crystallization conditions tested for RecRrCODH at 25 mg·mL⁻¹, mixed 50/50 with the crystallization solution.

0.1 M TrisHCl, pH 7.5, 1 mM DTT				
6 %	8 %	10 %	12 %	14 % PEG 8k
7.5 % MPD				
A1	A2	A3	A4	A5
0.2 M CaCl ₂				
				
B1	B2	B3	B4	B5
0.3M CaCl ₂				
				
C1	C2	C3	C4	C5
0.4 M CaCl ₂				
				

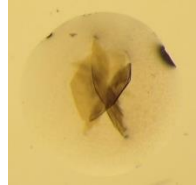
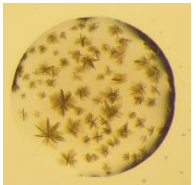
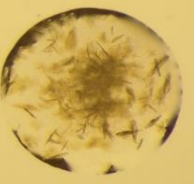
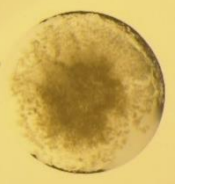
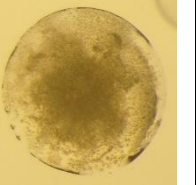
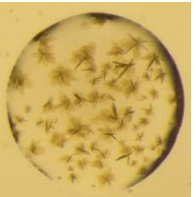
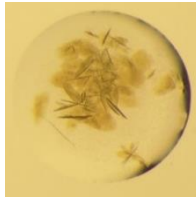
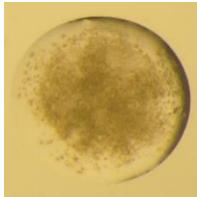
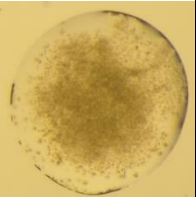
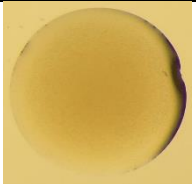
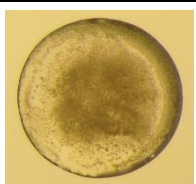
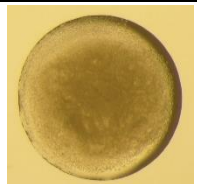
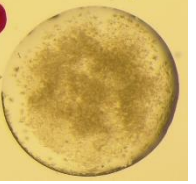
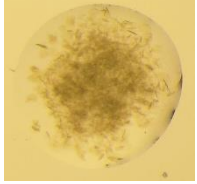
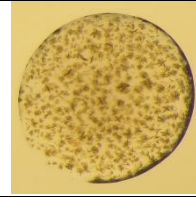
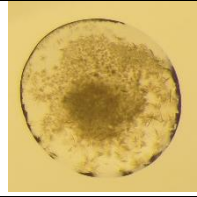
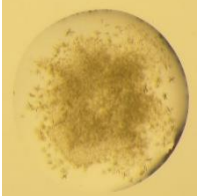
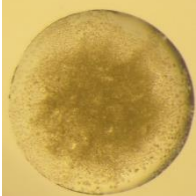
These results revealed the appearance of the first brown protein crystals with CaCl_2 and PEG 8k concentrations below 0.3 M and 10%, respectively. Based on these results we set the same range of PEG 8k concentration, with lower concentration of CaCl_2 . The results are reported in Table 9.

Table 9 Crystallization conditions tested for RecRrCODH at $25 \text{ mg}\cdot\text{mL}^{-1}$, mixed 50/50 with the crystallization solution.

0.1 M TrisHCl, pH 7.5, 1 mM DTT				
6 %	8 %	10 %	12 %	14 % PEG 8k
7.5 % MPD				
A1	A2	A3	A4	A5
0.1 M CaCl_2				
				
B1	B2	B3	B4	B5
0.15 M CaCl_2				
				
C1	C2	C3	C4	C5
0.2 M CaCl_2				
				

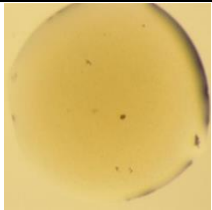
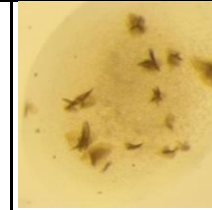
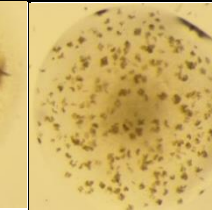
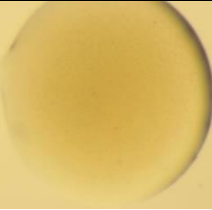
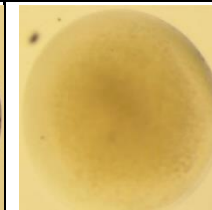
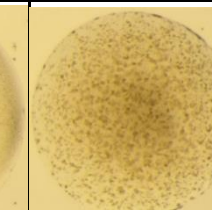
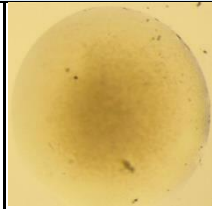
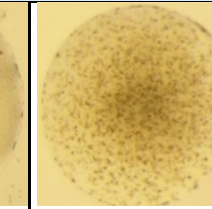
The results reported in Table 9 show a precipitation gradient of RecRrCODH. Therefore, we decided to test different percentage of MPD (Table 10). Two enzyme concentrations were tested (25 and $17.5 \text{ mg}\cdot\text{mL}^{-1}$). The first monocrystals of RecRrCODH were obtained with the A1 precipitation conditions of TrisHCl 0.1 M, pH 7.5, DTT 1 mM, CaCl_2 0.1 M, PEG 8k 6% and MPD 6%.

Table 10 Crystallization conditions tested for RecRrCODH at 25 and 17.5 mg·mL⁻¹, mixed 50/50 with the crystallization solution.

0.1 M TrisHCl, pH 7.5, 1 mM DTT					
	6 %	8 %	10 %	12 %	14 % PEG 8k
	A1	A2	A3	A4	A5
6 % MPD					
0.1 M CaCl ₂					
25 mg mL ⁻¹					
17.5 mg mL ⁻¹					
	B1	B2	B3	B4	B5
8 % MPD					
0.15 M CaCl ₂					
25 mg mL ⁻¹					
17.5 mg mL ⁻¹					
	C1	C2	C3	C4	C5
10 % MPD					
0.2 M CaCl ₂					
25 mg mL ⁻¹					
17.5 mg mL ⁻¹					

Therefore, to confirm the possibility of crystallizing the RecRrCODH, new assays were performed with a freshly purified enzyme. The conditions were screened according to the ones described in Table 10 and the best results are reported in Table 11.

Table 11 Crystallization conditions tested for RecRrCODH at 25 mg·mL⁻¹, mixed 50/50 with the crystallization solution.

TrisHCl 0.1 M, pH 7.5, DTT 1 mM				
2 %	4 %	6 %	8 %	10 % PEG 8k
A1	A2	A3	A4	A5
MPD 4 %				
CaCl₂ 0.1 M				
				
B1	B2	B3	B4	B5
MPD 6 %				
CaCl₂ 0.15 M				
				
C1	C2	C3	C4	C5
MPD 8 %				
CaCl₂ 0.2 M				
				

The results obtained with the A4, B4 and C4 conditions of Table 11 confirm that the RecRrCODH precipitation conditions are around: 6-8 % PEG 8k, 0.1 M TrisHCl, pH 7.5, 1 mM DTT, 0.1-0.2 M CaCl₂ and 4-8 % MPD. The protein crystals obtained from these last tests were cryoprotected in a mother liquor containing glycerol at 35 % and were flash-cooled by quick immersion in liquid N₂.

4.3 - Discussion & Conclusion

Based on the recent results obtained on *Dv*CODH suggesting that the [2Fe2S] D-cluster affords a better O₂ stability to the enzyme, we designed the G₄₄C/C₄₉T mutant in order to convert the [4Fe4S] D-cluster to a [2Fe2S] one in *Rr*CODH. However, in our hands, the results were very different from what was observed with *Dv*CODH. Unexpectedly, the G₄₄C/C₄₉T mutations led to the loss of almost all FeS clusters, Ni and catalytic activities. Therefore, it is possible to conclude that a simple change in the sequence of the D-cluster binding motif from C-X₇-C to C-X₂-C as performed in reverse in *Dv*CODH, is not possible in *Rr*CODH.

Hence, if we take into considerations the results of the C₄₉T mutant which showed a Fe(II) content and UV-visible absorption spectra consistent with the loss of D-cluster, the homodimeric organization appears to be unaffected which excludes a role of D-cluster in the stabilization of [NiFe]-CODHs dimers. This is also supported by high interface areas of 3846, 3469 and 3756 Å² observed in the crystal structures of *Rr*CODH, *Ch*CODH and *Dv*CODH, respectively. Furthermore, C₄₉T also displays a CO oxidation activity in solution and direct electrochemical CO/CO₂ interconversion when immobilized on the functionalized MWCNT surface. All these results show that it is possible to observe an electron transfer directly from the B-clusters to the mediator or MWCNT. This is in line with the minimal distance of 10 Å between the B-cluster and the surface of the protein allowing electron tunnelling. If we then consider a linear correlation between Ni content and catalytic activities (Figure 13A), the performance of C₄₉T is lower than expected from its Ni content, in solution: 4 271 U·mg⁻¹ vs. a theoretical value of ~7 881 U·mg⁻¹ considering 1.2 Ni/dimer and for the immobilized enzyme: 1.3 mA·cm⁻² vs. a theoretical value of 2.2 mA·cm⁻². However, some mutants, such as C₄₉T and C₄₁A/C₄₉S, appear to be less affected by the removal of the D-cluster, based on the normalized ratio of Ni content to CO₂RR activity, which showed approximately 60 % of expected specific activity (Figure 13B).

This hypothesis, in addition to the lower TOF, suggest that the D-cluster is dispensable, although its presence improves the catalytic efficiency of the enzyme. These results are reminiscent of the work performed with multicopper oxidases. In several examples, it has been shown that the type 1 copper site in MCOs, responsible for the electron relay to the trinuclear copper centre, could be bypassed or suppressed.

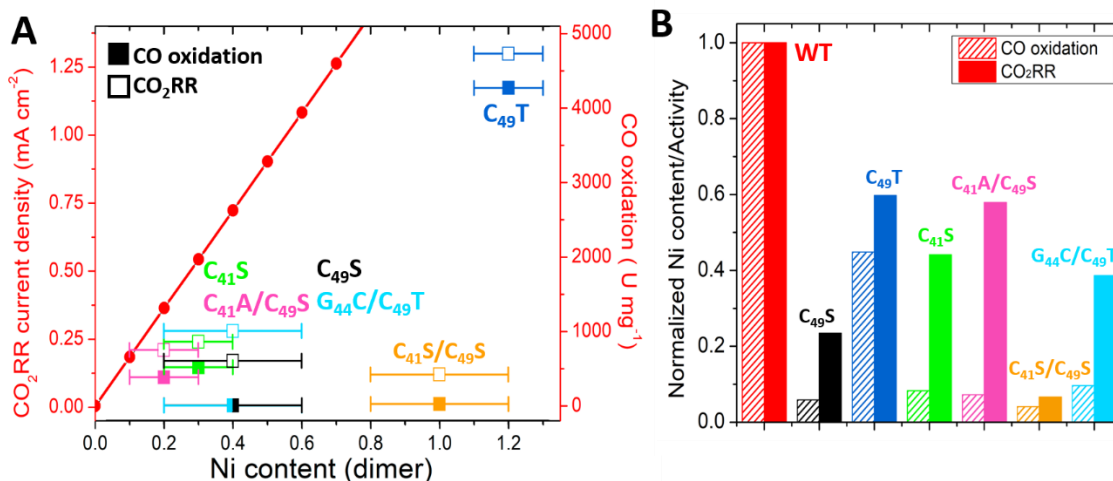


Figure 13 (A) Linear relation between Ni content of the dimer and specific activities of the RrCODH D-cluster mutants was derived from the specific activity and Ni content of the WT recombinant enzyme by using a simple equation: $y = mx$. Where y are the specific activities of CO oxidation in solution (■) or the CO₂RR current densities of the immobilized enzymes (□), m is the slope (6567.5 U·mg⁻¹ or 1,813 mA·cm⁻² derived from 1.6 Ni/dimer : 10508 U·mg⁻¹/2.9 mA·cm⁻²) and x the Ni content of the dimer. **(B)** Normalized ratio of Ni content per Activities in solution (CO oxidation) and immobilized (CO₂RR) of the WT and D-cluster mutants of RrCODH.

Without this relay, the MCOs were still able to perform the reduction of O₂ into H₂O by directly connecting the trinuclear copper centre at the electrode (Gentil et al., 2020)(Sekretareva et al., 2021)(Scheiblbrandner et al., 2017)(Lalaoui, Holzinger, et al., 2016)(Dagys et al., 2017). Regarding the role of the D-cluster in O₂ protection, it is difficult to conclude on this part since the G₄₄C/C₄₉T mutations did not yield a mutant with a [2Fe2S] D-cluster, supposed to increase the stability of the enzyme.

However, our preliminary results show that O₂ has an impact on the overall stability of the enzyme, as observed in SEC-MALLS-RI experiments. Conversely, the [4Fe4S] cluster content in C₄₉T is visibly not strongly impacted by O₂, compared to that of WT. At this stage, it is only possible to speculate that it is not required on the basis of the CA experiments shown in Figure 12, if it is assumed that the O₂ protection is not totally due to the AcPyTACN anchoring. On the contrary, if such protection resulted only from the favourable orientation of the enzyme on the surface of the MWCNT, these preliminary results did not allow any further conclusions.

4.4 - Perspectives

These first results encourage us to pursue the characterization of the *RrCODH* D-cluster mutants. First of all, in order to better understand the possible role of the D-cluster in [NiFe]-CODHs, we plan an EPR characterization under anaerobic and aerobic conditions of the metalloclusters of the *RrCODH* D-cluster mutants. Second, we will seek to investigate the impact of the different mutations on the structure/activity relationships through X-ray crystallography. Furthermore, these results raise up the attention of setting up further experiments to demonstrate a possible protective role of D-cluster in *RrCODH*. In this regard, we can think of designing and studying an evolved D-cluster *RrCODH* for O₂ tolerance. As described for [NiFeSe]-Hydrogenases, which present a pronounced O₂ tolerance and improved catalytic performances compared to the standard [NiFe]-Hydrogenases, it is possible to consider the evolution of a [NiFe]-CODH to a [NiFeSe]-CODH by mutating the cysteine residues that coordinate the D-cluster into selenocysteine residues. In support of this, the possibility of interconverting hydrogenases between the [NiFe]- and [NiFeSe]-hydrogenase has already been shown recently (Marques et al., 2017)(R. M. Evans et al., 2021).

Cloning and expression.

The plasmids harboring the native *cooS* (WT) (pCDF-Duet1-LIC1_*RrCooS*) and *cooCTJ* genes (pRSF_*RrCooCTJ*) were obtained as previously described (Chapter 2). Regarding the *R.r. cooS* mutants Dr. Julien Perard cloned the C₄₉S, C₄₉T, C₄₁S, C₄₁A/C₄₉S and C₄₁S/C₄₉S mutants from the native *Rr cooS* gene and the synthetic G₄₄C/C₄₉T gene was obtained from GenScript. All *cooS* genes were cloned in the pCDF-Duet1-LIC1 plasmid which contains a TEV cleavage site downstream the histidine tag at the N-terminus (662 residues, 69547 Da for WT).

E. coli BL21 (DE3) or *E. coli* Rosetta2^{ΔiscR} (for _aG₄₄C/C₄₉T^{ΔiscR}) were co-transformed with pRSF_*RrCooCTJ* and pCDF-Duet1-LIC1_*RrCooS* and cultured under aerobic conditions in auto-induction medium, supplemented with appropriate antibiotics, 1 mM Fe(II)SO₄ (Sigma Aldrich), 2 mM L-Cysteine (Sigma Aldrich) and 0.5 mM NiSO₄ (ACROS ORGANICS, omitted for _aG₄₄C/C₄₉T^{ΔiscR}), as previously described in chapter 2. *E. coli* BL21 (DE3) co-transformed with pRSF_*RrCooCTJ* and pCDF-Duet1-LIC1_*RrCooS*- G₄₄C/C₄₉T were cultured under anaerobic conditions (_{an}G₄₄C/C₄₉T^{ΔiscR}) as previously described for the recombinant *ChCODH* II and IV (J. H. Jeoung & Dobbek, 2007)(Domnik et al., 2017). In this latter case, the expression was induced by addition of 0.2 mM IPTG supplemented with 0.5 mM NiSO₄ (ACROS ORGANICS), 1 mM Na₂S (Sigma Aldrich), 1 mM Fe(II)SO₄ (Sigma Aldrich) once the culture reached an OD₆₀₀ of 0.5. Bacteria were first cultivated aerobically prior to induce the recombinant expression cultures under anaerobic conditions. Cultures were centrifuged and cell pellets collected under argon flow before being stored in liquid nitrogen.

Protein Purification.

All *RrCODH* D-cluster mutants and WT enzymes were purified following our previously described protocol, which led to the obtention of pure preparations of almost all enzymes (except _aG₄₄C/C₄₉T and _{an}G₄₄C/C₄₉T).

Table 8 Yield of pure preparation of *RrCODH* D-cluster mutants.

<i>RrCODH</i> :	Pure enzyme (mg·L ⁻¹)
C ₄₉ S	5.5 ± 0.4
C ₄₉ T	4.8 ± 0.2
C ₄₁ S	3.1
C ₄₁ A/C ₄₉ S	~ 5.1
C ₄₁ S/C ₄₉ S	4.7
^a G ₄₄ C/C ₄₉ T	~ 7.1
^a nG ₄₄ C/C ₄₉ T	~ 0.8
^a G ₄₄ C/C ₄₉ T ^{ΔiscR}	~ 9.7

Size-exclusion chromatography to multi-angle laser light scattering with online refractive index (SEC-MALLS-RI).

Purified *RrCODH* D-cluster mutants and WT samples were injected manually into a SEC-MALLS system (Wyatt Dawn HELEOS-II 18-angle light scattering detector and Wyatt Optilab rEX refractive index monitor linked to a Shimadzu HPLC system comprising a LC-20AD pump and SPD20A UV/Vis. detector) using a Superdex 200 10/300 Increase size exclusion column eluted with buffer containing 50 mM TrisHCl, pH 8.5, 150 mM NaCl. An in-line refractive index detector (Optirex, Wyatt Instruments) was used to follow the differential refractive index relative to the solvent. The data analyzed using the ASTRA software v.6.1 and the molecular masses were calculated for each sample. Protein concentration in all samples was determined by integration of the differential refractive index (dRI) peak after injection of 20 μL protein. Oligomerization percentage contributes were calculated by integration of the dRI peaks.

UV-visible spectroscopy.

Oxidized enzymes were buffer exchanged to 50 mM TrisHCl pH 8.5 by using Micro Bio-Spin® 6 (Bio-Rad). The UV-visible spectra of oxidized *RrCODH* preparations were recorded on a UV-1800 spectrophotometer (Shimadzu Corporation) under anaerobic condition and aerobic conditions every 15 minutes for a total time of 390 minutes. The spectral decomposition of [4Fe4S] and [2Fe2S] was carried out by using Fit-Fes v.1.1.1 which is available and used on Microsoft Excel. This tool is designed for semi-quantitative analysis of iron-sulfur cluster formation/decomposition reactions over time, based on the fitting of the spectra from library of FeS clusters spectra.

Metal content determination and Methyl Viologen mediated CO oxidation activity in solution.

Metal content was determined thanks to colorimetric assay as previously described in Chapter 2. CO oxidation activity in solution was measured, as previously described in Chapter 2, in “standard conditions” in CO saturated 50 mM TrisHCl, pH 8.5, 12 mM Methyl Viologen at 25 °C. RrCODH D-cluster mutants were suitably diluted in a range of concentrations from 10 to 500 nM monomer, in order to be able to measure accurate kinetics.

Electrochemical measurements.

The electrochemical experiments were carried out in a three-electrode electrochemical gas tight cell inside an anaerobic glove box ($O_2 < 2\text{ppm}$, Jacomex) using a Biologic VMP3 Potentiostat. 1-pyrenebutyric acid adamantyl amide (ADA) and 1-acetate-4-(1-pyrenyl)-1,4,7-triazacliclononane (AcPyTACN) modified MWCNT electrodes (MWCNT^{ADA} and MWCNT^{AcPyTACN}) were prepared as previously described in Chapter 2 and 3. The RrCODH immobilization on different functionalized MWCNT was carried out as previously described in Chapter 2, MWCNT-bioelectrodes were used as working electrodes. Pt wire was used as counter electrode and the Saturated Calomel served as reference electrode. Potentials are reported to the Standard Hydrogen Electrode according to $E_{SHE} = E_{SCE} + 0.242\text{ V}$. Current densities are normalized towards the geometrical surface of the glassy carbon electrode (0.071 cm^2). The experiments were conducted at glove box temperature, 21 °C. The electrolyte was 50 mM TrisHCl, pH 8.5. Chronoamperometry experiments were carried out as previously described in Chapter 2.

Electrochemical analysis.

Γ_{\max} : the surface coverage is defined as the number of mole of enzymes immobilized for cm^{-2} of electrode surface and it is calculated according to:

$$\Gamma_{\max} = \frac{Q}{FnA}$$

Where Q is the charge expressed in Coulomb obtained from the integration of the oxidative peak, F is the Faraday constant expressed in C mol^{-1} ($96485.34\text{ C mol}^{-1}$), n is the number of electrons involved in the redox $C_{\text{red}2} \rightarrow C_{\text{red}1}$ system (2 electrons) and A is

the electrode surface expressed in cm^2 which for a glassy carbon electrode with a diameter of 3 mm correspond to 0.071 cm^2 .

TOF: the Turnover Frequency (also termed k_{cat}) is defined as the maximum number of chemical conversions of substrate molecules per second. It is calculated according to:

$$TOF = \frac{I_{max}}{Fn\Gamma_{max}}$$

Where I_{max} is the maximum current density measured, expressed in $\text{A}\cdot\text{cm}^{-2}$.

$E_{1/2}$: Half Wave potential of the reversible $C_{\text{red1}}/C_{\text{red2}}$ redox system of the different D-cluster *RrCODH* mutants at pH 8.5 was calculated by the average of the peak potentials of the redox couple.

Protein crystallization under anaerobic conditions.

In order to remove the His tags, Rec*RrCODH* were incubated in presence of TEV protease (his-tagged) 1:50 overnight at $10 \text{ }^\circ\text{C}$, thus the sample was loaded on NTA-Ni and the Rec*RrCODH* without his tags was collected as not bound. Then the buffer of Rec*RrCODH* was exchanged in 100 mM TrisHCl, pH 7.5 and DTT 1 mM by using a Superdex 200 10/300 Increase size exclusion column. To further confirm the removal of the His tag a dot-blot analysis using anti-His tag antibody coupled to HRP was carried out. No signal was detected for the Rec*RrCODH* without His tag also after long time exposure, with a detection limit in the range of nanomolar. Finally, the enzymatic preparations were concentrated to 25 and $17.5 \text{ mg}\cdot\text{mL}^{-1}$. Crystallization drops were made by diluting $1.5 \text{ }\mu\text{L}$ of Rec*RrCODH* with $1.5 \text{ }\mu\text{L}$ of a precipitating solution (total reservoir of 0.5 mL). Crystallization trials were performed under argon in a glove box (Jacomex, $\text{O}_2 < 2 \text{ ppm}$) at $21 \text{ }^\circ\text{C}$ using the vapor diffusion technique (hanging-drop method), equilibrating the drop against 0.5 mL of the precipitating solution using EasyXtal® 15-Well Tools (Qiagen). Protein precipitation, nucleation or crystallization occurs from 1 day to 1 month.

Conclusion & Perspectives

The main purpose of this work was to bring the scientific community's attention back to an ancestral biocatalyst such as Carbon Monoxide Dehydrogenase. As previously described, also thanks to the catalytic efficiency of this ancient enzyme, during the early stage of Holocene it has promoted the development and spread of life on our planet as complex as we know it today. Geologists recently said that the Holocene is over and that we are actually living in the geological era of the Anthropocene. Although not widely endorsed by the geological community, this term indicates the beginning of the era when human socio-economic trends began to induce a dramatic change in the biological and geological balance of the Earth, known as Human-induced Climate Change. This is precisely in this regard that the need to reduce excessive CO₂ emissions related to human activity motivated us to undertake this study. Obviously, with this work we do not intend to propose an alternative applicable today, but rather to help and facilitate the study of future viable ecological alternatives, based on what Nature selected long ago.

Furthermore, we are not the first ones to try to show the potential of this robust biocatalyst. However, we hope that our contribution will help further work. Our protocol successfully achieved the easy access to highly active and stable *R. rubrum* [NiFe]-CODH allowing further biochemical, spectroscopic and structural characterizations. In addition, for the first time we have electrochemically shown the interest in using [NiFe]-CODH as a potential biocatalyst of CO₂RR. Based on the same goal, the integration of *Rr*CODH into a functional device, such as a Gas Diffusion Electrode, provides a proof of concept in development of concrete CODH-based nanodevices. Based on our recent findings, we have also begun to decipher the inherent drawbacks of [NiFe]-CODHs, such as low tolerance toward dioxygen and the role of metal cofactors, such as the D-cluster. Among all the future prospects that our results shed light, I would like to propose objectives that can be achieved in the near future. To this end, I would like to mention

that in the context of the development of this project, Thomas Pichon has recently joined our group to start a PhD.

As briefly described in Chapter 1, Synthesis Gas or Syngas represents an economical and versatile substrate with widespread applications (Figure 1A). In the last decade, world production of syngas has almost tripled reaching about 900 GWth per year (Figure 1B)(Stratas Advisors, 2016).

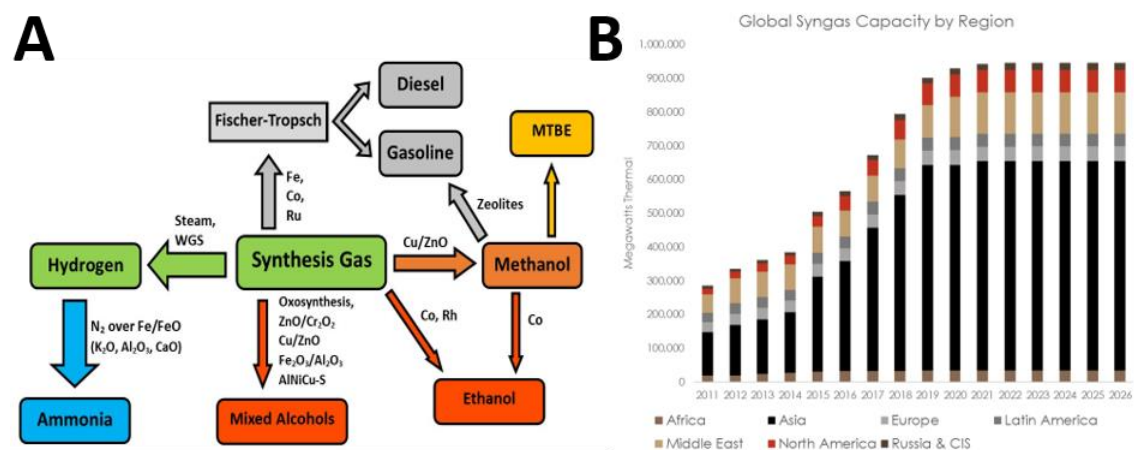


Figure 1 (A) Synthesis Gas usage and final products of its conversion with relatively reactions. (B) World wide production of Syngas (Stratas Advisors, 2016).

Actually, the ecologic problem of syngas production is due to the fact that its mainly produced from the gasification of fossil fuels, but it can alternatively be generated from biomass or other ecofriendly sources as shown in Table 1. Regardless the carbon source, the raw syngas is mainly composed by carbon monoxide. In fact, the H₂/CO ratio is between 0.2 and 0.66 but for many applications a H₂-enrichment processes is absolutely required (Nanda et al., 2017).

Table 1 Composition of synthesis gas derived from various carbon sources (Adapted from Alfano & Cavazza, 2018)

Source	Composition (vol %)						
	H ₂	CO	H ₂ /CO	CO ₂	N ₂	CH ₄	Other
Coal gasification	29.4	59.4	0.49	10	0.6	-	0.6
Charcoal	29	48	0.60	-	-	48	-
Grass straw	2.6	12.9	0.20	17.4	64.2	2.1	0.8
Demolition wood/paper residue	6.1	9.2	0.66	16.1	63.2	2.8	2.6
Biomass (Updraft gasifier)	11	24	0.46	9	53	3	-

However, while gasification and purification of gas from fossil raw materials is a well-established technology, relevant differences still exist when using biomass as feedstock and specific challenges still must be addressed. For example, the impurity levels in the

gas are different in eco-derived gasses. The WGSR is the key reaction for the purification and upgrading of syngas. To date, WGSR is industrially performed and consists of two sequential stages: the first with a high temperature reactor at 350-500 °C with an iron-based catalyst ($\text{Fe}_2\text{O}-\text{Cr}_2\text{O}_3$) and a second low temperature reactor at 200-220 °C with Cu-based catalyst ($\text{Cu}-\text{ZnO}/\text{Al}_2\text{O}_3$) (Nanda et al., 2017). In addition, the presence of contaminant species, such as sulfur or nitrate compounds in the inlet gas, even at concentrations as low as 100 ppm, can lead to catalyst poisoning and a decrease in the global process efficiency (Ratnasamy & Wagner, 2009)(Alfano & Cavazza, 2018). Another important limitation of the reaction is the H_2/CO ratio, which needs to be relatively high to avoid side reactions. To date, one challenge is the development of Power-to-syngas processes, allowing the production of syngas from water, CO_2 and renewable energy *via* different possible ways. For example, the photo-electrolysis of water can be coupled with the reverse water gas shift reaction (RWGSR)(Figure 2) (Daza & Kuhn, 2016).

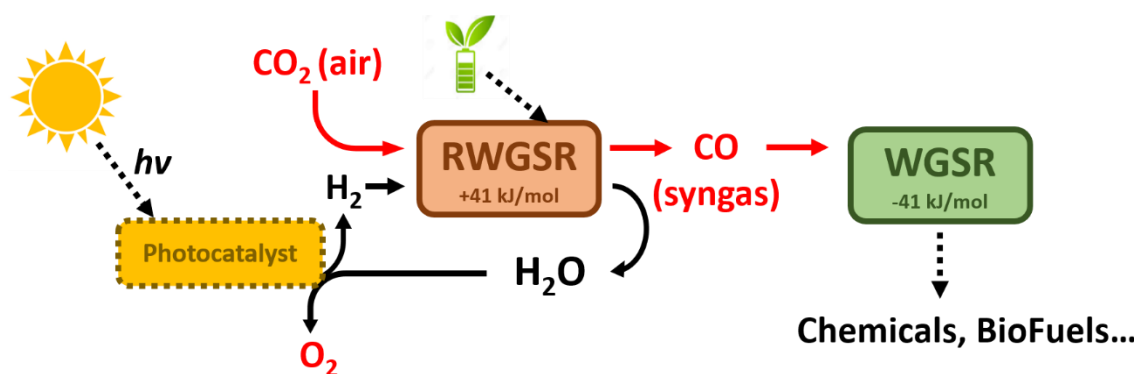


Figure 2 Schematic representation of power-to-syngas process. Photocatalyst performs the electrolysis of water which is coupled to the reduction of atmospheric CO_2 in the reverse WGSR (RWGSR) to obtain syngas.

The optimization of WGSR, in its direct or reverse way, appears then as an attractive research topic in the field of catalysis for sustainable chemistry for the development of biomass, waste and CO_2 valorization processes in order to close the carbon cycle. Ideally our goal will be to provide an enzymatic device to perform WGSR and RWGSR under thermodynamically favorable conditions, such as room temperature and atmospheric pressure with high selectivity avoiding side reactions. In other words, this means a reduced impact on climate change. Therefore, by observing the *in vivo* multiprotein complex that performs the biological WGSR, the feasibility of exploiting this multiprotein complex *in vitro* represents a fantastic challenge.

Acknowledgments

Here we are, the acknowledgments section. After these three years, I can understand what it means to do a PhD. Reaching this aim was/is challenging. It was a phase of growth from a scientific point of view, as now I feel more confident in myself and in the contribution, I can make to scientific research. Furthermore, this project has given me the opportunity to be more aware of the Human-Earth balance and how to try to contribute to the improvement of our society. In addition, it was also a time of personal growth, as this experience feels like the last stage of adolescence and the beginning of adulthood. I decided to put the acknowledgments here at the end, because I would like to thank to all the people who allowed me to be here today to finish writing this thesis. I will follow a chronological order, as I don't want any of the following people to think they are more or less important than the others. Personally, I do not like to classify/rank people, for me we are all the same.

This is for you **Gemma**.

Then, I thank my family and my parents, uncles **Gennaro**, **Lucia** and **Emmanuela**.

Francesco, for having financed my first academic studies, you are a real and good brother.

Mom, to always be there to think of me, to support me, to listen me complain (always), to advise me, for the patience and strength you had with me.

Dad, for giving me an optical microscope and letting me “play” since my childhood in your laboratory. This has allowed me since I was a child to be attracted to Nature and its complex mechanisms.

Lino and **Andrea**, I don't need to use words for you, just thank you for being part of my life and for being my non-biological brothers.

Thank to my non-biological sister, **Stella**. I met you when I still did not speak “correct” Italian, thanks for being my personal Italian teacher, for introducing me to and strengthening my interest in **Art!** *“Otherwise, Earth without Art is only Eh”*

Thank then to the friends of **Urbino** for having been there in the first academic steps. **Federica**, **Elisa**, **Valentina** and **Roberta**, you are all fantastic women, what a stupid and stubborn teenager needs to grow up. **Nikos**, **Kalvinos** and **coach Lazaros**, to be good friends and for introducing me to Greek culture. **Stevo**, the best roommate with whom I have shared many experiences, good and bad! **Dani**, **Carola** and **Laura** for adventures in the unknown region, advice and “teachings”.

So, thanks to all the **Bolognese** people! All my good friends: **Ste**, **Mariano**, **Alessandro (Il bello, NODO and Skänderbej)**, **Carlotta**, **Pusi**, **Marius** and **Lamberto**. **Serena** and **Maria**, for accepting me for who I am and for helping me in my personal and academic growth and thousands other reasons to thank you.

Then, a big thank you to the people at **LBIC**.

Muso, for accepting a “turbulent and non-ordinary” student and teaching me to analyze a scientific article and introducing, step by step, to the *in silico* scientific research.

Luca, you already know, but thanks again for having patience and trust in me in approaching the first manipulations in the laboratory. For solving all the problems, I have created, for sharing your method of doing research, for introducing me to the fascinating field of protein crystallography. And also, for being available in these years where I have continued to stress you from a distance.

Val, to be strict but fair, your teachings have been fundamental over the years.

Prof! for being my scientific father. You have been and are one of my main sources of inspiration, for giving me the opportunity and accompanying me in the first steps in research and for believing in me for this PhD project. The great esteem and admiration I have in you are the reasons why I want you to be part of the jury, to examine the results of these three years.

Finally, thanks to the people of [Grenoble](#) and [Marseille](#).

[Lorenzo](#)², for being a true and sincere friend, from the first day we met and for all the *bonheur* spent together. Of course, thanks to [Emm](#), for having patience with these two “bad guys”.

Thanks to my “unknown” neighbors, [Marc](#) and [Giovanna](#), you are amazing people!

[Martin](#), for being like a brother from day one. Thank you for teaching me the tricks of the trade, for introducing me to boulder. [Hind](#), for being the purest, most loyal and sincere person I know. The world needs people like you. [Manel](#), being a friend to talk to about everything from funny to very sad things, for example how sick our society is.

[Bruno](#), for introducing me to the EPR and your professionalism. I really appreciated and felt honored to work with you. In addition, to giving me the possibility of meet interesting and nice people from the [BIP](#) and for making me discover Marseille!

I would also like to thank all the [CDD](#) and [CDI](#) people I have met in these years at [LCBM](#) and [BEA](#), thank you for accepting me even though I am not too sociable. I won't list the names, just to make sure I don't forget anyone. But special thanks to [BIOCAT](#) and [BEE](#) people, in the end it is like I have been in the two *équipe*. I want also to thank some people in particular, [Sandrine](#) for being a source of scientific inspiration and for climbing, one of the strongest people I know.

[Clara](#) and [Gregory](#), for being there to help me even though I was always in a bad mood, at least you managed to make me smile in some moments of depression.

[Julien](#), thank you very much. For all the scientific advice and discussions, for your availability and for having helped me a lot over these three years, without you I would not have achieved these results and this level of knowledge and maturity.

[Marila](#), for having been my bridge between Italy and France, without you it would have been really hard, maybe now I wouldn't be here.

Thanks to the “director” [Stephane](#), the safety and the way of doing things are very inspiring. Thanks also for being able to find a way to make a smile and your humanity, I have great respect in you.

Special thanks to my CSI committee, [Carole](#), [Vincent](#) and [Sandrine](#), for the constructive discussions that prompted me to look at my research and goals from different perspectives.

Also, a great thank to [LabEx ARCANÉ](#) for the grant that allowed this thesis to happen.

I really thank the people who accepted to be part of the thesis committee: [Dr. Carole Baffert](#), [Prof. Luis M. Rubio](#), [Dr. Carole Duboc](#) and [Prof. Stefano Ciurli](#). I am sure that we will have the opportunity to have a constructive and interesting scientific discussion.

So, it is time to say thank you to the two people they have contributed mainly to the achievement of this important milestone, the [supervisors](#).

[Alan](#), thank you for introducing me to the field of electrochemistry as well as nanotechnology, for patiently teaching me from the first day to yesterday! Thank you for being there to motivate me and find good results where I was seeing only strange things. But as you say: “*I like strange things*”! We both know it was tough at certain times, but with a lot of *nonchalance* you managed to deflect my complaints and motivate me to try again and again.

[Christine](#), for being the best PhD supervisor I know. This is because you worry not only about work, but also about my sanity. Without you all this would have been impossible, you met me that I spoke little English and I was quite disoriented outside Italy. But thanks to you, who, like a mother, accompanied me in the first steps, I was able to acquire a good confidence in myself and also a good level of English and France, which helped me a lot to integrate into society. I think it is not obvious to feel free to discuss personal problems without any filter with your supervisor and receive support in the worst moments. You have always been available, on weekends, at night or early in the morning, on holidays and other situations. Thanks for everything you have done as mt scientific mother. Good luck managing the BEE team and good luck to you, Thomas and all people involved in continuing this ambitious project.

I miss one of the most important women in my life, **Tina**.

"No man succeeds without a good woman behind him. Wife or mother, if it is both, he is twice blessed indeed". [Godfrey Winn]

What you have done for me over the years I still can't get it done. Even if you think you are weak and defenseless, you are the opposite, you had the strength to do it all by yourself, you did not have a French mother like me. You supported me during the first Covid-19 lockdown when perhaps at that moment you were the one who needed it most. You have been constant in supporting my daily life, especially in recent times. I am really happy to share everything with you: thoughts, ambitions, interests such as sport, art and above all music and dance together.

I want to conclude these thanks with the lyrics of a song, since without **Music** my life would be empty.

[Verse 1]

*By nature, I'm curious
Science is serious
I wanna learn and study
Cos life is too mysterious
First step, state of the art
Reading searching summarizing
Strictness rigor and precision
I can't afford to make a mistake
I develop a strong methodology
Inspired by old astronomy
I need conclusive evidence
Results need to be concrete
Using statistics, physics and chemistry
My reasoning must be logical
By analogy, I gotta test and try, the solution may be biological*

[Verse 2]

*I got to experiment to get data
To analyze them later
Statistical relationship
Linear expo logarithmic
L-A-B: laboratory, that's the place where I like to be
Unknown territories I explore
Wow, I never seen this before
Ecosystemic influences, not a lot of differences
Between nature and urban systems
I got to analyze similarities
The world is complex, the flap of a wing can have many effects
Hazard spread through networks, boom, total blackout, shout!
Macro meso micro I know everything is a matter of scale
Multiscalar is the future
I'm a doctor I'm gonna teach you
[Stand High Patrol, My Research]*

Grenoble, 2021/10/23

- Agbo, P., Heath, J. R., & Gray, H. B. (2014). Modeling Dioxygen Reduction at Multicopper Oxidase Cathodes. *Journal of the American Chemical Society*, 136(39), 13882–13887. <https://doi.org/10.1021/ja5077519>
- Alfano, & Cavazza, C. (2018). The biologically mediated water-gas shift reaction: Structure, function and biosynthesis of monofunctional [NiFe]-carbon monoxide dehydrogenases. *Sustainable Energy and Fuels*, 2(8), 1653–1670. <https://doi.org/10.1039/c8se00085a>
- Alfano, & Cavazza, C. (2020). Structure, function, and biosynthesis of nickel-dependent enzymes. *Protein Science*, January, 1–19. <https://doi.org/10.1002/pro.3836>
- Alfano, M. (2019). *Deciphering the biosynthetic pathway of carbon monoxide dehydrogenase, a key enzyme of the watergas shift reaction.*
- Alfano, M., & et al., et al. (2019). The carbon monoxide dehydrogenase accessory protein CooJ is a histidine-rich multidomain dimer containing an unexpected Ni(II)-binding site. *Journal of Biological Chemistry*, 294(19), 7601–7614. <https://doi.org/10.1074/jbc.RA119.008011>
- Alfano, M., Pérard, J., Miras, R., Catty, P., & Cavazza, C. (2018). Biophysical and structural characterization of the putative nickel chaperone CooT from *Carboxydotherrmus hydrogenoformans*. *Journal of Biological Inorganic Chemistry*, 23(5), 809–817. <https://doi.org/10.1007/s00775-018-1576-2>
- Alfano, M., Veronesi, G., Musiani, F., Zambelli, B., Signor, L., Proux, O., Rovezzi, M., Ciurli, S., & Cavazza, C. (2019). A Solvent-Exposed Cysteine Forms a Peculiar Ni(II)-Binding Site in the Metallochaperone CooT from *Rhodospirillum rubrum*. *Chemistry - A European Journal*, 25(67), 15351–15360. <https://doi.org/10.1002/chem.201903492>
- Alonso-Lomillo, M. A., Rüdiger, O., Maroto-Valiente, A., Velez, M., Rodríguez-Ramos, I., Muñoz, F. J., Fernández, V. M., & De Lacey, A. L. (2007). Hydrogenase-coated carbon nanotubes for efficient H₂ oxidation. *Nano Letters*, 7(6), 1603–1608. <https://doi.org/10.1021/nl070519u>
- Andreu, R., Ferapontova, E. E., Gorton, L., & Calvente, J. J. (2007). Direct Electron Transfer Kinetics in Horseradish Peroxidase Electrocatalysis. *The Journal of Physical Chemistry B*, 111(2), 469–477. <https://doi.org/10.1021/jp064277i>
- Anwar, M. N., Fayyaz, A., Sohail, N. F., Khokhar, M. F., Baqar, M., Yasar, A., Rasool, K., Nazir, A., Raja, M. U. F., Rehan, M., Aghbashlo, M., Tabatabaei, M., & Nizami, A. S. (2020). CO₂ utilization: Turning greenhouse gas into fuels and valuable products. *Journal of Environmental Management*, 260(December 2019), 110059. <https://doi.org/10.1016/j.jenvman.2019.110059>
- Aquino Neto, S., Hickey, D. P., Milton, R. D., De Andrade, A. R., & Minteer, S. D. (2015). High current density PQQ-dependent alcohol and aldehyde dehydrogenase bioanodes. *Biosensors & Bioelectronics*, 72, 247–254. <https://doi.org/10.1016/j.bios.2015.05.011>
- Aquino Neto, S., Milton, R. D., Crepaldi, L. B., Hickey, D. P., de Andrade, A. R., & Minteer, S. D. (2015). Co-immobilization of gold nanoparticles with glucose oxidase to improve bioelectrocatalytic glucose oxidation. *Journal of Power Sources*, 285, 493–498. <https://doi.org/https://doi.org/10.1016/j.jpowsour.2015.03.121>

- Aquino Neto, S., Milton, R. D., Hickey, D. P., De Andrade, A. R., & Minteer, S. D. (2016). Membraneless enzymatic ethanol/O₂ fuel cell: Transitioning from an air-breathing Pt-based cathode to a bilirubin oxidase-based biocathode. *Journal of Power Sources*, 324, 208–214.
<https://doi.org/https://doi.org/10.1016/j.jpowsour.2016.05.073>
- Armstrong, F. A., Hill, H. A. O., & Walton, N. J. (1988). Direct electrochemistry of redox proteins. *Accounts of Chemical Research*, 21(11), 407–413.
<https://doi.org/10.1021/ar00155a004>
- Asplund-Samuelsson, J., & Elton P, H. (2021). Wide range of metabolic adaptations to the acquisition of the Calvin cycle revealed by comparison of microbial genomes. *PLOS Computational Biology*, 1–26. <https://doi.org/10.1371/journal.pcbi.1008742>
- Aulenta, F., Catapano, L., Snip, L., & Villano, M. (2012). Linking Bacterial Metabolism to Graphite Cathodes : Electrochemical Insights into the H₂ -Producing Capability of *Desulfovibrio sp* . *Chem. Sus. Chem.*, 1080–1085.
<https://doi.org/10.1002/cssc.201100720>
- Balland, V., Hureau, C., Cusano, A. M., Liu, Y., Tron, T., & Limoges, B. (2008). Oriented immobilization of a fully active monolayer of histidine-tagged recombinant laccase on modified gold electrodes. *Chemistry (Weinheim an Der Bergstrasse, Germany)*, 14(24), 7186–7192. <https://doi.org/10.1002/chem.200800368>
- Baughman, R. H., Zakhidov, A. A., & de Heer, W. A. (2002). Carbon nanotubes--the route toward applications. *Science (New York, N.Y.)*, 297(5582), 787–792.
<https://doi.org/10.1126/science.1060928>
- Benniston, A., Chaudhary, Y. S., Woolerton, T. W., Allen, C. S., Warner, J. H., Pierce, E., Ragsdale, W., & Armstrong, F. A. (2012). Visible light-driven CO₂ reduction by enzyme coupled CdS nanocrystals. *Chem Comm*.
<https://doi.org/10.1039/c1cc16107e>
- Benvenuti, M., Meneghello, M., Guendon, C., Jacq-Bailly, A., Jeoung, J., Dobbek, H., Léger, C., Fourmond, V., & Dementin, S. (2020). The two CO-dehydrogenases of *Thermococcus sp.* AM4. *Biochimica et Biophysica Acta (BBA) - Bioenergetics*, 148188. <https://doi.org/10.1016/j.bbabi.2020.148188>
- Berg, I. A., Kockelkorn, D., Buckel, W., & Fuchs, G. (2007). A 3-hydroxypropionate/4-hydroxybutyrate autotrophic carbon dioxide assimilation pathway in Archaea. *Science*, 318(5857), 1782–1786. <https://doi.org/10.1126/science.1149976>
- Bergey, D. H., & Holt, J. G. (1994). *Bergey's manual of determinative bacteriology*.
- Bethune, D. S., Klang, C. H., De Vries, M. S., Gorman, G., Savoy, R., Vazquez, J., & Beyers, R. (1993). Cobalt-catalysed growth of carbon nanotubes with single-atomic-layer walls. *Nature*, 363(6430), 605–607.
<https://doi.org/10.1038/363605a0>
- Betinol, I. O., Nader, S., & Mansy, S. S. (2021). Spectral decomposition of iron-sulfur clusters. *Analytical Biochemistry*, 629(April), 114269.
<https://doi.org/10.1016/j.ab.2021.114269>
- Birdsey, R. M. A., Mayes, P., Romero-Lankao, R. G. Najjar, S. C., Reed, N., Cavallaro, G., Shrestha, D. J., Hayes, L., Lorenzoni, A., Marsh, K., Tedesco, T., & Zhu, W. Z. (2018). *Second State of the Carbon Cycle Report (SOCCR2)*.
<https://carbon2018.globalchange.gov/>
- Blanford, C. F., Foster, C. E., Heath, R. S., & Armstrong, F. A. (2009). Efficient electrocatalytic oxygen reduction by the 'blue' copper oxidase{,} laccase{,} directly attached to chemically modified carbons. *Faraday Discuss.*, 140(0), 319–335.

- <https://doi.org/10.1039/B808939F>
- Blanford, C. F., Heath, R. S., & Armstrong, F. A. (2007). A stable electrode for high-potential, electrocatalytic O₂ reduction based on rational attachment of a blue copper oxidase to a graphite surface. *Chem. Commun.*, *17*, 1710–1712.
<https://doi.org/10.1039/B703114A>
- Blankespoor, R., Limoges, B., Schöllhorn, B., Syssa-Magalé, J.-L., & Yazidi, D. (2005). Dense Monolayers of Metal-Chelating Ligands Covalently Attached to Carbon Electrodes Electrochemically and Their Useful Application in Affinity Binding of Histidine-Tagged Proteins. *Langmuir*, *21*(8), 3362–3375.
<https://doi.org/10.1021/la047139y>
- Bollella, P., Gorton, L., & Antiochia, R. (2018). Direct Electron Transfer of Dehydrogenases for Development of 3rd Generation Biosensors and Enzymatic Fuel Cells. *Sensors (Basel, Switzerland)*, *18*(5). <https://doi.org/10.3390/s18051319>
- Bonam, D., & Ludden, P. W. (1987). Purification and characterization of carbon monoxide dehydrogenase, a nickel, zinc, iron-sulfur protein, from *Rhodospirillum rubrum*. *The Journal of Biological Chemistry*, *262*(7), 2980–2987.
- Bonam, D., McKenna, M. C., Stephens, P. J., & Ludden, P. W. (1988). Nickel-deficient carbon monoxide dehydrogenase from *Rhodospirillum rubrum*: in vivo and in vitro activation by exogenous nickel. *Proceedings of the National Academy of Sciences of the United States of America*, *85*(1), 31–35.
<https://doi.org/10.1073/pnas.85.1.31>
- Bourourou, M., Elouarzaki, K., Lalaoui, N., Agnès, C., Le Goff, A., Holzinger, M., Maaref, A., & Cosnier, S. (2013). Supramolecular Immobilization of Laccase on Carbon Nanotube Electrodes Functionalized with (Methylpyrenylaminomethyl)anthraquinone for Direct Electron Reduction of Oxygen. *Chemistry – A European Journal*, *19*(28), 9371–9375.
<https://doi.org/10.1002/chem.201301043>
- Callegari, A., Cosnier, S., Marcaccio, M., Paolucci, D., Paolucci, F., Georgakilas, V., Tagmatarchis, N., Va, E., Ciamician, C. G., & Selmi, V. (2004). Functionalised single wall carbon nanotubes / polypyrrole composites for the preparation of amperometric glucose biosensors. *Materials Chemistry*, *2*(C), 807–810.
- Calvin, M., & Benson, A. A. (1948). *The Path of Carbon in Photosynthesis*. *107*(14), 2–6.
- Campbell, W. H., Henig, J., & Plumeré, N. (2013). Affinity binding via zinc(II) for controlled orientation and electrochemistry of histidine-tagged nitrate reductase in self-assembled monolayers. *Bioelectrochemistry*, *93*, 46–50.
<https://doi.org/10.1016/j.bioelechem.2012.07.002>
- Can, M., Armstrong, F. A., & Ragsdale, S. W. (2014). Structure, function, and mechanism of the nickel metalloenzymes, CO dehydrogenase, and acetyl-CoA synthase. *Chemical Reviews*, *114*(8), 4149–4174.
<https://doi.org/10.1021/cr400461p>
- CCS Global Institute. (2020). Global Status of CCS 2020. In *Global CCS Institute* (Issue June). <https://www.globalccsinstitute.com/resources/global-status-report/>
- Chan, Y. H., Nor, S., Syed, F., Rahman, A., Lahuri, H. M., & Khalid, A. (2021). Recent progress on CO-rich syngas production via CO₂ gasification of various wastes : A critical review on efficiency, challenges and. *Environmental Pollution*, *278*, 116843. <https://doi.org/10.1016/j.envpol.2021.116843>
- Chen, R. J., Zhang, Y., & Wang, D. (2001). Noncovalent Sidewall Functionalization of

- Single-Walled Carbon Nanotubes for Protein Immobilization. *JACS*, *18*, 3838–3839.
- Chen, Y., Xu, C., & Vaidyanathan, S. (2020). Influence of gas management on biochemical conversion of CO₂ by microalgae for biofuel production. *Applied Energy*, *261*(December 2019), 114420. <https://doi.org/10.1016/j.apenergy.2019.114420>
- Christine Munk, A., Copeland, A., Lucas, S., Lapidus, A., del Rio, T. G., Barry, K., Detter, J. C., Hammon, N., Israni, S., Pitluck, S., Brettin, T., Bruce, D., Han, C., Tapia, R., Gilna, P., Schmutz, J., Larimer, F., Land, M., Kyrpides, N. C., ... Schwartz, D. C. (2011). Complete genome sequence of *Rhodospirillum rubrum* type strain (S1 T). *Standards in Genomic Sciences*, *4*(3), 293–302. <https://doi.org/10.4056/sigs.1804360>
- Ciaccafava, A., Infossi, P., Ilbert, M., Guiral, M., Lecomte, S., Giudici-orticoni, M. T., & Lojou, E. (2012). Electrochemistry, AFM, and PM-IRRA Spectroscopy of Immobilized Hydrogenase: Role of a Hydrophobic Helix in Enzyme Orientation for Efficient H₂ Oxidation. *Angewandte Chemie (International Ed. in English)*, 953–956. <https://doi.org/10.1002/anie.201107053>
- Ciaccafava, A., Tombolelli, D., Domnik, L., Fessler, J., Jeoung, J. H., Dobbek, H., Mroginiski, M. A., Zebger, I., & Hildebrandt, P. (2016). When the inhibitor tells more than the substrate: The cyanide-bound state of a carbon monoxide dehydrogenase. *Chemical Science*, *7*(5), 3162–3171. <https://doi.org/10.1039/c5sc04554a>
- Cosnier, S. (2007). Recent Advances in Biological Sensors Based on Electrogenenerated Polymers: A Review. *Analytical Letters*, *40*(7), 1260–1279. <https://doi.org/10.1080/00032710701326643>
- Cosnier, Serge, & Holzinger, M. (2011). Electrosynthesized polymers for biosensing. *Chem. Soc. Rev.*, *40*(5), 2146–2156. <https://doi.org/10.1039/C0CS00090F>
- Cosnier, Serge, Holzinger, M., & Goff, A. Le. (2014). Recent advances in carbon nanotube-based enzymatic fuel cells. *Frontiers in Bioengineering and Biotechnology*, *2*(OCT), 1–6. <https://doi.org/10.3389/fbioe.2014.00045>
- Crable, B. R., Plugge, C. M., McInerney, M. J., & Stams, A. J. M. (2011). Formate Formation and Formate Conversion in Biological Fuels Production. *Enzyme Research*, *2011*, 532536. <https://doi.org/10.4061/2011/532536>
- Dagys, M., Laurynėnas, A., Ratautas, D., Kulys, J., Vidžiūnaitė, R., Talaikis, M., Niaura, G., Marcinkevičienė, L., Meškys, R., & Shleev, S. (2017). Oxygen electroreduction catalysed by laccase wired to gold nanoparticles via the trinuclear copper cluster. *Energy Environ. Sci.*, *10*(2), 498–502. <https://doi.org/10.1039/C6EE02232D>
- Darnault, C., Volbeda, A., Kim, E. J., Legrand, P., Vernède, X., Lindahl, P. A., & Fontecilla-Camps, J. C. (2003). Ni-Zn-[Fe₄-S₄] and Ni-Ni-[Fe₄-S₄] clusters in closed and open α subunits of acetyl-CoA synthase/carbon monoxide dehydrogenase. *Nature Structural Biology*, *10*(4), 271–279. <https://doi.org/10.1038/nsb912>
- Darrouzet, E., Rinaldi, C., Zambelli, B., Ciurli, S., & Cavazza, C. (2021). Revisiting the CooJ family, a potential chaperone for nickel delivery to [NiFe] - carbon monoxide dehydrogenase. *Journal of Inorganic Biochemistry*, *225*(May), 111588. <https://doi.org/10.1016/j.jinorgbio.2021.111588>
- Daza, Y. A., & Kuhn, J. N. (2016). CO₂ conversion by reverse water gas shift catalysis: comparison of catalysts, mechanisms and their consequences for CO₂ conversion to liquid fuels. *RSC Adv.*, *6*(55), 49675–49691.

- <https://doi.org/10.1039/C6RA05414E>
- De Volder, M. F. L., Tawfick, S. H., Baughman, R. H., & Hart, A. J. (2013). Carbon nanotubes: Present and future commercial applications. *Science*, *339*(6119), 535–539. <https://doi.org/10.1126/science.1222453>
- Diender, M., Stams, A. J. M., Sousa, D. Z., Robb, F. T., & Guiot, S. R. (2015). *Pathways and Bioenergetics of Anaerobic Carbon Monoxide Fermentation*. *6*(November), 1–18. <https://doi.org/10.3389/fmicb.2015.01275>
- Do, T. Q. N., Varničić, M., Hanke-Rauschenbach, R., Vidaković-Koch, T., & Sundmacher, K. (2014). Mathematical Modeling of a Porous Enzymatic Electrode with Direct Electron Transfer Mechanism. *Electrochimica Acta*, *137*, 616–626. <https://doi.org/10.1016/j.electacta.2014.06.031>
- Dobbek, H., Svetlitchnyi, V., Gremer, L., Huber, R., & Meyer, O. (2001). Crystal structure of a carbon monoxide dehydrogenase reveals a [Ni-4Fe-5S] cluster. *Science*, *293*(5533), 1281–1285. <https://doi.org/10.1126/science.1061500>
- Dobbek, Holger, Gremer, L., Kiefersauer, R., Huber, R., & Meyer, O. (2002). Catalysis at a dinuclear [CuSMo(=O)OH] cluster in a CO dehydrogenase resolved at 1.1-Å resolution. *Proceedings of the National Academy of Sciences of the United States of America*, *99*(25), 15971–15976. <https://doi.org/10.1073/pnas.212640899>
- Domnik, L. (2018). *Biochemische und strukturelle Untersuchungen der Kohlenmonoxid-Dehydrogenasen CODH-II und CODH-IV aus Carboxydothemus hydrogenoformans*.
- Domnik, L., Merrouch, M., Goetzl, S., Jeoung, J. H., Léger, C., Dementin, S., Fourmond, V., & Dobbek, H. (2017). CODH-IV: A High-Efficiency CO-Scavenging CO Dehydrogenase with Resistance to O₂. *Angewandte Chemie - International Edition*, *56*(48), 15466–15469. <https://doi.org/10.1002/anie.201709261>
- Doukov, T. I., Iverson, T. M., Seravalli, J., Ragsdale, S. W., & Drennan, C. L. (2002). A Ni-Fe-Cu center in a bifunctional carbon monoxide dehydrogenase/acetyl-CoA synthase. *Science*, *298*(5593), 567–572. <https://doi.org/10.1126/science.1075843>
- Drahansky, M., Paridah, M. ., Moradbak, A., Mohamed, A. ., Owolabi, F. Abdulwahab taiwo, Asniza, M., & Abdul Khalid, S. H. . (2016). Syngas Production, Properties, and Its Importance. *Intech, i(tourism)*, 13. <https://doi.org/http://dx.doi.org/10.5772/57353>
- Drennan, C. L., Heo, J., Sintchak, M. D., Schreiter, E., & Ludden, P. W. (2001). Life on carbon monoxide: X-ray structure of Rhodospirillum rubrum Ni-Fe-S carbon monoxide dehydrogenase. *Proceedings of the National Academy of Sciences of the United States of America*, *98*(21), 11973–11978. <https://doi.org/10.1073/pnas.211429998>
- Duan, X., Xu, J., Wei, Z., Ma, J., Guo, S., & Wang, S. (2017). *Metal-Free Carbon Materials for CO₂ Electrochemical Reduction*. *1701784*, 1–20. <https://doi.org/10.1002/adma.201701784>
- Dubacheva, G. V., Van der Heyden, A., Dumy, P., Kaftan, O., Auzély-Velty, R., Coche-Guerente, L., & Labbé, P. (2010). Electrochemically controlled adsorption of Fc-functionalized polymers on beta-CD-modified self-assembled monolayers. *Langmuir : The ACS Journal of Surfaces and Colloids*, *26*(17), 13976–13986. <https://doi.org/10.1021/la102026h>
- Ed, D., & Pieter, T. (2021). *Trends in Atmospheric Carbon Dioxide*. NOAA/ESRL. www.esrl.noaa.gov/gmd/ccgg/trends/
- Ensign, S. A. (1995). Reactivity of Carbon Monoxide Dehydrogenase from

- Rhodospirillum Rubrum with Carbon Dioxide, Carbonyl Sulfide, and Carbon Disulfide. *Biochemistry*, 34(16), 5372–5381. <https://doi.org/10.1021/bi00016a008>
- Ensign, S. A., Bonam, D., & Ludden, P. W. (1989). Nickel is required for the transfer of electrons from carbon monoxide to the iron-sulfur center(s) of carbon monoxide dehydrogenase from *Rhodospirillum rubrum*. *Biochemistry*, 28(12), 4968–4973. <https://doi.org/10.1021/bi00438a010>
- Evans, M. C., Buchanan, B. B., & Arnon, D. I. (1966). A new ferredoxin-dependent carbon reduction cycle in a photosynthetic bacterium. *Proceedings of the National Academy of Sciences of the United States of America*, 55(4), 928–934. <https://doi.org/10.1073/pnas.55.4.928>
- Evans, R. M., Krahn, N., Murphy, B. J., Lee, H., Armstrong, F. A., & Söll, D. (2021). Selective cysteine-to-selenocysteine changes in a [NiFe]-hydrogenase confirm a special position for catalysis and oxygen tolerance. *Proceedings of the National Academy of Sciences*, 118(13), e2100921118. <https://doi.org/10.1073/pnas.2100921118>
- Feng, J., & Lindahl, P. A. (2004). Carbon Monoxide Dehydrogenase from *Rhodospirillum rubrum*: Effect of Redox Potential on Catalysis. *Biochemistry*, 43(6), 1552–1559. <https://doi.org/10.1021/bi0357199>
- Feng, W., & Ji, P. (2011). Enzymes immobilized on carbon nanotubes. *Biotechnology Advances*, 29(6), 889–895. <https://doi.org/10.1016/j.biotechadv.2011.07.007>
- Førgaard, C., Lange, L., & Meyer, A. S. (2019). Classification and enzyme kinetics of formate dehydrogenases for biomanufacturing via CO₂ utilization. *Biotechnology Advances*, 37(7), 107408. <https://doi.org/10.1016/j.biotechadv.2019.06.007>
- Fox, J. D., Kerby, R. L., Roberts, G. P., & Ludden, P. W. (1996). Characterization of the CO-induced, CO-tolerant hydrogenase from *Rhodospirillum rubrum* and the gene encoding the large subunit of the enzyme. *Journal of Bacteriology*, 178(6), 1515–1524. <https://doi.org/10.1128/jb.178.6.1515-1524.1996>
- Fox, J. D., Yiping, H. E., Shelver, D., Roberts, G. P., & Ludden, P. W. (1996). Characterization of the region encoding the CO-induced hydrogenase of *Rhodospirillum rubrum*. *Journal of Bacteriology*, 178(21), 6200–6208. <https://doi.org/10.1128/jb.178.21.6200-6208.1996>
- Fuchsberger, K., Goff, A. Le, Gambazzi, L., Toma, F. M., Goldoni, A., Giugliano, M., Stelzle, M., & Prato, M. (2011). Multiwalled Carbon-Nanotube-Functionalized Microelectrode Arrays Fabricated by Microcontact Printing: Platform for Studying Chemical and Electrical Neuronal Signaling. *Small*, 7(4), 524–530. <https://doi.org/https://doi.org/10.1002/sml.201001640>
- Gao, D., Zhou, H., Wang, J., Miao, S., Yang, F., Wang, G., Wang, J., & Bao, X. (2015). Size-Dependent Electrocatalytic Reduction of CO₂ over Pd Nanoparticles. *JACS*, 4288–4291. <https://doi.org/10.1021/jacs.5b00046>
- Gao, F. (2020). Iron–Sulfur Cluster Biogenesis and Iron Homeostasis in Cyanobacteria. *Frontiers in Microbiology*, 11, 165. <https://doi.org/10.3389/fmicb.2020.00165>
- Gao, Y., & Kyratzis, I. (2008). Covalent Immobilization of Proteins on Carbon Nanotubes Using the Cross-Linker 1-Ethyl-3-(3-dimethylaminopropyl)carbodiimide—a Critical Assessment. *Bioconjugate Chemistry*, 19(10), 1945–1950. <https://doi.org/10.1021/bc800051c>
- Gasper, R., Scrima, A., & Wittinghofer, A. (2006). Structural insights into HypB, a GTP-binding protein that regulates metal binding. *The Journal of Biological Chemistry*, 281(37), 27492–27502. <https://doi.org/10.1074/jbc.M600809200>

- Gentil, S., Mansor, S., Jamet, H., Cosnier, S., Cavazza, C., & Le Goff, A. (2018). Oriented Immobilization of [NiFeSe] Hydrogenases on Covalently and Noncovalently Functionalized Carbon Nanotubes for H₂/Air Enzymatic Fuel Cells. *ACS Catalysis*, 8. <https://doi.org/10.1021/acscatal.8b00708>
- Gentil, S., Pifferi, C., Rousselot-Pailley, P., Tron, T., Renaudet, O., & Le Goff, A. (2021). Clicked Bifunctional Dendrimeric and Cyclopeptidic Addressable Redox Scaffolds for the Functionalization of Carbon Nanotubes with Redox Molecules and Enzymes. *Langmuir*, 37(3), 1001–1011. <https://doi.org/10.1021/acs.langmuir.0c02095>
- Gentil, S., Rousselot-Pailley, P., Sancho, F., Robert, V., Mekmouche, Y., Guallar, V., Tron, T., & Le Goff, A. (2020). Efficiency of Site-Specific Clicked Laccase–Carbon Nanotubes Biocathodes towards O₂ Reduction. *Chemistry – A European Journal*, 26(21), 4798–4804. <https://doi.org/10.1002/chem.201905234>
- Georgakilas, V., Kordatos, K., Prato, M., Guldi, D. M., Holzinger, M., & Hirsch, A. (2002). Organic functionalization of carbon nanotubes. *Journal of the American Chemical Society*, 124(5), 760–761. <https://doi.org/10.1021/ja016954m>
- Getrey, L., Krieg, T., Hollmann, F., Schrader, J., & Holtmann, D. (2014). Enzymatic halogenation of the phenolic monoterpenes thymol and carvacrol with chloroperoxidase. *Green Chemistry, Scheme 1*, 1104–1108. <https://doi.org/10.1039/c3gc42269k>
- Giroud, F., & Minteer, S. D. (2013). Anthracene-modified pyrenes immobilized on carbon nanotubes for direct electroreduction of O₂ by laccase. *Electrochemistry Communications*, 34, 157–160. <https://doi.org/10.1016/j.elecom.2013.06.006>
- Gómez, J. M., Romero, M. D., & Fernández, T. M. (2005). Immobilization of β -Glucosidase on carbon nanotubes. *Catalysis Letters*, 101(3), 275–278. <https://doi.org/10.1007/s10562-005-4904-4>
- Gong, F., Cai, Z., & Li, Y. (2016). *Synthetic biology for CO₂ fixation. March 2017*. <https://doi.org/10.1007/s11427-016-0304-2>
- Gong, F., Zhu, H., Zhou, J., & Zhang, Y. (2019). *An Economy Based on Carbon Dioxide and Water* (Issue July). <https://doi.org/10.1007/978-3-030-15868-2>
- Gong, W., Hao, B., Wei, Z., Ferguson, D. J., Tallant, T., Krzycki, J. A., & Chan, M. K. (2008). Structure of the α 2 ϵ 2 Ni-dependent CO dehydrogenase component of the Methanosarcina barkeri acetyl-CoA decarbonylase/synthase complex. *Proceedings of the National Academy of Sciences of the United States of America*, 105(28), 9558–9563. <https://doi.org/10.1073/pnas.0800415105>
- Gu, W., Gencic, S., Cramer, S. P., & Grahame, D. A. (2003). The A-Cluster in Subunit β of the Acetyl-CoA Decarbonylase/Synthase Complex from Methanosarcina thermophila: Ni and Fe K-Edge XANES and EXAFS Analyses. *Journal of the American Chemical Society*, 125(50), 15343–15351. <https://doi.org/10.1021/ja036602a>
- Gupta, G., Lau, C., Rajendran, V., Colon, F., Branch, B., Ivnitski, D., & Atanassov, P. (2011). Direct electron transfer catalyzed by bilirubin oxidase for air breathing gas-diffusion electrodes. *Electrochemistry Communications*, 13, 247–249. <https://doi.org/10.1016/j.elecom.2010.12.024>
- Gupta, R., & Chaudhury, N. K. (2007). Entrapment of biomolecules in sol-gel matrix for applications in biosensors: problems and future prospects. *Biosensors & Bioelectronics*, 22(11), 2387–2399. <https://doi.org/10.1016/j.bios.2006.12.025>

- Haddour, N., Cosnier, S., & Gondran, C. (2005). Electrogeneration of a poly(pyrrole)-NTA chelator film for a reversible oriented immobilization of histidine-tagged proteins. *Journal of the American Chemical Society*, *127*(16), 5752–5753. <https://doi.org/10.1021/ja050390v>
- Hadj-Saïd, J., Pandelia, M. E., Léger, C., Fourmond, V., & Dementin, S. (2015). The Carbon Monoxide Dehydrogenase from *Desulfovibrio vulgaris*. *Biochimica et Biophysica Acta - Bioenergetics*, *1847*(12), 1574–1583. <https://doi.org/10.1016/j.bbabi.2015.08.002>
- Hedderich, R., & Forzi, L. (2006). Energy-converting [NiFe] hydrogenases: More than just H₂ activation. *Journal of Molecular Microbiology and Biotechnology*, *10*(2–4), 92–104. <https://doi.org/10.1159/000091557>
- Heo, J., Staples, C. R., & Ludden, P. W. (2001). Redox-dependent CO₂ reduction activity of CO dehydrogenase from *Rhodospirillum rubrum*. *Biochemistry*, *40*(25), 7604–7611. <https://doi.org/10.1021/bi002554k>
- Heyrovsky, J., & Babicka, J. (1930). Polarographic studies with the dropping mercury kathode.- Part XIII.- The effect of Albumins. *Collection of Czechoslovak Chemical Communications*.
- Higgins, S. R., Lau, C., Atanassov, P., Minteer, S. D., & Cooney, M. J. (2011). Hybrid Biofuel Cell: Microbial Fuel Cell with an Enzymatic Air-Breathing Cathode. *ACS Catalysis*, *1*(9), 994–997. <https://doi.org/10.1021/cs2003142>
- Hirsch, A. (2002). Functionalization of Single-Walled Carbon Nanotubes. *Angewandte Chemie International Edition*, *41*(11), 1853–1859. [https://doi.org/https://doi.org/10.1002/1521-3773\(20020603\)41:11<1853::AID-ANIE1853>3.0.CO;2-N](https://doi.org/https://doi.org/10.1002/1521-3773(20020603)41:11<1853::AID-ANIE1853>3.0.CO;2-N)
- Holzinger, M., Baur, J., Haddad, R., Wang, X., & Cosnier, S. (2011). Multiple functionalization of single-walled carbon nanotubes by dip coating. *Chem Comm*, 2450–2452. <https://doi.org/10.1039/c0cc03928d>
- Holzinger, M., Goff, A. Le, & Cosnier, S. (2017). Synergetic Effects of Combined Nanomaterials for Biosensing Applications. *Sensors*. <https://doi.org/10.3390/s17051010>
- Holzinger, M., Le Goff, A., & Cosnier, S. (2014). Nanomaterials for biosensing applications: a review. *Frontiers in Chemistry*, *2*, 63. <https://doi.org/10.3389/fchem.2014.00063>
- Horst, A. E. W., Mangold, K., & Holtmann, D. (2016). *Application of Gas Diffusion Electrodes in Bioelectrochemical Syntheses and Energy Conversion*. *113*(2), 260–267. <https://doi.org/10.1002/bit.25698>
- Huang, X., Zhang, L., Zhang, Z., Guo, S., Shang, H., Li, Y., & Liu, J. (2019). Wearable biofuel cells based on the classification of enzyme for high power outputs and lifetimes. *Biosensors & Bioelectronics*, *124–125*, 40–52. <https://doi.org/10.1016/j.bios.2018.09.086>
- Huber, H., Gallenberger, M., Jahn, U., Eylert, E., Berg, I. A., Kockelkorn, D., Eisenreich, W., & Fuchs, G. (2008). A dicarboxylate/4-hydroxybutyrate autotrophic carbon assimilation cycle in the hyperthermophilic Archaeum Ignicoccus hospitalis. *Proceedings of the National Academy of Sciences*, *105*(22), 7851 LP – 7856. <https://doi.org/10.1073/pnas.0801043105>
- IEA, I. E. A. (2020). *World Energy Balances 2020*. <https://www.iea.org/reports/world-energy-balances-overview>
- IEA, I. E. A. (2021). *Total primary energy supply (TPES) by source, World 1990-2018*.

- https://iea.blob.core.windows.net/assets/fffa1b7d-b0c5-4e64-86aa-5c9421832d73/WORLDBAL_Documentation.pdf
- Iijima, S. (1991). Helical microtubules of graphitic carbon. *Nature*, *354*, 56–58.
- Iijima, S., & Ichihashi, T. (1993). Single-shell carbon nanotubes of 1-nm diameter. *Nature*, *363*(6430), 603–605. <https://doi.org/10.1038/363603a0>
- Inoue, H., Nojima, H., & Okayama, H. (1990). High efficiency transformation of *Escherichia coli* with plasmids. *Gene*, *96*(1), 23–28. [https://doi.org/https://doi.org/10.1016/0378-1119\(90\)90336-P](https://doi.org/https://doi.org/10.1016/0378-1119(90)90336-P)
- Inoue, T., Takao, K., Fukuyama, Y., Yoshida, T., & Sako, Y. (2014). Over-expression of carbon monoxide dehydrogenase-I with an accessory protein co-expression: A key enzyme for carbon dioxide reduction. *Bioscience, Biotechnology and Biochemistry*, *78*(4), 582–587. <https://doi.org/10.1080/09168451.2014.890027>
- Inoue, T., Yoshida, T., Wada, K., Daifuku, T., Fukuyama, K., & Sako, Y. (2011). A simple, large-scale overexpression method of deriving carbon monoxide dehydrogenase II from thermophilic bacterium *Carboxydotherrmus hydrogenoformans*. *Bioscience, Biotechnology and Biochemistry*, *75*(7), 1392–1394. <https://doi.org/10.1271/bbb.110159>
- Jeon, W. B., Cheng, J., & Ludden, P. W. (2001). *Purification and Characterization of Membrane-associated CooC Protein and Its Functional Role in the Insertion of Nickel into Carbon Monoxide Dehydrogenase from Rhodospirillum rubrum* *. *276*(42), 38602–38609. [https://doi.org/10.1074/jbc.276\(42\), 38602-38609](https://doi.org/10.1074/jbc.276(42), 38602-38609)
- Jeon, W. B., Singer, S. W., Ludden, P. W., & Rubio, L. M. (2005). New insights into the mechanism of nickel insertion into carbon monoxide dehydrogenase: Analysis of *Rhodospirillum rubrum* carbon monoxide dehydrogenase variants with substituted ligands to the [Fe₃S₄] portion of the active-site C-cluster. *Journal of Biological Inorganic Chemistry*, *10*(8), 903–912. <https://doi.org/10.1007/s00775-005-0043-z>
- Jeoung, J.-H., & Dobbek, H. (2007). Carbon dioxide activation at the Ni,Fe-cluster of anaerobic carbon monoxide dehydrogenase. *Science (New York, N.Y.)*, *318*(5855), 1461–1464. <https://doi.org/10.1126/science.1148481>
- Jeoung, J. H., & Dobbek, H. (2007). Carbon dioxide activation at the Ni,Fe-cluster of anaerobic carbon monoxide dehydrogenase. *Science*, *318*(5855), 1461–1464. <https://doi.org/10.1126/science.1148481>
- Jeoung, J. H., & Dobbek, H. (2012). n-Butyl isocyanide oxidation at the [NiFe₄S₄O₄H₄] cluster of CO dehydrogenase. *Journal of Biological Inorganic Chemistry*, *17*(2), 167–173. <https://doi.org/10.1007/s00775-011-0839-y>
- Jeoung, J. H., Giese, T., Grünwald, M., & Dobbek, H. (2010). Crystal structure of the ATP-dependent maturation factor of Ni,Fe-containing carbon monoxide dehydrogenases. *Journal of Molecular Biology*, *396*(4), 1165–1179. <https://doi.org/10.1016/j.jmb.2009.12.062>
- Jeoung, J. H., Martins, B. M., & Dobbek, H. (2019). Carbon monoxide dehydrogenases. *Methods in Molecular Biology*, *1876*, 37–54. https://doi.org/10.1007/978-1-4939-8864-8_3
- Jeuken, L. J. C. (2003). Conformational reorganisation in interfacial protein electron transfer. *Biochimica et Biophysica Acta (BBA) - Bioenergetics*, *1604*, 67–76. [https://doi.org/10.1016/S0005-2728\(03\)00026-4](https://doi.org/10.1016/S0005-2728(03)00026-4)
- Karajanagi, S. S., Vertegel, A. A., Kane, R. S., & Dordick, J. S. (2004). Structure and Function of Enzymes Adsorbed onto Single-Walled Carbon Nanotubes. *Langmuir*,

- 20(26), 11594–11599. <https://doi.org/10.1021/la047994h>
- Karapinar, D., Zitolo, A., Huan, N., Zanna, S., & Taverna, D. (2020). Carbon-Nanotube-Supported Copper Polyphthalocyanine for Efficient and Selective Electrocatalytic CO₂ Reduction to CO. *Chem Sus Chem*, 173–179. <https://doi.org/10.1002/cssc.201902859>
- Karmann, S., Panke, S., & Zinn, M. (2019). Fed-batch cultivations of *Rhodospirillum rubrum* under multiple nutrient-limited growth conditions on syngas as a novel option to produce poly(3-hydroxybutyrate) (PHB). *Frontiers in Bioengineering and Biotechnology*, 7(APR), 1–11. <https://doi.org/10.3389/fbioe.2019.00059>
- Kerby, R. L., Ludden, P. W., & Roberts, G. P. (1995). Carbon monoxide-dependent growth of *Rhodospirillum rubrum*. *Journal of Bacteriology*, 177(8), 2241–2244. <https://doi.org/10.1128/jb.177.8.2241-2244.1995>
- Kerby, R. L., Ludden, P. W., & Roberts, G. P. (1997). In vivo nickel insertion into the carbon monoxide dehydrogenase of *Rhodospirillum rubrum*: Molecular and physiological characterization of cooCTJ. *Journal of Bacteriology*, 179(7), 2259–2266. <https://doi.org/10.1128/jb.179.7.2259-2266.1997>
- Kim, Y., Minami, N., Zhu, W., Kazaoui, S., Azumi, R., & Matsumoto, M. (2003). Langmuir–Blodgett Films of Single-Wall Carbon Nanotubes: Layer-by-layer Deposition and In-plane Orientation of Tubes. *Japanese Journal of Applied Physics*, 42(Part 1, No. 12), 7629–7634. <https://doi.org/10.1143/jjap.42.7629>
- King, G. M., & Weber, C. F. (2007). Distribution, diversity and ecology of aerobic CO-oxidizing bacteria. *Nature Reviews Microbiology*, 5(2), 107–118. <https://doi.org/10.1038/nrmicro1595>
- Knoche, K. L., Hickey, D. P., Milton, R. D., Curchoe, C. L., & Minteer, S. D. (2016). Hybrid Glucose/O₂ Biobattery and Supercapacitor Utilizing a Pseudocapacitive Dimethylferrocene Redox Polymer at the Bioanode. *ACS Energy Letters*, 1(2), 380–385. <https://doi.org/10.1021/acscenergylett.6b00225>
- Kontani, R., Tsujimura, S., & Kano, K. (2009). Air diffusion biocathode with CueO as electrocatalyst adsorbed on carbon particle-modified electrodes. *Bioelectrochemistry*, 76(1), 10–13. <https://doi.org/https://doi.org/10.1016/j.bioelechem.2009.02.009>
- Krajewska, B. (2004). Application of chitin- and chitosan-based materials for enzyme immobilizations: A review. *Enzyme and Microbial Technology*, 35, 126–139. <https://doi.org/10.1016/j.enzmictec.2003.12.013>
- Kramer, W. W., & McCrory, C. C. L. (2016). *Polymer coordination promotes selective CO₂ reduction by cobalt phthalocyanine*. 7(4). <https://doi.org/10.1039/c5sc04015a>
- Krzycki, J. A., Mortenson, L. E., & Prince, R. C. (1989). Paramagnetic centers of carbon monoxide dehydrogenase from acetivlastic *Methanosarcina barkeri*. *The Journal of Biological Chemistry*, 264(13), 7217–7221.
- Kung, Y., Doukov, T. I., Seravalli, J., Ragsdale, S. W., & Drennan, C. L. (2009). Crystallographic snapshots of cyanide- and water-bound C-clusters from bifunctional carbon monoxide dehydrogenase/acetyl-CoA synthase. *Biochemistry*, 48(31), 7432–7440. <https://doi.org/10.1021/bi900574h>
- Kung, Y., & Drennan, C. L. (2011). A role for nickel-iron cofactors in biological carbon monoxide and carbon dioxide utilization. *Current Opinion in Chemical Biology*, 15(2), 276–283. <https://doi.org/10.1016/j.cbpa.2010.11.005>
- Kung, Y., & Drennan, C. L. (2017). CHAPTER 7 One-Carbon Chemistry of Nickel-

- Containing Carbon Monoxide Dehydrogenase and Acetyl-CoA Synthase. In *The Biological Chemistry of Nickel* (pp. 121–148). The Royal Society of Chemistry. <https://doi.org/10.1039/9781788010580-00121>
- Küngas, R. (2020). Review — Electrochemical CO₂ Reduction for CO Production : Comparison of Low- and High-Temperature Electrolysis Technologies Review — Electrochemical CO₂ Reduction for CO Production : Comparison of Low- and High-Temperature Electrolysis Technologies. *Journal of the Electrochemical Society*. <https://doi.org/10.1149/1945-7111/ab7099>
- Kwon, O. S., Song, H. S., Park, T. H., & Jang, J. (2019). Conducting Nanomaterial Sensor Using Natural Receptors [Review-article]. *Chemical Reviews*, *119*(1), 36–93. <https://doi.org/10.1021/acs.chemrev.8b00159>
- Lalaoui, N., David, R., Jamet, H., Holzinger, M., Goff, A. Le, Cosnier, S., Lalaoui, N., David, R., Jamet, H., Holzinger, M., Goff, A. Le, & Cosnier, S. (2016). Hosting adamantane in the substrate pocket of laccase : direct bioelectrocatalytic reduction of O₂ on functionalized carbon nanotubes Hosting adamantane in the substrate pocket of laccase : direct bioelectrocatalytic reduction of O₂ on functionalized car. *ACS Catalysis*. <https://doi.org/10.1021/acscatal.6b00797>
- Lalaoui, N., Elouarzaki, K., Goff, A. Le, Holzinger, M., & Cosnier, S. (2013). Efficient direct oxygen reduction by laccases attached and oriented on pyrene-functionalized polypyrrole/carbon nanotube electrodes. *Chem. Commun.*, *49*(81), 9281–9283. <https://doi.org/10.1039/C3CC44994G>
- Lalaoui, N., Holzinger, M., Le Goff, A., & Cosnier, S. (2016). Diazonium Functionalisation of Carbon Nanotubes for Specific Orientation of Multicopper Oxidases: Controlling Electron Entry Points and Oxygen Diffusion to the Enzyme. *Chemistry – A European Journal*, *22*(30), 10494–10500. <https://doi.org/https://doi.org/10.1002/chem.201601377>
- Lalaoui, N., Le Goff, A., Holzinger, M., & Cosnier, S. (2015). Fully Oriented Bilirubin Oxidase on Porphyrin-Functionalized Carbon Nanotube Electrodes for Electrocatalytic Oxygen Reduction. *Chemistry – A European Journal*, *21*(47), 16868–16873. <https://doi.org/https://doi.org/10.1002/chem.201502377>
- Lalaoui, N., Poulpiquet, A. De, Haddad, R., Goff, A. Le, Holzinger, M., Mermoux, M., Infossi, P., Mano, N., Lojou, E., & Cosnier, S. (2015). A membraneless air-breathing hydrogen biofuel cell based on direct wiring of thermostable enzymes on carbon nanotube electrodes †. *Chem Comm, i*, 7447–7450. <https://doi.org/10.1039/c5cc02166a>
- Lazarus, O., Woolerton, T. W., Parkin, A., Lukey, M. J., Reisner, E., Seravalli, J., Pierce, E., Ragsdale, S. W., Sargent, F., & Armstrong, F. A. (2009). Water - Gas Shift Reaction Catalyzed by Redox Enzymes on Conducting Graphite Platelets. *JACS*, 14154–14155.
- Le Goff, A., & Holzinger, M. (2018). Molecular engineering of the bio/nano-interface for enzymatic electrocatalysis in fuel cells. *Sustainable Energy & Fuels*, 2555–2566. <https://doi.org/10.1039/c8se00374b>
- Le Goff, A., Holzinger, M., & Cosnier, S. (2015). Recent progress in oxygen-reducing laccase biocathodes for enzymatic biofuel cells. *Cellular and Molecular Life Sciences : CMLS*, *72*(5), 941–952. <https://doi.org/10.1007/s00018-014-1828-4>
- Le Goff, A., Moggia, F., Debou, N., Jegou, P., Artero, V., Fontecave, M., Jusselme, B., & Palacin, S. (2010). Facile and tunable functionalization of carbon nanotube electrodes with ferrocene by covalent coupling and π -stacking interactions and

- their relevance to glucose bio-sensing. *Journal of Electroanalytical Chemistry*, 641(1), 57–63. <https://doi.org/https://doi.org/10.1016/j.jelechem.2010.01.014>
- Léger, C., Jones, A. K., Albracht, S. P. J., & Armstrong, F. A. (2002). Effect of a Dispersion of Interfacial Electron Transfer Rates on Steady State Catalytic Electron Transport in [NiFe]-hydrogenase and Other Enzymes. *The Journal of Physical Chemistry B*, 106(50), 13058–13063. <https://doi.org/10.1021/jp0265687>
- Lehman, L. J., & Roberts, G. P. (1991). Identification of an alternative nitrogenase system in *Rhodospirillum rubrum*. *Journal of Bacteriology*, 173(18), 5705–5711. <https://doi.org/10.1128/jb.173.18.5705-5711.1991>
- Li, P., Liu, H., Ding, Y., Wang, Y., Chen, Y., Zhou, Y., Tang, Y., Wei, H., Cai, C., & Lu, T. (2012). Synthesis of water-soluble phosphonate functionalized single-walled carbon nanotubes and their applications in biosensing. *Journal of Materials Chemistry*, 22(30), 15370–15378. <https://doi.org/10.1039/C2JM31350B>
- Liang, F., Zhang, K., Zhang, L., Zhang, Y., Lei, Y., & Sun, X. (2021). Recent Development of Electrocatalytic CO₂ Reduction Application to Energy Conversion. *Small*, 2100323, 2100323. <https://doi.org/10.1002/sml.202100323>
- Lin, S., Diercks, C. S., Zhang, Y., Kornienko, N., Yaghi, O. M., & Chang, C. J. (2015). Covalent organic frameworks comprising cobalt porphyrins for catalytic CO₂ reduction in water. *Science*, 349(6253), 33–37.
- Lindahl, P. A. (2002). The Ni-containing carbon monoxide dehydrogenase family: Light at the end of the tunnel? *Biochemistry*, 41(7), 2097–2105. <https://doi.org/10.1021/bi015932+>
- Lindahl, P. A., & Ragsdale, S. W. (1990). CO Dehydrogenase from *Clostridium Thermoaceticum*. *Journal of Biological Chemistry*, 265(7), 3873–3879.
- Liu, H., Cui, Y., Li, P., Zhou, Y., Chen, Y., Tang, Y., & Lu, T. (2013). Polyphosphonate induced coacervation of chitosan: encapsulation of proteins/enzymes and their biosensing. *Analytica Chimica Acta*, 776, 24–30. <https://doi.org/10.1016/j.aca.2013.03.040>
- Liu, M., Pang, Y., Zhang, B., Luna, P. De, Voznyy, O., Xu, J., Zheng, X., Dinh, C. T., Fan, F., Cao, C., Arquer, F. P. G. De, Safaei, T. S., Mepham, A., Klinkova, A., Kumacheva, E., Filleter, T., Sinton, D., Kelley, S. O., & Sargent, E. H. (2016). Enhanced electrocatalytic CO₂ reduction via field-induced reagent concentration. *Nature*, 537(7620), 382–386. <https://doi.org/10.1038/nature19060>
- Logan, B. E., Rossi, R., Ragab, A., & Saikaly, P. E. (2020). Electroactive microorganisms in bioelectrochemical systems. *Nature Reviews Microbiology*, 1. <https://doi.org/10.1038/s41579-019-0173-x>
- Lu, Q., Rosen, J., Zhou, Y., Hutchings, G. S., Kimmel, Y. C., Chen, J. G., & Jiao, F. (2014). A selective and efficient electrocatalyst for carbon dioxide reduction. *Nature Communications*, 1–6. <https://doi.org/10.1038/ncomms4242>
- Mallakpour, S., & Soltanian, S. (2016). Surface functionalization of carbon nanotubes: fabrication and applications. *RSC Adv.*, 6(111), 109916–109935. <https://doi.org/10.1039/C6RA24522F>
- Maréchal, E. (2021). Carburants à base d'algues oléagineuses Principes , filières , verrous. *Techniques de L'ingénieur*, 33(0).
- Marietou, A., Røy, H., Jørgensen, B. B., & Kjeldsen, K. U. (2018). *Sulfate Transporters in Dissimilatory Sulfate Reducing Microorganisms : A Comparative Genomics Analysis*. 9(March), 1–21. <https://doi.org/10.3389/fmicb.2018.00309>
- Marques, M. C., Tapia, C., Gutiérrez-Sanz, O., Ramos, A. R., Keller, K. L., Wall, J. D., De

- Lacey, A. L., Matias, P. M., & Pereira, I. A. C. (2017). The direct role of selenocysteine in [NiFeSe] hydrogenase maturation and catalysis. *Nature Chemical Biology*, 13(5), 544–550. <https://doi.org/10.1038/nchembio.2335>
- Mastroleo, F., Monsieurs, P., & Leys, N. (2010). *Insight into the radiotolerance of the life support bacterium Rhodospirillum rubrum S1H by means of phenotypic and transcriptomic methods.*
- Matsuura, K., Saito, T., Okazaki, T., Ohshima, S., Yumura, M., & Iijima, S. (2006). Selectivity of water-soluble proteins in single-walled carbon nanotube dispersions. *Chemical Physics Letters*, 429(4), 497–502. <https://doi.org/https://doi.org/10.1016/j.cplett.2006.08.044>
- Maurin, A., & Robert, M. (2016). Noncovalent Immobilization of a Molecular Iron-Based Electrocatalyst on Carbon Electrodes for Selective, Efficient CO₂ - to - CO Conversion in Water. *JACS*, 3–6. <https://doi.org/10.1021/jacs.5b12652>
- Mazzei, L., Cianci, M., Benini, S., & Ciurli, S. (2019). The Structure of the Elusive Urease–Urea Complex Unveils the Mechanism of a Paradigmatic Nickel-Dependent Enzyme. *Angewandte Chemie International Edition*, 58(22), 7415–7419. <https://doi.org/10.1002/anie.201903565>
- Meneghello, M., Leger, C., & Fourmond, V. (2020). Electrochemical studies of CO₂ - reducing metalloenzymes. *Chemistry - A European Journal*. <https://doi.org/10.1002/chem.202102702>
- Meredith, M. T., Minson, M., Hickey, D., Artyushkova, K., Glatzhofer, D. T., & Minteer, S. D. (2011). Anthracene-Modified Multi-Walled Carbon Nanotubes as Direct Electron Transfer Scaffolds for Enzymatic Oxygen Reduction. *ACS Catalysis*, 1683–1690.
- Merrouch, M., Hadj-Said, J., Domnik, L., Dobbek, H., Leger, C., Dementin, S., & Fourmond, V. (2015). O₂ Inhibition of Ni-Containing CO Dehydrogenase Is Partly Reversible. *Chemistry - A European Journal*, 18934–18938. <https://doi.org/10.1002/chem.201502835>
- Meyer, O., & Schlegel, H. G. (1983). Biology of aerobic carbon monoxide-oxidizing bacteria. *Annual Review of Microbiology*, 37, 277–310. <https://doi.org/10.1146/annurev.mi.37.100183.001425>
- Migneault, I., Dartiguenave, C., Bertrand, M. J., & Waldron, K. C. (2004). Glutaraldehyde: behavior in aqueous solution, reaction with proteins, and application to enzyme crosslinking. *BioTechniques*, 37(5), 790–802. <https://doi.org/10.2144/04375RV01>
- Miller, M., Robinson, W. E., Oliveira, A. R., Heidary, N., Kornienko, N., Warnan, J., Pereira, I. P. A. C., & Reisner, E. (2019). Interfacing Formate Dehydrogenase with Metal Oxides for the Reversible Electrocatalysis and Solar-Driven Reduction of Carbon Dioxide. *Angewandte Chemie - International Edition*, 4601–4605. <https://doi.org/10.1002/anie.201814419>
- Miraula, M., Ciurli, S., & Zambelli, B. (2015). Intrinsic disorder and metal binding in UreG proteins from Archae hyperthermophiles: GTPase enzymes involved in the activation of Ni(II) dependent urease. *Journal of Biological Inorganic Chemistry : JBIC : A Publication of the Society of Biological Inorganic Chemistry*, 20(4), 739–755. <https://doi.org/10.1007/s00775-015-1261-7>
- Nanda, S., Li, K., Abatzoglou, N., Dalai, A. K., & Kozinski, J. A. (2017). Advancements and confinements in hydrogen production technologies. In *Bioenergy Systems for the Future: Prospects for Biofuels and Biohydrogen*. <https://doi.org/10.1016/B978-0->

- Nazaruk, E., Sadowska, K., Biernat, J. F., & Rogalski, J. (2010). Enzymatic electrodes nanostructured with functionalized carbon nanotubes for biofuel cell applications. *Anal Bioanal Chem*, 1651–1660. <https://doi.org/10.1007/s00216-010-4012-1>
- Nepal, D., & Geckeler, K. E. (2006). pH-sensitive dispersion and debundling of single-walled carbon nanotubes: lysozyme as a tool. *Small (Weinheim an Der Bergstrasse, Germany)*, 2(3), 406–412. <https://doi.org/10.1002/smll.200500351>
- Nevin, K. P., Woodard, T. L., Franks, A. E., Summers, Z. M., & Lovley, D. R. (2010). Microbial Electrosynthesis : Feeding Microbes Electricity To Convert Carbon Dioxide and Water to Multicarbon Extracellular Organic Compounds. *ASM Journals / MBio*, 1(2), 1–4. <https://doi.org/10.1128/mBio.00103-10>. Editor
- Newman, J. D., & Turner, A. P. F. (2005). Home blood glucose biosensors : a commercial perspective. *Biosensors & Bioelectronics*, 20, 2435–2453. <https://doi.org/10.1016/j.bios.2004.11.012>
- Nitopi, S., Bertheussen, E., Scott, S. B., Liu, X., Engstfeld, A. K., Horch, S., Seger, B., Stephens, I. E. L., Chan, K., Hahn, C., Nørskov, J. K., Jaramillo, T. F., & Chorkendor, I. (2019). *Progress and Perspectives of Electrochemical CO₂ Reduction on Copper in Aqueous Electrolyte*. <https://doi.org/10.1021/acs.chemrev.8b00705>
- Nitschke, W., McGlynn, S. E., Milner-white, E. J., & Russell, M. J. (2013). Biochimica et Biophysica Acta On the antiquity of metalloenzymes and their substrates in bioenergetics. *BBA - Bioenergetics*, 1827(8–9), 871–881. <https://doi.org/10.1016/j.bbabi.2013.02.008>
- Nybo, S. E., Khan, N. E., Woolston, B. M., & Curtis, W. R. (2015). Metabolic engineering in chemolithoautotrophic hosts for the production of fuels and chemicals. *Metabolic Engineering*, 30, 105–120. <https://doi.org/10.1016/j.ymben.2015.04.008>
- O’Connell, M. J. (2006). *Carbon Nanotubes Properties and Applications: Properties and Applications (1st ed.)*. CRC Press.
- Oelgeschläger, E., & Rother, M. (2008). Carbon monoxide-dependent energy metabolism in anaerobic bacteria and archaea. *Archives of Microbiology*, 190(3), 257–269. <https://doi.org/10.1007/s00203-008-0382-6>
- Osman, M. H., Shah, A. A., & Walsh, F. C. (2011). Recent progress and continuing challenges in bio-fuel cells. Part I: Enzymatic cells. *Biosensors and Bioelectronics*, 26(7), 3087–3102. <https://doi.org/https://doi.org/10.1016/j.bios.2011.01.004>
- Oughli, A. A., Conzuelo, F., Winkler, M., Happe, T., Lubitz, W., Schuhmann, W., Rüdiger, O., & Plumeré, N. (2015). A redox hydrogel protects the O₂-sensitive [FeFe]-hydrogenase from *Chlamydomonas reinhardtii* from oxidative damage. *Angewandte Chemie (International Ed. in English)*, 54(42), 12329–12333. <https://doi.org/10.1002/anie.201502776>
- Peng, B., Locascio, M., Zapol, P., Li, S., Mielke, S. L., Schatz, G. C., & Espinosa, H. D. (2008). Measurements of near-ultimate strength for multiwalled carbon nanotubes and irradiation-induced crosslinking improvements. *Nature Nanotechnology*, 3(10), 626–631. <https://doi.org/10.1038/nnano.2008.211>
- Plumeré, N., Rüdiger, O., Oughli, A. A., Williams, R., Vivekananthan, J., Pöller, S., Schuhmann, W., & Lubitz, W. (2014). A redox hydrogel protects hydrogenase from high-potential deactivation and oxygen damage. *Nature Chemistry*, 6(9), 822–827. <https://doi.org/10.1038/nchem.2022>
- Pop, E., Mann, D., Wang, Q., Goodson, K., & Dai, H. (2006). Thermal Conductance of an

- Individual Single-Wall Carbon Nanotube above Room Temperature. *Nano Letters*, 6(1), 96–100. <https://doi.org/10.1021/nl052145f>
- Ratnasamy, C., & Wagner, J. (2009). Water gas shift catalysis. *Catalysis Reviews - Science and Engineering*, 51(3), 325–440. <https://doi.org/10.1080/01614940903048661>
- Ren, S., Joulié, D., Salvatore, D., Torbensen, K., Wang, M., Robert, M., & Berlinguette, C. P. (2019). Molecular electrocatalysts can mediate fast, selective CO₂ reduction in a flow cell. *Science*, 369(July), 367–369.
- Reuillard, B., Le, A., Holzinger, M., & Cosnier, S. (2014). Non-covalent functionalization of carbon nanotubes with boronic acids for the wiring of glycosylated redox enzymes in oxygen-reducing. *Journal of Materials Chemistry B, Dcm*, 2228–2232. <https://doi.org/10.1039/c3tb21846e>
- Reuillard, B., Ly, K. H., Rosser, T. E., Kuehnel, M. F., Zebger, I., & Reisner, E. (2017). Tuning Product Selectivity for Aqueous CO₂ Reduction with a Mn(bipyridine)-pyrene Catalyst Immobilized on a Carbon Nanotube Electrode. *JACS*, 14425–14435. <https://doi.org/10.1021/jacs.7b06269>
- Revelles, O., Tarazona, N., García, J. L., & Prieto, M. A. (2016). Carbon roadmap from syngas to polyhydroxyalkanoates in *Rhodospirillum rubrum*. *Environmental Microbiology*, 18(2), 708–720. <https://doi.org/10.1111/1462-2920.13087>
- Riebeek, H. (2011). The Carbon Cycle. *Earth Observatory. NASA*. <https://earthobservatory.nasa.gov/features/CarbonCycle>
- Robb, F. T., & Techtmann, S. M. (2018). Life on the fringe: microbial adaptation to growth on carbon monoxide. *F1000Research*, 7(0), 1981. <https://doi.org/10.12688/f1000research.16059.1>
- Roberts, G. P., Kerby, R. L., Youn, H., & Conrad, M. (2005). CooA, a paradigm for gas sensing regulatory proteins. *Journal of Inorganic Biochemistry*, 99(1), 280–292. <https://doi.org/10.1016/j.jinorgbio.2004.10.032>
- Rountree, K. J., Mccarthy, B. D., Rountree, E. S., Eisenhart, T. T., & Dempsey, J. L. (2017). *A Practical Beginner's Guide to Cyclic Voltammetry*. <https://doi.org/10.1021/acs.jchemed.7b00361>
- Ruff, A., Szczesny, J., Zacarias, S., Pereira, I. A. C., Plumeré, N., & Schuhmann, W. (2017). Protection and Reactivation of the [NiFeSe] Hydrogenase from *Desulfovibrio vulgaris* Hildenborough under Oxidative Conditions. *ACS Energy Letters*, 2(5), 964–968. <https://doi.org/10.1021/acsenergylett.7b00167>
- Sakai, K., Kitazumi, Y., Shirai, O., Takagi, K., & Kano, K. (2016). Electrochemistry Communications Efficient bioelectrocatalytic CO₂ reduction on gas-diffusion-type biocathode with tungsten-containing formate dehydrogenase. *Electrochemistry Communications*, 73, 85–88. <https://doi.org/10.1016/j.elecom.2016.11.008>
- Saleem G., R., Ling, H., Wahyu, S., & Seunghun, H. (2003). Large-scale assembly of carbon nanotubes. *Nature*, 425(September), 36–37.
- Samanta, D., & Sarkar, A. (2011). Immobilization of bio-macromolecules on self-assembled monolayers: methods and sensor applications. *Chem. Soc. Rev.*, 40(5), 2567–2592. <https://doi.org/10.1039/C0CS00056F>
- Saran, N., Parikh, K., Suh, D., Mun, E., Kolla, H., & Manohar, S. K. (2004). Fabrication and Characterization of Thin Films of Single-Walled Carbon Nanotube Bundles on Flexible Plastic Substrates. *JACS*, 4462–4463.
- Scheiblbrandner, S., Breslmayr, E., Csarman, F., Paukner, R., Führer, J., Herzog, P. L.,

- Shleev, S. V., Osipov, E. M., Tikhonova, T. V., Popov, V. O., Haltrich, D., Ludwig, R., & Kittl, R. (2017). Evolving stability and pH-dependent activity of the high redox potential *Botrytis aclada* laccase for enzymatic fuel cells. *Scientific Reports*, 7(1), 13688. <https://doi.org/10.1038/s41598-017-13734-0>
- Schlager, S., Dibenedetto, A., Aresta, M., Apaydin, D. H., Dumitru, L. M., Neugebauer, H., & Sariciftci, N. S. (2017). Biocatalytic and Bioelectrocatalytic Approaches for the Reduction of Carbon Dioxide using Enzymes. *Energy Technology*, 5(6), 812–821. <https://doi.org/10.1002/ente.201600610>
- Schmitz, L. M., & Rosenthal, K. (2017). Enzyme-Based Electrobiotechnological Synthesis. *Adv Biochem Eng Biotechnol*. <https://doi.org/10.1007/10>
- Schoelmerich, M. C., & Müller, V. (2019). Energy-converting hydrogenases: the link between H₂ metabolism and energy conservation. *Cellular and Molecular Life Sciences*. <https://doi.org/10.1007/s00018-019-03329-5>
- Schulman, M., Parker, D., Ljungdahl, L. G., & Wood, H. G. (1972). Total synthesis of acetate from CO₂. V. Determination by mass analysis of the different types of acetate formed from 13 CO₂ by heterotrophic bacteria. *Journal of Bacteriology*, 109(2), 633–644. <https://doi.org/10.1128/jb.109.2.633-644.1972>
- Segura, F., & Andu, J. M. (2009). *Fuel cells : History and updating . A walk along two centuries*. 13, 2309–2322. <https://doi.org/10.1016/j.rser.2009.03.015>
- Sekretareva, A., Tian, S., Gounel, S., Mano, N., & Solomon, E. I. (2021). Electron Transfer to the Trinuclear Copper Cluster in Electrocatalysis by the Multicopper Oxidases. *Journal of the American Chemical Society*. <https://doi.org/10.1021/jacs.1c08456>
- Sell, D., & Kreysa, G. (1989). Use of an oxygen gas diffusion cathode at three-dimensional packed bed anode in a bioelectrochemical fuel cell. *Applied Microbiology Biotechnology*, 211–213.
- Shafer, W. D., Gnanamani, M. K., Graham, U. M., Yang, J., Masuku, C. M., Jacobs, G., & Davis, B. H. (2019). Fischer-tropsch: Product selectivity-the fingerprint of synthetic fuels. *Catalysts*, 9(3). <https://doi.org/10.3390/catal9030259>
- Sharkey, T. D. (2019). Discovery of the Canonical Calvin-Benson Cycle. *Photosynthesis Research*.
- Sheldon, R. A., & van Pelt, S. (2013). Enzyme immobilisation in biocatalysis: Why, what and how. *Chemical Society Reviews*, 42(15), 6223–6235. <https://doi.org/10.1039/c3cs60075k>
- Shin, W., Lee, S. H., Shin, J. W., Lee, S. P., & Kim, Y. (2003). Highly Selective Electrocatalytic Conversion of CO₂ to CO at -0.57 V (NHE) by Carbon Monoxide Dehydrogenase from *Moorella thermoacetica*. *JACS*, 14688–14689.
- Singh, P., Campidelli, S., Giordani, S., Bonifazi, D., Bianco, A., & Prato, M. (2009). Organic functionalisation and characterisation of single-walled carbon nanotubes. *Chem. Soc. Rev.*, 38(8), 2214–2230. <https://doi.org/10.1039/B518111A>
- So, K., Kitazumi, Y., Shirai, O., Nishikawa, K., Higuchi, Y., & Kano, K. (2016). Direct electron transfer-type dual gas diffusion H₂/O₂ biofuel cells. *J. Mater. Chem. A*, 4(22), 8742–8749. <https://doi.org/10.1039/C6TA02654K>
- Soboh, B., Linder, D., & Hedderich, R. (2002). Purification and catalytic properties of a CO-oxidizing: H₂-evolving enzyme complex from *Carboxydotherrmus hydrogenoformans*. *European Journal of Biochemistry*, 269(22), 5712–5721. <https://doi.org/10.1046/j.1432-1033.2002.03282.x>
- Sokol, K. P., Robinson, W. E., Oliveira, A. R., Warnan, J., Nowaczyk, M. M., Pereira, A.

- C., Reisner, E., & Ru, A. (2018). Photoreduction of CO₂ with a Formate Dehydrogenase Driven by Photosystem II Using a Semi-artificial Z - Scheme Architecture. *JACS*. <https://doi.org/10.1021/jacs.8b10247>
- Sokol, K. P., Robinson, W. E., Oliveira, A. R., Zacarias, S., Lee, C., Pereira, A. C., Reisner, E., Madden, C., Bassegoda, A., & Hirst, J. (2019). Reversible and Selective Interconversion of Hydrogen and Carbon Dioxide into Formate by a Semi-artificial Formate Hydrogenlyase Mimic. *JACS*, *2*(1), 0–4. <https://doi.org/10.1021/jacs.9b09575>
- Sokolova, T. G., Henstra, A., Sipma, J., Parshina, S. N., Stams, A. J. M., & Lebedinsky, A. V. (2009). *Diversity and ecophysiological features of thermophilic carboxydophilic anaerobes*. <https://doi.org/10.1111/j.1574-6941.2009.00663.x>
- Sosna, M., Boer, H., & Bartlett, P. N. (2013). A His-tagged *Melanocarpus albomyces* laccase and its electrochemistry upon immobilisation on NTA-modified electrodes and in conducting polymer films. *Chem Phys Chem*, *14*(10), 2225–2231. <https://doi.org/10.1002/cphc.201300340>
- Spangler, N. J., Lindahl, P. A., Bandarian, V., & Ludden, P. W. (1996). Spectroelectrochemical characterization of the metal centers in carbon monoxide dehydrogenase (CODH) and nickel-deficient CODH from *Rhodospirillum rubrum*. *Journal of Biological Chemistry*, *271*(14), 7973–7977. <https://doi.org/10.1074/jbc.271.14.7973>
- Spangler, N. J., Meyers, M. R., Gierke, K. L., Kerby, R. L., Roberts, G. P., & Ludden, P. W. (1998). *Substitution of Valine for Histidine 265 in Carbon Monoxide Dehydrogenase from Rhodospirillum rubrum Affects Activity and Spectroscopic States* *. *273*(7), 4059–4064.
- Spath, P. L., & Dayton, D. C. (2003). Preliminary Screening -- Technical and Economic Assessment of Synthesis Gas to Fuels and Chemicals with Emphasis on the Potential for Biomass-Derived Syngas. *National Renewable Energy Laboratory, December*, 1–160. <https://doi.org/10.2172/15006100>
- Stratas Advisors. (2016). *Global Trends in Syngas*.
- Styring, P., Quadrelli, E. A., & Armstrong, K. (2015). Preface. In *Carbon Dioxide Utilisation: Closing the Carbon Cycle: First Edition* (pp. xv–xxiv). <https://doi.org/10.1016/B978-0-444-62746-9.05001-5>
- Sun, L., Huang, Z., Reddu, V., Su, T., & Fisher, A. C. (2020). A Planar, Conjugated N₄-Macrocyclic Cobalt Complex for Heterogeneous Electrocatalytic CO₂ Reduction with High Activity. *Angewandte Chemie (International Ed. in English)*, 17104–17109. <https://doi.org/10.1002/ange.202007445>
- Svetlichny, V. A., Sokolova, T. G., Gerhardt, M., Ringpfeil, M., Kostrikina, N. A., & Zavarzin, G. A. (1991). *Carboxydotherrmus hydrogenoformans* gen. nov., sp. nov., a CO-utilizing Thermophilic Anaerobic Bacterium from Hydrothermal Environments of Kunashir Island. *Systematic and Applied Microbiology*, *14*(3), 254–260. [https://doi.org/10.1016/S0723-2020\(11\)80377-2](https://doi.org/10.1016/S0723-2020(11)80377-2)
- Svetlitchnyi, V., Peschel, C., Acker, G., & Meyer, O. (2001). Two membrane-associated NiFeS-carbon monoxide dehydrogenases from the anaerobic carbon-monoxide-utilizing eubacterium *Carboxydotherrmus hydrogenoformans*. *Journal of Bacteriology*, *183*(17), 5134–5144. <https://doi.org/10.1128/JB.183.17.5134-5144.2001>
- Takanabe, K., & Rodionov, V. (2016). Simultaneous Reduction of CO₂ and Splitting of H₂O by a Single Immobilized Cobalt Phthalocyanine Electrocatalyst. *ACS Catalysis*.

- <https://doi.org/10.1021/acscatal.6b00543>
- Tarasevich, M. R., Yaropolov, A. I., Bogdanovskaya, V. A., & Varfolomeev, S. D. (1979). Electrocatalysis of a cathodic oxygen reduction by laccase. *Journal of Electroanalytical Chemistry and Interfacial Electrochemistry*, *104*, 393–403. [https://doi.org/https://doi.org/10.1016/S0022-0728\(79\)81047-5](https://doi.org/https://doi.org/10.1016/S0022-0728(79)81047-5)
- Tartakovsky, B., Manuel, M., Neburchilov, V., Wang, H., & Guiot, S. R. (2008). Biocatalyzed hydrogen production in a continuous flow microbial fuel cell with a gas phase cathode. *Journal of Power Sources*, *182*, 291–297. <https://doi.org/10.1016/j.jpowsour.2008.03.062>
- Tartakovsky, B., Manuel, M., Wang, H., & Guiot, S. R. (2009). High rate membrane-less microbial electrolysis cell for continuous hydrogen production. *International Journal of Hydrogen Energy*, *34*(2), 672–677. <https://doi.org/10.1016/j.ijhydene.2008.11.003>
- Tielmann, P., Kierkels, H., Zonta, A., Ilie, A., & Reetz, M. T. (2014). Increasing the activity and enantioselectivity of lipases by sol-gel immobilization: further advancements of practical interest. *Nanoscale*, *6*(12), 6220–6228. <https://doi.org/10.1039/c3nr06317h>
- Timm, J., Brochier-Armanet, C., Perard, J., Zambelli, B., Ollagnier-De-Choudens, S., Ciurli, S., & Cavazza, C. (2017). The CO dehydrogenase accessory protein CooT is a novel nickel-binding protein. *Metallomics*, *9*(5), 575–583. <https://doi.org/10.1039/c7mt00063d>
- Tiquia-arashiro, S. M. (2014). Thermophilic Carboxydrotrophs and Their Applications in Biotechnology. Chapter 2. *Extremophilic Bacteria*, *10*(October 2014), 973–978. <https://doi.org/10.1007/978-3-319-11873-4>
- Torbensen, K., Boudy, B., Joulié, D., Wolff, N. Von, & Robert, M. (2020). Emergence of CO₂ electrolyzers including supported molecular catalysts. *Current Opinion in Electrochemistry*. <https://doi.org/10.1016/j.coelec.2020.07.001>
- Ünlü, A., Duman-Özdamar, Z. E., Çaloğlu, B., & Binay, B. (2021). Enzymes for Efficient CO₂ Conversion. *Protein Journal*, *June*. <https://doi.org/10.1007/s10930-021-10007-8>
- Vashist, S. K., Zheng, D., Al-Rubeaan, K., Luong, J. H. T., & Sheu, F.-S. (2011). Advances in carbon nanotube based electrochemical sensors for bioanalytical applications. *Biotechnology Advances*, *29*(2), 169–188. <https://doi.org/10.1016/j.biotechadv.2010.10.002>
- Vidakovic-Koch, T. (2019). Electron Transfer Between Enzymes and Electrodes. In F. Harnisch & D. Holtmann (Eds.), *Bioelectrosynthesis* (pp. 39–85). Springer International Publishing. https://doi.org/10.1007/10_2017_42
- Villalonga, R., Cao, R., & Fragoso, A. (2007). Supramolecular chemistry of cyclodextrins in enzyme technology. *Chemical Reviews*, *107*(7), 3088–3116. <https://doi.org/10.1021/cr050253g>
- Wächtershäuser, G. (2006). From volcanic origins of chemoautotrophic life to Bacteria, Archaea and Eukarya. *Philosophical Transactions of the Royal Society B: Biological Sciences*, *361*(1474), 1787–1806. <https://doi.org/10.1098/rstb.2006.1904>
- Wang, J., Vine, C. E., Balasiny, B. K., Rizk, J., Bradley, C. L., Tinajero-Trejo, M., Poole, R. K., Bergaust, L. L., Bakken, L. R., & Cole, J. A. (2016). The roles of the hybrid cluster protein, Hcp and its reductase, Hcr, in high affinity nitric oxide reduction that protects anaerobic cultures of *Escherichia coli* against nitrosative stress. *Molecular Microbiology*, *100*(5), 877–892. <https://doi.org/10.1111/mmi.13356>

- Wang, M., Chen, L., Lau, T., & Robert, M. (2018). Hybrid Catalysis A Hybrid Co Quaterpyridine Complex / Carbon Nanotube Catalytic Material for CO₂ Reduction in Water. *Angewandte Chemie (International Ed. in English)*, 2(Cl), 7769–7773. <https://doi.org/10.1002/anie.201802792>
- Wang, M., Torbensen, K., Salvatore, D., Ren, S., Joulié, D., Dumoulin, F., Mendoza, D., Lassalle-kaiser, B., Umit, I., Berlinguette, C. P., & Robert, M. (2019). CO₂ electrochemical catalytic reduction with a highly active cobalt phthalocyanine. *Nature Communications*. <https://doi.org/10.1038/s41467-019-11542-w>
- Wang, V. C.-C., Can, M., Pierce, E., Ragsdale, S. W., & Armstrong, F. A. (2013). A unified electrocatalytic description of the action of inhibitors of nickel carbon monoxide dehydrogenase. *Journal of the American Chemical Society*, 135(6), 2198–2206. <https://doi.org/10.1021/ja308493k>
- Wang, V. C.-C., Islam, S. T. A., Can, M., Ragsdale, S. W., & Armstrong, F. A. (2015). Investigations by Protein Film Electrochemistry of Alternative Reactions of Nickel-Containing Carbon Monoxide Dehydrogenase. *The Journal of Physical Chemistry. B*, 119(43), 13690–13697. <https://doi.org/10.1021/acs.jpcc.5b03098>
- Wang, V. C.-C., Ragsdale, S. W., & Armstrong, F. A. (2013). Investigations of Two Bidirectional Carbon Monoxide Dehydrogenases from *Carboxydotherrmus hydrogenoformans* by Protein Film Electrochemistry. *ChemBioChem*, 14(14), 1845–1851. <https://doi.org/https://doi.org/10.1002/cbic.201300270>
- Watt, R. K., & Ludden, P. W. (1998). The Identification, Purification, and Characterization of *CooJ*. *Journal of Biological Chemistry*, 273(16), 10019–10025. <https://doi.org/10.1074/jbc.273.16.10019>
- Watt, R. K., & Ludden, P. W. (1999). Ni²⁺ Transport and Accumulation in *Rhodospirillum rubrum*. *Journal of Bacteriology*, 181(15), 4554–4560.
- Weaver, P. (1971). Temperature-sensitive mutations of the photosynthetic apparatus of *Rhodospirillum rubrum*. *Proceedings of the National Academy of Sciences of the United States of America*, 68(1), 136–138. <https://doi.org/10.1073/pnas.68.1.136>
- Wei, B. Q., Vajtai, R., & Ajayan, P. M. (2001). Reliability and current carrying capacity of carbon nanotubes. *Applied Physics Letters*, 79(8), 1172–1174. <https://doi.org/10.1063/1.1396632>
- Windsor, L. J., & Steele, D. L. (2010). Expression of recombinant matrix metalloproteinases in *Escherichia coli*. *Methods in Molecular Biology (Clifton, N.J.)*, 622, 67–81. https://doi.org/10.1007/978-1-60327-299-5_4
- Wittenborn, E. C., Cohen, S. E., Merrouch, M., Léger, C., Fourmond, V., Dementin, S., & Drennan, C. L. (2019a). Structural insight into metallofactor maturation in carbon monoxide dehydrogenase. *Journal of Biological Chemistry*, 294(35), 13017–13026. <https://doi.org/10.1074/jbc.RA119.009610>
- Wittenborn, E. C., Cohen, X. S. E., Merrouch, M., Léger, X. C., Fourmond, X. V., Dementin, S., & Drennan, X. C. L. (2019b). *Structural insight into metallofactor maturation in carbon monoxide dehydrogenase*. 294, 13017–13026. <https://doi.org/10.1074/jbc.RA119.009610>
- Wittenborn, E. C., Guendon, C., Merrouch, M., Benvenuti, M., Fourmond, V., Léger, C., Drennan, C. L., & Dementin, S. (2020). The Solvent-Exposed Fe-S D-Cluster Contributes to Oxygen-Resistance in *Desulfovibrio vulgaris* Ni-Fe Carbon Monoxide Dehydrogenase. *ACS Catalysis*, 10(13), 7328–7335. <https://doi.org/10.1021/acscatal.0c00934>
- Wittenborn, E. C., Merrouch, M., Ueda, C., Fradale, L., Fourmond, V., Leger, C.,

- Pandelia, M., Dementin, S., & Drennan, C. L. (2018). *Redox-dependent rearrangements of the NiFeS cluster of carbon monoxide dehydrogenase*. 1–17.
- Wong, L. S., Khan, F., & Micklefield, J. (2009). *Selective Covalent Protein Immobilization : Strategies and Applications*. 4025–4053.
- Woolerton, T. W., Sheard, S., Pierce, E., Ragsdale, W., & Armstrong, F. A. (2011). CO₂ photoreduction at enzyme-modified metal oxide nanoparticles †. *Energy & Environmental Science*, 2393–2399. <https://doi.org/10.1039/c0ee00780c>
- Woolerton, T. W., Sheard, S., Reisner, E., Pierce, E., Ragsdale, S. W., & Armstrong, F. A. (2010). Efficient and Clean Photoreduction of CO₂ to CO by Enzyme-Modified TiO₂ Nanoparticles Using Visible Light. *JACS*, 2132–2133.
- Wu, M., Ren, Q., Scott Durkin, A., Daugherty, S. C., Brinkac, L. M., Dodson, R. J., Madupu, R., Sullivan, S. A., Kolonay, J. F., Nelson, W. C., Tallon, L. J., Jones, K. M., Ulrich, L. E., Gonzalez, J. M., Zhulin, I. B., Robb, F. T., & Eisen, J. A. (2005). Life in hot carbon monoxide: The complete genome sequence of carboxydotherrmus hydrogenoformans Z-2901. *PLoS Genetics*, 1(5), 563–574. <https://doi.org/10.1371/journal.pgen.0010065>
- Yaropolov, A. I., Tarasevich, M. R., & Varfolomeev, S. D. (1978). 192 - Electrochemical Properties of Peroxidase. *Bioelectrochemistry and Bioenergetics*, 5(1), 18–24. [https://doi.org/https://doi.org/10.1016/0302-4598\(87\)87002-2](https://doi.org/https://doi.org/10.1016/0302-4598(87)87002-2)
- Younesi, H., Najafpour, G., Ku Ismail, K. S., Mohamed, A. R., & Kamaruddin, A. H. (2008). Biohydrogen production in a continuous stirred tank bioreactor from synthesis gas by anaerobic photosynthetic bacterium: Rhodospirillum rubrum. *Bioresource Technology*, 99(7), 2612–2619. <https://doi.org/10.1016/j.biortech.2007.04.059>
- Yuan, M., Sahin, S., Cai, R., Abdellaoui, S., Hickey, D. P., Minter, S. D., & Milton, R. D. (2018). Redox Polymers Creating a Low-Potential Redox Polymer for Efficient Electroenzymatic CO₂ Reduction. *Angewandte Chemie - International Edition*, 6582–6586. <https://doi.org/10.1002/anie.201803397>
- Zambelli, B., Uversky, V. N., & Ciurli, S. (2016). Biochimica et Biophysica Acta Nickel impact on human health : An intrinsic disorder perspective. *BBA - Proteins and Proteomics*, 1864(12), 1714–1731. <https://doi.org/10.1016/j.bbapap.2016.09.008>
- Zhang, M., Fang, S., Zakhidov, A. A., Lee, S. B., Aliev, A. E., Williams, C. D., Atkinson, K. R., & Baughman, R. H. (2005). Strong, transparent, multifunctional, carbon nanotube sheets. *Science (New York, N.Y.)*, 309(5738), 1215–1219. <https://doi.org/10.1126/science.1115311>
- Zhang, X., Wu, Z., Zhang, X., Li, L., Li, Y., Xu, H., Li, X., & Yu, X. (2017). Highly selective and active CO₂ reduction electro- catalysts based on cobalt phthalocyanine/carbon nanotube hybrid structures. *Nature Communications*, March, 1–8. <https://doi.org/10.1038/ncomms14675>
- Zhou, Y., Fang, Y., & Ramasamy, R. P. (2019). Non-covalent functionalization of carbon nanotubes for electrochemical biosensor development. *Sensors (Switzerland)*, 19(2). <https://doi.org/10.3390/s19020392>
- Zhu, W., Zhang, Y., Zhang, H., Lv, H., Li, Q., Michalsky, R., Peterson, A. A., & Sun, S. (2014). Active and Selective Conversion of CO₂ to CO on Ultrathin Au Nanowires. *JACS*.
- Zhuangchun, W., Zhihong, C., Xu, D., M., L. J., Jennifer, S., Maria, N., Katalin, K., R., R. J., B., T. D., F., H. A., & G., R. A. (2004). Transparent, Conductive Carbon Nanotube Films. *Science*, 305(5688), 1273–1276. <https://doi.org/10.1126/science.1101243>

CO₂ metabolism plays a fundamental role in biology, as it represents a “building block” for the synthesis of organic molecules in living organisms. On the other hand, the excessive CO₂ emissions due to human activity in recent decades requires today the search for effective solutions dedicated to the closure of the carbon cycle. Thus, it is interesting to develop some alternatives inspired by nature. In particular, carbon monoxide dehydrogenase (CODH) catalyzes the reversible reduction of CO₂ to CO and represents an attractive biocatalyst in terms of activity, selectivity, ability to operate in mild conditions with low overpotentials. In addition, it does not require high production costs and uses earth abundant-metals. For these reasons, several studies have been conducted on [NiFe]-CODHs for applications in electrocatalytic CO₂ reduction reaction (CO₂RR). [NiFe]-CODHs consist of a complex multimetallic NiFe₄S₄ active site, unique in biology, and additional FeS clusters involved in the electron transfer from the buried active site to the protein surface. Here, we present a novel and efficient method to overproduce the fully active recombinant [NiFe]-CODH from *Rhodospirillum rubrum* in the easy-to-handle bacteria *E. coli*. We also developed the stable and favorable immobilization of the enzyme on non-covalently functionalized carbon nanotubes (CNTs), subsequently integrated in a gas-diffusion electrode device. This device has comparable performance to molecular and metal catalysts for CO₂RR. To go further, the understanding of the intramolecular electron transfer within the enzyme has been undertaken, in order to optimize its capacity to work in direct electron transfer with the electrode. Other optimizations are considered, such as the direct evolution of the enzyme to provide a better resistance towards O₂. All together, the results of this work have paved the way to study and use this powerful biocatalyst in the near future for biotechnological applications.

Le métabolisme du CO₂ joue un rôle fondamental en biologie, car il représente un "élément de base" pour la synthèse de molécules organiques chez les organismes vivants. D'autre part, les émissions excessives de CO₂ dues à l'activité humaine au cours des dernières décennies, nécessite aujourd'hui la recherche de solutions efficaces dédiées à la fermeture du cycle du carbone. Ainsi, il est intéressant de développer certaines alternatives inspirées de la nature. En particulier, la monoxyde de carbone deshydrogénase (CODH) catalyse la réduction réversible du CO₂ en CO et représente un biocatalyseur intéressant en termes d'activité, de sélectivité et de capacité à fonctionner dans des conditions douces avec de faibles surtensions. En outre, sa production est économiquement intéressante et est basée sur l'utilisation des métaux abondants sur terre. Pour ces raisons, plusieurs études ont été menées sur les [NiFe]-CODH pour des applications dans des réactions de réduction du CO₂ (CO₂RR). Les [NiFe]-CODH sont constituées d'un site actif complexe multi-métallique NiFe₄S₄, unique en biologie, et de centres FeS additionnels impliqués dans le transfert d'électrons du site actif enfoui au sein de la protéine jusqu'à la surface de la protéine. Au cours de la thèse, nous avons développé une nouvelle méthode efficace pour surproduire la [NiFe]-CODH recombinante active de *Rhodospirillum rubrum* chez la bactérie *Escherichia coli*, largement utilisé en biotechnologie. Nous avons également développé l'immobilisation stable et favorable de l'enzyme sur des nanotubes de carbone (CNTs) fonctionnalisés de manière non covalente, intégrés dans un dispositif d'électrode de diffusion de gaz. Ce dispositif possède des performances comparables à celles des catalyseurs moléculaires et métalliques pour le CO₂RR. Pour aller plus loin, la compréhension du transfert d'électrons intramoléculaire au sein de l'enzyme a été entreprise, afin d'optimiser sa capacité à travailler en transfert direct d'électrons vers l'électrode. D'autres optimisations sont envisagées, comme l'évolution dirigée de l'enzyme vers une meilleure résistance à l'O₂. Dans l'ensemble, les résultats de ce travail ont ouvert une nouvelle voie pour étudier et utiliser ce puissant biocatalyseur dans un avenir proche pour des applications biotechnologiques.